TECHNISCHE UNIVERSITÄT MÜNCHEN
FAKULTÄT FÜR MASCHINENWESEN

Defect evaluation with superimposed 3D thermo-tomography model

Somen Dutta, M.Sc.

Vollständiger Abdruck der von der Fakultät für Maschinenwesen der Technischen Universität München zur Erlangung des akademischen Grades eines

Doktor-Ingenieurs

genehmigten Dissertation.

Vorsitzender :

Prof. Dr.-Ing. Christian Große

Prüfer der Dissertation :

1. Prof. Dr.-Ing. Klaus Drechsler
2. Prof. Dr.-Ing. Michael Kupke

Die Dissertation wurde am 11.07.2019 bei der Technischen Universität München eingereicht und durch die Fakultät für Maschinenwesen am 23.04.2020 angenommen.

Defect evaluation with superimposed 3D thermo-tomography model

Automated 3D model generation and defect localisation of thermography measurement results on large components utilising an industrial robot and a laser system

A DISSERTATION SUBMITTED TO THE CHAIR OF CARBON
COMPOSITES AND THE FACULTY GRADUATE CENTER
MECHANICAL ENGINEERING OF
THE TECHNICAL UNIVERSITY OF MUNICH

IN PARTIAL FULFILMENT OF THE REQUIREMENTS FOR THE ACADEMIC
DEGREE Dr.-Ing.

by

Somen Dutta

Augsburg July 12, 2019

First Reviewer :

Univ.-Prof. Dr.-Ing. Klaus Drechsler
Technical University of Munich, Department of Mechanical Engineering TUM,
Head of the Chair of Carbon Composites

Director of the Institute Fraunhofer Research Institution for Casting,
Composite and Processing Technology IGCV

Second Reviewer :

Univ.-Prof. Dr.-Ing. Michael Kupke
Augsburg University, (MRM) Institute of Materials Resource Management
Chair of Polymer Composites Technology

German Aerospace Center (DLR), Institute of Structures and Design (IBT),
Head of Center for Lightweight Production Technology (ZLP), Augsburg

Mentor :

Dr.-Ing. Alfons Schuster
German Aerospace Center (DLR), Institute of Structures and Design (IBT),
Group leader for Production Integrated Quality Assurance at (ZLP), Augsburg

Acknowledgements

This research was conducted during my work as a scientific assistant at the Center for Lightweight Production Technology (ZLP) Augsburg, a department of the Institute of Structures and Design (IBT). At this point I would like to thank everyone who contributed to the success of this work.

The dissertation was submitted at the Institute for Carbon Composites, Faculty of Mechanical Engineering, Technical University Munich, Germany. I would like to specially thank Prof. Dr.-Ing. Klaus Drechsler for the given scope to accomplish the dissertation at TUM, for his supervision and for his constructive suggestions.

My sincere thanks goes to Prof. Dr.-Ing. Michael Kupke, serving as second advisor, for his time and interest in reviewing the thesis. Further, I would like to thank him for several hours of discussion and his valuable suggestions.

I would like to sincerely thank Prof. Dr.-Ing. Heinz Voggenreiter for his motivation, support, and trust and for the freedom he gave me in the implementation of this work. Further, I would like to thank him for the excellent working environment. To the same extent, I would like to express my gratitude to Dr. Wolfgang Dudenhausen for his trust since my recruitment and his outstanding support in the form of intensive discussions during the topic-finding phase.

I express my deepest thanks to my group leader, mentor and colleague Dr. Alfons Schuster, who contributed valuable technical input to my thesis and who also gave me confidence in my own work. Furthermore, I am particularly indebted for his good ideas and enduring encouragement.

I gratefully acknowledge Thomas Schmidt, in particular for his research on hand-eye calibration, and Christoph Frommel for the discussion about their cooperative research work. An essential part of my work is based on their great work. The experiment of this thesis would not have been conducted if Florian Krebs and Monika Mayer had not integrated the thermography system into a robot cell. Thanks for their contribution. I am deeply indebted to many colleagues at ZLP who have supported me in the course of crafting this thesis and contributed to its development. My experience also originated from my colleagues at the Center for Lightweight and Production Technology. Their technical and personal support within many discussions, conversations and chats challenged my research and added useful ideas.This thesis would not have been close to where it is if several dedicated students had not gone through the pains of working with me.

Last, but not least, I would like to thank my wife for supporting me in all aspects of life. I would most probably not be here today to write my thesis without her sacrifices. I am very grateful that I could always count on you. I dedicate my milestone to my 4 old year daughter Moksha as a recognition that I couldn't spend valuable time with her. I hope that she will understand one day.

Abstract

Automated inline quality assurance with NDT systems like thermography on a large aircraft component (e.g. fuselage sections, wing structures etc.) is still a major challenge for industry. These challenges basically lie in the system accuracy, NDT process time and in analysis of information gained from the measurement result. The system accuracy challenge can basically be divided into positioning and path planning for a robot-based automated NDT system. Robot tool-centre-point (TCP) positional accuracy depends mostly on the robot pose and its orientation. Many other factors like gravitational or deflecting forces may affect the absolute positional accuracy of robot TCP positions. For example, ± 0.1 ° absolute robot inaccuracy (TCP) can cause for 1 meter working distance up to ± 1.74 mm positional error. Each individual NDT process step needs to be optimised to reduce the complete process time. A major drawback of a thermography system is that certified examiners evaluate every 2D-thermography image per measuring field one by one. This unwieldy and less intuitive method for a large amount of numerical data is inappropriate for industrial applications. There are plenty of existing methods and technologies for 3D texture mapping like the stereo vision method, using 3D features, or the multi-view method. These methods require either a second camera or time-consuming additional processes like several images taken from different views for each single measuring field. Furthermore, the measurement results should be used to improve the product.

This work introduces the development of a prototype robot based thermography measuring system for rapid automated inspection of complex geometrical composite components and a new method for 3D visualisation of thermography results, which minimises the drawbacks described above. Full-scale evaluation in 3D component coordinates gives complex but complete 3D error propagation information. The DLR-PQS department is working on two different methods to calculate 2D-3D camera projection parameters. The first approach is the 3D-visualisation method using a thermography camera, which is also used for NDT, and a laser system mounted above the robotic cell, which eliminates the uncertainty of robot position accuracy. Through an easy calibration process, within a few minutes the laser system is calibrated to the component coordinate systems and projects predefined 3D points for every measuring field. These 3D points are captured by the thermography camera; afterwards a 2D-3D point correspondence algorithm is applied to calculate 2D-3D camera projection parameters. The second method uses the robot pose and a kinematic-coordinate-relationships algorithm is applied to the images. For both methods, single thermal images are captured using a thermography camera. The first method is suited for research and development as well as for production inspection with or without using a robot for camera positioning, while the second method requires a robot. The first method also enables contactless localisation of detected defects. The accuracy, reproducibility and flexibility of both methods are compared and discussed in this work. The 3D results are imported directly into the CAD environment for further structural analysis and to close the manufacturing loop. Furthermore, a 3D thermo-tomography model with superimposed manufacturing information is introduced. The 3D thermo-tomography model represents thermography measurements results according to their thermal penetration depth. Thus the evaluation time, which influences the total NDT process time, can be reduced. The improvements achieved in development are accuracy, reliability, time savings and the interlinking of measurement data with CAD and manufacturing data.

The proposed systems and methods are evaluated and verified experimentally. Experimental results are carried out to demonstrate the feasibility of the implementation and introduce the applicable measuring scope for the in-line quality assurance with the first prototype measuring system of this type. This work describes the design of the measuring system, analyses the process chain of implemented methods and evaluates their accuracy in an automated production environment, and outlines of test the results obtained from the prototype system.

Contents

List of Figures

List of Tables

Acronyms and Symbols

Acronyms

2D	Two-dimensional
3D	Three-dimensional
ACUT	Air-coupled ultrasonic testing
BAM	Bundesanstalt für Materialforschung und -prüfung
$\mathrm{BT_C}$	Transformation between component and camera coordinates
C	Camera coordinate
CCD	Charge-coupled device
CAD	Computer-aided design
CFRP	Carbon fibre reinforced plastics
CPD	Composite part design
CT	Computed tomography
DLR	German Aerospace Center
DLT	Direct linear transformation
E1	External axis 1
EPnP	Efficient perspective-n-Point
IGES	Initial graphics exchange specification
IQZ	Inline Qualitätssicherungszelle
HA	High accuracy
HEC	Hand-eye calibration
Hz	Hertz
FACC	Fischer Advanced Composite Components
FPAs	focal plane arrays
$\mathrm{FT_C}$	Transformation between flange and camera coordinates
IR	Infrared
KRC	Kuka robot control
LIN	Linear movement
LHM	LU Hager Method
LT	Laser tracker
mk	Milli kelvin
MFZ	Multifunktionalen Zelle
MSP	Multi-sided probe

NCFs	Non-crimp fabric
NDI	Non-destructive inspection
NDT	Non-destructive testing
OLP	Off-line programming
PQS	Production Integrated Quality Assurance
PnP	Perspective-n-Point
PPnP	Procrustes perspective-n-Point
PTFE	Polytetrafluorethylen
PTP	Point to point movement
QA	Quality assurance
RFST	Resonant frequency sweep thermography
RMS	Root Mean Square
ROI	Region of interest
BT_R	Transformation between robot and component coordinates
RT_F	Transformation between robot and flange coordinates
SA	Special Analyzer
SNR	Signal-to-noise ratio
STL	Standard triangulation/tessellation language
SVD	Singular value decomposition
TCP	Tool-centre-point
TEZ	Technologie Erprobungszelle
VAP	Vacuum assisted process
VARI	Vacuum assisted resin infusion process
VRML	Virtual reality modelling language
W	World coordinate
WCUS	Water-coupled ultrasonic
WT_B	Transformation between world and component coordinates
WT_R	Transformation between world and robot coordinates
XML	Extensible markup language
ZLP	Center for Lightweight Production Technology

Symbols

Symbol	**Designations**
α	Thermal diffusivity
α_c	Skew
λ	Scalar product of the equation of a plane
$\Delta\phi$	Aperture angle of lens
μ	Thermal penetration depth
a	x coefficient of the equation of a plane
b	y coefficient of the equation of a plane
c	z coefficient of the equation of a plane

$\mathbf{c}$	Virtual control point in camera coordinate
d	Distance
f	Focal length
f	Measurement frequency
h	Distance between camera and object
i	Counting variable
k	Constant
k_c	Radial distortion coefficient
$\bar{p}_i$, $\bar{q}_i$	Set of corresponding points
r_x, r_y, r_z	Coordinate directions
s	Skew
t	Translational vector in $\mathbb{R}^3$
w	Assigned element to transfer a image point from cartesian coordinate into homogeneous coordinate
x	x direction of a point in image plane
$\bar{x}$	x direction of a point in homogenous image plane
y	y direction of a point in image plan
$\bar{y}$	y direction of a point in homogenous image plan
x_0, y_0	Principal point
C	Camera coordinate
C_{Plane}	Camera plane
C_M or C_m	Centroid of points
D	Diagonal matrix for singular value decomposition
I_{Plane}	Image plane
J_X, J_Y, J_Z	Moment of inertia in X, Y and Z directions
K	Intrinsic matrix 3×3
M	Transformations matrix 4×4
P	Projections matrix 3×4
R	Rotational matrix 3×3
$R_x(\alpha)$	Euler angle rotation in x direction
$R_y(\beta)$	Euler angle rotation in y direction
$R_z(\gamma)$	Euler angle rotation in z direction
X peak	Image coordinates in X and Y direction
X	x direction of a point in object, camera or world coordinate
$\bar{X}$	x direction of a point in homogenous object or world coordinate
Y	y direction of a point in object, camera or world coordinate
$\bar{Y}$	y direction of a point in homogenous object or world coordinate
Z	z direction of a point in object, camera or world coordinate
$\bar{Z}$	z direction of a point in homogenous object or world coordinate
$\mathbb{R}^3$	Three dimensional euclidean space
$\mathbb{P}^3$	Three dimensional projective space
$\mathbb{R}^2$	Two dimensional euclidean space
$\mathbb{P}^2$	Two dimensional projective space

Chapter 1

Introduction

1.1 Motivation

Over the last decades the demand for carbon fibre composites components is increasing in the automobile and particularly aerospace industries [2]. Industries desire to cope with the increased demand, as most of those components are still manufactured manually. All of this adds up to a development with a long lead time, amount of manual labour leading to cost inefficiency connected to a high scrap rate and finally too small of a throughput. An economical and automated production process may help to meet the industrial target. Starting with the design and analysis of modern composite materials, new strategies, tools and testing method need to be developed to certify the production process. One can observe that a change in composite production towards automation has already started [3]. But these automated manufacturing processes are new compared to metallic industry. The goal is to improve the automation level in the manufacturing technology, reduce the manufacturing cost and improve the part's quality. An improved rework rate will lead to a higher output at production. It may actually be imaginable to decrease the amount of testing at the final stage. A final quality approval based on a few samples or random checks could be possible. Such a major change in a QA strategy needs to be certified for sure. Nevertheless, a higher degree of flexible automation in measurement and evaluation is necessary to enable a continuous improvement. Besides the final inspection of components, NDT can be used during manufacturing in terms of monitoring and even control of process quality. Therefore, every manufacturing process step in the production line should be monitored to improve the added value without derogating the quality of the components. The aim of Inline-QA is to detect manufacturing failure of CFRP component as early as possible and during the process. Implementing new measuring and evaluation technology throughout the production line could be the key to avoid or minimise the manufacturing irregularity. One such measurement system must meet the following criteria: being contactless, having higher measurement speed, easy-to-interpret, being automatic and obviously economic. Inspection tools also must meet measurement specifications for complex and large components at high speeds. On the other side process integrated NDT has to fulfil the requirements of industrial production concerning integrability and data management. NDT has to deliver proper indicators to evaluate the quality of a part or structure. Quality control with NDT combines the advantages of both classical methods of process control: on the one hand, the collected statistics data will assist to develop the manufacturing process and on the other hand, monitoring of process variables. The aerospace industry relies on non-destructive testing (NDT) methods to detect and characterise the manufacturing induced defects. As a part of the production integrated NDT for CFRP components it is necessary to automate the NDT Inspections system. Additionally, the aerospace industry has a very strict regime on quality assurance which is obvious because safety is one of the most important aspects. These issues are to be addressed in the near future to make the use of composites successful. The NDT methods need to be highly accurate, flexible and defect selective. Additionally, all NDT technologies need to be certified to withstand aerospace requirements as well as the ability to deliver the same throughput at production. Otherwise NDT ends up as a bottleneck that holds up the assembly of structures and then produces high costs. Using NDT methods in a wider range could support the development of robust production processes in the future.

1.2 Quality assurance in CFRP production line and industrial applications

This process chain in figure 1.1 with dry fibre placement for the production of CFRP components is subdivided into eight main manufacturing steps: 1.) Cutting of Plys, 2.) Fibre Placement, 3.) Preforming, 4.)Vacuum bagging, 5.) Resin infiltration, 6.) curing and 7.) with subsequent de-bagging or de-moulding and 8.) further processing or finishing of the CFRP component. Most of the process steps are still done manually. Inspection between each step is only done visually or acoustically on a very qualitative scale. Quality assurance takes place but it is more or less only documented if each step was performed. But no information about how accurate it was or what size or location of anomaly was detected.

The final quality check is usually performed by classical ultrasonic inspection. In nearly all cases water coupled ultrasonic inspection is the choice [4]. The inspection machines reach from gantry solutions with linear and rotational axis using submersion and squirter technology (see figure 1.2). A sampled phased array in transmission and pulse/echo finds a very wide spread usage. However, water coupling delivers disadvantages like pressure variations and therefore amplitude variations, air-bubbles, lime scales and algae on the components. Also, incoming water can destroy the component by freezing, as some of these CFRP components are porous, depending on CFRP manufacturing technology. Therefore these components have to be sealed before the quality check. Although new machines with high accuracy

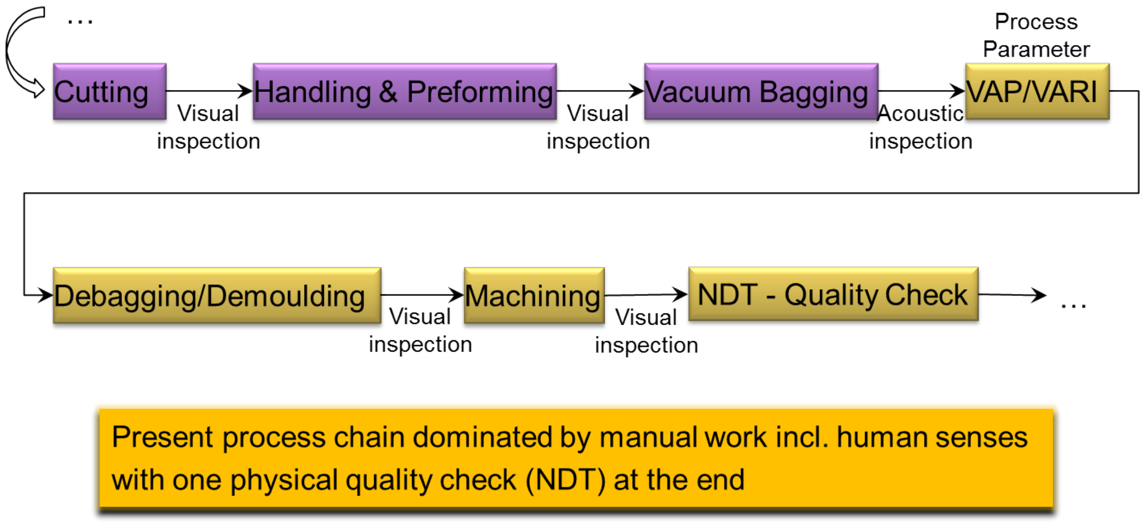

Figure 1.1: Visual inspection in CFRP production line | Source: Paper 16 in 5th International Trade Fair for Automation and Mechatronics

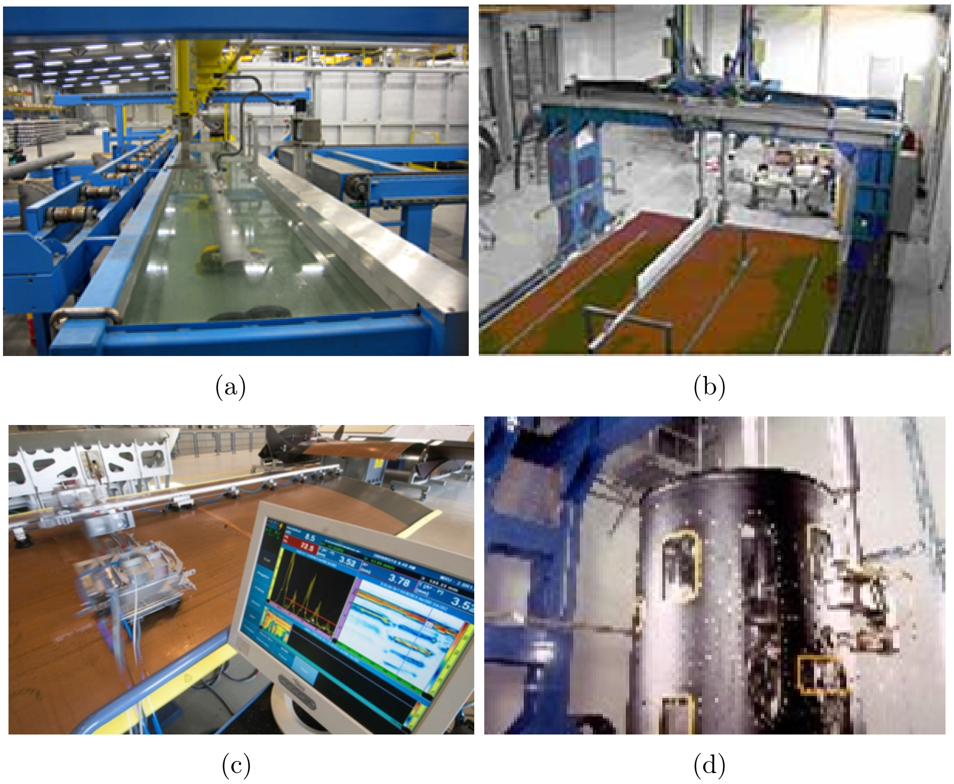
(a) (b) (c) (d)

Figure 1.2: Water coupled ultrasonic inspection | Source: National Composite Network, Premium Aerotec, Intelligent NDT, HPI

and speed as well as new ultrasonic transducers are being developed the scanning time has still a big influence on lead time. In addition to that the maintenance cost for this machines are high. Furthermore water coupled Ultrasonic measurements results are evaluated by examiners in 2D with so called C-Scan images, which consumes unnecessary time and effort. For some clinical and industrial applications 3D ultrasound visualisation techniques are developed [5] [6]. Evaluation and defect localisation in 3D may improve the automation, as simulation results, design and manufacturing informations are available in 3D. With a continuous 3D documentation process, all informations can be superimposed.
Searching a NDT method that is suitable to cover all needs, such as contactless, accurate, of high performance, able to integrate into existing production scenarios, research at ZLP Augsburg amongst others is focused on active thermography. Using industrial robots as manipulators one could achieve a very flexible and highly accurate solution with the highest rate of automation. The choice of active thermography was made because it is capable to visualise defects on dry carbon fibre preforms as well as on cured parts. This capability fulfils the requirements to detect features like missing roving, fuzz-balls or even the fibre orientation on textile preforms. The more common use is to detect anomalies in cured parts such as delamination, dry spots, porosity or dis-bondings. Unlike ultrasound technology which needs water as a couple medium and huge water tank, thermography instruments are flexible and components are low-maintenance. Thermography provides a high sensitivity for most defects, high accuracy in locating defects and mostly used in reflection mode, which is important for complex and large aerospace components. Furthermore, due to focal plane array detector, a large area can be measured comparatively in much less time than ultrasound inspection. There are different components, such as not load-bearing structures, huge surfaces with less than 6 mm thickness. By measuring these components with thermography the load of water coupled ultrasonic machine can be relieved. Recently, for the first time FACC [7] has qualified thermography inspection method for CFRP components and has reduced the inspection time up to 50 %, although measurement is conducted manually. The author of the paper [8] showed a strategy to the user for implementing new testing solutions for industrial thermography application. Mahler and Eitzinger presented [9] a concept for robot-based automated thermography for the automobile industry. The main limitation of IR-thermography is that, it is purely two dimensional technique, while the observed object has a non-planar geometry. In addition to the individual automation approaches and concepts, there are also individual solutions or examples for the 3D representation of the measurement results. There are several mathematical approaches and also software to purchase, e.g. "PhotoModeller", to establish a relationship between the image acquisition and the associated 3D models. In the visible range there are numerous application possibilities. In the infrared range, however, there are only a handful of examples for special applications. The first theoretical results were delivered by Wiedenmann [10]. They investigated the possibility of using a thermographic camera to apply the strip projection principle to the infrared. In

principle, this is possible and especially conceivable for weakly reflecting structures, but the geometric resolution of available infrared cameras allows only low-resolution results. The Federal Institute for Materials Research and Testing (BAM) [11] also investigated whether strip light projection can simultaneously serve as thermal excitation for active thermographic testing. However, a parallel application of the two methods with the same light source would not be possible because the energy input is too low for thermography. A much higher power density or longer illumination time would be necessary. Carl and Eisler [12] investigated the same principle, a thermal fringe projection. In this case, however, with an infrared laser. While the excitation power was now sufficient, they failed due to the large calibration effort. They therefore moved away from 3D data acquisition and concentrated on manually superimposing thermographic data on CAD data. Coneardone [13] presented a possible application. Here temperature values were assigned to the measurement object. The component with a test surface of 16 x 12 cm was installed in a testing device (wind tunnel) and a calibration plate was mounted in the background to calculate the camera position. Special holes were drilled on the calibration plate, which serve as correspondence marks, in order to achieve a better emissivity difference to the component. Thus the camera position to the component could be determined for this or a single image and the infrared image could be assigned to the 3D component. The method is not flexible enough to test different parts that are larger than the camera's field of view. As little research is carried out in this area so far, technological development and research for automated single view 3D model generation and defect localisation of thermography measurements is still necessary for industrial applications.

1.3 Physical principle of thermography and its equipment

In this section, the physical principles of thermography and general technical implementation of equipment is described in short. IR-thermography distinguishes between passive and active methods, where active thermography is a fast and accurate non-destructive evaluation technique, and is of particular relevance to the aerospace industry for the inspection of primary and secondary structures. thermography means the representation of objects by making use of the information provided through emitted thermal electromagnetic radiation. As all NDT methods, the active thermography method is also used to excite the component from the outside with preferred excitation method and its thermal response behaviour is used to characterize the component. Figure 1.3 represents technically implemented and purchasable excitation sources.

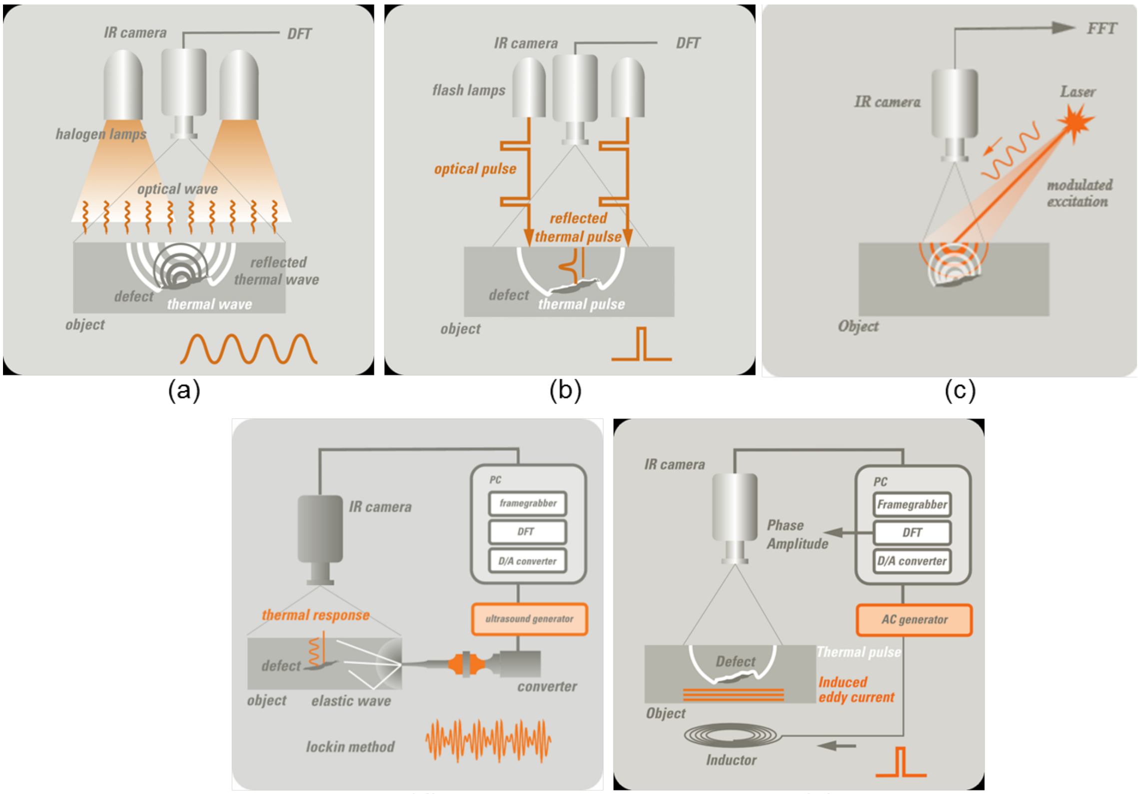

(a) (b) (c)

(d) (e)

Source: Edevis GmbH | www. Edevis.com

Figure 1.3: Thermography modulation methods: (a) Lock-in thermography (b) Pulse thermography (c) Laser thermography(d) Ultrasonic thermography and (e) Induction thermography

The most circulated excitation sources for industrial applications are e.g. halogen or flash lamps. Besides traditional optical excitation, there are other excitation methods such as elastic waves (ultrasonic) or by electrical losses (resistance heating, eddy current). In general all excitation methods differ physically between optical, ultrasonic, inductive and convective methods.

Optical excitation

Optical excitation causes a thermal imbalance in the component by means of lamps over the whole surface or by means of a laser beam point by point. As with most types of excitation, a distinction is made between pulse excitation (pulse thermography) and periodic excitation (lock-in thermography). For lock-in thermography, components are excited explicitly with one specific wavelength. Averages are then over several periods are calculated to adjust the signal-to-noise ratio (SNR), specifically to increase the thermal depth. Hereby, for Pulse thermography, a short high-energy pulse of a few ms is generated, which has a broad spectrum of thermal wavelengths. According to the surface, characteristic parts of the optical rays will be reflected, absorbed and transmitted. This photo thermal measuring method enables the measurement of the thermal response behaviour at a sample point. In case the defects are not too deep below the surface, they influence the amplitude or phase of the detector signal. The decisive value here is the thermal penetration depth μ (mm), which depends on the modulation frequency f and the thermal diffusivity α (mm^2/s) of the material:

$$\mu = \sqrt{\frac{\alpha}{\pi f}} \tag{1.1}$$

With all these excitation methods, the object is heated locally and starts temperature compensation processes, depending on the material properties. The temporary temperature differences on the object surface can be captured with a thermal camera. The captured thermal emissivity signal over measurement time (depending on modulation frequency) will be transformed through discrete Fourier transformation in amplitude and phase image. For amplitude image thermal depth is μ, whereby for phase image 2μ. For further detailed information refer to [14].

Ultrasonic excitation

The ultrasonic thermography method belongs to one of the defect selective methods. In contrast to non-contact optical excitation, this method uses a mechanical coupling of a sonotrode to thermally excite the component. The temperature profile is generated thereby on the surface of the component, which is recorded with a thermographic camera. The flow of ultrasounds in main material is disturbed due to anomalies in internal friction or absorption, which lead to change in characteristic temperature distribution. Thermal effects are to be expected at defects, where boundary friction or plastic deformation converts from mechanical energy to thermal energy. Therefore ultrasound activated thermography is a defect selective NDT-technique as only defects to be detected are heated while the substrate ideally remains unaffected. Furthermore there are several investigation methods with this technique to characterise certain defects in certain materials. A short overview of the developed technique can be found in Rahamer [15], where this technology is developed to a further extent, which is called resonant frequency sweep thermography (RFST).

Inductive excitation

Another excitation method for active thermography is induction thermography or pulsed eddy current thermography, which uses electromagnetic pulses to excite eddy currents in electrically conductive materials. According to the law of induction, a magnet field (changes with time) will be generated by using a coil with eddy currents. This generates heat by resistive losses and releases heat. The heat can be detected on the surface by an infrared camera. Compare to other excitation methods, inductive method is not flexible, as the geometry of the coil needs to be adjusted according to the component's shape. Moreover this technology is practicable only for defects like cracks, which are close to surface. Although this method was used to investigate a few CFRP components, the strong dependence of induction on the top layer orientation and the poor coupling of the individual layers have so far prevented industrial success. Riegert [16] carried out a comprehensive study about induction thermography for CFRP materials.

For thermographic testing it is decisive which temperature differences are realised at which locations, at what times and with which modulation by the respective excitation source. These characteristics have to be selected and adapted for each examination in order to induce optimal heat shots with regard to the defect detectability. Thermal excitation of test objects is either continuous, amplitude modulated or pulsed. In a recent paper [17] authors have analysed in detail different excitation methods in numerous examples with different damage scenarios and aerospace components.

Thermography Camera

A thermography system includes the thermography camera on the one hand and the excitation method with the respective regulation and control unit on the other. The cameras available in the market today differ fundamentally and are sorted in two different detector types. These are uncooled micro bolometer detector and cooled high end Quantum detector. With the help of cooled detector technology, thermal resolution below 20 mk can be distinguished. Moreover they differentiate between hand held and stationary systems. The high end cameras now have a cooled photon detector of (2,048 x 1,536) IR-pixels [18], which allows efficiently measuring the smallest structures on large-scale objects. Also Bolometer camera offers 25 mk thermal resolution with (1,024 x 768) IR-Pixels. These high detector resolution brings advantages towards industrial applications, as large scale components can be measured in extraordinarily less time. Furthermore, the thermal cameras work in different wavelength ranges. Specialised thermal imaging cameras offers focal plane arrays (FPAs) with mid-wavelength ($3\,\mu m - 5\,\mu m$) and with longer wavelengths ($7\,\mu m - 14\,\mu m$). For the investigation of CFRP components, however, medium wavy detectors are more suitable, since most of the radiation is emitted in this range. The long-wave camera is more suitable for use at higher temperatures. Furthermore, the integration time of the camera and the possibility of external triggers play a key role in the industrialisation of the method. Looking at the thermographic cameras offered by Flir and Infratec, the above mentioned properties are present.

1.4 Scope of the work

The key performance indicators for production integrated thermography are measuring speed, interpretability, economic efficiency, reliability and also flexibility. Most of these requirements (except for the high flexibility at large complex component) can be achieved by means of a measuring system (laboratory unit) and its integration into a robot system. Therefore, in this thesis a flexible thermographic end-effector, which would be integrated in a different robotic cell, has to be developed. This prototype end-effector should be developed from already existing laboratory systems. As the complexity of this work is significantly dependent on the component geometry, the development of end-effector was focused on for single and multiple curved aeronautical components. Since the use of robots for precise component inspection is still problematic today, the physical influences on system accuracy of the proposed system are to be analysed scientifically and verified experimentally. Furthermore, entire process chain will be examined in this thesis and a road map for the improvement and process extension of the evaluation method will be derived. In order to validate the developed system through out the work the dry fibre placement in combination with the thermography was chosen as use case.

The main goal of the work is the reproducible, complete thermography measurement, in both a production line (robot-based) and the laboratory. One issue that exists so far is the interpretation of the obtained thermographic results, as the thermal diffusivity of materials is influenced not only by defects in the material, but also by the geometric properties of the test specimen. Significant progress and a competitive advantage would be a thermographic inspection system that can filter out the geometric influences. The integrated viewing of thermographic test data and surface information results brings numerous advantages for the industrial test environment. For example, artefacts from thermographic testing can be assigned to specific surface properties and geometric structures, such as edges or holes, can be evaluated thus more precisely. Since repeated measurement must be carried out regularly for aircraft maintenance, and the test results are clearly assigned thanks to their 3D location information, earlier measurement results can be compared. Therefore, all individual 2D thermography images must be assigned to 3D components for both robot-based measurement and for laboratory application. Since the camera position plays an essential role for the 3D representation of the component, an alternative method is required besides the common procedure, where the camera position and orientation are derived from the robot position data. For this purpose, a concept will be developed and the feasibility will be systematically examined in this thesis work. Another aim is to create 3D thermographic maps for 3D defect localisation. To identify the advantages and disadvantages of both methods for 3D visualisation and defect localisation, both methods will be validated on at least one demonstrator. In order to monitor and even to control the process quality, a closed-loop manufacturing process will be developed and exemplary validated. Figure 1.4 represents the building blocks for the closed-loop manufacturing process, which will ensure the knowledge from automated manufacturing process an reuse them with NDT inspection data in order to analyse in an adequate environment.

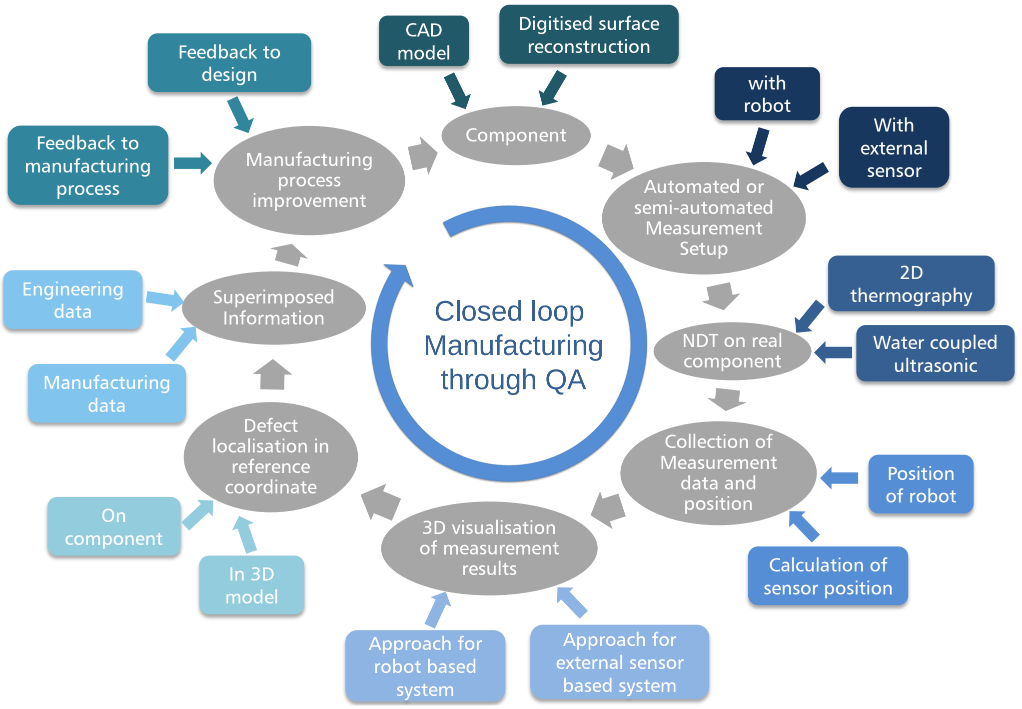

Figure 1.4: Closed-loop manufacturing process

The following aspects will be researched in detail in this thesis: How can flexible and contactless features be placed on the component in order to determine a camera pose without robot data? Which additional sensors and process steps will be required for 3D reconstruction? Which method can be applied to superimpose 2D thermographic images with 3D simulations and manufacturing information, in order to precisely evaluate on the production line as well as in laboratory application? Is this new method of 3D visualisation more advantageous than the most applied robot-based camera pose calculation? Is a contactless visualisation of defect size and position on component possible? In order to develop the measurement method and clarify the above research aspects the following topics will be discussed academically:

- Basics of geometric projection
- Geometric and hand-eye camera calibration
- Influence of intrinsic and extrinsic parameters on 3D visualisation results
- Geometry measurement and surface reconstruction of manufactured components for the 3D reconstruction
- Mathematical approaches for planar and non-planner 3D reconstruction methods

Chapter 2

Production integrated automated thermography

Preliminary tests in the laboratory stage and individual industrial applications show a great potential for the further development of automated thermography in the CFRP production line. The aim is to find a comprehensive solution that allows integration of automated thermography measurement in existing and also in new production lines with minimum effort. During the manufacturing process, it is desirable to examine parts to confirm they are defect free and fit for service without their destruction. In order to design a thermographic end-effector for industrial applications, the operating conditions must already be clarified at the beginning of the design. For this purpose, large CFRP components from aviation were assumed as boundary conditions. Large object measurements are always difficult and very expensive to automate. Because most large objects are bigger than the working envelope of measuring machines. Using industrial robots as manipulators one could achieve a very flexible and highly accurate solution with the highest rate of automation.Therefore DLR Augsburg and KUKA Systems have developed 3 different robotic cells, namely TEZ, MFZ and IQZ, (figure 2.1)which are flexible enough and solve the automation purpose. Both the automated NDT method and the automated production method of CFRP components are developed in these robotic cells. The "Multifunktionalezelle (MFZ)" work cell in figure 2.1(c) consists of 4 major gantry portals. Each of them has a move- and tiltable vertical axis with a robotic arm at its end. The entire working volume (32 m x 15 m x 7m - LxWxH)can be split into quadrants to allow parallel work on different projects. The goal was to demonstrate and perform active thermography within this work cell. As mentioned, a work cell is huge in its dimension, so the decision was made to proceed in several steps. One of the reasons is risk mitigation; therefore, the first concepts were started on a smaller scale. As shown in figure 2.1(a), integration of the thermography setup was started on "Technologieerprobungszelle (TEZ)" work cell that consists of a 15 m long linear axis, which is mounted on the ground. The linear axis carries two robots. Both have a nominal reach of 3000 mm in diameter at a load capacity of 210kg. Later on the system was integrated in "Inline-Qualitätssicherungszelle (IQZ)" Work cell 2.1(b). Robot-based automated thermography also means the development of an automated process chain that enables reproducible measurement. It must be ensured that all areas of the component (without gaps) are measured with the same camera orientation and distance. This also means development of a method to determine the camera TCP. Since the measurement is contactless and several measuring positions are required to cover a large component area, offline path planning is required to create the robot program. Furthermore, the measuring system must not collide with the component during measurement.

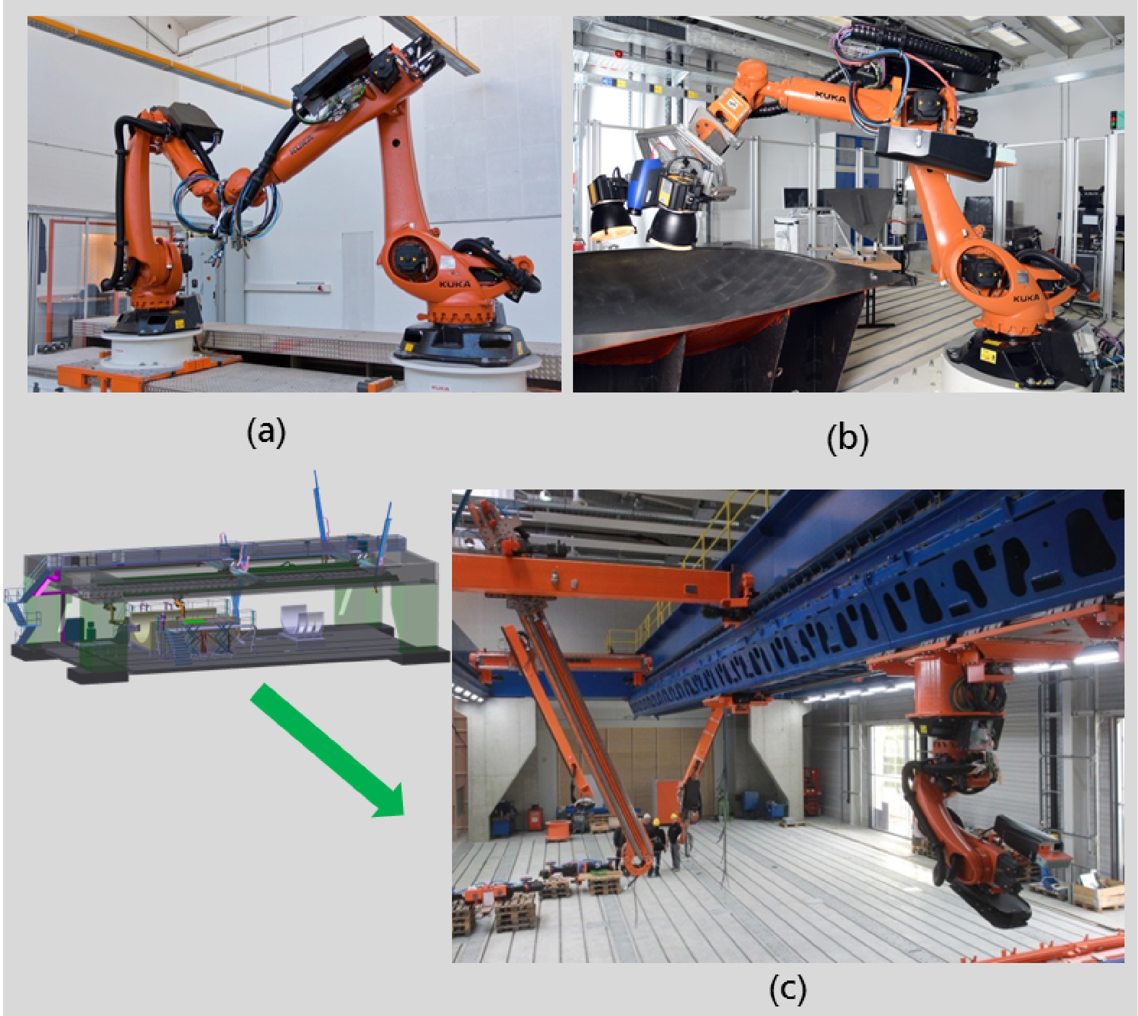

Figure 2.1: Robotic cells: (a) Robot with linear axis (TEZ) (b) High accuracy robot without linear axis (IQZ)(c) Robot from hanging linear axis (MFZ)

2.1 Development and integration of prototype end-effectors

End-effector development

The thermography system, which was bought as a laboratory setup (see figure 2.3 (a)), consists of 4 main parts: the robot control system (KRC), the thermography control system including Dim Pack and Flash Generator, the measuring devices including IR-camera, halogen lamps and flash lamps, and the DLR network system (see figure 2.2). Each of these four systems contains the relevant electronics, mechanics and software for its special functionality. For thermography it is important that the measuring surface is excited homogeneously. For this purpose, the camera and lamp orientation must be adapted for the complex 3D geometry. This requirement must be met by the end effector to be developed. The developed measuring systems consists of two or more halogen lamps and an integrated IR-thermography camera, which is mounted on an industrial robot as a fully automated test head to ensure reliable defect detection in the component (See figure 2.3 (b) and (c)). This measuring system is designed to achieve homogenous excited measuring filed and it is convenient to measure 3D complex components. The end-effector is designed so that it can be converted into a laboratory system for testing small components (See figure 2.3 (a). The orientation of lamps and camera to the component are to be adjusted manually for the prototype design, but can be motorised later. It is intended to gain initial experience with this end-effector.

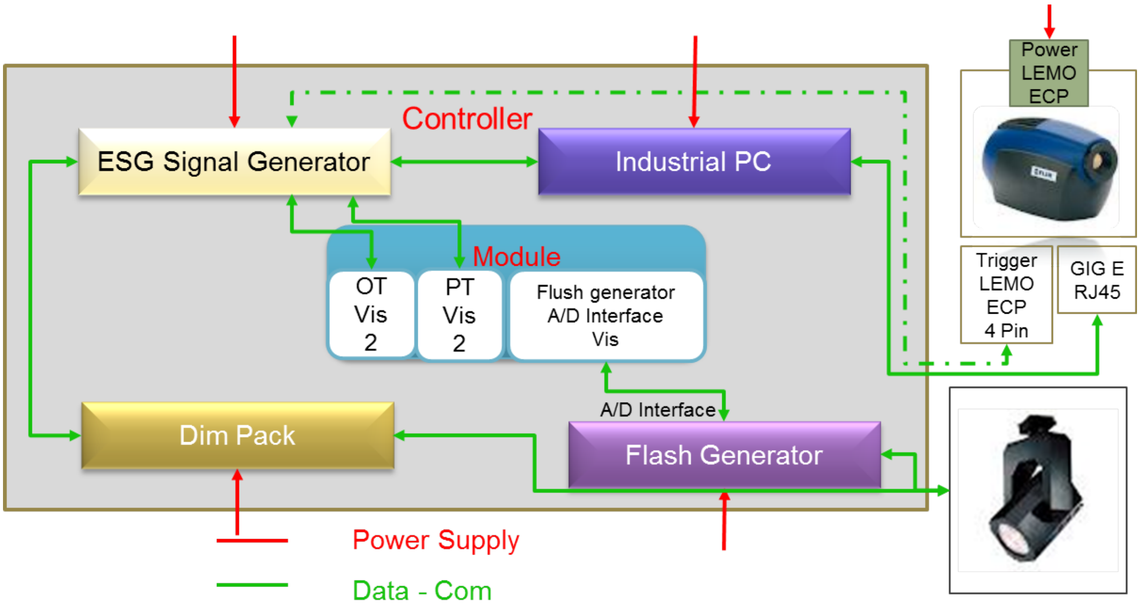

Figure 2.2: Principal design of a thermography system

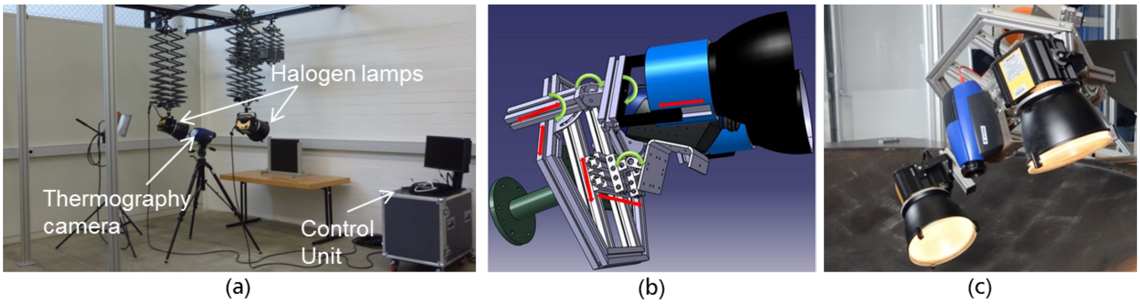

Figure 2.3: Development of thermography end-effector

System integration

As a matter of principle there are a number of scenarios possible to integrate a system for active thermography on the shown robot. Thermography methods are not yet used in inline testing of CFRP components. The integration of a thermography system for inline quality assurance was focused on automation, real time capability, reliability and flexibility. Therefore, on the one hand, interfaces were designed for the communication between robot and thermography system and on the other hand, a concept for the end-effector construction and mounting of the individual thermography components to the robot was developed. The components can be mounted only on axis 6 and 3, which enables to carrying the additional load. All concepts can be categorized in three different types as the following figures 2.4 for concept 1 and 2.5 for concept 2 and 3 illustrates. The concept was developed together with another DLR colleague and implemented by them. These three different proposed approaches demonstrate the advantages and drawbacks of system integration. In order to the integrate the thermography system in MFZ, all 3 scenarios require more than 50m of cable for data transmission and power supply. Since MFZ was developed for flexible research and differentiates with the usual industrial plant, this limitation can be neglected. In the end, the scenario 3 emerged as the optimal method. Scenario 1 and 2 are very similar. In scenario 1, the thermography control system is mounted on the robot arm (axis no. 3) and measuring devices are mounted on the robot hand (axis no. 6). In scenario 2, both systems are mounted on axis 6. The advantages of both scenarios are easy to integrate on a robotic cell without changing the system architecture, and also allow data analysis and measurement to be performed in real time. But there are several drawbacks for both of these scenarios:

- To include the tools load data in a robotic system, the centre of gravity of tools is required. Due to the huge and complex construction of the measuring system, it is difficult to locate. This can lead to robot inaccuracy. Furthermore, every robot has a different load caring capacity (e.g. 120 kg for HA robot, mounted on ground), which can be exceeded easily.

- This construction does not allow measuring complex components and a large measuring volume, as accessibility into the component is not given.
- A heavy weight carrier robot is necessary, which will decrease the measuring accuracy.

Derived from the drawbacks, reaching a high measuring accuracy in a large measuring volume on 3D curved components, the measuring system has to be as simple as possible to locate the centre of gravity of tools, and able to measure and evaluate in real time. In order to fulfil the boundary conditions for the tasks, alternative strategies for the implementation of the mechanics, electronics and software into a mechatronic system was evaluated and implemented. Therefore for scenario 3 only the measuring devices are mounted on axis no. 6 and are connected via Ethercat with a thermography control system, which stays on the ground. Graphical user interfaces were developed to enable the user to interact with the robot in a comfortable way, and to ensure electronic documentation. The proposed system and schemes were evaluated and verified experimentally in chapter 2.3. The experiment results have demonstrated the feasibility of the implementation of a thermography system and introduced the applicable measuring scope for the inline quality assurance. This is the first of its kind of prototype measuring systems and it evolved from earlier laboratory based systems.

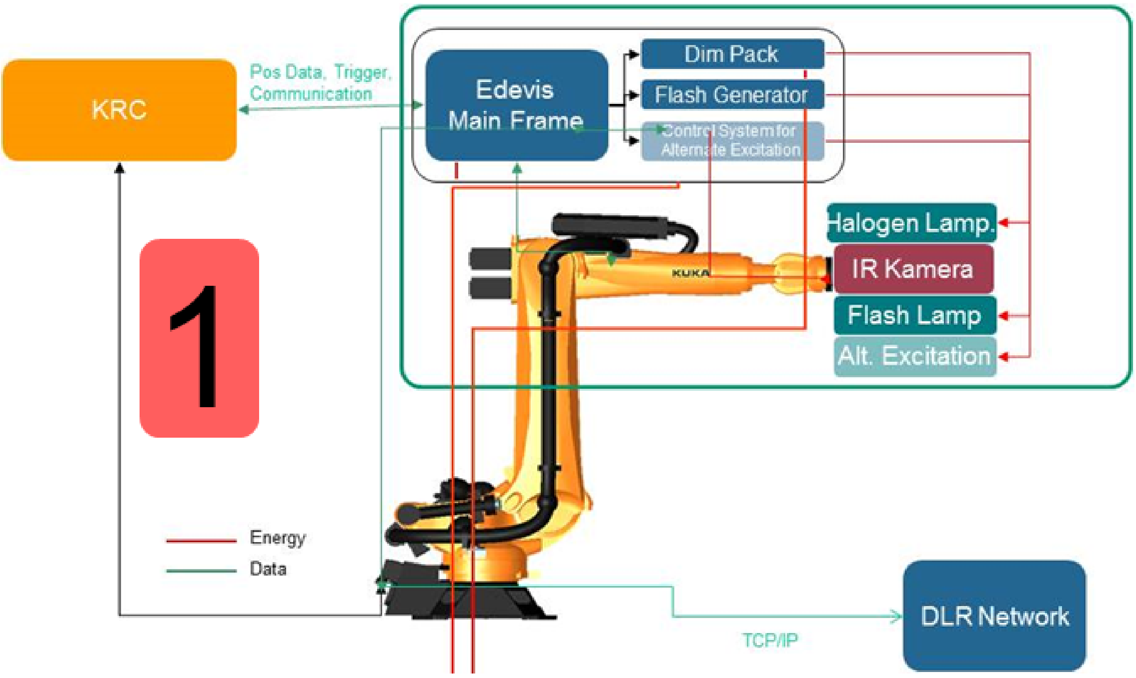

Figure 2.4: Scenario 1 – Control system mounted on robot axis 3, excitation and camera on axis 6

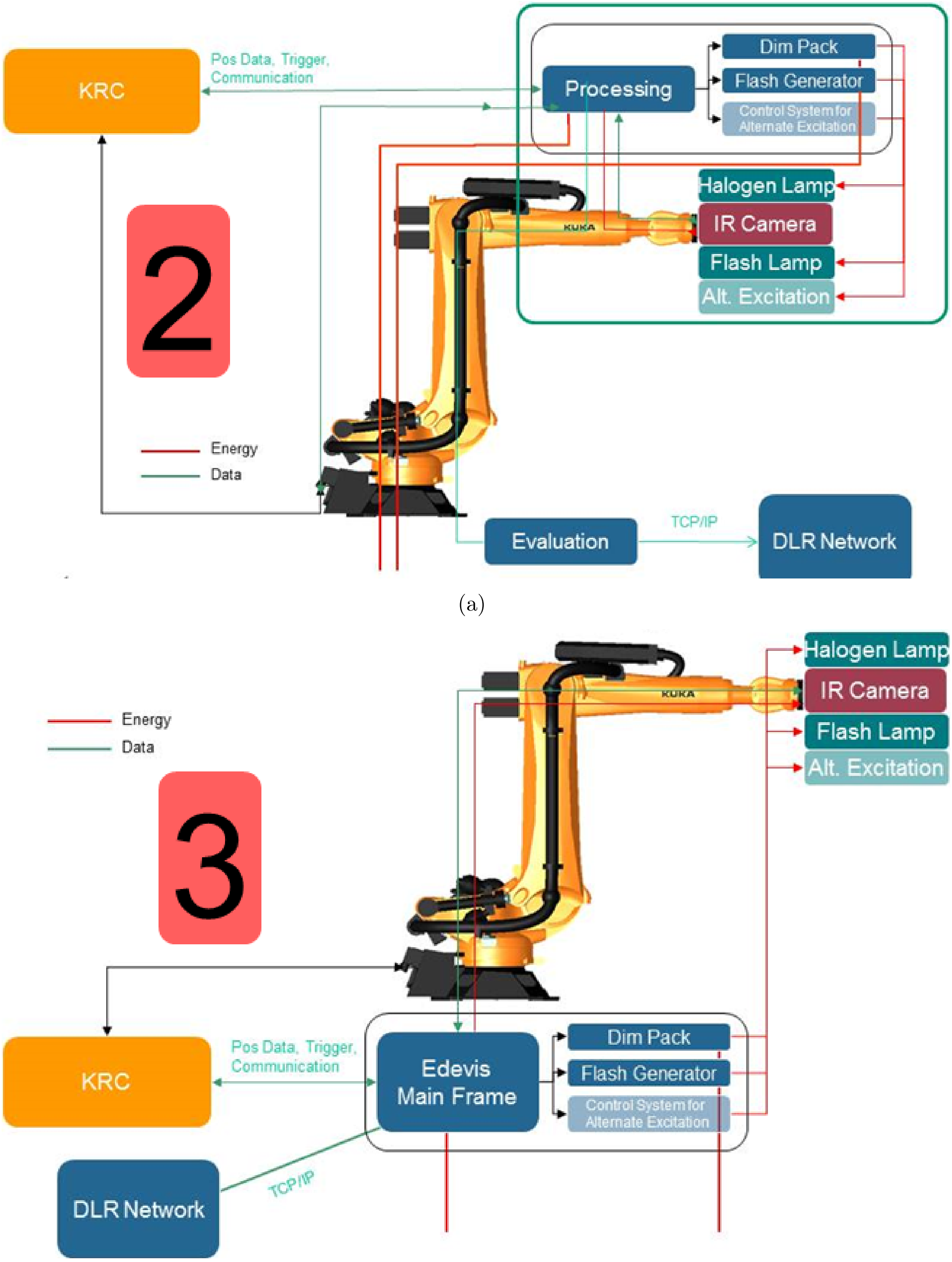

(a)

(b)

Figure 2.5: Integration scenarios: (a) Scenario 2 - Control system, excitation and camera mounted on robot axis 6; (b) Scenario 3 - excitation and camera mounted on robot axis 6, control system locally separated

2.2 Automation along the process chain

The integration of a robot, a set of Halogen lamps and a thermography camera offer a workbench for contactless non-destructive testing. The process step in figure 2.6 of automated inline thermography begins very early with the measurement of the component position to the robot. Here, a coordinate system (e.g. base position) is determined. Then the tool center point (TCP) for the thermography end-effector is determined. For these two process steps either a measuring tip with the robot or, to achieve a higher accuracy, a laser tracker (a external high accurate measurement system, here: Leica) can be applied. Generally for a robot-based automated system an external system is required to measure TCP and base position when required accuracy of the robot used is not enough. TCP contains information where the built-in camera detector related to robot flange is located. This position cannot be touched with a measuring tip and therefore requires a hand-eye calibration procedure. The hand-eye calibration method is discussed elaborately in chapter 3.4.2. In this initial development phase, TCP was deliberately measured with a measuring tip that was mechanically mounted under the camera. The measuring positions were then defined in a virtual environment and a robot program was generated for path planning in order to avoid a collision with the component. Thus the measurement was triggered at every measuring position with the predefined measuring parameters. With the measurement results (2D information), an automatic evaluation process (not a research part of this thesis) will classify and detect the defect positions on every thermal image. It is conceivable in the near future to develop a closed manufacturing loop. It will allow to detect and discard all nonconforming components. Only good components will go to manufacturing process. Consequently, the process limits can be extended, allowing increasing productivity. Additionally, process disturbances affecting the product quality can be detected and located directly. The process can be controlled using its quality characteristics as control variables directly. For this purpose diverse information from CAD Draping simulation and 3D Output are required and can be used for measurement strategy. For example, to set the measurement parameters and distance in measuring system material properties, the component's thickness and number of plies can be used. All these steps will control the process continuation and keep all raw data for process understanding.

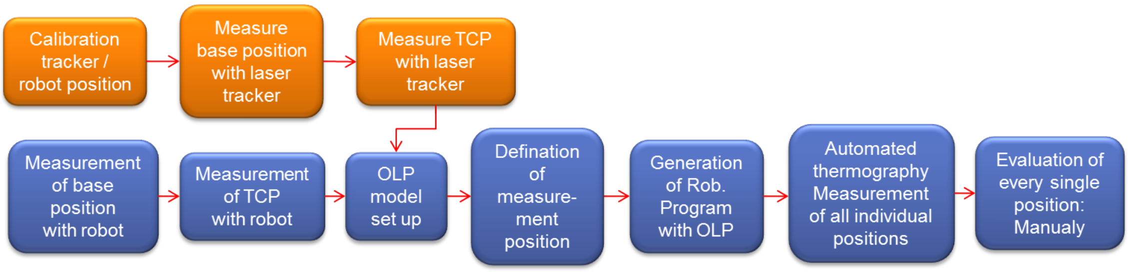

Figure 2.6: Process chain of automated thermography

2.3 Automated thermography measurement of component

After development of thermography end-effector and automated measurement process chain, an experiment was conducted. The results were published [19]. In order to investigate the process described above, a testing scenario was worked out which covers the complete process chain, including design and manufacturing as well as the inline quality assurance aspects. As an example found in the industry, an aerospace structure was selected and modified to accommodate quality assurance aspects to be proven as well as achievable requirements. The choice was therefore made on the approximate rear pressure bulk head of a typical single aisle A320 aircraft. It is a double curved structure which is built in metal so far, and trials were performed to investigate a composite design. Consequently, a material and manufacturing process choice had to be made. For such a large structure of double curvature and integrated foam core stringer, it was quite obvious to investigate a dry textile layup process in a combination of NCFs and fabrics with a consecutive infiltration process according to aerospace VAP® standards.

Description and manufacturing of specimen

For handling reasons the decision was made to use just a section of the entire part. The section itself was chosen from a size that was large enough to reflect all necessary features needed for this investigation. As the part is almost spherical and therefore rotational symmetric, the sector size was chosen with an angle of 60 ° taking symmetry reasons into account. The specimen therefore incorporates monolithic areas with large shear angles in terms of draping as well as sandwich areas in the foam core stringer region with complex draping behaviour, see figure 2.7(a). Regarding the material specification and chosen layup: please refer to paper [19]. The component was manufactured manually together with the production team. For the design of the large scale specimen, a digital process chain was applied, which means based on a digital model of the mould, the composite ply layup was defined using *Catia* CPD. This led to a draping simulation, and finally to 2D cut-pieces. A laser projection system, fed with data from CAD, to project a 3D contour of cut-pieces and to help to place the cut-pieces in the correct positions in the mould, is shown in figure 2.7(b). The edges were then cut by hand. The laser projection system was also used for the positioning of artificial defects which is detected by thermography later on. These artificial defects (see figure 2.7(c)), made out of PTFE foils, simulate delamination. After the layup the preform was put in a vacuum bag and resin was infiltrated by using a VAP® process. The curing at room temperature was followed by debagging and manual trimming to achieve the final contour.

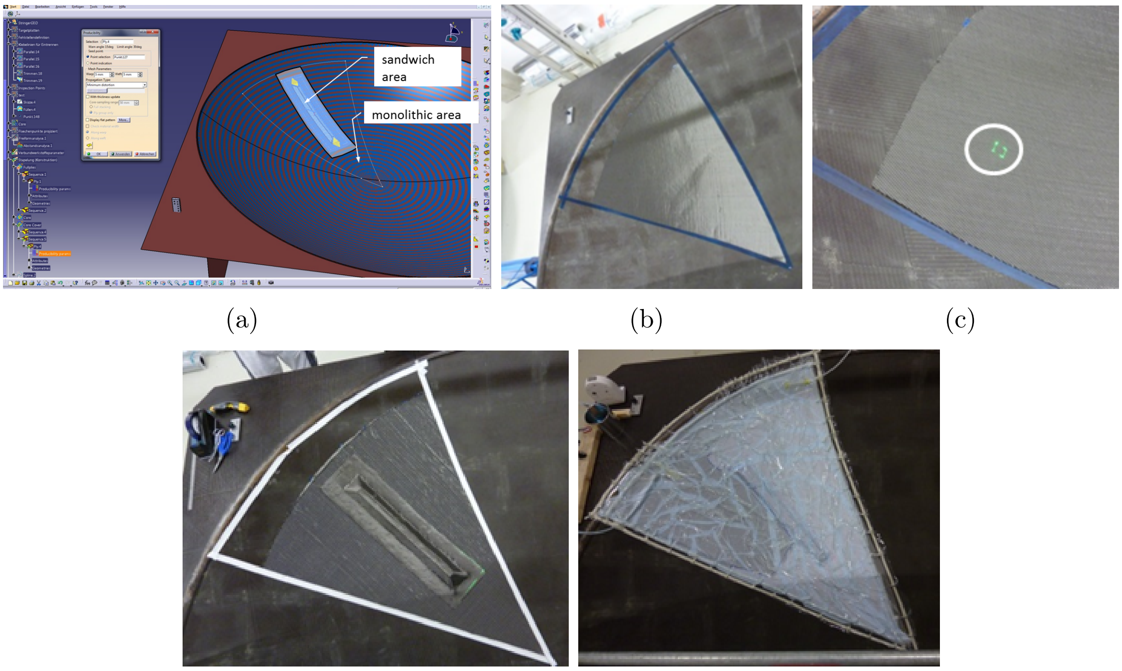

(a) (b) (c)

(d) (e)

Figure 2.7: Design and manufacturing of approximate A320 pressure bulkhead: (a) CPD design, (b) Preforming, (c) Placement of artificial defect, (d) Vacuum bagging, (e) Infiltration

Measurement on a specimen at preform stage and on a cured component

The goal of this experiment was to demonstrate inline quality assurance along with the manufacturing process. As thermography measurement can be performed at the preform stage as well as on a cured component, two measurement setups were prepared. Therefore the cured component was fixed to a jig and 2D cut-pieces were placed again on pressure bulkhead to produce a preform stage. In order to achieve an automated measurement, measurement was performed with the thermography end-effector in combination with an industrial robot. To demonstrate the capability with such a complex structure and to prove the reachability by investigating possible crashes of the robot at the same time, a simulation-based offline programming toolbox was used. After setting up the work cell with all necessary components (robot, end-effector, mould, part etc.), the work cell was calibrated. That means the position and orientation between robot coordinate system and mould/specimen coordinate system was measured and entered in the simulation as well as the robot controller.

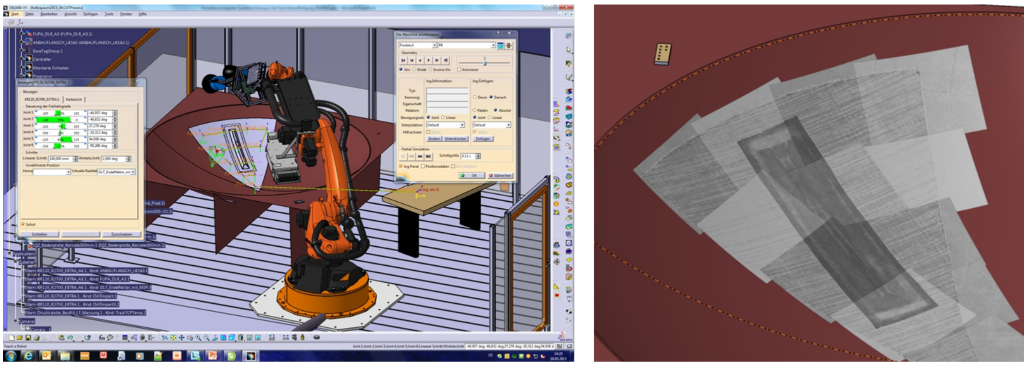

(a) (b)

Figure 2.8: Automated thermography measurement of preform: (a) Offline robot program for a preform stage, (b) Positioning of 2D images in *Catia* manually

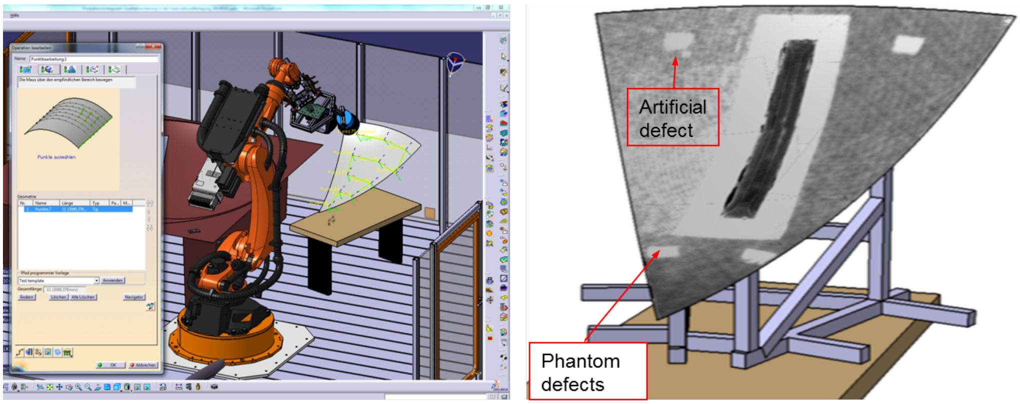

(a) (b)

Figure 2.9: Automated thermography measurement of cured component: (a) Offline robot program for a cured specimen, (b) Positioning of 2D images in *Catia* manually

Thus, the measurement strategy could be defined with the simulation model. Due to the component's curvature and larger specimen than a single view of the thermography camera view, the camera positions were tilted differently. The camera field view was 360 mm × 300 mm. Figures 2.8 (a) and 2.9 (a) depict simulation model for the offline robot program. With the generated robot programs, measurements were performed on both specimens. In total 11 measurement positions were required to cover each specimen. The measurement of the cured specimen was performed similarly to the specimen at preform stage. One may have noticed a phase angle difference between images in figure 2.8 (b) and images in 2.9 (b). This is due to the fact that dry fibre preforms have a different thermal conductivity than cured components. With 0.5 Hz modulation frequency the artificial defect was detected. Furthermore, the four fixing positions (see phantom defects in figure 2.9 (b)), where the component is mounted on the jig, are visible. All individual images were imported in *Catia* and placed manually on the constructed design (see figure

2.8 (b)). For the cured component, images were imported in same way in *Catia* and the edges were trimmed manually (see figure 2.9(b)). With this test the feasibility of automated lock-in thermography in the context of manufacturing process chain observation especially at different process steps e.g. at preform stage as well as at cured parts was successfully demonstrated.

2.4 Evaluation of robot-based automated thermography process

Industrial robots are used in many applications that require moderate levels of accuracy and repeatability. Up to date the use of robots for precise component inspection has been problematic. Compared to a gantry, the vertical joined-arm robot is more flexible and less accurate. For historical reasons, the robot is designed for pick-and-place or handling repeated tasks and less for dynamic tasks. Unfortunately, industrial robots have good repeatability but not good absolute accuracy. There are numerous research results and suggestions for improving the accuracy of a robot. In these papers [20] [21] [22], various influencing factors for robot accuracy are described. Nevertheless, robots for today's automation tasks are also becoming increasingly important in non-destructive testing where robots are used as manipulators.

2.4.1 System accuracy analysis along process chain

The process inaccuracy starts with the first step (measurement base position) of the process step (see figure 2.6). As base and TCP positions are measured manually, there is always a minimum angular and positional error. A small angular error causes several millimetres of total error. Poor robot accuracy is caused by geometric factors such as geometric parameters, joints offset errors and TCP definition, as well as by non-geometric factors such as, thermal effects of gear, encoder resolution, gearboxes backlashes, kinematic errors, gravity, load etc.. The influence of external axis and stop and go movement of robots play a major role in the accuracy. In addition, the angle position of lamps and camera of the thermographic end-effector (due to its flexibility) must be changed according to the measuring position. This means that the load and centre of gravity of the end effector will change depending on the setting. This requires a continuous robot configuration. Depending on the components, geometry and measurement positions on the component, the measurement field size may change. The camera perspective must be adjusted in order to change the measurement field size. Otherwise, overlapping or missing measuring ranges may occur between the measuring fields. The measured thermographic images must be processed separately to determine the defect position. Due to robot inaccuracy, the defect positions cannot be specified precisely. The error indication of the defect position can be several millimetres. Without an external sensor, no countermeasures can be taken to eliminate the error. In addition, there are differences between the CAD model and the manufactured component, and differences between the real and theoretical world of the virtual OLP model. In the next section, some aspects of robot accuracy are experimentally investigated and analysed. The manufacturer's specifications for absolute and repeated accuracy refer to the quasi stationary state of the robot without taking process-specific influences into account. Influences from dynamic processes therefore usually lead to a deterioration of the absolute accuracy. A contribution of this work is an experimental investigation of the robot positioning accuracy by changing the mass, mass moment of inertia, centre of gravity, Euler angels and temperature, as well as determination of the influences of the external axis for existing robot cells at DLR. A Leica laser tracker was used for the detailed measurement of the system accuracy. The laser tracker (LT) tracks the movement of a reflector in space and measures its 3D position. Two experiments, namely " absolute robot accuracy" and "influence of the linear axis on robot position accuracy" were conducted to determine the absolute accuracy of Technological Test Cell (TEZ). Another experiment was conducted at inline quality assurance Cell (IQZ) to determine influences such as mass, mass moment of inertia, centre of gravity, Euler angels and temperature. Furthermore, the following essential points for a reproducible measurement were considered:

- All robot axes were calibrated before the test.
- A best-fit transformation was carried out in order to bring the robot and laser tracker in same coordinate system. It was performed in the robot ISO-CUBE area, since the robot is more accurate in this area.
- Determination of additional loads of axes 1, 2 and 3, since the robot position deviates if the load data is incorrect.
- Deactivation or decoupling of the linear axis by commenting out the line "ERSYS" in machine.dat file, in order to determine the error influence of the external axis on the overall system.
- After the end-effector assembly or disassembly, TCP was always remeasured to avoid the assembly error and the associated TCP error.
- The robot path program was generated with OLP, because the absolute position accuracy requirements of the industrial robots cannot be verified by the teach-in method. This is especially true for the first measurement.
- The base position was measured with the LT because, it is known that the repeatability accuracy of industrial robots is higher than the absolute position accuracy. This means that nearer to the base position, accuracy will be higher.
- Robot path travel was carried out in T2 mode with 100 % override

2.4.2 Experimental set-up and measurement results

Absolute robot accuracy without influence of linear axis

To determine the absolute robot accuracy for both cases (with and without influence of linear axis), the robot was moved at different positions with various poses and the current position was measured with the laser tracker. A pose always consists of the XYZ position of the TCP (Tool Center Point) and the three orientation angles in space. The positioning accuracy of the robot can then be determined on the basis of a target/actual comparison. To make these measurements, the robot and the laser tracker were brought into a common coordinate system. The laser tracker coordinate system was transformed into the robot coordinate system by a best-fit transformation. For the best-fit, the robot program was created with eight points representing the corner points of a cuboid. For each position, orientation of the TCP point were changed. The TCP points were measured with the laser tracker in each approached pose. The same TCP points were recorded by the robot controller (once related to rob-root and once related to World) and constructed in *Spatial Analyser* software. The measured TCP points could then be transferred into the robot or world coordinate system by a best-fit. The calculated RMS best-fit transformation error with *Spatial Analyser* is 0.54. To compare the best-fit transformation error, the transformation was calculated with another software, the "KUKA Special Software", which was developed for such calculations. The error here is 0.643. It is to note that both the calculated errors are dimensionless. The smaller error indicates better absolute position accuracy between calculated software data (target position) and actual position data (where the robot is). The best-fit transformation error for both calculations corresponds approximately to the positioning error of the absolutely measured robot. The further tests were carried out with the best-fit transformation calculated with *Spatial Analyser*. For the determination of the system accuracy (robot + linear axis) as well as the robot accuracy (robot only) a common coordinate system with the LT was created in each case. These are:

1. Laser tracker coordinate system = Rob-root coordinate system (robot only)
2. Laser Tracker coordinate system = World coordinate system (robot + linear axis)

To check the absolute robot accuracy without linear axis E1, a robot program was created based on rob-root coordinate system with 45 points. The orientation of the flange was kept unchanged for all points. The robot was moved linearly from the rear side of the linear axis to the front side of the linear axis. Figure 2.10 shows the measuring positions. In order to assess the repeatability of the tracker measurements, several measurement series were carried out on the initial position of the robot. The TCP positions measured (with the LT) were compared with the positions recorded (by the robot controller). Many of the measuring positions were outside the robot ISO cube range. Thus the robot was completely extended in X, Y and Z directions.

The absolute deviations in robot position accuracy (without linear axis) were:
Max. deviation: dx = 0,69 mm dy = 1,82 mm dz = 2,58 mm
Min. deviation: dx = -0,77 mm dy = -1,36 mm dz= - 0,38 mm
The comparison of the target positions with the actual positions showed an asymmetrical deviation distribution in the front and rear areas of the linear axis. The deviation in its ISO cube range corresponds to the absolute position accuracy specified by the manufacturer. From the graph in figure 2.10 it can be seen that the deviation depends on the pose. It can also be seen that the deviation in the Z direction (in the direction of gravity) is greater than in the X and Y directions. The measuring positions are illustrated in figure 2.11.

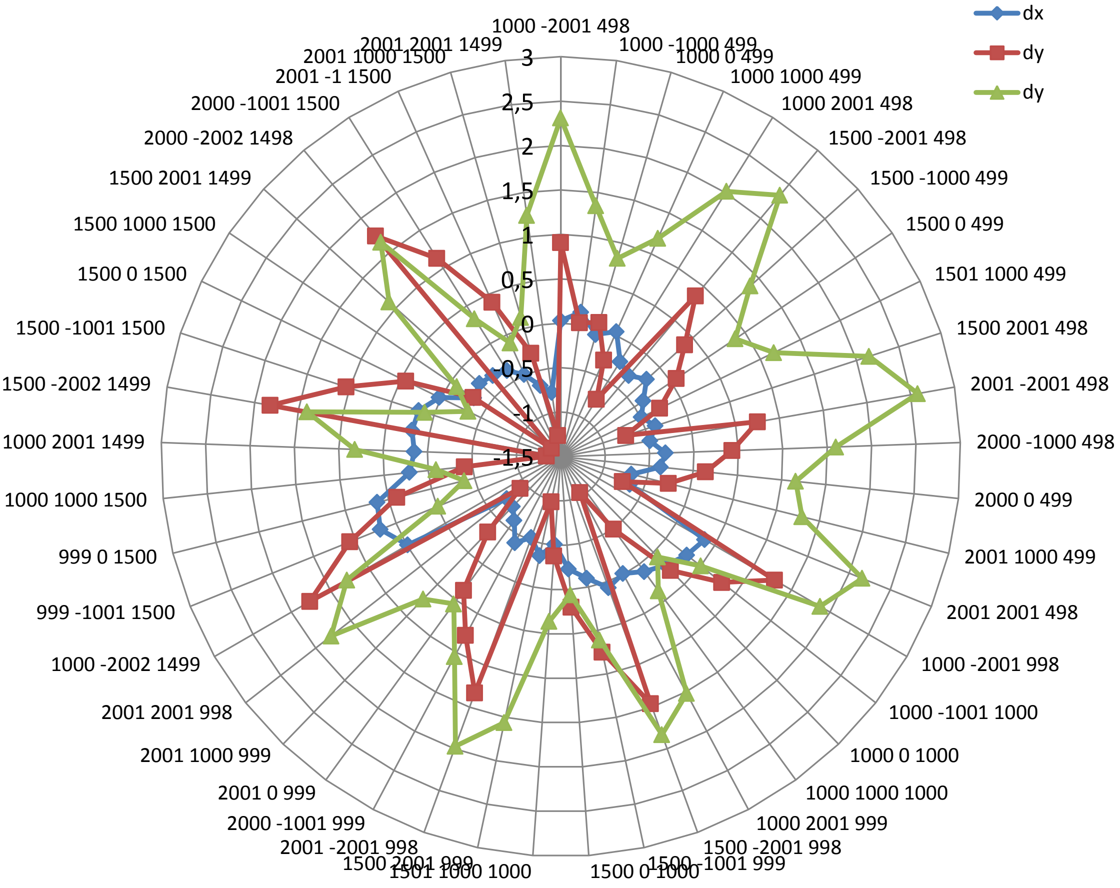

Figure 2.10: Absolute robot position accuracy without influence of linear axis

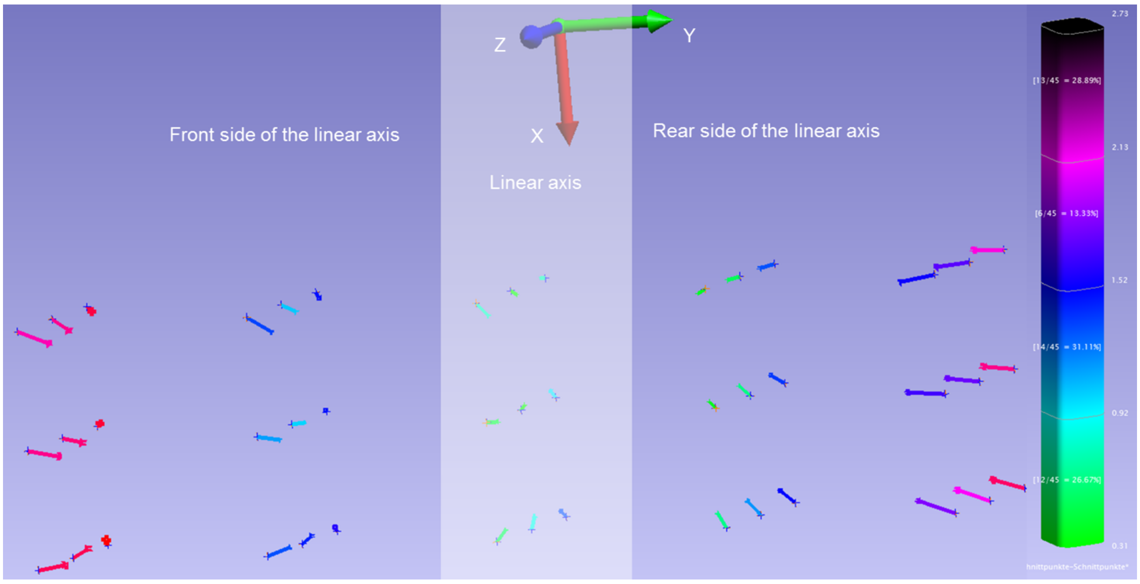

Figure 2.11: Measuring positions inside and outside of ISO-CUBE range

Absolute robot accuracy with the influence of linear axis

To determine the accuracy of the linear axis, five TCP positions on the linear axis were measured in rob-root coordinates after the best-fit transformation was performed. The TCP positions to be measured were programmed in robot ISO-CUBE area and the robot moves on the linear axis, in 1000 mm increments in the (+)X direction. The orientation of the TCP point remained unchanged. Since the linear axis is no longer coupled to the rob-root, the value (LT measurement) should now theoretically only change in the (+)X direction. Figure 2.12 shows the results. From the measurement data it can be seen that the linear axis is not parallel to the (+)X axes. The E1 value changes by 1000 mm because in 1000 mm steps robot was moved on the linear axis. But the LT measurement shows that the TCP value changes not only in the X direction, but in all three axis directions. Thus, the entered theoretical values do not correspond with the realistic values. By taking a closer look at the graph, it can be easily seen that the error does not increase linearly in any of the three axes. This indicates that the linear axis does not consist of a single long rail, but of several rail sections welded together. Furthermore, it can be seen that the error in the X direction is unusually large. This indicates that the robot and linear axis are not correctly calibrated to each other. Figure 2.13 shows the CAD model of the linear axis and presents the measuring positions on the linear axis. In the real case, the linear axis is skewed and rotated to the coordinates. The blue, yellow and green rails are individual pieces that were welded together. Furthermore, the linear axis stands on several support elements. Although the unevenness of the floor and the associated height of these support elements were taken into account to manufacture and assemble the linear axis, the linear axis error may also have been caused by this problem.

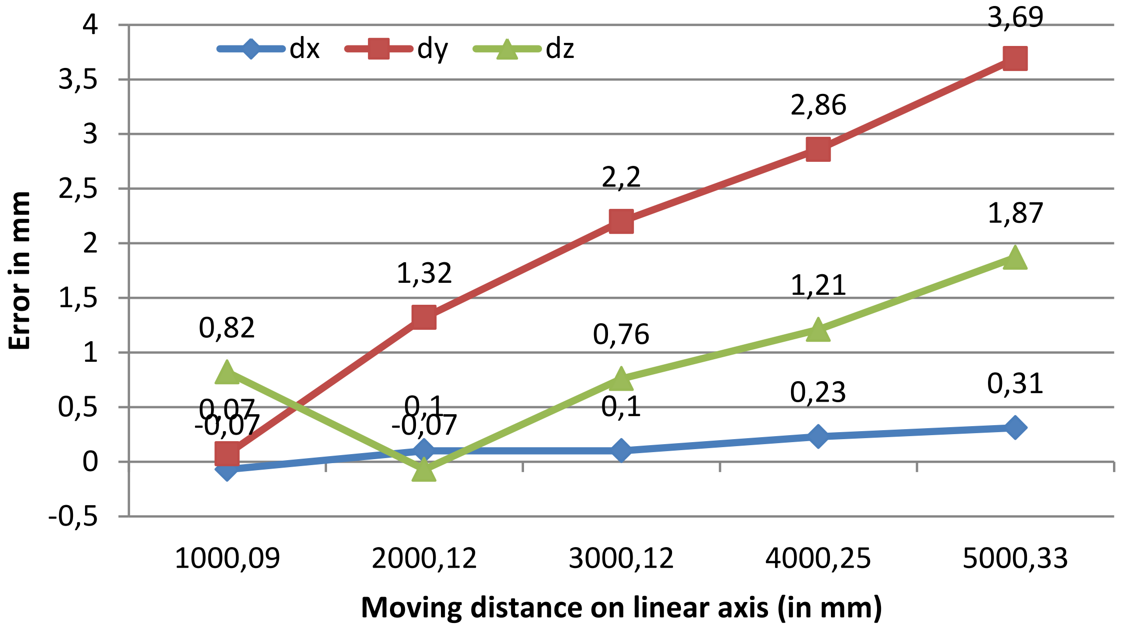

Figure 2.12: Deviation of absolute position accuracy influenced by linear axis

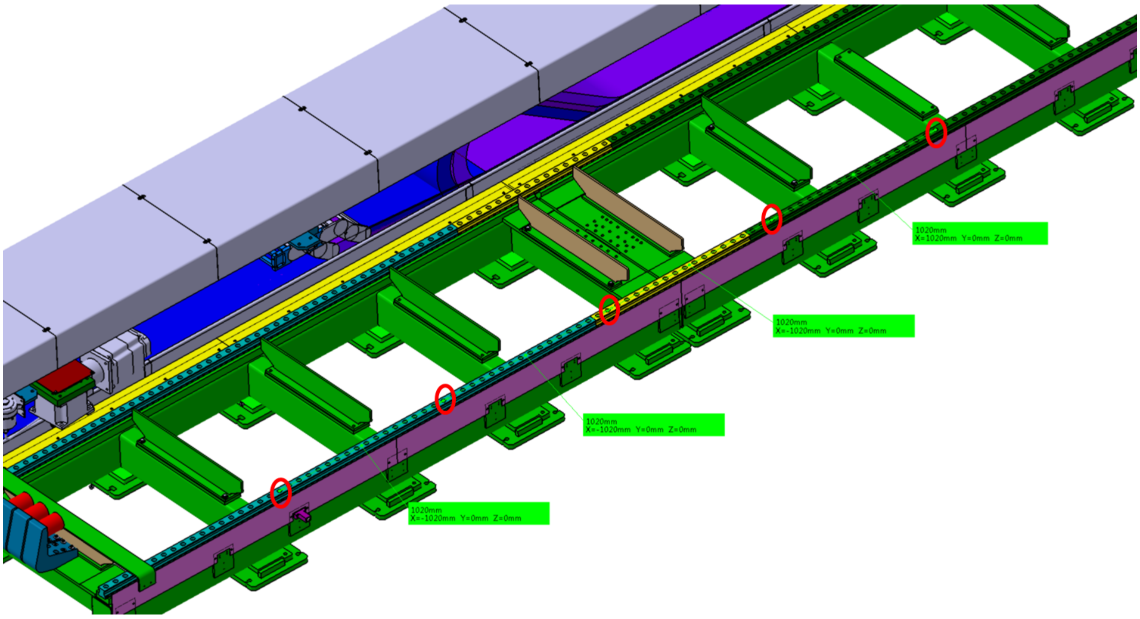

Figure 2.13: CAD model of linear axis

Determination of the influencing factors on axes 3 and 6

Another experimental verification was performed with a high accuracy(HA) robot, in order to determine robot positioning accuracy influenced by parameters such as mass, mass moment of inertia, centre of gravity, Euler angels and temperature. A precondition for identifying the parameters is the measurement of the robot TCP. Therefore a reflector was placed on robot flange (centre Plane of the no. 6 Axis) and the laser tracker was best fitted into robot coordinate system. With the sensor-based method, the deviation of positions were measured by means of laser to reflector position. In order to determine the positions, deviation influencing parameters were changed for axis 3 and 6 in machine configuration one at a time. Other parameters were kept at that time unchanged as an actual value. It is to note that the robot will compensate its position according to entered data in the machine configuration. The CAD model was used to determine the actual load data on axis 3 and axis 6. To investigate the influences, the robot was first moved to 12 positions without changing the load data, and the actual positions were recorded with LT. Afterwards, incorrect load data, such as mass, mass moment of inertia, centre of gravity, Euler angels, were deliberately changed (see table 2.1) individually in machine configuration, and those 12 positions were measured every time after changing the individual parameter.The coordinates of the target and actual positions were then compared with each other.

Table 2.1: Changed machine data for determination of influencing factors

Factors	Axis	Actual value	Changed value
Mass	Axis 3	76.7 kg	150 kg
Euler angel A °	Axis 3	155.096 °	- 155.096 °
Euler angel B °	Axis 3	52.107 °	- 52.107 °
Euler angel C °	Axis 3	83.571 °	- 83.571 °
Moment of inertia J_X	Axis 3	- 5.066 kg.m^2	5.066 kg.m^2
Moment of inertia J_Y	Axis 3	- 10.963 kg.m^2	10.963 kg.m^2
Moment of inertia J_Z	Axis 3	- 12.87 kg.m^2	12.87 kg.m^2
Centre of gravity X	Axis 3	- 185.587 mm	185.587 mm
Centre of gravity Y	Axis 3	166.951 mm	- 166.951 mm
Centre of gravity Z	Axis 3	-1374.825 mm	1374.825 mm
Mass	Axis 6	4.7 kg	120 kg
Centre of gravity X	Axis 6	0 mm	270 mm
Centre of gravity Y	Axis 6	0 mm	0 mm
Centre of gravity Z	Axis 6	0 mm	240 mm

Experimental results of axis 3 and axis 6 are illustrated in figures 2.14 and 2.15 accordingly. As expected, position deviations in the KRC coordinate system were very small. Maximum deviations can be observed in LT coordinates (see in figure 2.14(b and d) as well as in figure 2.15 (b, d, e and f)). Especially by the changed mass value and the centre of gravity value for both axes, maximum deviations could be measured. On the other hand, small positional deviations in the LT coordinate system could be detected with the change of the moment of inertia and the Euler angle. However, these deviations are negligibly small. Furthermore, the inaccuracy caused by the moment of inertia plays a role in continuous motion. The investigation on axis 6 did not show any larger positional deviations when changing the Euler angle and the moment of inertia. This was probably due to the fact that nothing was mounted on axis 6.

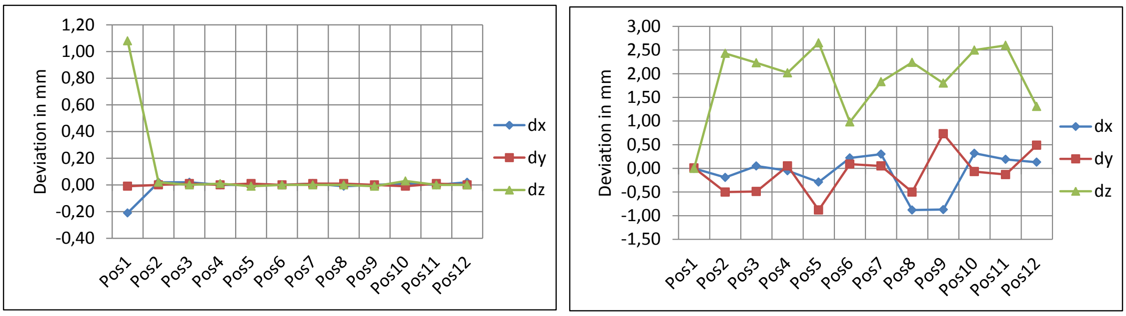

(a) KRC/Mass (b) LT/Mass

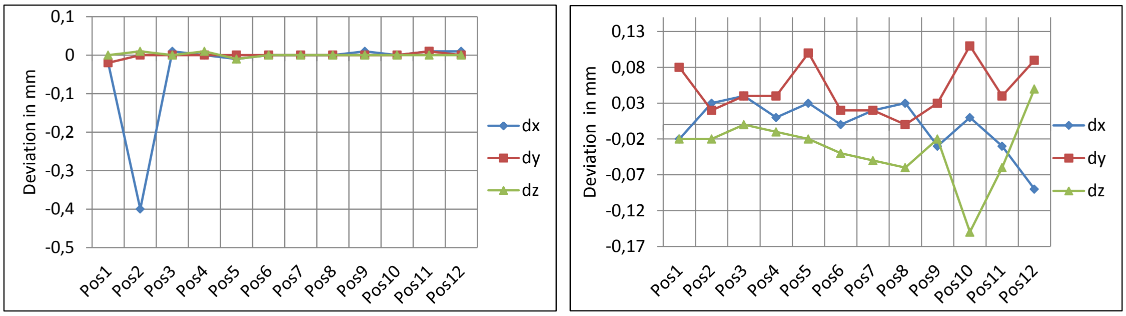

(c) KRC/Centre of gravity (d) LT/Centre of gravity

Figure 2.14: Robot inaccuracy from axis 6: (a) Deviation in KRC coordinate by changed mass ; (b) Deviation in LT coordinate by changed mass; (c) Deviation in KRC coordinate by changed centre of gravity; (d) Deviation in LT coordinate by changed centre of gravity

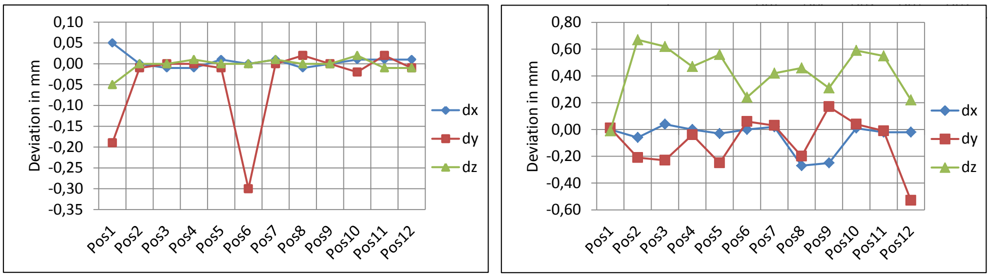

(a) KRC/Mass (b) LT/Mass

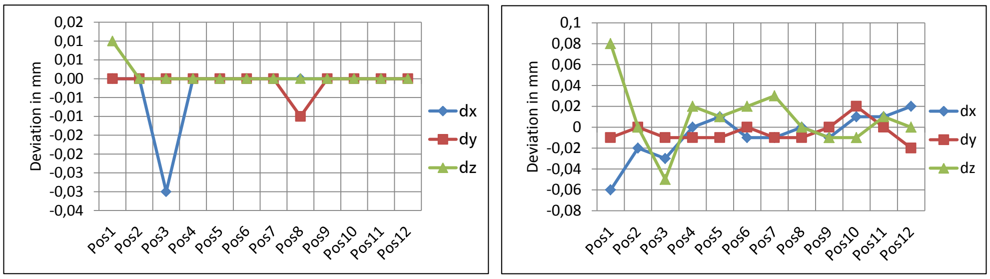

(c) KRC/Euler angel (d) LT/Euler angel

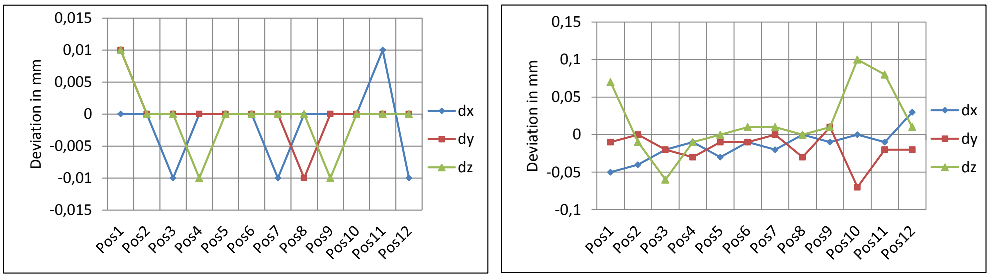

(e) KRC/Mass moment of interia (f) LT/Mass moment of interia

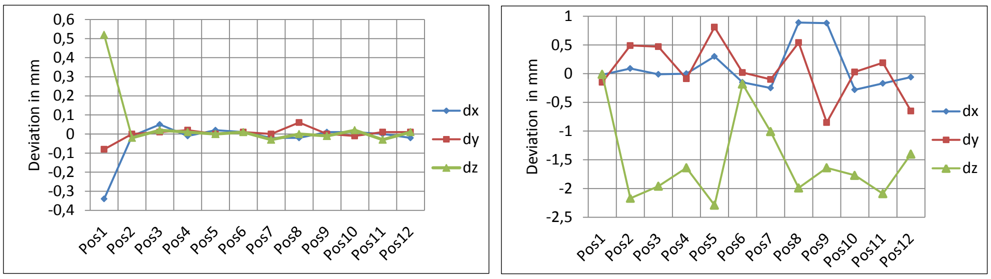

(g) KRC/Centre of gravity (h) LT/Centre of gravity

Figure 2.15: Robot inaccuracy from axis 3: (a) Deviation in KRC coordinate by changed mass ; (b) Deviation in LT coordinate by changed mass; (c) Deviation in KRC coordinate by changed Euler angles; (d) Deviation in LT coordinate by changed Euler angles; (e) Deviation in KRC coordinate by changed mass moment of inertia; (f) Deviation in LT coordinate by changed mass moment of inertia; (g) Deviation in KRC coordinate by changed centre of gravity; (h) Deviation in LT coordinate by changed centre of gravity

The second experiment was concerned with determining the temperature influences in continuous operation. The aim of the test was to determine whether the position of the robot changes due to increasing motor temperature (in continuous operation). The load data calculated with CAD was entered into the KRC controller in order to determine the specific temperature influence. During the test, the robot was continuously moved between 12 positions in automatic mode and all 12 positions were measured with LT every half hour. All results were compared with the first measurement.Figure 2.16(a) shows how the robot becomes less accurate over time. The position deviation is 1.25 mm for a 5 hour operation. Figure 2.16(b) shows the warming of the axis temperatures, which have increased over time. The temperature increase for each axis was steady. Since the A1 axis had mostly moved, the temperature in this case rose to 105 degrees.

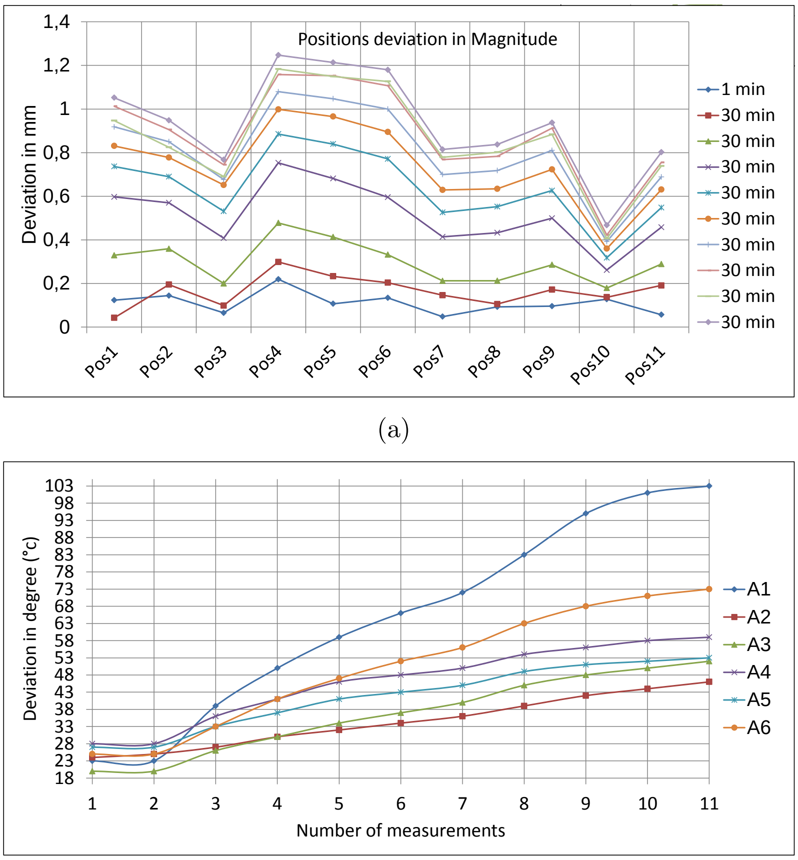

(a)

(b)

Figure 2.16: Robot inaccuracy from axis 6: (a) Positions deviation due to increasing axis temperature ; (b) Increased axis temperature

2.5 Conclusions

In this chapter, the entire CFRP process chain and advantages of inline automated thermography in a production line were roughly outlined. Furthermore, a flexible automated thermography end-effector was developed and integrated in different robotic cells, followed by automated measurement demonstration on a preform and a cured component. It was shown where in this process chain, inline thermography measurement is increasingly used. Thereafter all relevant influencing factors were examined individually. During the investigation, it was found that the larger positional deviations are due to the changed mass and centre of gravity. This is valid for axis 3 as well as for axis 6. Positions deviation caused by changing the Euler angle and the moment of inertia are negligible, as long as measurement takes place only when the robot stops. The incorrect load data entered for the determination of the influencing factors are far from reality (see table 2.1). By the exact determination of the load data, 1 mm to 3 mm positions deviation can be minimised or neglected. An accurate analysis with the correct load data was performed during the overall system check in section 3.8. It could be observed that a robot's absolute accuracy depends on its pose and external axis. The influences of the linear axis can be minimised by cell calibration. The unfavourable robot pose can also be avoided with the help of the virtual environment of the OLP. However, it is not possible for technical reasons to completely avoid the influence of temperature, since articulated gear groups of the kinematic chain generate heat under a load, leading to time dependent changes with angles. This results in a time dependent position deviation of the robot. The results of the robot accuracy analysis indicate some deficits in the automated thermography process chain. Various measures are necessary to increase the accuracy. Depending on industry requirements, these deficits can be partly solved with special methods (such as an external guidance system, work area-related robot calibration, etc.). But such cases will occur in the thermography measurement seldom or never. During thermography measurement, the robot stops for the measurement time. Thus, the gears temperature of the axis do not go beyond the operating temperature.

Besides system inaccuracy of automated thermography, results are still evaluated in 2D. These 2D images are projections of measurement objects, which prevent the determination of the accurate defect dimension and 3D defect propagation [12]. With a great of efforts all single images of measurements results (in section 2.3) were merged together. Therefore, the automated thermography method should be further developed. The solution should ignore robot inaccuracy and at the same time enable evaluation in 3D. Furthermore, a modulated thermal wave during lock-in thermography diffuses laterally to the surrounding surfaces of measurement filed, which prevents continuous measure to the very next measurement field. Therefore, for large components the thermography measurement position has to be distributed systematically to get a homogenous intensity of the measurement field. With the robot-based method, such measurements can be realised. But in a semi-automated application, gaps can occur between two measurement fields or, in the worst case, positions are not measured at all. Features are required within the component surface to avoid such errors. In most cases, a large CFRP area has little to no characteristics. In addition to this problem, the industry is reluctant to implement automated non-destructive testing due to the high investment costs of robots. An automatic solution must be developed for industrial applications. The solution will apply to both semi-automated such as [7] and fully automated applications. It is known that thermography method enables the detection of defects layer by layer according to selected modulation frequency. However, since no depth representation (like computer tomography) corresponding to individual images is possible, evaluation of the large number of images remains difficult and time consuming, which prevents the industrialisation of the method. A method needs to be developed to overcome these issues.

Chapter 3

Development of automated 3D-evaluation and defect localisation method of thermography measurement results

This chapter considers the development of 3D thermography with two different methods. For each method an overview, a description of the procedure and the possibilities for the execution are given, as well as a discussion of the advantages and disadvantages. After presenting the basic ideas about pnp and kinematic chain based 3D thermography visualisation in section 3.1, the feasibility study for pnp based method is demonstrated in section 3.2. The necessary basis for calculation of the camera perspective (in section 3.3), which was applied to both methods, as well as the results of camera calibration are presented and discussed in section 3.4. The applied mathematical approach to calculate the projection matrix for pnp method as well as the achieved results are presented in section 3.5. The optimisation of this method is performed in section 3.7, where further mathematical approaches were applied. The experimental setup and results for kinematic chain based 3D visualisation is presented in section 3.6. Afterwards, the accuracy of both methods as well as advantages and disadvantages are demonstrated and discussed in section 3.8.

3.1 3D reconstruction concept from single still images

Derived from the identified deficits of automated thermography, the technology needs to be developed toward 3D visualisation of the results. Hundreds of images generated during a large component measurement can be evaluated more easily by 3D visualisation. It is difficult to recognise from individual images whether a defect occurs in certain patterns and frequencies. Thus, the relationships between individual images and production-related defects can be overlooked. Also defects which propagate through several deeper layers can be better interpreted. This enables complete 3D defect propagation knowledge. The evaluation will become more intuitive for certified examiners. For instance if a gap is created between two measurement fields due to robot inaccuracy, it can be recognised or prevented through a 3D visualisation. The visualisation technology is to be integrated into both the semi-automated and fully automated production processes.

The approach at DLR Augsburg of a robot-based measuring system for industrial thermography applications and the concept of a 3D-thermography visualisation procedure with a thermography end-effector are published in previous papers [23], [24]. The essential information required to generate 3D thermography is object geometry, the location and orientation of objects with reference to the camera, particularly across separate images from all measurement fields [25]. When viewing an image humans have no difficulties understanding its 3D structure. However, inferring the 3D structure remains extremely challenging for current computer vision systems due to perspective projection, as there is an intrinsic ambiguity between local image features and the 3D location of the point.

There are plenty of existing methods and technologies for 3D model generation like the stereo vision method, using 3D features, or the multi-view method. These methods require either a second camera [25] or time consuming additional processes like several images taken from different views for each single measuring field. Features are required for the orientation of the camera to the measuring position. With larger and homogeneous components, such as an aircraft fuselage or a vertical tail, it is extremely difficult or impossible to attach such features or marks. This is because, for the preforming process after each layer build-up (due to the CFRP construction), features must be attached and removed again after the measurement. This makes the overall production process extremely slow. For the cured component, unique structural features like holes, boundary edges are required. These type of features, which may help to calculate camera perspective to the component, do not exist enough on the surface. Thus, this measuring method is no longer flexible enough for industrial suitability and automation. Therefore, contactless features are needed to implement this approach.

A second widely used approach for 3D reconstruction usually follows the multiplication of homogeneous coordinates. By the calculation in different steps of all right-handed coordinates, a scene with object and camera can be described.

Both of these methods can be implemented for the application described here. Therefore, two concepts for the 3D visualization of the measurement results are presented in the following sections. This has the advantage that a 3D visualisation is possible for a fully automated method (with robot application) as well as for a semi-automated method (without robot application). Furthermore, a combination of both methods can minimise the uncertainty of the robot-based method, where both fully automated processes and higher accuracy are required.

3.1.1 A new 2D-3D point correspondence approach

In order to establish 2D-3D correspondence relationship, most of the approaches use either geometric features of the object or previously applied marker points on the object. In this new approach, the projected features do not have the properties of common markers. The technique presented here concerns a method (see figure 3.1) for projecting and determining the measurement field, in particular for the orientation of the measurement position on a larger component. The aim is to establish a relationship between camera pose and the component via 2D-3D point correspondence features. A laser projector will be used to project the 3D point on the component. Markers, physically or optically to the component, are given in terms of size, shape and distance to each other, whereas the used laser point are not. The new concept with the thermography camera, which is also used for NDT, and a laser system mounted above the robotic cell, eliminates the uncertainty of the robot's position accuracy. Details of the laser projector are described in section 3.2.

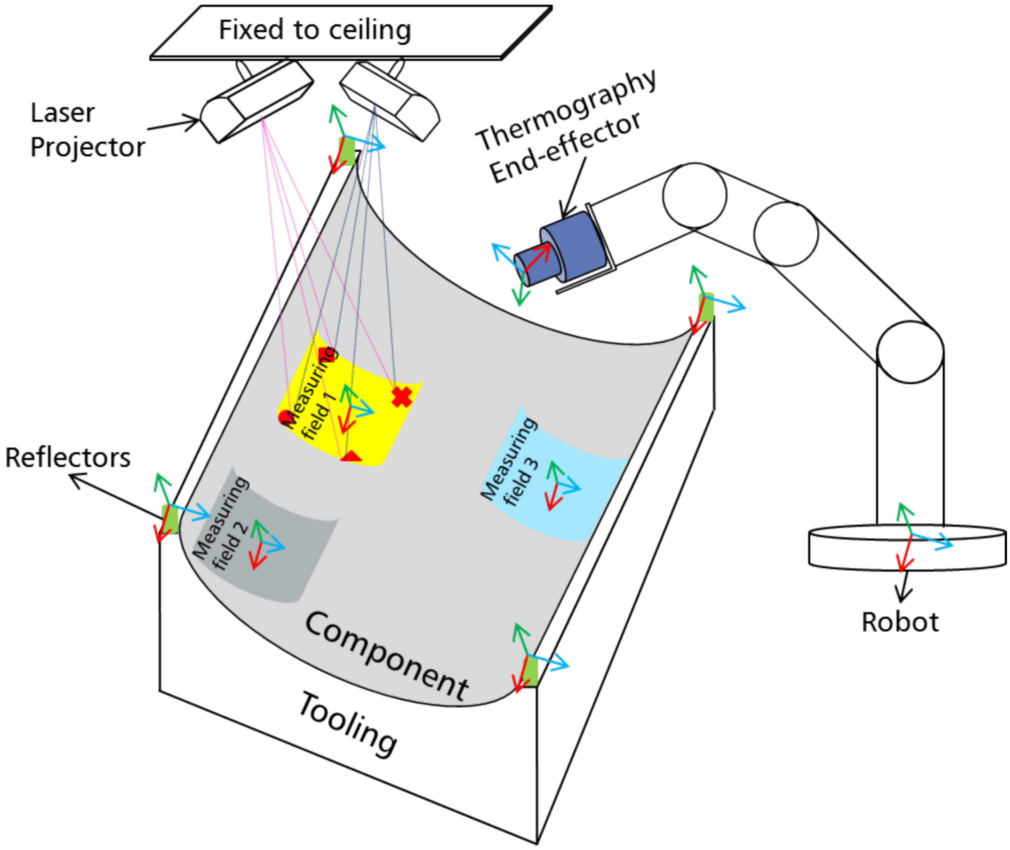

Figure 3.1: 2D to 3D point corresponding concept

According to requirements the laser projector will be coupled or not coupled with the thermography end-effector developed by DLR. The new method has the following advantages:

- The extended process step (see Figure 3.2), compared to the previous process step of automated thermography, can neglect entire inaccuracies in the process chain, because the relative position of the robot to the measurement field is improved. Therefore, no "high accuracy" robot is required. A precise measurement of the component position to the robot, TCP determination, OLP model or offline program generation can be avoided.
- No expensive external guidance like a laser tracker system is required.
- No additional camera systems are needed to detect the measurement field. Instead, only the thermography camera, which is used for component inspection, is used for the detection of the measurement field.
- The system can be applied to any complex component (not Component Specific).

Description of the extended process step

A few new process(see the green building blocks in figure 3.2) steps are certainly added to the automated thermography process chain (see figure 2.6) by including a new laser projector device. First, the position of the component in space to the laser source has to be determined. For this purpose, according to the CAD model, reflectors (see figure 3.1) are mounted at predefined positions on the component and the positions of the mounted reflectors are calibrated with the laser projector. The projected laser points represent features for each measurement field on the component. When the laser projector (e.g.: from the ceiling) projects the measurement field onto a component, it generates heat, which is registered by the thermography camera as a temperature image. Thus, the measurement field becomes visible and does not require any stickers as features. These laser points are used for the respective measurement fields as 3D reference points or contactless features. The measurement field size and the number of measurement field positions on the component are calculated and defined in CAD depending on the component geometry and component size. Although this new process step (see figure 3.2)"Construction of 3D reference points" by means of defining measurement field takes some time to prepare, the total automated inspection process time will not be affected, as this step is done in advance. The information is passed on to the laser projector. Thus, the measurement field on the component can be projected very precisely with the laser points. These laser hot spots on all thermography images need to be extracted in order to get corresponding 2D points of those projected 3D points for each respective measuring field. Since the generated 3D reference points and 3D model, which will be reconstructed, have a common reference coordinate system, all individual images can be assigned in three-dimensional space. The goal is an automatic stitching of the images for a 3D visualisation. This ensures a measurement without any gap, and a reproducible measurement can be guaranteed. The implemented mathematical approaches applied here to assign the 2D images to the 3D model are explained in more detail in sections 3.5 and 3.6 and the corresponding fundamental basics in section 3.3.

Furthermore, the robot should move ideally to the measurement field, as it is programmed with OLP software. Due to the robot inaccuracy, the robot usually moves incorrectly to the measurement field. However, because the laser projects the measurement field onto the component more accurately and the thermography camera recognises the laser points, the robot's position relative to the measurement field can be improved using an iteration algorithm. Since this technology would improve robot accuracy and will not generate 3D thermography model, the technology is not developed and discussed in this work. A similar approach was investigated and developed for the self-calibration of a camera-robot-system in this master thesis [26]. Also, Manuel Drust in his dissertation topic, "Development of a sensor system and a method for calculating the robot pose on a basis of projected structures" [27] has dealt with the laser system to project coded features.

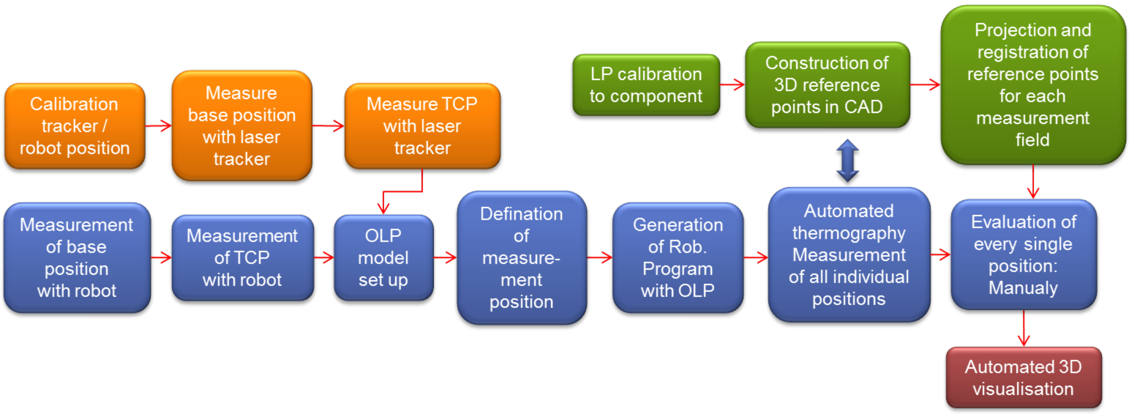

Figure 3.2: Extension of automated thermography process step for 3D visualisation

3.1.2 Kinematic chain based approach

The camera pose has to be calculated in relation to the component while 3D model generation is accomplished, using a robot kinematic coordinates relationship. There are many different approaches for the measurement of a six dimensional camera pose of an industrial robot, such as robot guidance for a machine vision system, robot-based texture mapping or camera calibration [28], [29] and [30]. All these approaches provide possible ways to calculate camera pose in order to improve robot deficiency. The proposed approach in this work is illustrated in figure 3.3.

For the transformation of the points of a coordinate system into another coordinate system, the use of homogeneous coordinates is common in robotics. To transform a coordinate from one to another, the coordinate data has to be converted into matrix form. The arrows in figure 3.3 represent the 3x3 rotational matrix and one translation vector, from one coordinate to next coordinate. The mathematical approaches in order to calculate this transformation are described in more detail in section 3.3. By using this coordinate transformation, all thermography images can be projected onto the 3D measuring model.

In robotics, the spatial positions are described by position vectors, which contain relative position information between two coordinates. Coordinate system C is represented in this thesis as a right-handed coordinate system consisting of the position vector t to the origin of the coordinate system and the coordinate directions r_X,r_Y and r_Z. In robot programming, the use of the following coordinate systems are common:

- **World coordinate:** Fixed common coordinate for a robot mounted on external axis. Also represents cell coordinate.
- **Rob-root:** Fixed coordinate for a robot, which is mounted on floor.
- **Base:** Object's or component's position relative to world or robroot coordinate.
- **Flange:** Connected to the hand flange, relative transformation between rob-root or world to moved position via kinematic chain of joints.
- **TCP:** Fixed transformation between flange coordinate and end-effector working point. Often describes transformation between chosen coordinate and TCP.

A robot manipulator is an electronically controlled mechanism and is composed of an assembly of links and joints. Links are defined as the rigid sections that make up the mechanism and joints are defined as the connection between two links. The attached thermography end-effector at flange is a rigid joint. Therefore, coordinate transformation FT_C (see figure 3.3) between the flange and the camera plane need only to be calculated once. This calibration was performed in section 3.4. Without a pre-calibration (hand-eye calibration) of the camera, the six dimensional pose measurements for every new image are not possible. Parallel geometric camera calibration is also required in order to undistort the images before these are mapped to the component. The BT_R coordinate transformations between the robot and the component need to be calculated whenever the component's positions change. In general, the world coordinate does not change, and the relation between rob-root and world coordinate are calibrated through KUKA robot language. This WT_R coordinate transformations data can be read from machine.dat file. Furthermore, KUKA software delivers the entire coordinate transformations data RT_F between rob-root and flange for all the new positions. BT_R and WT_B transformations data are generated through measuring the component's position by using a 4 point method, provided by KUKA. For a robot, which is mounted on floor, the BT_C transformations data can be calculated by multiplying the following transformations data in equation 3.1. Furthermore the transformation CT_T between camera and TCP is known by measurement distance. Therefore another possible option to calculate the camera position is the calculation of BT_T transformation, which is not implemented in this work.

$$BT_C = BT_R RT_F FT_C \tag{3.1}$$

This has to be done for every measuring field. For a robot with an external axis, BT_R will be replaced by the product of WT_B WT_R. In the following sections 3.6, 3.4 and 3.3 it is explained how the coordinate transformations between base and rob-root, between flange and camera and between Base and camera are calculated. Advantages of this approach are listed below:

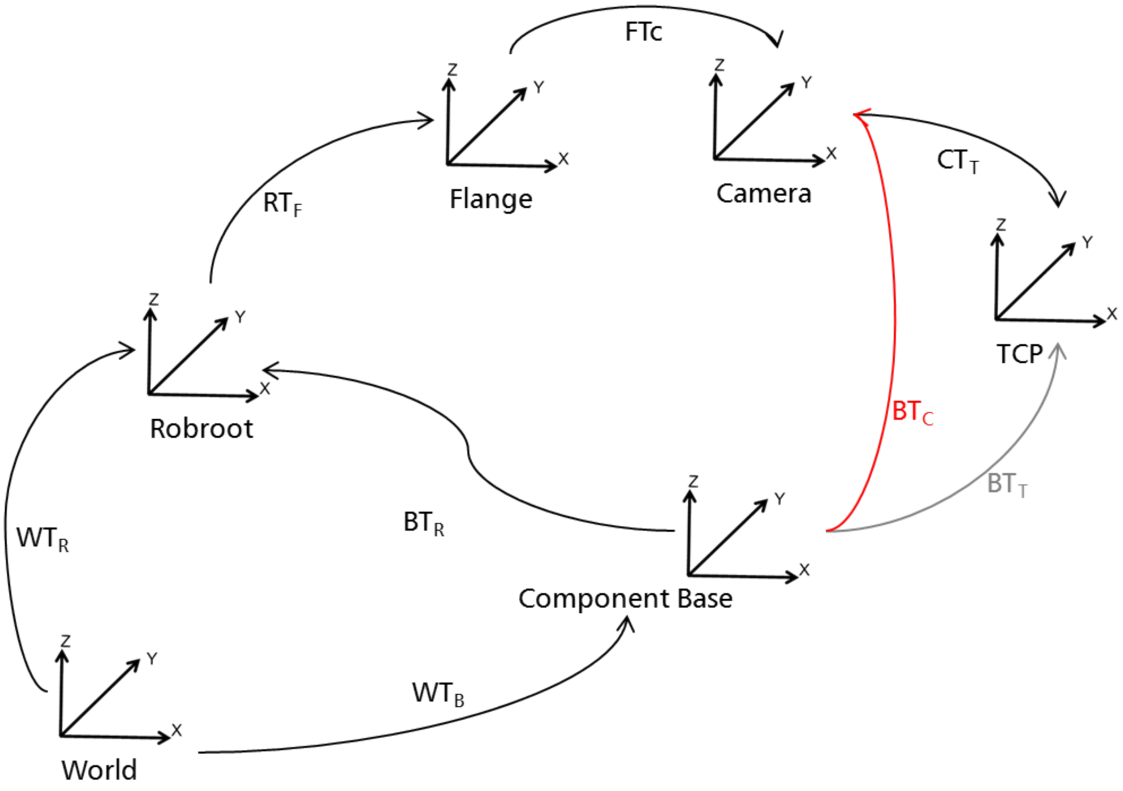

Figure 3.3: Kinematic coordinate chain approach

- No additional instrument or additional process steps are required
- Easy to implement in production line
- Method can also be applied for gantry portal

3.2 Feasibility analysis of 2D-3D point correspondence approach

Before developing the new approach, some boundary conditions should be defined, and foreseeable hardware limitations and increased accuracy should be identified. The aim is to take a close look at the feasibility of the extended process step and to register thermographic images with laser dots. The first image processing is carried out with these images. The aim is to determine to which extent the improvement concept can be applied for reproducible measurements. In order to design the concept for a semi-automated and fully automated application, the operating conditions must be clarified at the beginning of the design. To emphasize the core aspects of the system, the requirements are differentiated into necessary and desirable. The following are boundary conditions and assumptions that are relevant for concept review:

- **Requirement 1:** Generation of stationary laser beams as an unchangeable reference feature of a spatial coordinate system (necessary).
- **Requirement 2:** Since the system is to operate with and without an industrial robot, it is important and realistic in the sense of complexity avoidance not to influence or restrict the working space of the robot at all . On the other hand, for stationary referencing, the system must be set up in the robot cell in such a way that the laser beam is not interrupted by the robot movement. Any component in the working area that must be taken into account when moving the robot must be avoided (necessary).
- **Requirement 3:** Projected points have to be extracted with sub-pixel accuracy through an image processing algorithm (necessary).
- **Requirement 4:** Easy Calibration procedure of the laser system in the component's reference coordinate (necessary).
- **Requirement 5:** Possible interfaces for integration in the process chain (necessary).
- **Requirement 6:** 2M Laser class due to security reasons in the production line (desirable)
- **Requirement 7:** Process time must not be significantly increased by extending the process steps. (desirable)

Laser projector

Many laser projectors which are available in the market meet most of the above requirements. The company LAP LASER has specially developed for a high precision laser projector carbon fibre material (see figure 3.4). The latest model LAP-CAD-PRO, with 5 mW (laser class 2M) laser power, offers ±0.06 mm/m absolute projection accuracy, when the projection area is within ±30°and within 4 m distance. According to the intercept theorem, this accuracy is given for a projection area of approx. 25 m^2. The model (older version) which was used for this approach has, according to the manufacturer of the laser projector ± 0.5 mm/m projection error at a projection distance of 4 m. According to the intercept theorem, the error at 2 m distance is then $<$0.25 mm. Under the given (technical and economical) framework conditions, CAD-PRO model was the right choice for this approach. Laser projectors are used in manufacturing process to support the operator, for example by projecting the contour position of dry carbon fibre cut pieces onto the geometry. The shape of these contours are available from product design, constructed in CAD software. In the same way 3D features position, shape and size can be constructed. For 100% precise projection, an exact calibration, reliable CAD data and surfaces or tools that exactly match the CAD data are the fundament of each projection task. The calibration process is performed by using calibration data, which includes reflector positions on the component and a software provided by LAP. In order to implement the software in an automated thermography process, the projector system offers application programming interface. Further product details and the working principle of CAD-PRO laser projector are available in [31].

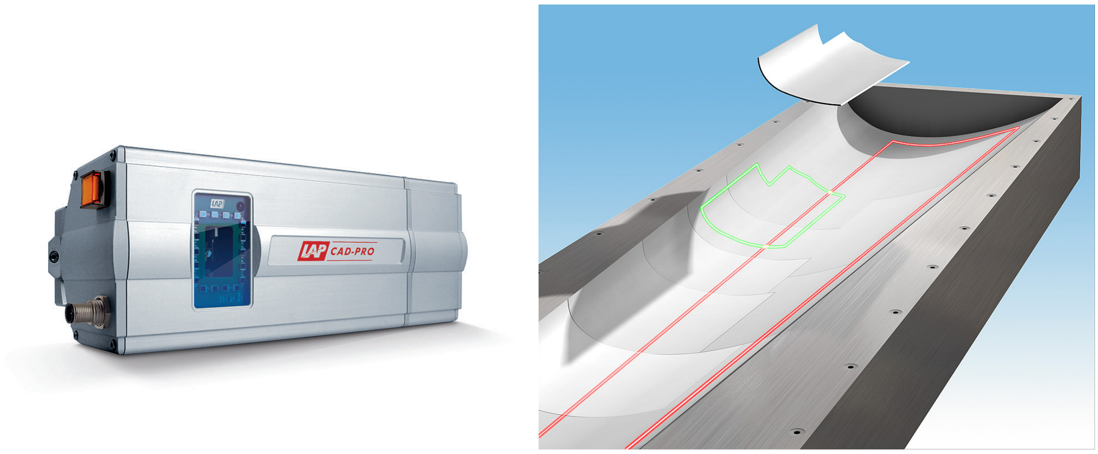

(a) Laser projector

(b) Laser projection during production of composite parts

Figure 3.4: Source: Lap Laser Website: (a) Laser projector; (b)Laser projection during production of composite parts

3.2.1 Image registration and 2D point extraction from thermal image

In this chapter, the automated image registration along with the 2D point extraction from the thermal image are experimentally validated. In order to detect laser spot (small thermal diffusion) with thermography camera, the used laser projector and thermographic camera were not additionally calibrated for the experiment. The experimental setup (see figure 3.5) consists of following components:

1. Halogen lamps (part of end-effector)
2. Thermography camera (part of end-effector)
3. High accuracy robot mounted on floor
4. 4 reflectors for laser projector calibration
5. Projector
6. Coplanar CFRP component

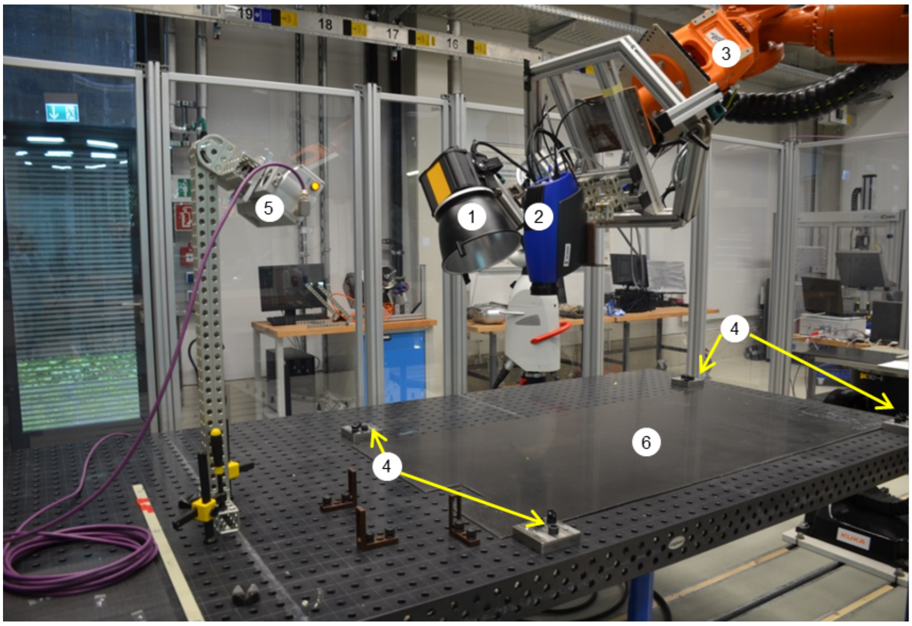

Figure 3.5: Experimental setup for feasibility study of 2D-3D point correspondence approach

After the experimental setup, the base position of CFRP plate and TCP of end-effector were measured by the laser tracker. Afterwards, (as in the previously presented automated thermography process chain in section 2.3) Fastsurf was used to create an offline robot program (see in figure 3.6(e)). 3D reference points (introduced additional process step in figure 3.2) for measurement fields were constructed with *Catia*(see figure 3.6(a and d)). These constructed points were then projected by the laser projector (see figure 3.6(b and c)).The aim of the investigations was to obtain meaningful and reproducible test results and to identify and evaluate physical influencing factors in the measurement results. In order to capture the laser points clearly with the thermography camera, the following criteria were examined:

1. Contour type (rectangle, circle and cross) and contour size from 2 mm to 4 mm. The aim was to find out which of the contour types and sizes is best detectable.

2. Capturing of laser points before and after the component is heated by halogen lamps. The aim was to find out the best projection time. This is due to the fact that during the thermography examination, components are excited with halogen lamps, which may influence the detection of the laser point.

3. Image acquisition as phase image, amplitude image, real/imaginary image and live image. The aim was to identify the best image with the most thermal contrast.

4. Material used to project points may affect detection results due to their reflection and absorption character. The aim was to find the influence of material properties.

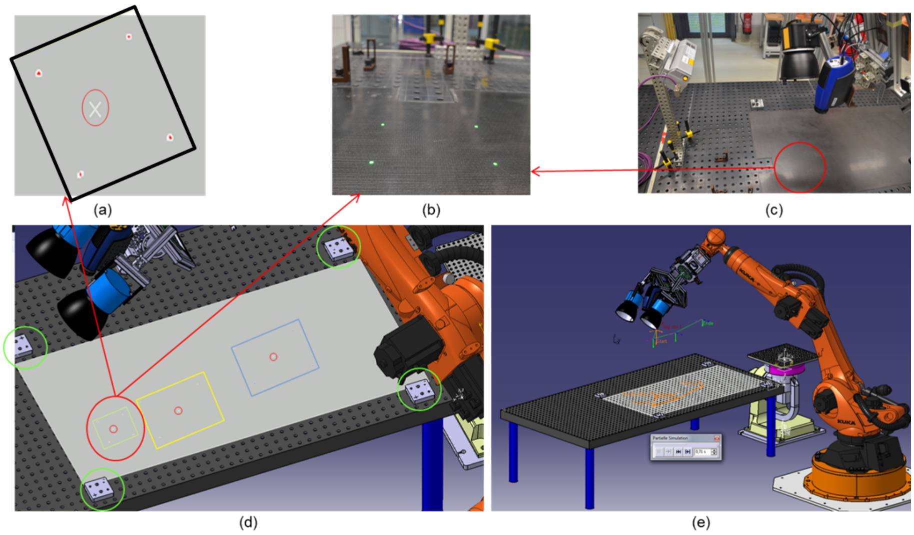

Figure 3.6: (a, d) Definition of measurement field in CAD, (b, c) projected laser points after calibration (e) generated Offline-Robot program

With the projector, all four contours or features could be projected simultaneously. However, the performance of the projector was so low that the thermography

camera did not recognise the contours all together, and prevented the distinguishing of different features. For this reason, individual features were projected as circle one after another, and four images were taken with the respective features. Similarly, no laser points could be detected after heating the component. For this reason, only a live image was saved for image processing before the component was preheated. In the experiment, points were projected on a different surface of CFRP plates. Depending on the degree of reflection and absorption of the material, a slight difference in both visible and image processing detection of laser points could be observed.
During the experiment some limitations to capture the laser points with a thermography camera could be observed. Although these limitations were observed, the decision was made first to investigate whether these points could be extracted automatically at all. After that, a detailed investigation was performed (see section 3.2.2)to determine the influencing factors of laser point extraction.

2D point extraction from thermal image

In principle, the laser points can be recognised with the thermography camera despite a lower performance. The projected laser points are easy for the human eye to recognise. Intuition in humans enables us to extract the projections from the background of the image and transfer them to a list of features. The automation of this chain of process is complicated and requires different interpretation steps and image processing operations. Object recognition in image processing is a complex process that has many uncertain factors. It is possible to find wrong objects or not find existing ones at all. In the last 20 years, there has been a keen research interest in automated feature recognition from images for 3D reconstruction purpose. This recognition may be in terms of vanishing points or lines [32] and [33], co-planarity [34] and spatial inter-relationship of features [35]. The most critical point in this process depends on the precise and reliable identification of structural elements that belong, which is provided interactively by the user. For the new concept (see above), the respectively provided projected laser points, which are visible by thermography camera due to local surface temperature differences, have to be recognised automatically. First of all, different lighting conditions (contrast) depending on surface reflection make it difficult to automatically extract the laser point. It is known that carbon fibres are conductive. Therefore, the heat flows faster in the fibre direction than in others. Thus, the circles appear as ellipses, which in turn makes automatic extraction difficult. Furthermore, a laser point does not have a smooth contour of an circle, but a blurred and diffuse contour. This reduces the contrast between the light spot and the background, and the closer surroundings of a light spot are noisy. The intensity curve of a laser spot can be compared with the Gaussian curve.
Template matching is part of model-based segmentation. The laser dot is 32x32 pixels in size. The maximum intensity of the laser is in the centre. For the automatic search of the maximum intensity of the laser point, a model (template) with

Corel Draw was created. The model consists of 32 x 32 pixels and has a radial brightness gradient from the centre to outside (see Figure 3.8 (a)). The template needed to be as large as possible. Centre (x- and y-component) of the detected laser spot and the percentage of how good the ideal template fits to the captured laser spot are the main outputs of the algorithm. This percentage match is the most important indicator of how precise the centre of the laser spot can be extracted. The laser points in individual images can be extracted by cross correlation with the template. Thus each laser point has a pixel coordinate and qualifies for the first feasibility study. Laser points were determined pixel-precisely for this experiment and a sub-pixel-precise extraction was implemented for later experiments. The pixel coordinates and the correlation value are listed in table 3.1. Currently, individual images were read and processed one after another in the *Matlab* program. Since this was primarily a feasibility study, no program structure was defined to reduce the overall processing time. The figure 3.7 shows the original or live images, ROI images (after conversion to a grey image) and the intensity value of the laser points according to the cross correlation. Although the laser points were already recognisable for further experiments, the algorithm could still be optimised to maximise correlation value. Although the correlation value of Point One is comparatively smaller than the other points, it is still enough to identify the spot.
In the next step, thermography measurement was performed without laser points. The evaluated phase image of the measurement position was then imported into *Matlab* and displayed together with four reference points, or laser points, according to pixel coordinates (see figure 3.8(b)). Thus each image receives the 2D reference points for the respective measuring position. Since these 2D reference points are generated from 3D reference points and both reference points have a common component coordinate system, all individual images can be assigned in three-dimensional space. The goal is an automatic stitching of the images for a 3D visualisation.

Table 3.1: 2D pixel coordinates and correlations value

Points	X peak	Y peak	Max correlation in %
point 1	12	596	52,77
point 2	428	590	78,27
point 3	422	79	77,48
point 4	8	85	76,81

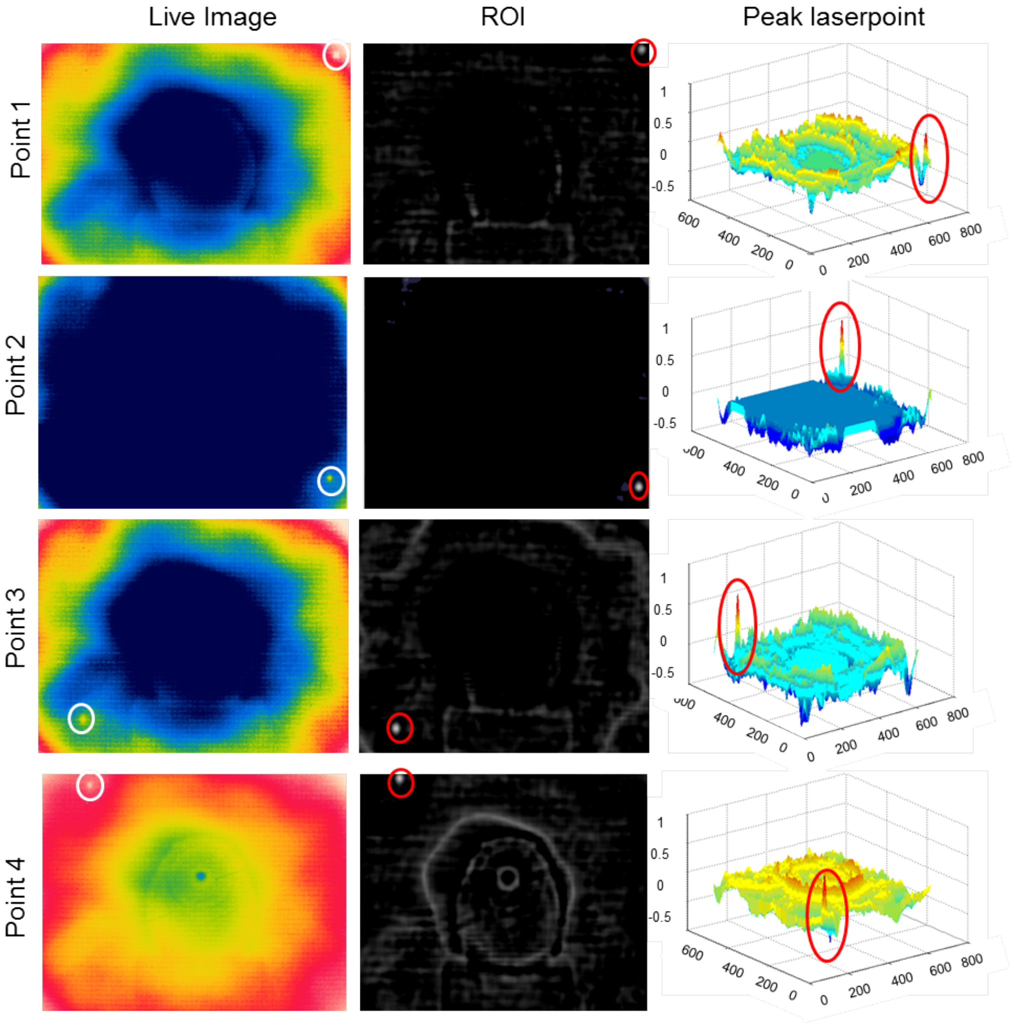

Figure 3.7: 2D laser point extraction

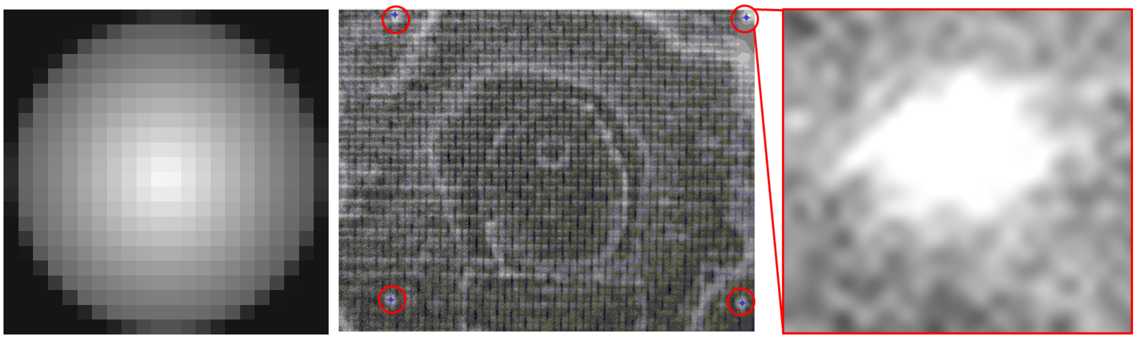
(a)

(b)

Figure 3.8: (a) Template; (b)Extracted 2D point on thermography image and enlarged laser point

Conclusions

The extraction of the laser points with the template showed promising results. It was observed that the laser projector used here does not have sufficient power to detect four points simultaneously with the thermography camera. Therefore, individual points were projected. This deficit could be overcome either by a high laser power or by simultaneous application of several laser projectors, or by an even more sensitive thermography camera. Overall, the correlation value after the automatic recognition of the laser points is well usable. These laser points serve as reference points for the thermographic image of the respective position. The results obtained here build the foundation for further investigations.

3.2.2 Influencing factors of laser point extraction

Although in the last investigation the laser point was clearly recognisable, there are still some factors which can influence the recognition of the laser point. The primary aim was to find the influencing factors by means of: whether two laser projectors instead of one projector, a small contour projection instead of a large contour, the change of the camera distance, or laser projector distance to the component brings clear advantages in the recognition of the laser point. The experimental setup is almost the same as in the last experiment. In this test series, two laser projectors were mounted on movable tripods in order to vary the projector distance to the component. The distance between the camera and the component was changed using a robot. The laser points were projected onto both a 2D component (plate) and a 3D component. The calibration error of the two projectors was 0.025, which is dimensionless.
Right at the beginning of the test series, it was found that minimal (from 1 m up to 4 m) change in the distance of the projectors has no measurable influence on the laser spot detection. Therefore, the distance was kept constant by 3 m and not changed during further experimentation. The Projected contours were in diameter 0.05 mm, 0,1 mm, 0,2 mm, 0,5 mm, 1 mm and 2 mm. The contours were projected on the 5 mm and 2 mm thick plate on the tool side (more reflection) and on the non-tool side (less reflection). The plates were made of different fabric materials. The contours were captured with the thermography camera at a distance of 250 mm and 500 mm. This process was performed twice (once with one laser projector and a second time with two projectors). Figures 3.9a and 3.9b show the extracted laser points after evaluation in image coordinates for approx. 250 mm camera distance to the 5 mm thick plate. The contours were projected on the non-tool side and also on the tool side. It could be noticed in these two figures that the uncertainty factor of point extraction on non-tooling side is one pixel compared to the tooling side by two pixels. The following three reasons are apparent for the uncertainty factor of the laser spot extraction in image coordinates:

1. Depending on the fibre orientation and position (the tool side reflects more

than the opposite side or the non-tool side) of the plate, the laser beam reflects differently (angle of incidence equal to the angle of reflection) and is registered accordingly in the thermographic camera. Since the camera distance to the component was too small (in this case 250 mm), the thermographic camera could not recognise the larger contours as a point, due to random reflection properties. Thus, the evaluation algorithm for laser point detection within a plate found different pixel values in image coordinates.

2. Furthermore, images are extracted with pixel accuracy and can be minimised or avoided with sub-pixel accuracy extraction.

3. A similar or more uncertainty factor was also observed for this configuration by using two projectors, as the projection was not congruent due to a not optimised calibration with only four reflectors. The uncertainty factor in this case was between 1 and 2 Pixels.

Further experiments were conducted with a 500 mm camera distance. Here too, experiment results had shown irregular reflections on both the tooling and non-tooling sides, which led to one pixel uncertainty factor. The projected 5 mm contour could be extracted compared to the results by 250 mm camera distance. The evaluated results of the experiments are shown in figures 3.9c and 3.9d. Both figures show a pixel value difference within the plate on the X-axis. This was most likely due to the random reflection and rounding error (1 pixel) of point extraction. The pixel value uncertainty factor on the Y-axis between two plates has arisen due to the difference in component thickness.The evaluation of this result is that the camera distance and the contour size are directly dependent on each other. The larger the contours, the larger the camera distance should be. According to test results, up to 1 mm couture size, the uncertainty factor at a camera distance of approx. 500 mm is one pixel. Therefore, for a stable point the smallest contour of 0.1 mm was used for further experiment of this work. A Flir camera SC500 model, which was used for this experimentation has a 20° × 16° optic with a camera resolution of 640 × 512 pixel. According to equation 3.2 a maximum 1 pixel uncertainty factor in one direction represents approx. 0,27 mm. With a sub-pixel detection accuracy this error can be reduced.

$$X = h\,tan\Delta\phi \tag{3.2}$$

$$\phi = 20^\circ, \Delta\phi = 20^\circ/640pixel \Rightarrow 0.031, h = 500\,mm \Rightarrow X \approx 0.27\,mm \tag{3.3}$$

Figure 3.9 (e) shows that no difference between two projectors can be seen in the correlation value, even though the contours were projected once with a projector and once with two projectors onto a 5 mm and a 2 mm thick component. The correlation value was between 70% and 80%. Thus, it could be stated that the number of projectors has no significant influence. The component reflection plays a certain role in laser point detection. However, this can be avoided by increasing the camera distance to the component and reducing projection contour (for example 0.1 mm). Furthermore, different filters to reduce noise and algorithm for sub-pixel detection were implemented for further experiments. Later on for 3D reconstruction, a new software version was used to detect corresponding 2D laser points on the image.

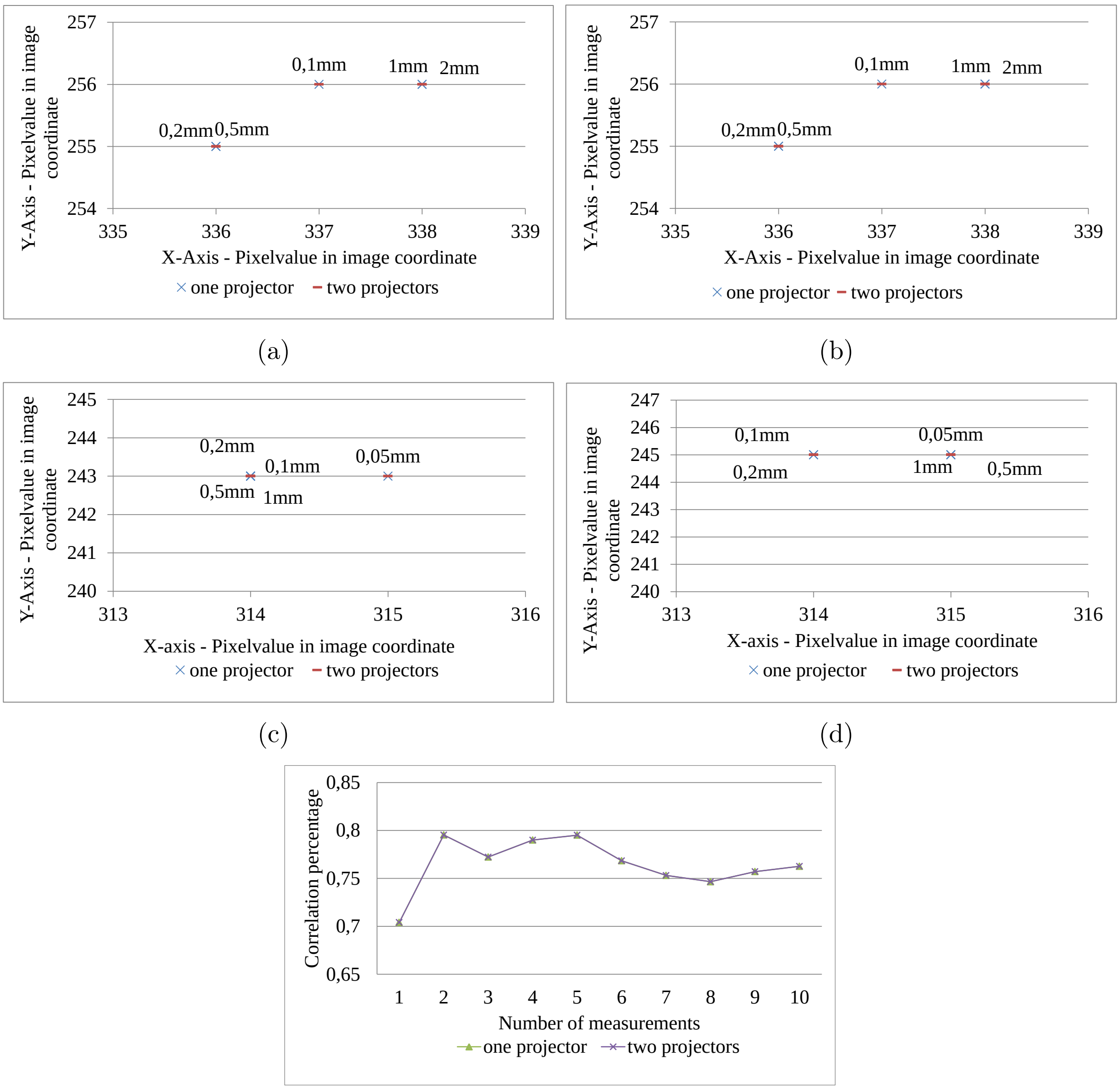

(a) (b)

(c) (d)

(e)

Figure 3.9: Influencing factors for laser point extraction (a) camera distance 250 mm, non-tool side, 5 mm plate; (b) camera distance 250 mm, tool side, 5 mm plate; (c) camera distance 500 mm, non-tool side, 5 mm plate; (d)camera distance 500 mm, non-tool side, 2 mm plate; (e) Correlation value of extracted laser points for 500 mm camera distance and number of laser projectors

3.2.3 Conclusions

In the experiment, all relevant influencing factors were examined individually. During the investigation it was found that the use of two projectors for point recognition does not bring any recognisable advantages. It could be shown that there is a direct correlation between the projected contour size and the camera distance from the component. For a random contour or point recognition, smaller circles with a diameter of 0.1 mm should be projected and the camera distance should be as large as possible. The correlation value for this test series was between 70% and 80%. Since only the laser spot generates heat within the measuring field, the thermal contrast is high enough compared to the rest of the measuring field. Thus this correlation value between 70% and 80% is very reliable. However, due to the component's properties, there was a random reflection on the tool side, and the accuracy of the points extraction is associated with this.

3.3 Geometric transformation

In general, objects can be described in euclidean space. In addition to the common Euclidean [36] space $\mathbb{R}^3$, there are two further specialisations of the projective space $\mathbb{P}^3$: affine space and metric space. By transforming an object's geometry into affine space and projective space, information about angles and parallelism are lost accordingly. An object differs in metric space from Euclidean space by its scaling factor.

The image captured by a camera represents the 2D projection of a real point, in the 3-dimensional space of the given point. For a complete reconstruction of a three-dimensional object from two-dimensional images, the actual position of the object and various transformation parameters must be known. Therefore, the following sections will introduce the relevant mathematical basics of the projective images, as well as the rotational and translational transformation, along with the applied mathematical notation. In order to understand the process of 3D reconstruction, the first geometrical projection in homogenous coordinates and the perspective projection based on the pinhole camera model are explained in this chapter. The pinhole camera model describes how a world point is projected onto the camera's sensor. All applied algorithms in this work are based on the understanding of the camera model and therefore require this during the creation of the a 3D reconstruction as shown in figure 3.10. The perspective projection in figure 3.10 represents the following transformations from the three-dimensional points in space $\mathbb{R}^3$ into 2D plane $\mathbb{R}^2$:

1. from world coordinate system (W) into camera coordinate system (C) by means of extrinsic parameters [37].
2. from camera coordinate system into image coordinate ($\mathrm{I}_{\mathrm{Plane}}$) by means of intrinsic parameters

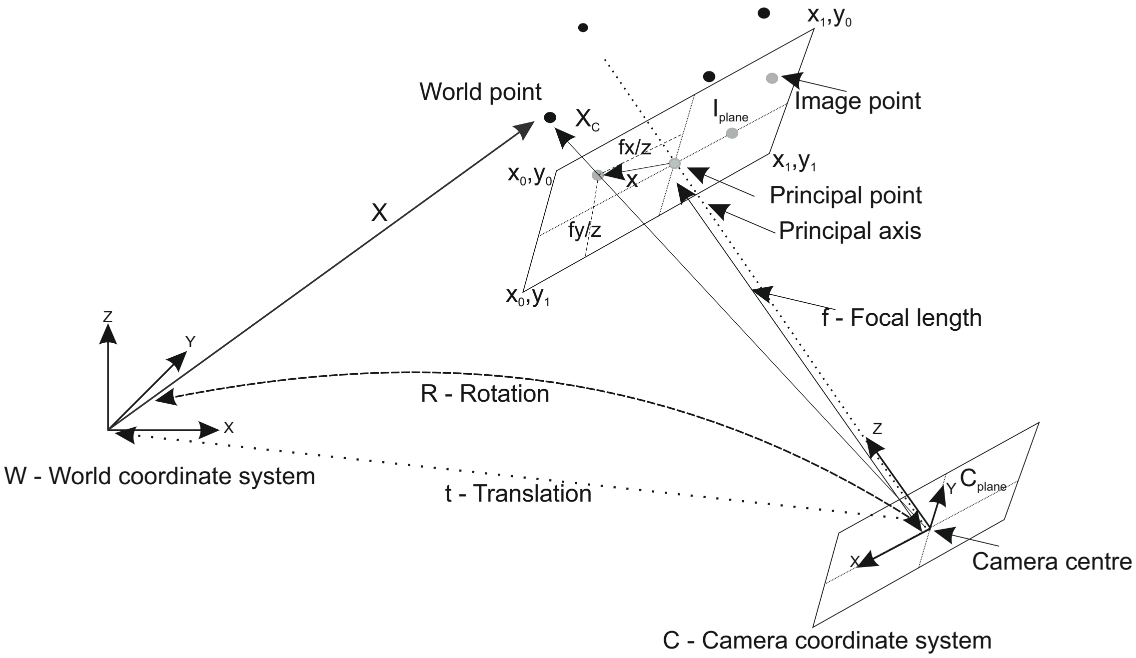

Figure 3.10: Geometric projection

3.3.1 Geometric projection in a homogeneous coordinate

For an ordinary plane, two lines will either intersect at one point, or do not intersect, as they are parallel to each other. But parallel lines seems to intersect at infinity in a projective plane. A common example of this effect is an image of a rail track, which seems to converge at the horizon. Typically, in ordinary plane $\mathbb{R}^2$, 2D points are represented by a pair of coordinates x and y (see equation 3.4)

$$\begin{pmatrix} x \\ y \end{pmatrix} = \bar{P}, \bar{P} \in \mathbb{R}^2 \tag{3.4}$$

In projective plane $\mathbb{P}^2$ this 2D point can be represented by assigning another coordinate $w = 1$, which is a non-zero constant $k \neq 0$. In general, it can be said that each point $x = (x, y)^{\mathrm{T}}$ in $\mathbb{R}^2$ has an equivalent $(\tilde{x}, \tilde{y}, 1)^{\mathrm{T}}$ in $\mathbb{P}^2$. In particular k can be multiplied in a homogenous coordinate into every x, as well as w. This alternative way of representing points is the called a homogeneous coordinate. The vector in a homogenous coordinate has the form:

$$\begin{pmatrix} kx \\ ky \\ k \end{pmatrix} = \begin{pmatrix} \tilde{x} \\ \tilde{y} \\ w \end{pmatrix} = P, P \in \mathbb{P}^2 \tag{3.5}$$

The equation 3.5 represents a linear transformation. As the homogenous coordinate is scale-invariant, the euclidean coordinate can be recalculated from the homogenous coordinate by dividing equivalently the last coordinate by w (see equation 3.6) [38].

For the case $(x, y, 0)^{\mathrm{T}}$ it would mean that the point lies in the infinite.

$$x = \frac{\tilde{x}}{w} \quad \text{and} \quad y = \frac{\tilde{y}}{w} \quad \text{for} \quad w \neq 0 \tag{3.6}$$

The same applies for 3D points. A euclidean 3D object point $X = (X, Y, Z)^{\mathrm{T}}$ in $\mathbb{R}^3$ space can be represented in homogeneous coordinates by extending the w coordinate into homogeneous coordinates $(\tilde{X}, \tilde{Y}, \tilde{Z}, 1)^{\mathrm{T}}$ and by dividing the same coordinate component back from projective space $\mathbb{P}^3$.

$$X = \frac{\tilde{X}}{W} \quad Y = \frac{\tilde{Y}}{W} \quad \text{and} \quad Z = \frac{\tilde{Z}}{W} \quad \text{for} \quad W \neq 0 \tag{3.7}$$

A projective transformation in $\mathbb{P}^2$ is the linear transformation, accompanied by any translation (by left-multiplying by a 3×3 non-singular matrix H) of three homogeneous points from $\mathbb{P}^2$ to $\mathbb{P}^2$. The same applies for $\mathbb{P}^3$ space. Recall that a 3D vector has to be preliminarily transformed from the 4x1 physical 3D coordinates into a homogeneous coordinate, which has an additional component $W = 1$ as a scaling factor. The introduction of an additional component allows all transformations to be expressed uniformly as matrix operations. This 4x4 matrix, M is known as the imaging transformation, or the perspective transformation matrix, or the projection matrix. Given X as the 3D points in homogenous coordinates and the homogeneous image coordinates x, the equation can be expressed by:

$$\begin{pmatrix} x \\ w \end{pmatrix} = M \cdot \begin{pmatrix} X \\ 1 \end{pmatrix} \tag{3.8}$$

This perspective transformation, which is linear in homogeneous coordinates and the matrix is invertible, is called homography. It is obvious to transform 3D points into a homogenous coordinate, where the third dimension has to be scaled by W in order to transform X into inhomogeneous coordinates. Recalling the equations 3.6 and 3.7, dividing X by W gives the desired position on the image plane. With this perspective transformation the points are transferred from $\mathbb{R}^3$ to $\mathbb{R}^2$. It can be seen that the model described is only unique in one direction, since the depth information is lost. In other words, 3D model vertices will be transformed to a thermography image pixel (see in section 3.5 and 3.6). The equation 3.8 can be written as follows:

$$\begin{bmatrix} x \\ y \\ z \\ 1 \end{bmatrix} = \begin{bmatrix} k_{\mathrm{x}} & 0 & 0 & t_{\mathrm{x}} \\ 0 & k_{\mathrm{y}} & 0 & t_{\mathrm{y}} \\ 0 & 0 & k_{\mathrm{z}} & t_{\mathrm{z}} \\ 0 & 0 & 0 & 1 \end{bmatrix} \cdot \begin{bmatrix} X \\ Y \\ Z \\ 1 \end{bmatrix} \Rightarrow \begin{bmatrix} k & 0 & 0 & t_{\mathrm{x}} \\ 0 & k & 0 & t_{\mathrm{y}} \\ 0 & 0 & k & t_{\mathrm{z}} \\ 0 & 0 & 0 & 1 \end{bmatrix} \cdot \begin{bmatrix} X \\ Y \\ Z \\ 1 \end{bmatrix} \tag{3.9}$$

Since the scaling distances (k_{x},k_{y}, k_{z}) in projective space are usually not preserved, an average ($\sqrt{3}$) scaling factor k must be calculated by translating the centroid into the coordinate origin. This will decrease the dependency condition number to solve the matrix M. Similar to points, lines can also be represented in homogeneous coordinates. For further detailed information on geometric projection such as lines, conics in homogeneous coordinates, please refer to [39].

3.3.2 Pinhole camera model

In order to describe a perspective representation of objects in $\mathbb{R}^3$ via one central projection C into the image plane, the camera parameters of the pinhole camera concept must be modelled. The pinhole camera model is inspired by the simplest cameras with a light sensible surface. The light from an object enters through a small hole (the pinhole) in the front and produces an image on the back camera wall (see figure 3.11).

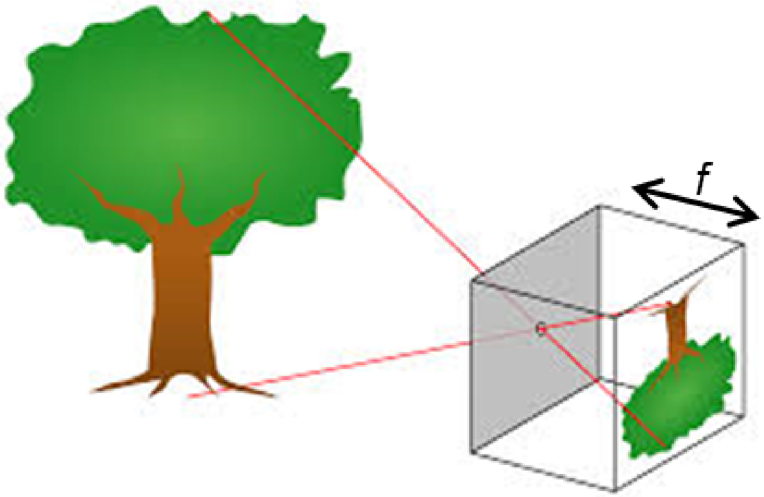

Figure 3.11: Pinhole camera model (source: Wikipedia)

The pinhole camera model therefore has no optics, but only the hole as an aperture, resulting in a theoretically infinite depth of field. This means that when imaging objects are near the camera, small differences in depth become more apparent. Furthermore, for the pinhole camera model, a world point and the corresponding image point lie on a straight line that passes through the origin C of the camera coordinate system (see figure 3.10). Therefore, world points can be projected onto pixels with central projection. In this case, points are projected on the image plane / real projective plane ($\mathrm{I}_{\mathrm{Plane}}$). With a homogeneous coordinate as, explained above, the central projective image can be linearised and the matrix can be inverted. The inversion is necessary for projective transformation between two and three dimensional space.

The line, which is perpendicular to the image plane and coming from the camera centre is called a principal axis. The intersecting point of this line on image plane is called a principal point. The focal length f has a distance (see figures 3.10 and 3.11) between image plane (I_{Plane}) and the origin C of the camera coordinate system, which has to always be bigger than 0 [40]. Under the pinhole camera model, a 3D point in a space coordinate system with coordinates $X = (X, Y, Z)^{\mathrm{T}}$ is mapped to image point $x = (x, y)^{\mathrm{T}}$ on the image plane with origin at position $(0, 0, f)$. The focal length f is considered in the image plane as $Z = f$ and has directional vector $(0, 0, 1)$. Now one can compute the central projection of the 3D point from the figure 3.10 by applying the intercept theorem. This is defined by:

$$x = X \cdot \frac{f}{Z} \quad \text{and} \quad y = Y \cdot \frac{f}{Z} \tag{3.10}$$

The equation 3.10 can be applied to 3D points, which then can be mapped non linearly in euclidean coordinates from space $\mathbb{R}^3$ to space $\mathbb{R}^2$. For linear mapping, the equation 3.10 can be transformed into homogenous coordinates and can be recomposed by:

$$\begin{pmatrix} x \\ y \\ w \end{pmatrix} \rightarrow \begin{pmatrix} f \cdot X \\ f \cdot Y \\ Z \end{pmatrix} \tag{3.11}$$

If the world point X with 4-vector $(X, Y, Z, 1)^{\mathrm{T}}$ and image point x with 3-vector $(x, y, w)^{\mathrm{T}}$ are represented in homogenous coordinates, the equation 3.11 can be recomposed by:

$$\begin{bmatrix} fX \\ f \\ Z \end{bmatrix} = \begin{bmatrix} f & 0 & 0 & 0 \\ 0 & f & 0 & 0 \\ 0 & 0 & 1 & 0 \end{bmatrix} \cdot \begin{bmatrix} X \\ Y \\ Z \\ 1 \end{bmatrix} \Leftrightarrow x = PX \tag{3.12}$$

P represents here a 3×4 transformation matrix. This transformation matrix can be extended and rearranged to a projection matrix, which is described in the next chapter. Furthermore, for pinhole camera models, the image plane must be located in front of the origin (see figure 3.10) so that the image is not inverted. In reality, the image plane lies behind the focal plane (see figure 3.11). Thus f has a negative value and pictures are therefore mirrored.

3.3.3 Projection matrix

The transformation matrix P in equation 3.12 represents a direct relationship between world points and image points, if the world points are given relative to the camera coordinates system. Since firstly, in reality, the position of the world points are given in their own world coordinate system and secondly, the pinhole camera model represents a simplified model (without lens distortion), the transformation matrix must be extended. One can note that the last column of the matrix P in equation 3.12 is 0. In other words the transformation matrix needs to be extended to intrinsic parameter (lens distortions) and 4x1 translation vector t. With these characteristics the transformation matrix can be converted into a projection matrix. In this case the projection matrix is simply

$$x = PX \Leftrightarrow x = K \cdot M \cdot X \quad where \quad M = [R|t] \tag{3.13}$$

K calibration matrix, represents a 3x3 intrinsic linear parameter, which are determined later in chapter 3.4. Also non-linear camera parameters are determined later in chapter 3.4. Furthermore M is a 3x3 matrix and contains information about the extrinsic parameters of R and t, which relate the camera orientation and position to the world coordinate system.Thus the specification of the matrix P is sufficient for the complete modelling of the camera properties. It describes the linear perspective transformation in the projective space from 3D to 2D and distinguishes between the world and camera coordinate system by the following representation: $X = RX + t$ [41]. Now the 3x4 projection matrix can be composed as follows:

$$x = PX \Leftrightarrow x = K \begin{bmatrix} 1 & 0 & 0 & 0 \\ 0 & 1 & 0 & 0 \\ 0 & 0 & 1 & 0 \end{bmatrix} \begin{bmatrix} R & t \\ 0 & 1 \end{bmatrix} X \tag{3.14}$$

In the case of the 3x4 transformation matrix in the equation 3.12, which describes the transformation from the camera coordinate system to the image coordinate system, some simplified assumptions were made about the sensor element of camera. Since the intrinsic camera parameter describes the image information, these parameters are expressed in pixel coordinates. The real intrinsic linear camera parameters K differs with the ideal pinhole camera parameters and can be expressed by:

$$K = \begin{bmatrix} f_{\mathrm{x}} & s & x_0 & 0 \\ 0 & f_{\mathrm{y}} & y_0 & 0 \\ 0 & 0 & 1 & 0 \end{bmatrix} \tag{3.15}$$

One can note from the equation 3.15, that the matrix has 5 degrees of freedom, which is defined by the upper triangle matrix. The following points describe these parameters in detail:

- Every sensor element of the CCD chip are in reality built with a non-square element and therefore needs to be scaled in both f_{x} and f_{y} directions of focal length. This has a direct effect on image, as images are represented in pixel coordinates.

- Similarly the principal point lies at image centre in the case of ideal pinhole camera. But due to manufacturing disorder, the optical axis does not intersect in reality at the image centre of the sensor. Therefore, the image centre is shifted to x_0 and y_0 and needs to be translated relative to the image centre.

- The fifth degree of freedom describes skew parameter s, which is for most of the cameras zero [42]. This means, x and y pixel elements in the CCD array are not perpendicular to each other. Later in chapter 3.4.1 this will be validated through geometric camera calibration.

In total the projection matrix P has 11 ($R : 3, t : 3, f, s, x_0$ and y_0) degrees of freedom which can be defined by:

$$P = \begin{bmatrix} p_{11} & p_{12} & p_{13} & p_{14} \\ p_{21} & p_{22} & p_{23} & p_{24} \\ p_{31} & p_{32} & p_{33} & p_{34} \end{bmatrix} \tag{3.16}$$

If the projection matrix P is multiplied in homogeneous coordinates with 3D world points, then by dividing the last component ($\mathrm{p}_{34} = 1$), the image points can be calculated in euclidean coordinates. In equation 3.17 x' and y' represent image coordinates in euclidean coordinates.

$$x' = \frac{p_{11} \cdot x + p_{12} \cdot y + p_{13} \cdot z + p_{14}}{p_{31} \cdot x + p_{32} \cdot y + p_{33} \cdot z + p_{34}} \quad y' = \frac{p_{21} \cdot x + p_{22} \cdot y + p_{23} \cdot z + p_{24}}{p_{31} \cdot x + p_{32} \cdot y + p_{33} \cdot z + p_{34}} \tag{3.17}$$

3.3.4 Weak perspective projection

Up to now, perspective projection is described by linear transformation using the simplified pinhole camera model. This simplified model can even be more simple, when objects are far away from the camera and perspective projection can be ignored. The figure 3.12 represents the small depth difference, when imaging objects are at infinity. Another camera model, which is based on a parallel to optical axis transformation of world point to image plane, is called an orthographic camera model. Also here the parameters of perceptive projections are less apparent. Weak perspective camera model differs from the orthographic model only by the scaling factor. In order to approximate the pinhole camera model for weak perspective model, the scaling factor can be expressed by $-f/Z$. In other words for the unit size of an object (no matter how far the object is) the equation 3.10 can be recomposed by:

$$x = X_{\mathrm{C}} \cdot \frac{-f}{Z_{\mathrm{C}}} \quad \text{and} \quad y = Y_{\mathrm{C}} \cdot \frac{-f}{Z_{\mathrm{C}}} \tag{3.18}$$

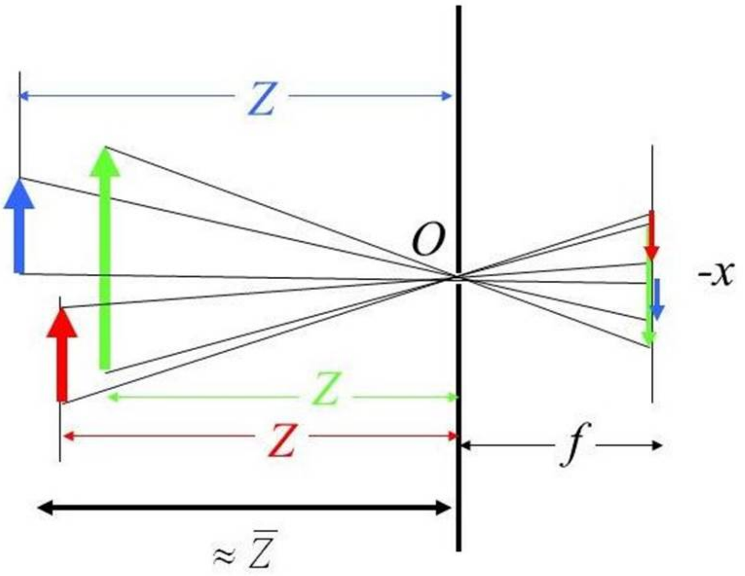

Source: https://slideplayer.com/slide/5110107/16/images/17/Weak+Perspective+Projection.jpg

Figure 3.12: Weak perspective projection model

3.3.5 Orthogonal distance regression to plane

For the selection of the mathematical approaches to calculate camera perspective, it is important to determine to what extent a set of points lies on a plane. There are different kinds of mathematical approaches, which minimise the distance between points and plane, for a best-fit of plane to the points. The applied approach here minimises perpendicular distances by an orthogonal distance regression.
Given are a set of 3D points in Cartesian coordinate $X_\mathrm{i} = (X_\mathrm{i}, Y_\mathrm{i}, Z_\mathrm{i})^\mathrm{T}$, which are lying on a plane. The plane is defined by:

$$Z_\mathrm{i} = aX_\mathrm{i} + bY_\mathrm{i} + c \tag{3.19}$$

The goal is to find out the orthogonal distance regression plane, which is overdetermined for more than 3 points and can be solved by utilising Singular Value Decomposition (SVD). This can be calculated by linear constellation

$$Ax = B \quad \Leftrightarrow \quad (X_\mathrm{i}, Y_\mathrm{i}, 1)\begin{bmatrix} a \\ b \\ c \end{bmatrix} = (Z_\mathrm{i}) = A\begin{bmatrix} a \\ b \\ c \end{bmatrix} = B \tag{3.20}$$

of a, b, c parameters. Now all coefficients of each points can be solved by left pseudo inverse:

$$\begin{bmatrix} a \\ b \\ c \end{bmatrix} = (A^\mathrm{T}A)^{-1}A^\mathrm{T}B \tag{3.21}$$

Furthermore the minimum distance between the point X_i and orthogonal distance regression plane needs to be calculated. The shortest distance between a point and plane is a straight line, which is a vector lying perpendicular on plane. This vector n (normal to plane) can be calculated for three different points (X_1, X_2, X_3) (minimum requirements to generate a plane) by:

$$n = (X_2 - X_1) \times (X_3 - X_1) \tag{3.22}$$

now the intersecting point q_i on the plane of a line in normal direction n (oriented perpendicular to the plane launched from the beginning of the coordinate system), which is passing through X_i can be expressed by:

$$d : q_\mathrm{i} = X_\mathrm{i} + n\lambda \tag{3.23}$$

d represents the shortest distance. Now the unknown parameter λ which is a scalar product with vectors n in orthogonal direction can be calculated by entering coordinates q_i in the equation 3.19 of plane:

$$q_{\mathrm{Z_i}} = aq_{\mathrm{X_i}} + bq_{\mathrm{Y_i}} + c \tag{3.24}$$

By establishing a substitution

$$c = -aX_\mathrm{i} - bY_\mathrm{i} - Z_\mathrm{i} \tag{3.25}$$

and entering the equation 3.25 in equation 3.23 parameter λ can be solved by:

$$\lambda = \frac{Z_\mathrm{i} - aX_\mathrm{i} - bY_\mathrm{i} - c}{an_\mathrm{x} - bn_\mathrm{y} - n_\mathrm{z}} \tag{3.26}$$

Unknown components of the normal vector of the plane $\prod = (a, b, c)^\mathrm{T}$ are made up of elements of the eigenvector corresponding to the minimum eigenvalue λ. Finally the orthogonal distance regression planes can be determined for k number of points by the relationship

$$d = \frac{1}{k} \sum_{j=1}^{k} \mid X_\mathrm{i} - q_\mathrm{i} \mid \tag{3.27}$$

3.3.6 Projection matrix from kinematic chain relationship

This section describes the mathematical approach for robot-based 3D reconstruction. In chapter 3.1, the concept for determining the camera pose via a kinematic chain relationship was explained. The kinematic chain in the equation 3.1 describes the 3x3 rotation matrix and one translation vector, which is the coordinate transformation in euclidean space. The coordinate transformation between the component base and the camera has to be especially determined. In the case of 3D point, which is given in the component's coordinate $X_\mathrm{obj} = (X, Y, Z)^\mathrm{T}$ can be transformed to the camera coordinate by:

$$X_\mathrm{cam} = RX_\mathrm{obj} + t \tag{3.28}$$

This coordinate to coordinate transformation introduces the basic concepts that are required to describe camera positions and orientations of rigid bodies in space. Since the transformation between the base and the camera is fixed, a homogeneous transformation matrix exists. Thus this homogenous transformation matrix M (see equation 3.8) can be recomposed by:

$$\tilde{X}_\mathrm{cam} = \begin{bmatrix} R & t \\ 0 & 1 \end{bmatrix} \tilde{X}_\mathrm{obj} = BT_\mathrm{C}\tilde{X}_\mathrm{obj} \tag{3.29}$$

As the camera is fixed to the flange, for each measuring position this transformation matrix must be defined separately. Furthermore the columns of the upper left 3x3 rotational matrix are orthogonal to each other and the inverse of a rotation matrix is equal to its transpose. So the scalar product of the inverted transformation matrix $\mathrm{BT_C}$ (Base to camera) and a 2D camera position $\tilde{X}_\mathrm{cam}$ delivers a 3D position $\tilde{X}_\mathrm{obj}$. The first three elements of a homogeneous position vector are the components of the corresponding position vector, and the fourth element is 1. One can note, that both the robot-based transformation matrix and the point-correspondence-based transformation matrix (see equation 3.14) has same Rank. Similarly for continuous transformation or kinematic chain relationship from one coordinate to other in euclidean space (with the help of homogenous coordinates), all transformation matrices need to be multiplied serially. The following equation represents the transformation of points for three successive transformations, which are applied to the equation 3.1. The numbers in 3.30 represents the coordinates.

$$^{4}T_1 = {^{4}T_3}{^{3}T_2}{^{2}T_1} \tag{3.30}$$

Basically there are two different conventions to rotate the axes to each other [43]. One is about moving axes and one is about fixed axes. Furthermore, the Euler angle [43], which represents the order of the rotations, is a commonly used representation that describes the successive three rotations. As the *KUKA* robot works with the $'ZYX'$ convention, the rotational matrices were calculated with this convention. As rotational matrices contains three degrees of freedom, the rotational position of a body can be determined by the sequence of rotation around the z-axis (called the angle α), followed by rotation around the co-rotated y-axis (called the angle β) and the final rotation around the x-axis (called the angle γ), which has already been rotated twice. In other words, these rotation angles can be expressed by [44]:

$$R_z(\alpha) = \begin{bmatrix} \cos(\alpha) & \text{-}\sin(\alpha) & 0 \\ \sin(\alpha) & \cos(\alpha) & 0 \\ 0 & 0 & 1 \end{bmatrix} \tag{3.31}$$

$$R_y(\beta) = \begin{bmatrix} \cos(\beta) & 0 & \sin(\beta) \\ 0 & 1 & 0 \\ \text{-}\sin(\beta) & 0 & \cos(\beta) \end{bmatrix} \tag{3.32}$$

$$R_x(\gamma) = \begin{bmatrix} 1 & 0 & 1 \\ 0 & \cos(\gamma) & \text{-}\sin(\gamma) \\ 0 & \sin(\gamma) & \cos(\gamma) \end{bmatrix} \tag{3.33}$$

By multiplying these three rotation angles in right convention the rotation matrix can be calculated by:

$$R = R_x(\gamma)R_y(\beta)R_z(\alpha) \tag{3.34}$$

After the rotation the translation is performed. This means that if the rotation between two coordinates remains the same, only the translational part should be added. Thus, the camera pose can be determined in relation to the component base. In order to finally perform this calculation or to close the kinematic chain, the camera and the base position related to rob-root (see figure 3.3) are determined beforehand. These were then shown in sections 3.4 and 3.6. In addition, the intrinsic camera parameters must be multiplied by this transformation matrix to enable perspective projection. By applying the equation 3.35 3D models can be mapped to 2D images.

$$x = PX \Leftrightarrow x = \begin{bmatrix} f_x & s & x_0 & 0 \\ 0 & f_y & y_0 & 0 \\ 0 & 0 & 1 & 0 \end{bmatrix} \begin{bmatrix} R & t \\ 0 & 1 \end{bmatrix} X \tag{3.35}$$

3.3.7 Rigid body transformation

The mathematical approaches described so far for the determination of the camera pose by means of points correspondences in sections 3.3.1 and 3.3.2 are about linear transformation in homogeneous coordinates. The projection matrix are determined hereby with a simplified pinhole camera model. Although the model takes perspective projection into account, the orthogonality constraint on rotation matrices are relaxed. Furthermore, a distinction is made between iterative and non-iterative methods, which consider orthogonality while calculating the rotation matrices. If orthogonality is not taken into account, an approximated solution is obtained, and an incorrect solution may also be obtained for correspondence points with a smaller depth difference.
The Perspective-n-Point algorithms LHM [1], EPnP [45] and PPnP [46] presented in this thesis use exactly this orthogonality to determine a camera pose in space. Therefore mathematical approaches for this point correspondence algorithm are explained in this section. The approaches are based on mainly rigid body transformation [47] with the *least square error criteria* [48]. Eggert compared in a paper [49] four major algorithms in order to estimate 3D rigid body transformations.
Let $p_\mathrm{i} = (p_1, p_2, ...p_\mathrm{n})$ and $q_\mathrm{i} = (q_1, q_2, ...q_\mathrm{n})$ be two sets of corresponding points in a euclidean orthogonal coordinate system. Thus, the rigid body transformation between the two correspondence points group can be expressed by:

$$p_\mathrm{i} = Rq_\mathrm{i} + t \tag{3.36}$$

where R and t represent the 3x3 orthogonal rotation matrix and 3D translational vector. It is to note, that rigid body transformation can be performed when the scale factor is equal to unity and attitude matrix is proper orthogonal [47]. This means, the transformation preserves the shape and size. This is in contrast to a weak perspective transformation, which includes scaling and shearing. Both transformations parameters (R, t) have to be calculated separately. At first, the rotation matrix will be calculated until it finds its optimum. Thereafter, the translation parameter will be determined. To solve the rotational matrix, centroids of both sets of points (see figure 3.13) have to be be calculated. The mean vectors, or centroid of p_i and q_i, can be computed by:

$$\tilde{p_\mathrm{i}} = \frac{1}{n}\sum_{i=1}^{n} p_\mathrm{i} \tag{3.37}$$

and

$$\tilde{q_\mathrm{i}} = \frac{1}{n}\sum_{i=1}^{n} q_\mathrm{i} \tag{3.38}$$

In order to determine optimal transformation $\tilde{R}$ and $\tilde{t}$, which minimises the error value between both point sets p_i and q_i typically requires a least-squares error

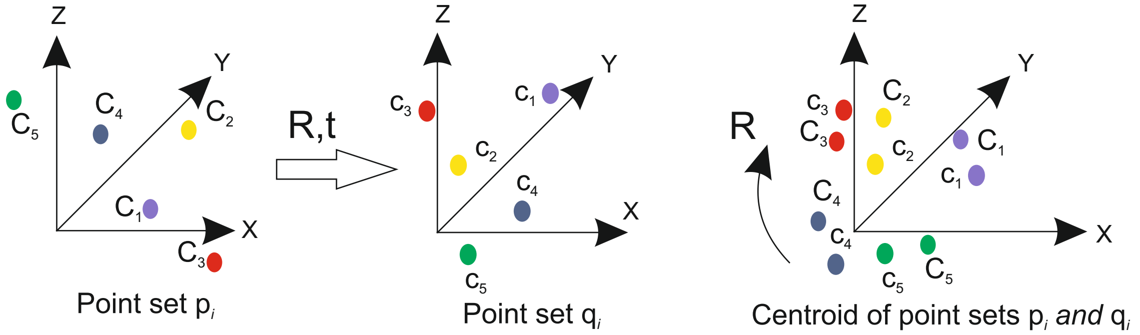

Figure 3.13: Centroid of two corresponding point groups

criterion given by:

$$(R,t) = \frac{1}{n}\sum_{i=1}^{n} \|(Rp_{\mathrm{i}} + t) - q_{\mathrm{i}}\|^2 \tag{3.39}$$

Furthermore t can be eliminated by:

$$t = \tilde{q}_{\mathrm{i}} - R\tilde{p}_{\mathrm{i}}, \tag{3.40}$$

In other words, the equation 3.41 represents the optimal translation t, which maps the transformed centroid of p to the centroid of q. A substitution of this relationship in equation 3.39 is expressed by:

$$\frac{1}{n}\sum_{i=1}^{n} \|(Rp_{\mathrm{i}} + t) - q_{\mathrm{i}})\|^2 \quad = \quad \frac{1}{n}\sum_{i=1}^{n} \|Rp_{\mathrm{i}} + \tilde{q}_{\mathrm{i}} - R\tilde{p}_{\mathrm{i}} - q_{\mathrm{i}})\|^2 \tag{3.41}$$

As mentioned before to calculate R in first step the equation 3.41 can be simplified by setting the following vectors such that the translation would be zero:

$$p'_i = p_i - \tilde{p}_{\mathrm{i}} \quad and \quad q'_i = q_i - \tilde{q}_{\mathrm{i}}, \tag{3.42}$$

Applying the equation 3.42 in equation 3.41 after rearranging it, the R can be expressed by:

$$R = \frac{1}{n}\sum_{i=1}^{n} \|R(p_{\mathrm{i}} - \tilde{p}_{\mathrm{i}}) - (q_{\mathrm{i}} - \tilde{q}_{\mathrm{i}})\|^2 \quad = \quad \frac{1}{n}\sum_{i=1}^{n} \|Rp'_i - q'_i\|^2 \tag{3.43}$$

The short form of the equation 3.43 can be simplified after expanding by

$$\|Rp'_i - q'_i\|^2 = \frac{1}{n}\sum_{i=1}^{n} (p_i'^T p'_i - p_i'^T Rq'_i - (Rq'_i)^T p'_i + (Rq'_i)^T Rq'_i) \tag{3.44}$$

Since $(Rq'_i)^T q'_i$ is a scalar product and the following equivalents exist,

$$(Rq'_i)^T q'_i = q_i'^T Rq'_i \tag{3.45}$$

$$(Rq_i')^T Rq_i' = q_i'^T R^T Rq_i' = q_i'^T q_i'. \tag{3.46}$$

the equation 3.44 can be recomposed as:

$$\frac{1}{n}\sum_{i=1}^{n}(p_i'^T p_i' + q_i'^T q_i' - 2p_i'^T Rq_i') \tag{3.47}$$

The above expression is after some minimisation and rearrangement equivalent to equation 3.39, and can be maximised by:

$$\frac{1}{n}\sum_{i=1}^{n}(p_i'^T Rq_i') = tr(R^T \frac{1}{n}\sum_{i=1}^{n} p_i' q_i'^T) = tr(R^T S) \tag{3.48}$$

It is to note that the function trace $tr()$ of a given square matrix is the sum of the elements on the diagonal, where S is a correlation matrix defined by:

$$\frac{1}{n}\sum_{i=1}^{n}(p_i' - \tilde{p})(q_i - \tilde{q})^T = \frac{1}{n}\sum_{i=1}^{n} p_i' q_i'^T \tag{3.49}$$

If a singular value decomposition [50] of S is given by:

$$S = UDV^T, \tag{3.50}$$

Optimal rotational matrix can be calculated by:

$$R = UV^T. \tag{3.51}$$

After calculating the optimal rotational matrix the translation matrix can be determined. The optimal translation aligns the centroid of the set $\tilde{p}_\mathrm{i}$ with the rotated centroid of the set $\tilde{q}_\mathrm{i}$ and with a given scale factor s can be expressed by:

$$t = \tilde{q}_\mathrm{i} - sR\tilde{p}_\mathrm{i}, \tag{3.52}$$

This is valid when the determinant of R is $+1$. However, when the two point sets are planar, or large amounts of noise exist, the matrix R has a determinant of -1, which indicates a reflection [51] rather than a rotation.

3.4 Determination of camera parameters

In the previous chapter, the basic mathematical knowledge of the perspective projection of 3D objects onto a 2D plane are explained. Based on these mathematical approaches, a projection matrix was derived for both (points correspondence and kinematic chain) methods. The projection matrix contains the intrinsic and extrinsic parameters. These matrix representations are already presented in section 3.3

(see equations 3.14, 3.16 and 3.35). Through a camera calibration process, the extrinsic parameters of the camera, rotation and translation, as well as the intrinsic, focal length, principal point and other lens distortion parameters can be determined. Several camera calibration procedures exist. In this chapter, a few different methods of camera calibration will be presented and then the method of choice applied in this work and the results are discussed in detail. These parameters are determined in two step methods [52] [53] by using one experimental setup. First, the intrinsic parameters are roughly estimated with linear least-squares techniques following a non-linear optimisation step to refine the complete set of parameters of the camera model. Secondly, the extrinsic parameters are also roughly estimated and refined by a non-linear optimisation algorithm, which is repeated several times. A calibration object is required to determine both parameters. Historically, the first calibration object in 3D was used by Faguras [54] to determine these camera parameters. Later on, the complexity of these 3D objects (since very accurate knowledge of the relative 3D coordinates of points on the object is needed) were reduced to 2.5D calibration process by Tsai [52] and Zhang [55]. Authors Sturm and Maybank [34] had published a similar algorithm as that from Zhang for 2D calibration from a planar object using two homogeneous linear constraints on the matrix. The focus of this thesis does not lie in the analysis of these three methods, but in the 3D reconstruction of thermographic images. Therefore, only the applied method related to the thermography camera is described here and its accuracy is analysed.

The method, which determines these two parameters for the 3D reconstruction was implemented by Thomas Schmidt [56] at DLR. Schmidt has combined Jean-Yves Bouguet's *"Camera Calibration Toolbox for Matlab"* [57] with Christian Wengert's *"hand-eye calibration add-on for the Matlab camera calibration toolbox"* [58]. *"Camera Calibration Toolbox for Matlab"* was used to determine the intrinsic camera parameters. Its initialization algorithm is similar to [55] and Bouguet has extended this algorithm with two additional distortions coefficients according to [59]. *"hand-eye calibration add on for the Matlab camera calibration toolbox"* was used to determine the extrinsic parameters. Wengert has implemented the Tsai [60] method for hand-eye calibration. The results of Schmidt's experimental study were published in papers [61], [62] and [56], where geometric and hand-eye camera calibration was performed and analysed for different camera distances as well as for two different lenses. The parameters, which are applied in this work on various components (see in chapters 3.5, 3.6 and 3.7) in order to generate a 3D model, were determined for a 550 mm (except for one component) camera distance with a 27 mm normal lens. Therefore, a test was carried out with this configuration and the results are shown in the following sections.

3.4.1 Geometric camera calibration

The intrinsic camera parameters based on the pinhole camera model are already presented in section 3.3.3 in the equation 3.15. These are so-called linear parameter for the ideal pinhole camera model. In contrast to this simplified pinhole model, cameras usually use lenses that bundle visible beams to achieve higher illuminance. The disadvantage of using lenses is optical deformations (distortion), which make the geometric similarity of the image obsolete. A distinction is made between two types of lens and sensor distortions, namely tangential and radial distortion. A radial lens distortion can be divided into two types, cushion-shaped and barrel-shaped distortion. The method *"Camera Calibration Toolbox for Matlab"* with the Zhang model does not consider the tangential distortions, as these are in most cases very small and by default the last three component of kc [57] are set to zero. Therefore, Bouguet has implemented according to [59] two more coefficients, which represent the tangential component. These two types of distortions are modelled by Brown-Conrady [63] and can be expressed by:

$$\begin{gathered} d_x = u_x(1 + kc_1 r^2 + kc_2 r^4) + 2p_1 u_x u_y + p_2(r^2 + 2u_x^2) \\ d_y = u_y(1 + kc_1 r^2 + kc_2 r^4) + 2p_2 u_x u_y + p_1(r^2 + 2u_y^2) \\ r = \sqrt{(u_x - c_x)^2 + (u_y - c_y)^2} \end{gathered} \tag{3.53}$$

where

d_x, d_y = Distorted image point [px]
u_x, u_y = Undistorted image point [px]
c_x, c_y = Principal point [px]
kc_1 = 1st radial distortion coefficient
kc_2 = 2nd radial distortion coefficient
p_1 = 1st tangential distortion coefficient
p_2 = 2nd tangential distortion coefficient
r = Distance to the centre of distortion (usually the centre of the image)

Modelling of such non-linear image error functions is not included in the model of the projection-matrix P (see equations 3.14, 3.16 and 3.35), but can be combined with it. Once distortion is applied, the new image point can be calculated by multiplying with the intrinsic matrix (see equation 3.15) and can be expressed by:

$$\begin{bmatrix} x_p \\ y_p \\ 1 \end{bmatrix} = \begin{bmatrix} f_{\mathrm{x}} & s & x_0 \\ 0 & f_{\mathrm{y}} & y_0 \\ 0 & 0 & 1 \end{bmatrix} \begin{bmatrix} d_x \\ d_y \\ 1 \end{bmatrix} \tag{3.54}$$

where

x_p, y_p = final pixel coordinate [px]

The new intrinsic camera matrix (with linear and non-linear parameters), which is used in *"Camera Calibration Toolbox for Matlab"* has different notation and is defined by:

$$\begin{bmatrix} f_c(1) & alpha_c * f_c1 & cc(1) \\ 0 & f_c(2) & cc(2) \\ 0 & 0 & 1 \end{bmatrix} \tag{3.55}$$

In addition to determining the linear and non-linear camera parameters, the accuracy of the results are dependent on image quality. In general, the calibration provides the intrinsic and extrinsic camera parameters as well as the coefficients of lens distortion on the basis of several recorded images of a checker board or circle pattern. The procedure consists of localising a set of calibration points from the template used within a calibration image with previously known dimensions. However, due to the pattern's thermal conditions, IR-acquisition processes are physically limited and the localisation of the calibration points often poses difficulties, subsequently leading to unsatisfying calibration results. Therefore a choice of a pattern and its thermal condition has demonstrated to be highly effective and convenient for the task of calibrating a thermal-infrared image. Furthermore, the proposed toolbox is an adaption of Zhang's method and involves the use of planar calibration pattern.
A number of approaches exist for IR-geometric camera calibration. For instance, the authors in paper [64] have calibrated a thermography camera with one visible camera by using 3D calibration grids and standard artefacts. Luhmann [65] and his team have analysed patterns with active lamps equidistantly mounted on a planar calibration board, and came up with a 3D calibration pattern. A similar experiment was performed by [66]. Authors in both papers have observed that the centre of the lamps can not be measured due to elliptical illumination. But later authors have dealt with this topic in paper [67] and developed an algorithm, which "models the radiation pattern of each light bulb as an ellipse and considers the centre of mass of the extracted ellipsoidal region as the starting calibration point, which is refined iteratively using alternating mappings to and from an undistorted grid model".
The most popular method is a heated chessboard with flood lamp for few seconds. Prakash [68] has applied the chessboard to calibrate a visible and thermal camera. Although thermal images are blurred compare to visible images, they argued for possible extraction of the corner points of the chessboard pattern by heating from the lamp. The same effect could be observed by Shinko in paper [69]. As expected authors in paper [70] report the inefficient process, as the temperature of the pattern starts to become uniform after a few seconds of warming and prevents the localisation of the crisp chessboard corner. Therefore they have suggested a new geometric mask with a high thermal contrast, by means of a clustering-based algorithm which utilizes " Maximally Stable External region".
DLR also conducted preliminary investigations to generate a sharp thermographic image. It was found that dotted patterns are better suited for thermal calibration than chessboard patterns [62]. In contrast to normal temperature images, amplitude images were used at DLR. The amplitude images were calculated with the software

DisplayIMG using the following equation [71].

$$A_{tw}(x,y) = \sqrt{[S_1(x,y) - S_3(x,y)^2] + [S_2(x,y) - S_4(x,y)^2]}$$

where

$S_1, S_2, S_3, S_4 =$ are equally time spaced thermal images, temperature data

The images were then inverted. For the determination of the intrinsic parameters, this developed method was used, which is based on the work of Schmidt, published in papers [61], [62] and [56]. 10 Amplitude images (see figure 3.14 (a)) were taken for the calibration. Normally with the chessboard pattern, each picture is framed by hand with the help of a graphical user interface. By using the point based pattern, the calibration points (centre of the black circles) are easily located automatically in the image with high precision due to the image contrast. The Toolbox provides at first roughly estimated intrinsic parameters with linear least-squares techniques. Afterwards, calibration parameters are optimised by a non-linear step. The non-linear optimisation step, which minimises the total re-projection error (in the least squares sense) over all the calibration parameters, is illustrated in figure 3.15. The individual colour in figure 3.15 represents per image the deviation between the specified and calculated center distance between two points of the pattern.

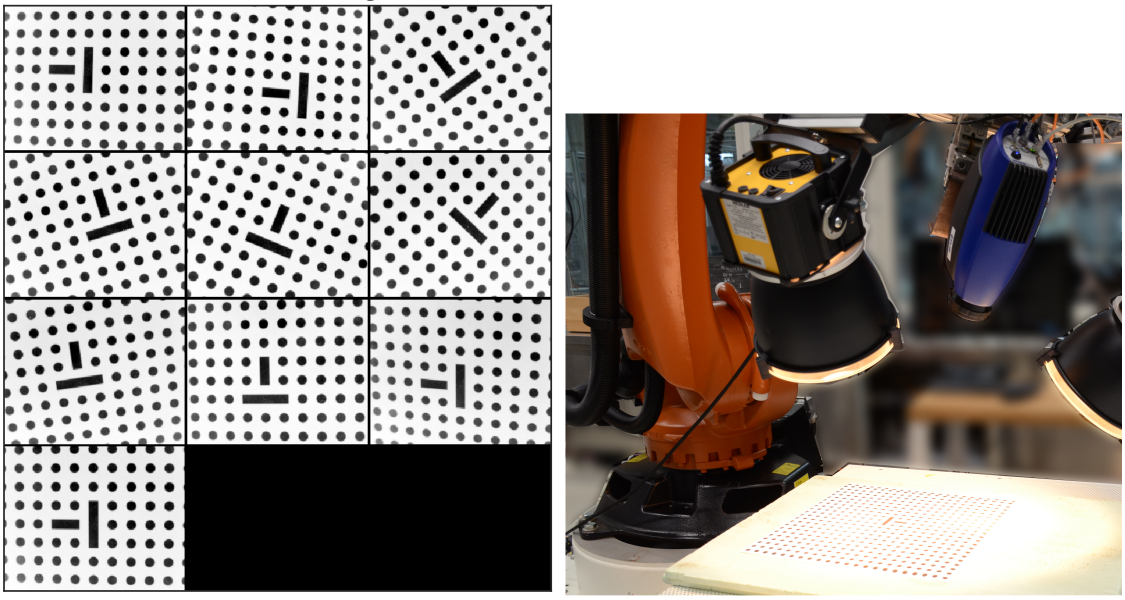

(a) Amplitude images (b) Flange camera calibration

Figure 3.14: (a)Amplitude images; (b) Flange camera calibration

Additionally, the *"Camera Calibration Toolbox for Matlab"* provides a large set of tools to improve the results, such as the new editing of the images with the strongest deviation.

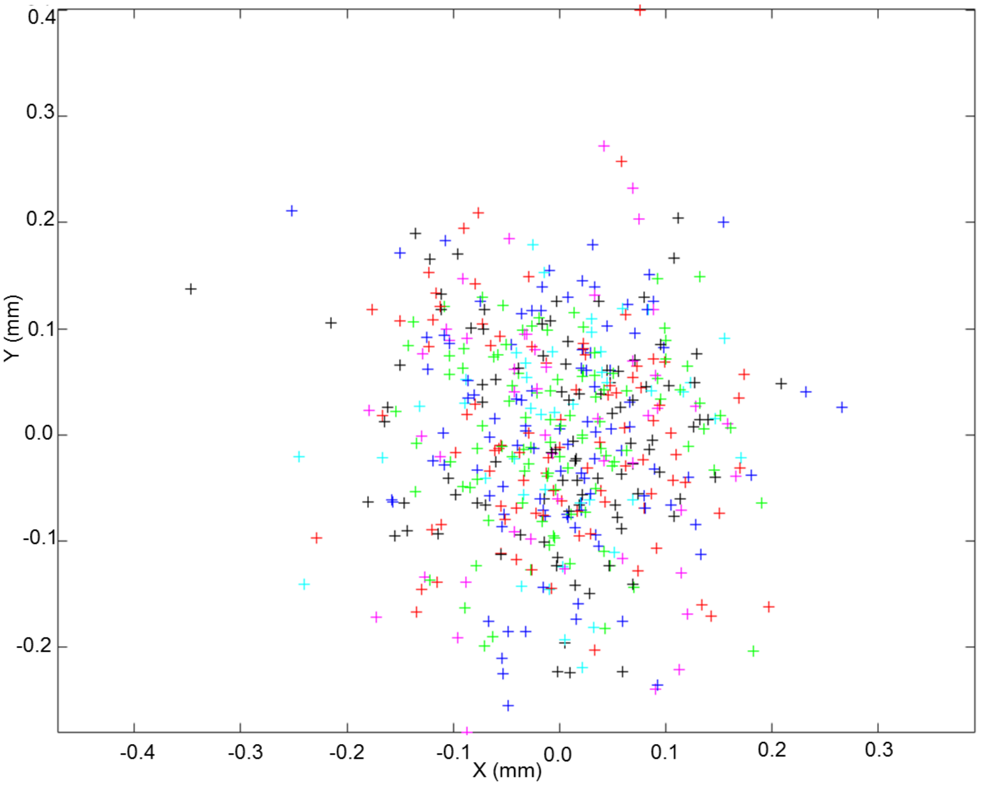

Figure 3.15: Re-projection error of geometric calibration

The remaining coefficients with the extension ± represent in table 3.2 the standard deviation of the respective parameter. Thus, determined intrinsic parameters were used for further image processing steps such as rectification. Afterwards these rectified images were applied by both approached methods in order to generate 3D thermography (see in chapters 3.5, 3.6 and 3.7) reconstruction.

Table 3.2: Intrinsic camera parameters

Focal Length (f_c):	[1972.2576 1967.28746] ± [5.6907 5,64439]
Principal point (cc):	[311.06954 250.61192] ± [5.14864 4.29913]
Skew (α_c):	[-0.00031] ± [0.00025]
	angle of pixel axis = 90.01767 ± 0.0146 degrees
Distortion (K_c):	[-0.25504 -3.90877 0.00015 -0.00021 0.00000] ±
	[0.04094 1.34223 0.00051 0.00044 0.00036]
Pixel error(err):	[0.07619 0.07325]

3.4.2 Hand-eye camera calibration

As described in chapter 3.3 *Geometric Transformation*, the extrinsic parameters describe the position of the camera in relation to a global or world coordinate system. The equation 3.29 calculates the projection matrix BT_C, which represents the relationship between the component's Base and Camera TCP. The position of the robot flange RT_F is known at all times via the kinematic chain of the robot (provided by KUKA), but the transformation between camera TCP and robot flange is unknown. The mounted thermography end-effector is fixed to flange and represents a rigid body transformation. Thus, TCP position needs to be calculated only once. In order to calculate TCP (see the matrix FT_C in figure 3.3 and equation 3.1), which represents the transformation between the robot hand coordinate system and the camera coordinate system, hand-eye calibration needs to be performed. During the first investigations in section 3.2, TCP was determined from CAD data and verified with LT measurement. For a higher accuracy this process is not recommended, because there is no inner knowledge about the camera optics and inaccuracies that occur in assembly and manufacturing processes.

Similar to intrinsic parameters, there are different calibration patterns and methods for the determination of extrinsic parameters. Tsai and Lenz [60], Shiu and Ahmed [72] have developed methods, which can be applicable for two- and three-dimensional calibration object. Furthermore, these methods differ in the calculation approaches regardless of whether the rotational part and translational part are calculated separately or together. As mentioned above, Wengert [58] has implemented the Tsai method for hand-eye calibration, and it was also adopted for thermography hand-eye calibration at DLR.

The same planar point pattern and experimental setup was used to perform the hand-eye calibration. Therefore, the thermography end-effector of the robot was moved in n different poses (position and orientation). The camera takes a picture of a calibration body at each pose (typically n = 10). A flange camera calibration performed with the *Matlab* toolbox requires at least ten images of a pattern. The distance between the sample and the camera must remain the same so that the images remain sharp. This was achieved using an OLP model. Therefore, first the base position, which lies in the middle of the pattern, was measured, and in an offline environment, the robot program was generated with a 550 mm camera distance. If the internal orientation is known, the calibration images are used to determine the external orientation of the calibration body in the image. In any case, the pose of the calibration body in each image is known because the pose of the end-effector relative to the base in the image is obtained from the robot controller. Furthermore, to retain intrinsic parameters, the camera's autofocus was triggered during calibration until all images were captured.

Details of program generation, influence of pattern and the complete hand-eye calibration procedure as well as systematic influences, like absolute robot accuracy errors due to weight compensation and influences due to non-uniform radiation be-

Table 3.3: Hand-eye calibration results for 550 mm camera distance

X	17.710999	mm	A	150.584128 °
Y	38.240218	mm	B	-0.236413 °
Z	705.075962	mm	C	-35.484677 °

haviour of the patterns during excitation by the halogen lamps are investigated and published in paper [56]. The absolute hand-eye calibration accuracy was performed in section 3.8. The calibration was carried out with a total of 12 images. It became obvious that only after 4 iterations did not change the TCP position measurably. The results in table 3.3 were generated after the 5th iteration. After each iteration the new TCP value is entered in the OLP and a new robot program is created with it. Thus, new intrinsic and extrinsic parameters are generated at each iteration. The following requirements for the generation of the robot program were considered:

- The robot should be calibrated as accurately as possible to the object. This means that the base measurement must be accurate.
- The angle between the two robot axes for two different positions should be as large as possible. This also applies to geometric calibration.
- The distance between the projection centre of the camera and the calibration body should remain the same during the process.

By entering the TCP data in the equations 3.31, 3.32 and 3.33 the $3x3$ rotational matrix can be calculated. The $4x4$ transformation matrix FT_C is then arranged with the rotational matrix and the translational vector by:

$$FT_C = \left(\begin{array}{ccc|c} & & & t_{\mathrm{x}} \\ & R_{\mathrm{z}} R_{\mathrm{y}} R_{\mathrm{x}} & & t_{\mathrm{y}} \\ & & & t_{\mathrm{z}} \\ 0 & 0 & 0 & 1 \end{array}\right) = \begin{pmatrix} 0.8112 & -0.5090 & -0.2878 & 17.71099 \\ -0.5848 & -0.7072 & -0.3973 & 38.240218 \\ -0.0013 & 0.4906 & -0.8714 & 705.705962 \\ 0 & 0 & 0 & 1 \end{pmatrix} \tag{3.56}$$

This matrix remains the same for all measurement fields, which was applied to the robot-based 3D reconstruction method (see in section 3.5).

3.5 Implementation of Point to Point (PnP) based 3D thermography model

Initially, two concepts for 3D thermography were introduced in section 3.1, in order to improve the automated thermography process. After the feasibility study in section 3.2 and the description of the mathematical basics for geometric transformation in section 3.3, the intrinsic and extrinsic parameters were determined in the previous section. In this section and in the following sections 3.6 and 3.7 the two concepts mentioned above were implemented and applied to various components in order to generate 3D thermography models.

If for the pose estimation, n 2D projected points and their 3D corresponding points of relative geometry are used, the method is then called Perspective-n-point (PnP). In this section, a 3D model was generated using the point correspondence method and validated against three different parts. The first goal was to visualise thermographic images on a single curved 3D geometry. The second goal was to apply the developed method to a double-curved 3D geometry. Lastly, the method was validated on an aircraft fuselage with a stringer. In the concrete case, the following work steps for 3D visualisation and 3D defect localisation are to be implemented and evaluated:

- Determination of the camera position and orientation (projection matrix P) from the point correspondences without any prior knowledge of camera position
- Manufacturing and generation of a homogeneous meshed triangle model of the following components:
  - single curved fuselage demopanel
  - single curved fuselage demopanel with stringer
  - double-curved pressure bulkhead with stringer
- Generation and projection of 3D points
- Capturing and 2D point extraction of 3D laser points
- Transformation of 3D triangles to 2D images
- 3D reconstruction and visualisation of all images

The determination of the projection matrix P, introduced in section 3.3 is of central importance for any applications that attempts to supplement a camera image with virtual objects. If the three-dimensional geometry and the corresponding image is known, P can be determined directly from 3D to 2D correspondence. Researchers have proposed in the last decades various algorithms in the literature. These algorithms can be differentiated between linear and non-linear solutions. The quality of both methods depends on the number of corresponding points, whereby with a known intrinsic parameter, a minimum of 3 corresponding points is required to recover the pose [73]. The advantages of linear methods are that they are fast, and calculate the projection matrix with fewer correspondence points without any initial assumptions. Linear methods calculate this projection matrix as a function of the current rotation matrix and translation vector by establishing and solving linear systems of equations in closed form. Furthermore, linear equations provide a unique solution for less noisy correspondence points and do not require any abrupt criteria for iteration. The disadvantage of linear solutions is the minimisation of algebraic value instead of geometric error. Other disadvantages are lower accuracy compared to iterative or numerical methods, and its sensitivity to noisy image data, which leads to non-unique solutions. As 3D points are known in this work and images are not noisy, a fast and unique solution with fewer correspondence points can be achieved with a linear solution. In the case of non-linear algorithms, an algebraic solution of a linear method can be used for the initial assumption. Therefore, a linear method was selected for the first implementation. The implemented non-linear solutions are presented in section 3.7.

3.5.1 Direct Linear Transformation (DLT)

The most popular approximate method is direct linear transformation (DLT). DLT can solve the projection matrix (see equation 3.16), which has 11 degrees of freedom ($R:3, t:3, f, s, x_0$ and y_0), but at the same time becomes unstable with less point correspondence. According to equation 3.17, for each point correspondence two equations can be established. Although 6 points are sufficient to determine 11 unknown parameters, 9 points were used to calculate the projection matrix. This will make the camera pose estimation more robust. As these 11 unknown parameters of the projection matrix are actually extrinsic and intrinsic (only linear) parameters, only non-linear camera parameters (determined through geometric calibration) were applied to undistort the thermography image before calculating the projection matrix. But this is only applicable for the DLT algorithm. For other PnP algorithms, which are implemented in section 3.7, and for the robot-based method, intrinsic parameters were multiplied by the transformation matrix (rotation and translation) in order to calculate the projection matrix.

The general mathematical approaches for calculating the projection matrix in the projection space using a linear equation system are already described in detail in section 3.4. DLT algorithms based on the pinhole camera model use a set of similarities to solve the coefficients of the projection matrix and have a similar formulation to equation 3.13 :

$$m_i \propto PM_i, \quad i = 1, ..., n \tag{3.57}$$

where $M_i = \begin{pmatrix} x_i \\ y_i \\ z_i \\ 1 \end{pmatrix}$ are the scene points in world coordinate and $m_i = \begin{pmatrix} u_i \\ v_i \\ 1 \end{pmatrix}$ are their projections.

These 3D to 2D projective transformations are linear in homogenous coordinate, so that the projection matrix is homogenous. Therefore, it is difficult to solve the unknown scaling factor, which changes with i. The p_{34} coefficient of the projection matrix (see equation 3.16) will be set at starting 1. To find the other 11 unknown parameters, the equation 3.57 can be converted by the vector cross product from the left with m_i into the form of an equation system:

$$m_i \times PM_i = 0 \tag{3.58}$$

with the condition, that the vectors are parallel, so that the cross product of a vector with itself results in the zero vector. If p_i, i =1,2,3 represents 4x1 vectors containing the rows of projections matrix P, which is

$$P = \begin{pmatrix} p_1^T \\ p_2^T \\ p_3^T \end{pmatrix} \tag{3.59}$$

then according to [74] the outer product of two vectors can be determined by calculating the formal determinant and can be written as:

$$\begin{aligned} &\text{I.} \quad\; vp_3^T M - p_2^T M = 0 \\ &\text{II.} \;\; p_1^T XM - up_3^T M = 0 \\ &\text{III.} \; up_2^T XM - vp_1^T M = 0 \end{aligned} \tag{3.60}$$

Due to linear dependency of the first two equations, the third one can be calculated by adding the first and second one. This linear equation system always has a special solution, also known as trivial solution. By considering a 3D point $M = (x\ y\ z\ 1)^T$ and a 2D point $m = (u\ v\ 1)^T$ (as stated before), the first two equations can be expressed as:

$$\begin{aligned} xp_{21} + yp_{22} + zp_{23} + p_{24} - vxp_{31} - vyp_{32} - vzp_{33} - vp_{34} = 0 \\ xp_{11} + yp_{12} + zp_{13} + p_{14} - uxp_{31} - uyp_{32} - uzp_{33} - up_{34} = 0 \end{aligned} \tag{3.61}$$

Since each point correspondence between a world coordinate and a pixel coordinate provides two conditions, the projection matrix for 9 such correspondences can be calculated by putting them in matrix form, which can be expressed by $AP = 0$:

$$\underbrace{\begin{bmatrix} x_1 & y_1 & z_1 & 1 & 0 & 0 & 0 & 0 & -u_1x_1 & -u_1y_1 & -u_1z_1 & -u_1 \\ 0 & 0 & 0 & 0 & x_1 & y_1 & z_1 & 1 & -v_1x_1 & -v_1y_1 & -v_1z_1 & -v_1 \\ x_2 & y_2 & z_2 & 1 & 0 & 0 & 0 & 0 & -u_2x_2 & -u_2y_2 & -u_2z_2 & -u_2 \\ 0 & 0 & 0 & 0 & x_2 & y_2 & z_2 & 1 & -v_2x_2 & -v_2y_2 & -v_2z_2 & -v_2 \\ \vdots & \vdots & \vdots & \vdots & \vdots & \vdots & \vdots & \vdots & \vdots & \vdots & \vdots & \vdots \\ x_n & y_n & z_n & 1 & 0 & 0 & 0 & 0 & -u_nx_n & -u_ny_n & -u_nz_n & -u_n \\ 0 & 0 & 0 & 0 & x_n & y_n & z_n & 1 & -v_nx_n & -v_ny_n & -v_nz_n & -v_n \end{bmatrix}}_{\text{A}} \underbrace{\begin{pmatrix} p_{11} \\ p_{12} \\ p_{13} \\ p_{14} \\ p_{21} \\ p_{22} \\ p_{23} \\ p_{24} \\ p_{31} \\ p_{32} \\ p_{33} \\ p_{34} \end{pmatrix}}_{\text{p}} = \begin{pmatrix} 0 \\ 0 \\ 0 \\ 0 \\ 0 \\ 0 \\ 0 \\ 0 \\ 0 \\ 0 \\ 0 \\ 0 \end{pmatrix} \tag{3.62}$$

In general, the matrix can be calculated up to a scale factor (as stated before). It should also be noted that for a unique solution normally $2n$ x 12 matrix A has rank 11 and a one-dimensional zero space is necessary for six-point correspondence. It might be possible that, due to the inaccuracy of the 2-D coordinates, the matrix A of the equation system has full rank and there is no exact solution for P. Therefore, generally more than six-point correspondences are used, which is the case here. The system is then called (also when only using six correspondences) overdetermined, because A has more equations than necessary for calculating the solution. Furthermore, the trivial solution $P = 0$ is not interesting; a correct solution can be found with the help of the singular value decomposition Svd of A.

$$A = Svd(A) = U\Sigma V^T \tag{3.63}$$

The solution vector for P is the vector of V corresponding to the smallest singular value. The values of p give the inputs of the projection matrix A helping to determine the camera parameters except for a global scaling factor. A detailed breakdown of the Svd equation is explained in paper [50].A solution for noisy image data was not implemented, first because the points are not noisy and secondly because more than six points were used for more stability.
In general, DLT is not invariant to the choice of image origin and scaling along axis, because image points which are measured in pixel can have a value of a thousand, but scene points can reach values up to a few thousand [75]. Due to these different magnitudes of data sets, a normalisation of both data set needs to be performed prior to Svd, as different divisions and transformations are performed inside Svd. This normalisation will increase the numerical stability and will prevent getting an ill-conditioned matrix, which could result in numerical error in terms of less difference in the magnitude value of p. According to paper [75] both data sets M and m (Q is the transformation matrix for the 3D point and R is the transformation matrix for the 2D point) can be normalised after transforming by:

$$M' = QM \quad \text{and} \quad m' = Rm \tag{3.64}$$

M' and m' represent the normalised version of M and m. In order to calculate Q and R, data sets need to be translated to their centroid C_M and C_m by:

$$C_M = \frac{1}{n}\sum_{i=1}^{n} M_\mathrm{i} \quad \text{and} \quad C_m = \frac{1}{n}\sum_{i=1}^{n} m_\mathrm{i} \tag{3.65}$$

The points in the world coordinate system as well as the image coordinate system are also scaled in such that their average distance for the 3D point to the origin is $\sqrt{3}$ and for the 2D point $\sqrt{2}$. In the last step, both scale and centroid can be assembled together by:

$$Q = scale(s_M) \cdot translate(C_M) \quad \text{and} \quad R = scale(s_m) \cdot translate(C_m) \tag{3.66}$$

Whereby scale and translation create one matrix each. M and m are replaced by M' and m' in order to calculate the projection matrix P. After estimating the projection matrix P' for the normalized data, projection matrix P for the original data has to be reverted by:

$$P = Q^{-1} P' R \tag{3.67}$$

In addition to data normalisation, another condition has to be fulfilled in order to get reliable results. The 3D points must not be coplanar. Again, the matrices might get near singularity through this approach, thereby possibly producing falsified results.

3.5.2 System validation on single-curved component

Experimental setup

To visualise the thermography images in 3D, a single-curved component with approx. 4 m diameter was manufactured first. Figure 3.16 shows a mini-fuselage shell design with the layer structure (CPD) and the inserted defects. There are a total of ten layers with a material thickness of 0.2 mm. The artificial flaws were prepared with two welded foils. During production, these flaws were placed between each layer (green ply to red ply) at depths of 0.2 mm, 0,6 mm, 1 mm, 1.4 mm and 1.8 mm respectively. The smallest defects are 2x2 mm and the largest 20x20 mm. A template was used to position the defects. As 3D reconstruction was the main objective of this experiment, no thermography measurement was carried out to detect the artificial defects. The component can be used in the future for the validation of the NDT method due to the inserted defects.

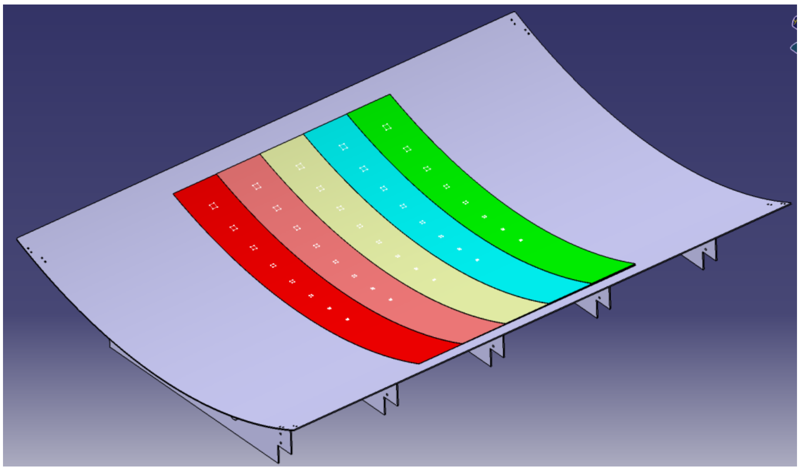

Figure 3.16: Layer structure of the single-curved fuselage with defects

The component was infiltrated with room-temperature resin and cured. After manufacturing, the component was fixed on a supporting structure (see Figure 3.17) and target plates (in total 8) were mounted to the component. These target plates were used to calibrate the laser projector. Due to manufacturing and assembly tolerances the component's shape was measured by using a T-scan measuring device from *ZEISS* and a software called *Spatial Analyser*. The created point cloud had a distance of approx. 0.5 mm between two neighbouring points. Also the positions of the target plates were measured with a T-probe device from *ZEISS*. Thereafter, points were exported to the base coordinate of the component and imported to *Catia* to generate triangulated mesh from the measured point cloud. This mesh model (STL file) represents real geometry on which the thermographic images can be textured. From the triangulated mesh a real surface was generated on which 3D points needed to be defined. The positions of the reflectors mounted on the target plates were also measured. After creating the real surface of the geometry, the 3D points were constructed in *Catia*. There are nine such points per measurement field, which are colour-coded for exemplification(see Figure 3.18). They are defined so that there are at least three common points between two measurement fields (see Figure 3.18). The aim was to stitch the images with the common points between two measurement fields. In order to minimise the effort, only 16 measurement fields in the corner of the part were defined for the first investigation. The defined nine correspondence points for each measurement field are projected onto the component by the laser projector. Prior to this, the component was calibrated to the laser projector via the reference points of the reflectors. The test setup (see Figure 3.19) consists mainly of the following components:

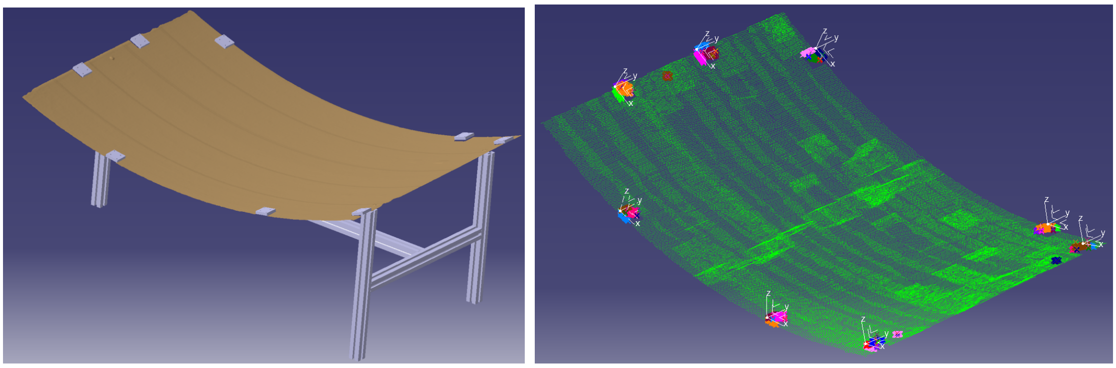

(a) (b)

Figure 3.17: (a)Mini fuselage component on the supporting stand with the target plates; (b) T-scan measurement

- thermography end-effector (1)
- robot (2)
- one laser projector (3) and 8 reflectors for calibration (4)
- component to be tested (5)

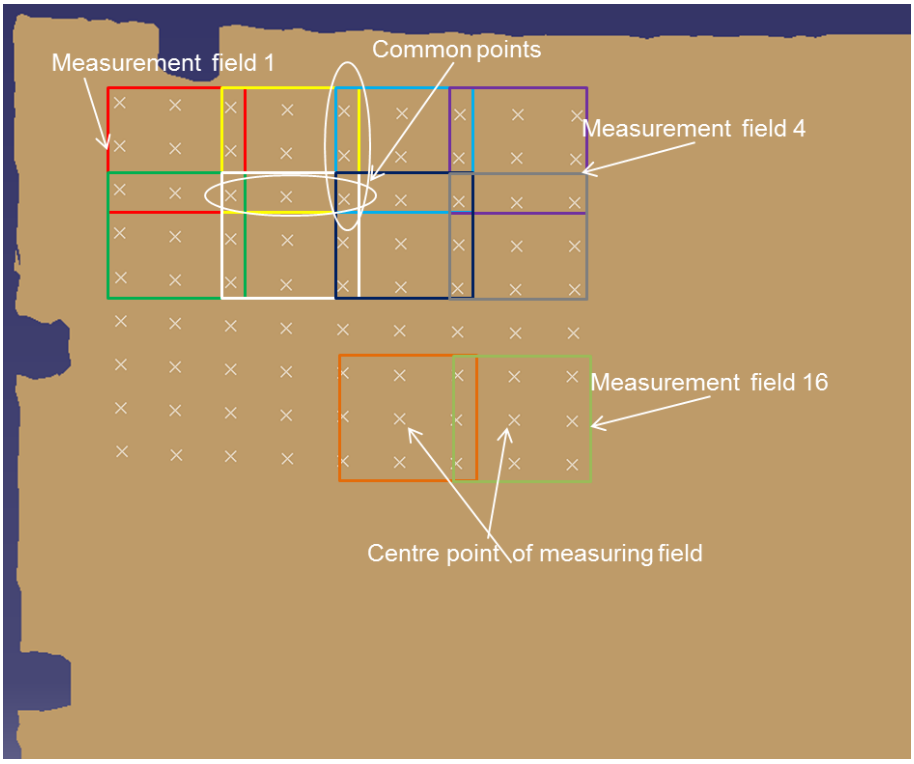

Figure 3.18: Defined 3D points on single curve component

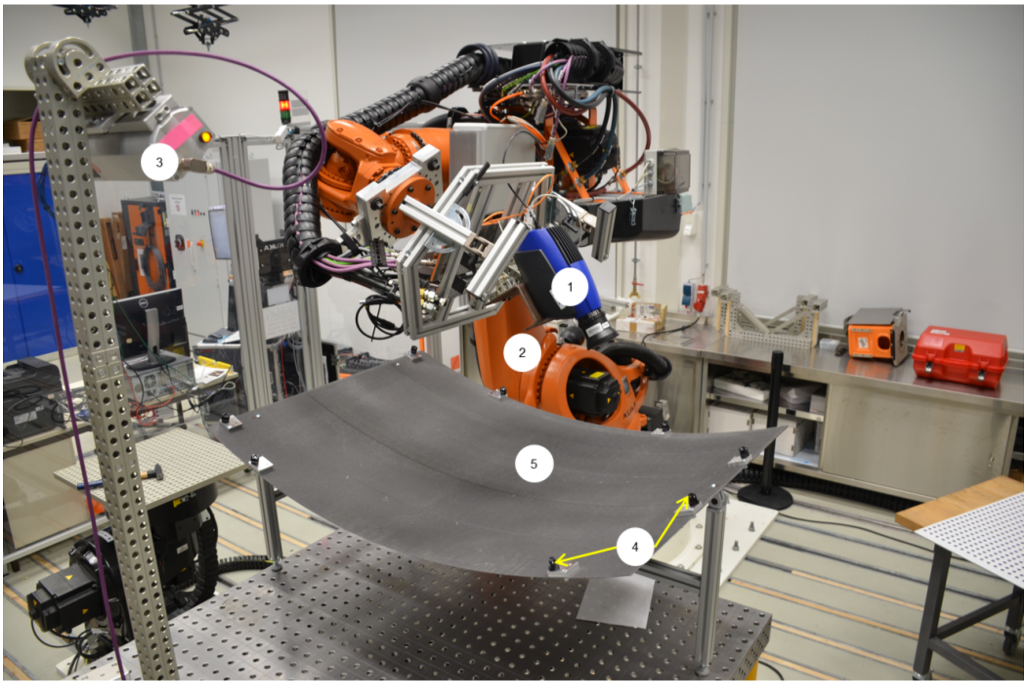

Figure 3.19: Experimental setup for single curve component

Measurement orthogonal distance was 550 mm. No hand-eye calibration was performed (which is in general required when a end-effector is being re-mounted on a robot), as it is not required for the PnP-based method. The previously-determined TCP in section 3.4 was taken in order to use a robot as a manipulator for this experiment. The centre points (see figure 3.18) of each measurement field were used to generate the robot program in *FastSurf*. In the next step, the laser projector was calibrated to the component using the created calibration file and 0.4 calibration error was achieved. The reason for the 0.4 calibration error was, that the component was not sufficiently clamped and moved during the measurement. This caused an error in the calibration file. Thus the robot move with the thermographic end-effector to the respective measuring field and the thermal camera capture live images of projected laser points. As mentioned in section 3.2, for each point a new image was captured and this resulted in a total of 9 images for each measuring field.

Results and discussion

The images captured from the measurement position were then evaluated in *Matlab* and displayed together with the nine reference points or laser points using pixel coordinates (see Figure 3.20(c)). Thus each image receive the reference points for the respective position. Prior to that, thermographic images were undistorted with intrinsic parameters which were determined by geometric camera calibration in section 3.3. For a higher performance in 3D reconstruction and the existing libraries that offer PnP algorithms, `C#` was preferred as an object-oriented programming language for this work, and therefore the fundament was created in the scope of a master's

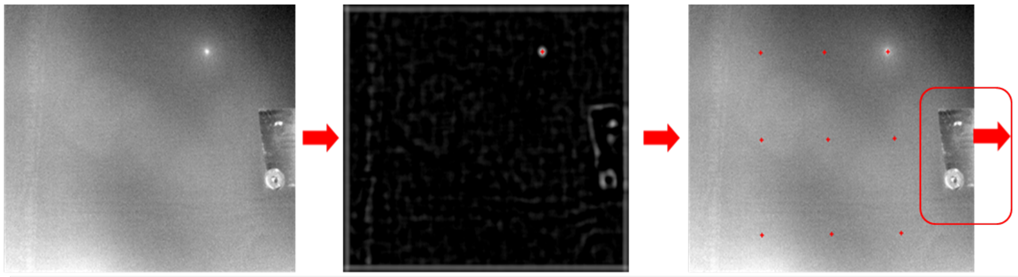

(a) Thermography live image (b) Laser point extraction (c) Measurement filed 1 with 9 points

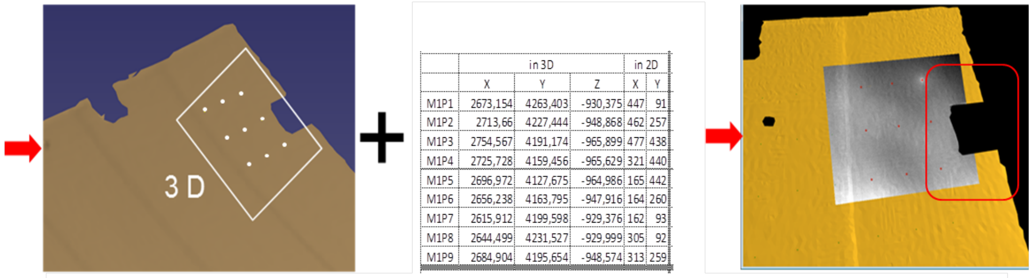

	in 3D			in 2D	
	X	Y	Z	X	Y
M1P1	2673,154	4263,403	-930,375	447	91
M1P2	2713,66	4227,444	-948,868	462	257
M1P3	2754,567	4191,174	-965,899	477	438
M1P4	2725,728	4159,456	-965,629	321	440
M1P5	2696,972	4127,675	-964,986	165	442
M1P6	2656,238	4163,795	-947,916	164	260
M1P7	2615,912	4199,598	-929,376	162	93
M1P8	2644,499	4231,527	-929,999	305	92
M1P9	2684,904	4195,654	-948,574	313	259

(d) 3D points (f) Extracted 2D points (g) 3D reconstruction of measurement field 1

Figure 3.20: 3D reconstruction of measurement field one

thesis [76]. Now the data, such as the triangulated mesh model (STL file), thermography images, 2D-3D corresponding points (XML file) and intrinsic parameter (XML file), can be selected by a user interface, and the 3D result after applying the DLT algorithm and post-processing can be visualised.

The projection matrix was calculated for each measurement field using a mathematical approach (DLT - discrete linear transformation and SVD - single value decomposition). As mentioned in section 3.3.3, the projection matrix contains the relationship between the 2D image and the 3D part, since the reference points are related to the part coordinate system. By multiplying all triangles (components) with the projection matrix, all triangles are projected onto the image plane. Prior to that, images are cut along the 2D points to avoid overlapping between two images. Furthermore, it may happen that image corners will most probably not coincide with the triangle vertices. Therefore, in a post-processing step, new meshes will be generated when a triangle intersect an image. Thus each of these triangles gets a colour value or grey value. The last step is now the transformation of the 2D triangles with the corresponding colour value information on the 3D component. It is done by converting the 2D triangles into barycentric coordinates and from barycentric coordinates into 3D Cartesian coordinates. This method is described in detail in master's thesis [76]. If one considers the red-marked area in the two images (see Figure 3.20(c and g)), it will be revealed that the target plate was not reconstructed in the 3D image, because there were no triangles in this area. The entire process described above is applied for each image. The results of all 12 images are illustrated in figure 3.21(a)). All images were cut along the correspondence points before the reconstruction and then stitched together. Four further positions were omitted because the functionality of the method was tested successfully.

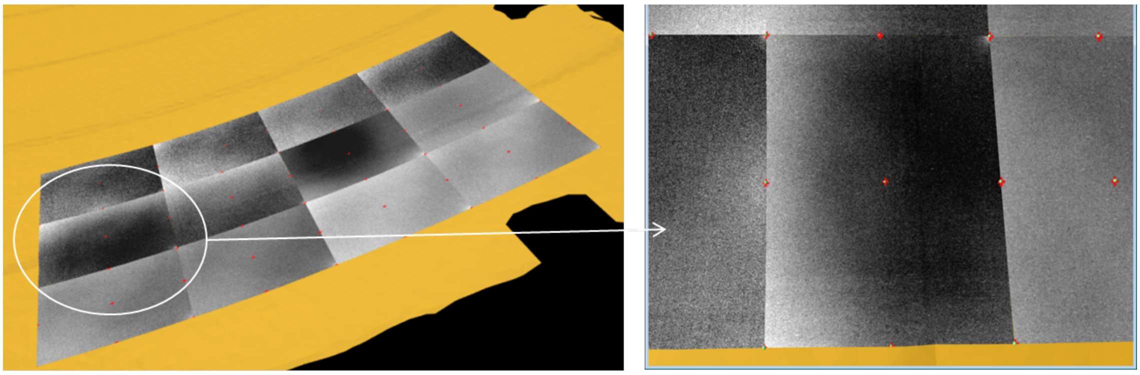
(a) 3D reconstruction of 12 images
(b) Enlarged image of position 11

Figure 3.21: 3D thermography visualisation of single curved component

Afterwards an analysis was carried out to determine how well the reconstructed image lay on the component. For that, the positions between extracted 2D points and constructed 3D points lying on the part were compared. In figure 3.22 the red cross represents the 2D point and the green sphere the 3D point. The image was reconstructed without cutting the original image along the points. The red cross itself represents 2 pixels. It is easy to recognise that both points lie on top of each other. The deviations are in average less than half a pixel. A relative accuracy examination between the pictures as well as an absolute accuracy examination are carried out in a double-curved component in the next section.

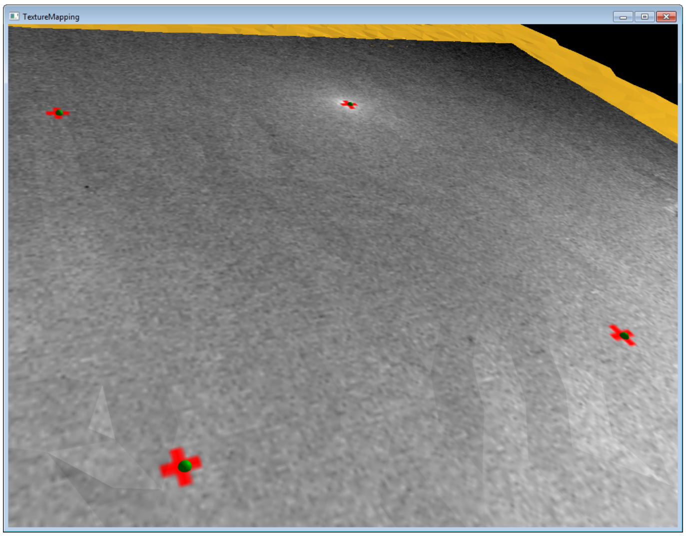

Figure 3.22: Accuracy analysis between two-point correspondence

3.5.3 System validation on double-curved component

The second aim of the work was to apply the developed method to a double-curved component. For this the same component (rear pressure bulkhead) was used that was already used in section 2.3. A gross 3D thermography model was created then manually with *Catia*. Now a 3D model was to be generated by using the developed method. During an event *JEC2016*, the entire automatic thermography process chain (from geometric calibration to 3D model generation) was demonstrated on the basis of this component.

Experimental setup

In general, cured components are mounted on a suitable Jig with a reference coordinate system. In order to generate a reference coordinate system, the process was simplified by attaching the target plates directly to the test component, here the pressure bulkhead. Afterwards the surface and the positions of those reflectors which were attached to target plates were measured with T-scan and T-probe devices (see figure 3.23 (b)). The distance between two points in the point cloud was 0.2 mm. Furthermore, in the marked yellow circle (see figure 3.23(a)) a dent was created by chipping on the stringer, in order to get the emission difference in a thermography image. This was later used to analyse absolute accuracy. The point clouds from all screw areas were cut out (see red marked circle area in figure 3.23) to analyse the reconstruction accuracy. The test setup (see Figure 3.23 (a)) looks very similar to the test with the fuselage shell. Figure 3.24 (a) shows a calibration pattern (No. 6). The other components of the test setup are a thermography end-effector (No. 1), a robot (No. 2), a laser projector (No. 3), reflectors (No. 4) and the pressure bulkhead (No. 5).

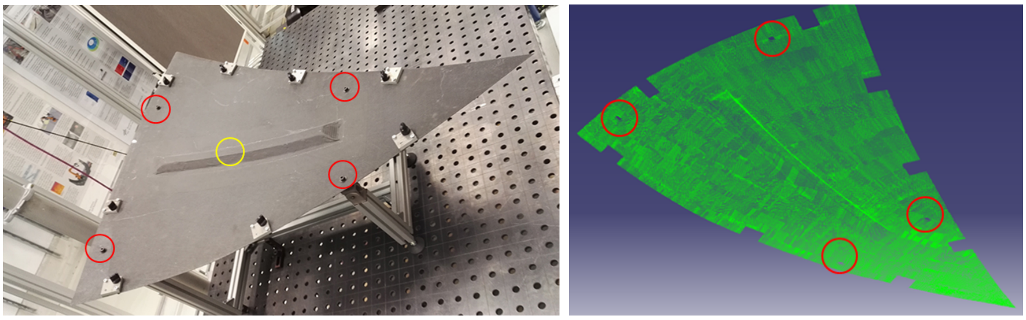

(a) (b)

Figure 3.23: (a)Pressure bulkhead with target plates and reflectors; (b) T-scan measurement of pressure bulkhead

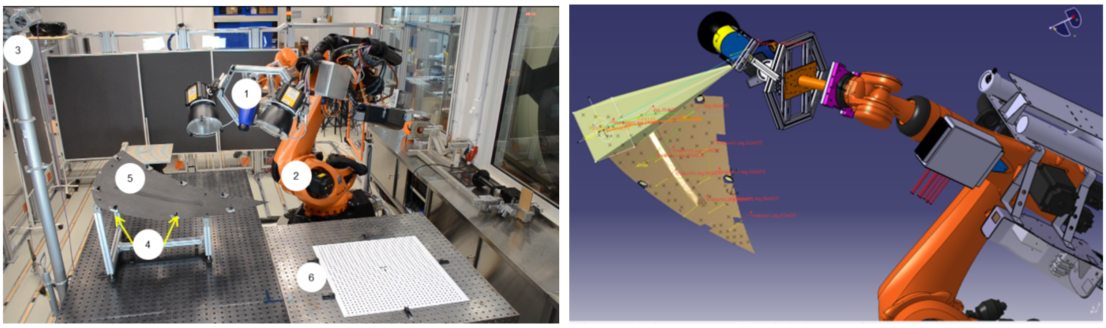

(a) (b)

Figure 3.24: (a)Experimental setup for pressure bulkhead and camera calibration; (b) Offline robot program for pressure bulkhead. The field of view is shown as yellow pyramid

The camera was calibrated with the established method before the thermography measurement. The robot moves to all measurement positions with the determined TCP. The robot program was generated with *FastSurf*. The nine points per measurement field were distributed differently this time. The reason for this was the geometric mapping, especially with the stringer. The aim was to find out whether double-curved and complex stringer geometry has an influence on both laser projection and reconstruction. No common points were constructed between the two measurement fields. Thus there are only slightly overlapping areas between the measurement fields. Figure 3.25 shows the projected laser points. Then the same steps were performed (see previous subsection) as for the fuselage shell. The camera perspective was different for measurement fields. The projection matrix was able to calculate any position or rotation. The laser points captured from the pressure bulkhead were extracted in the sub-pixel range instead of the pixel range. The approach of stitching individual images was chosen in such a way that a check was performed prior to texturing the images to find whether it was already reconstructed in the area by another image. If yes, the new image was cut with triangles so that the previous textured image was not covered. This was necessary because the taken images were overlapped and prior to reconstruction the original images did not need to be cut along the points. After the 9th image was captured, thermography measurement was performed with a 0.3 Hz measuring frequency, and a phase image was saved for reconstruction.

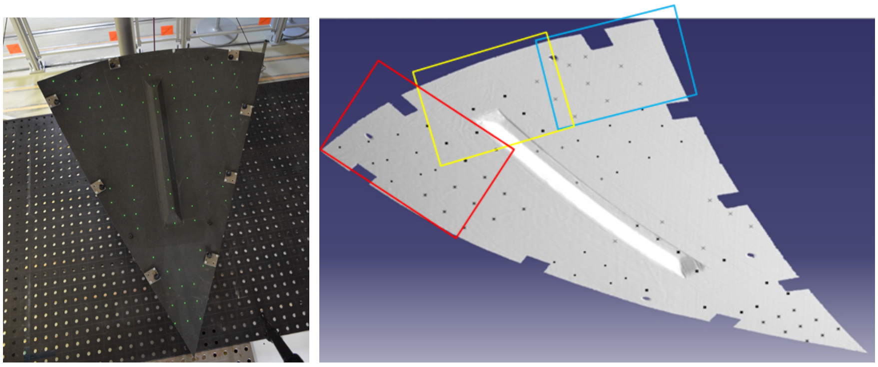
(a) (b)

Figure 3.25: (a)Projected laser points for 11 measurement fields on pressure bulkhead; (b) Defined 3D points on pressure bulkhead

The above described steps were repeated until all measurement fields were covered. All the phase images were saved with the same phase angle value. Thereafter, all thermographic images (in this case ten images, see figure 3.26) of the pressure bulkhead with the stringer were reconstructed (see in figure 3.27). Due to structural and material differences (monolithic with two different thicknesses and a sandwich as stringer), thermography phase images appear in light and dark grey values. The same applies to the screws and target plates. Therefore these areas can be distinguished after reconstruction and will help to evaluate the reconstruction accuracy. The individual process steps of automated thermography described so far are shown together in figure 3.28. The first two steps only have to be performed once. Measurement of a real geometry is only necessary if the manufactured component is outside the tolerance range. The automated evaluation step which may detect the defects automatically is presented here as an example, but is not part of this thesis.

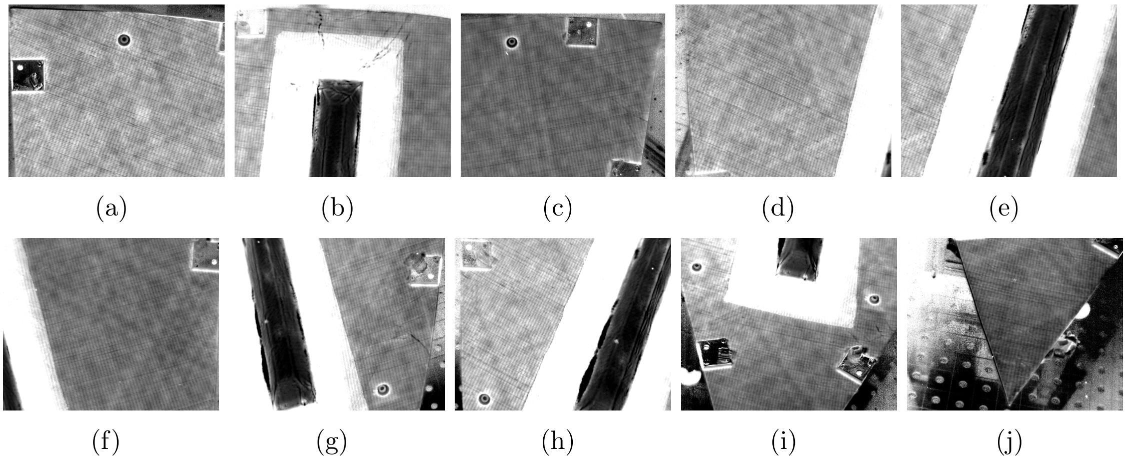

Figure 3.26: Thermography images (a)M1; (b) M2; (c) M3; (d) M4; (e) M5; (f) M6; (g) M7; (h) M8; (i)M9; (j) M10

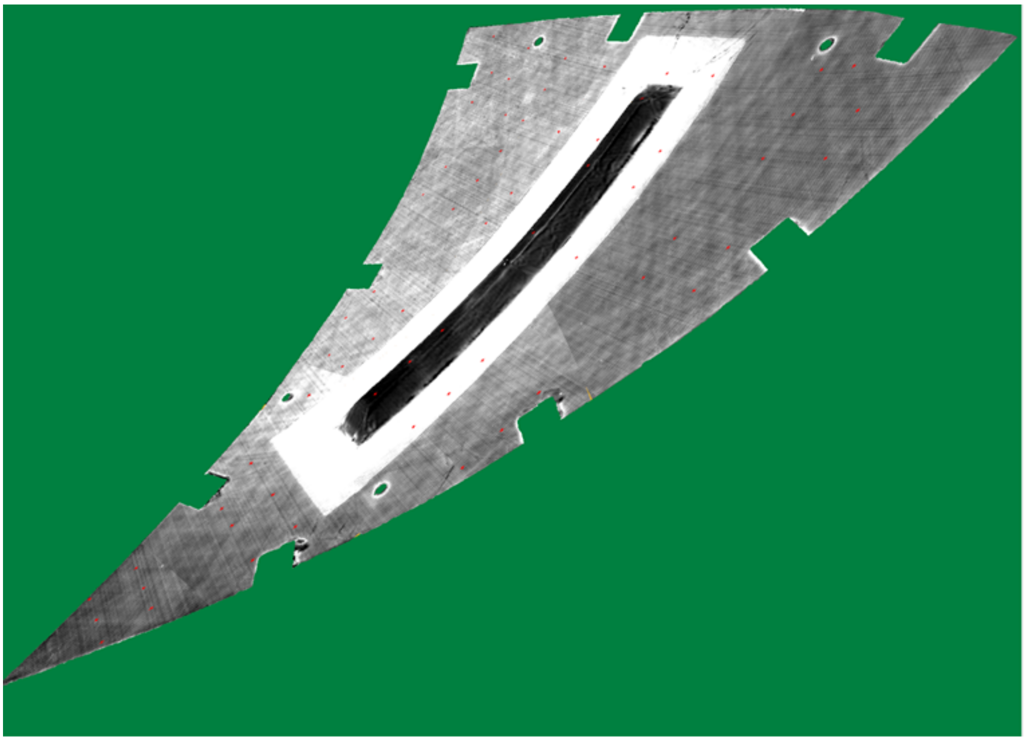

Figure 3.27: Automatically-generated 3D thermography model of pressure bulkhead

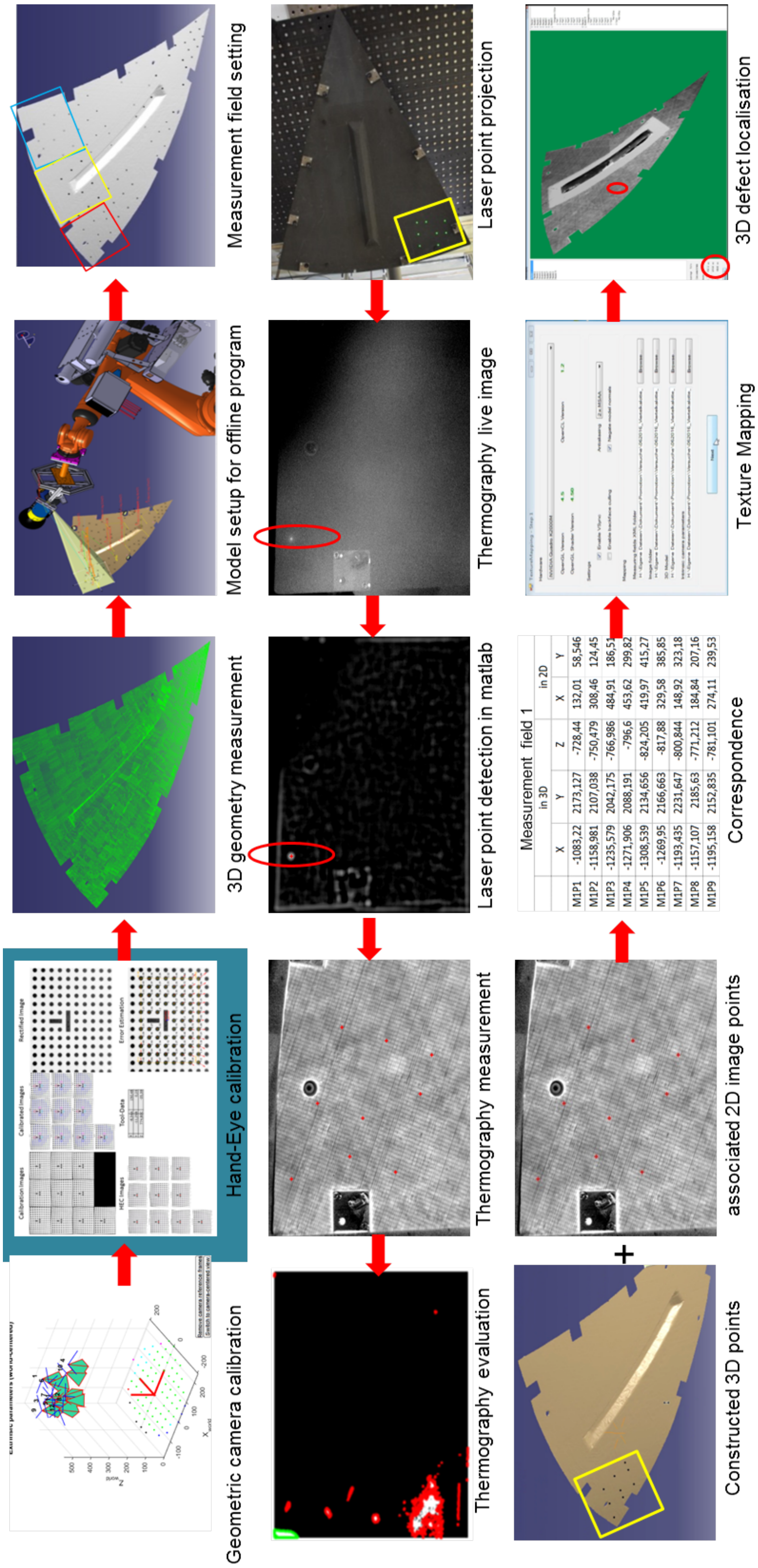

Measurement field 1

	in 3D			in 2D	
	X	Y	Z	X	Y
M1P1	-1083,22	2173,127	-728,44	132,01	58,546
M1P2	-1158,981	2107,038	-750,479	308,46	124,45
M1P3	-1235,579	2042,175	-766,986	484,91	186,51
M1P4	-1271,906	2088,191	-796,6	453,62	299,82
M1P5	-1308,539	2134,656	-824,205	419,97	415,27
M1P6	-1269,95	2166,663	-817,88	329,58	385,85
M1P7	-1193,435	2231,647	-800,844	148,92	323,18
M1P8	-1157,107	2185,63	-771,212	184,84	207,16
M1P9	-1195,158	2152,835	-781,101	274,11	239,53

Figure 3.28: 3D thermography process chain

Results and Discussion

The evaluation was performed on the basis of the thermal influences of the geometric properties. If one considers the images in the illustration 3.29, a white circle border around the screw (here holes) is clearly visible. As mentioned above, point clouds were cut out from the screw area. Due to manual trimming, not all point clouds in this area could be cut out. Thus a triangulated mesh was generated with this point cloud (without the screw surface) and used for the reconstruction. Due to a different thermal conductivity the CFRP and the screw emit differently. Thus a white ring appears around the screw. Dark grey values are also visible inside the holes. This proves in the reverse conclusion that the reconstruction was successful.

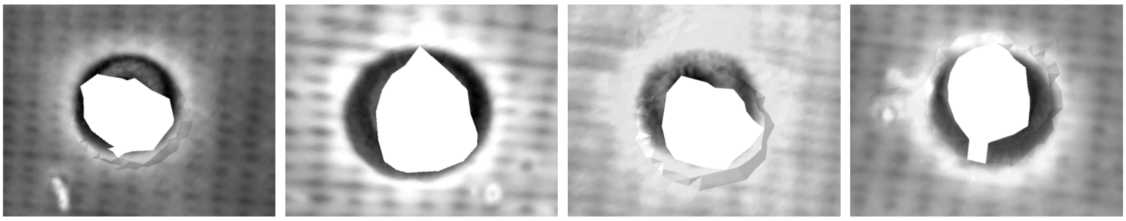
(a) (b) (c) (d)

Figure 3.29: Zoomed-in images at screw positions

A second comparison was carried out on the dented point and the stringer contour. When looking at the figure 3.30, the bright area lies on the dented position. Due to the missing measurement functions, the exact deviation could not be determined. The white line on the thermographic image also coincides exactly with the string contour. The entire geometry of the stringer is clearly recognisable from these enlarged images. Figure 3.31 shows two areas (chosen arbitrarily) for the accuracy examination. Two images were merged along the red dotted line. The individual rovings are approx. 1 to 2 mm wide. In the figure it is clearly visible that the


(a) (b)

Figure 3.30: Zoomed in images at screw positions

offset is greater at the edges than in the middle of the picture. However, it can be assumed that the larger part of the error is caused by the camera calibration parameters. Due to the camera distance to the object, the error at the edge is greater than in the centre of the image. Of course, there are also errors in laser projection, point recognition, surface reconstruction from the point cloud, texture mapping, etc. These topics will be examined in more detail in the further test series (in section 3.8).

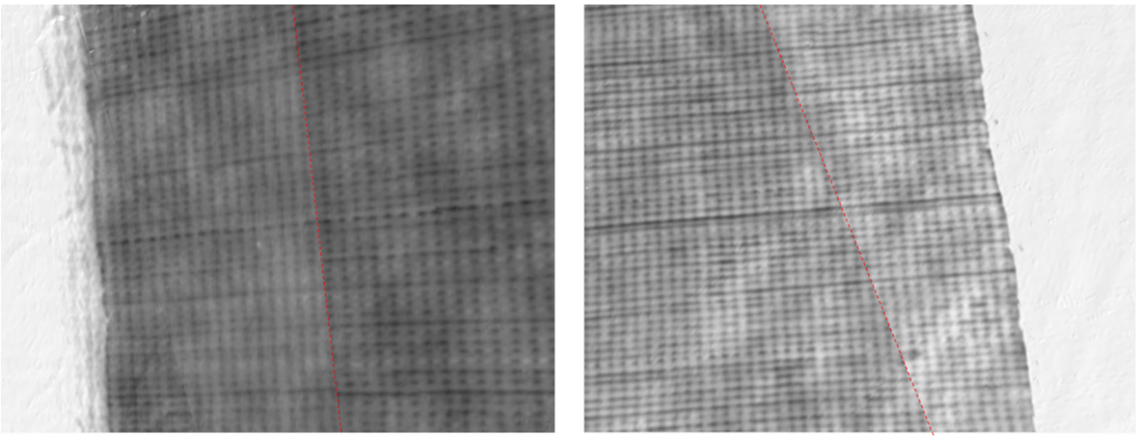

Figure 3.31: Relative accuracy between two images of pressure bulkhead

3.5.4 System validation on large component

Experimental setup and results

The aim here was not to investigate the absolute and relative accuracy but the process stability and limit of the new PnP method. Therefore a demopanel fuselage was selected for the test. The following shall be investigated:

- If there is any influence such as shadowing of robots during projection?
- How many laser projectors are required to cover the complete area?
- How complex is the measurement?
- Are there any limitations for larger datasets?

The chosen fuselage panel for the experiment was manufactured manually at DLR and has 6 stringers. It has the approximate dimensions of 4 m in diameter and 2 m width. In order to get high 3D mapping accuracy, the real surface of the fuselage was measured again with T-scan and a total number of 1640555 vertices were generated. The positions of 8 target plates were also measured, and calibration data for two laser projectors was created. Due to large surface area, two laser projectors were

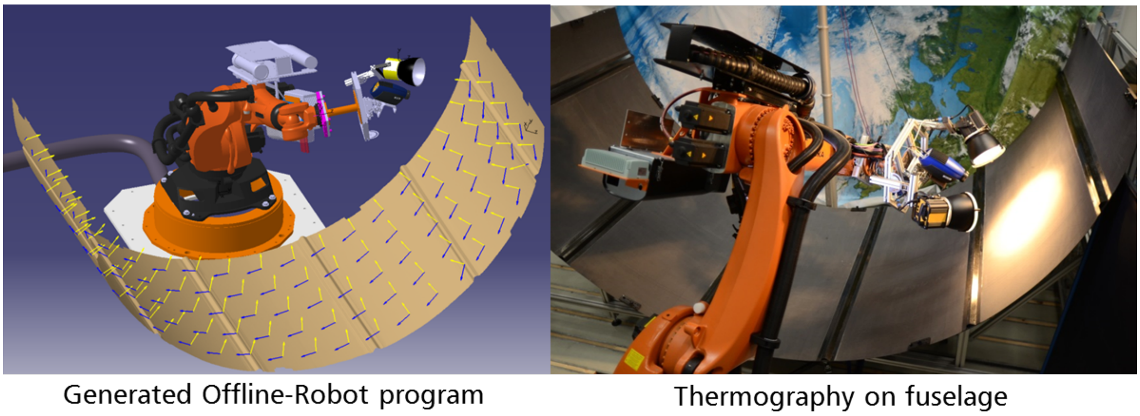

Figure 3.32: Conducted experiment at fuselage

calibrated for each half of the surface area. Due to the robot's limited reachability at all measurement positions, measurement distances for thermography varied between 1 and 1.2 m. Pixel resolution for approx. 1.2 m camera distance was 0.6 Pixel/mm. Hereby, the tool centre point, which was determined previously for 550 mm camera distance, was extended in CAD to 1 m and set for an approximate offline robot program (see figure 3.32). Prior to that the component's base position was measured, and later measurement positions were manually improved according to accessibility and reachability with a teach-in method. Due to manufacturing and engineering edges, 50 mm from the border side was not measured. In total, 105 measurement fields were required to cover the complete surface. The figure (see figure 3.33) represents the vertices and real surface. The constructed corresponding 3D points in *Catia* are enlarged and illustrated in figure 3.33. For each measurement field, 9 laser points were projected and captured by the camera. After that, thermography measurement was executed with 0.02 Hz frequency.

To avoid lateral thermal diffusion during thermography measurement execution, measurement fields were chosen arbitrarily. Total measurement time with 0,02Hz was (EP = 1; MP = 3): 200 (s) x 105 = 5.83 hours. With the new developed software it took less than 2 minutes to visualise 3D thermography (see figure 3.34). Laser points were constructed randomly. Therefore on a few measuring fields the points were on a stringer. All pictures were very well reconstructed. No error could be detected from the measuring surfaces where the points were not projected on the stringer. At certain positions it could be observed that at some positions, laser points could not be projected because of the unsuitable robot position between laser projector and component. Therefore the robot pose had to be improved at these positions. However, this should not be a problem as both smaller lamps and other projector positions can be selected. Furthermore, no other influences were noticed.

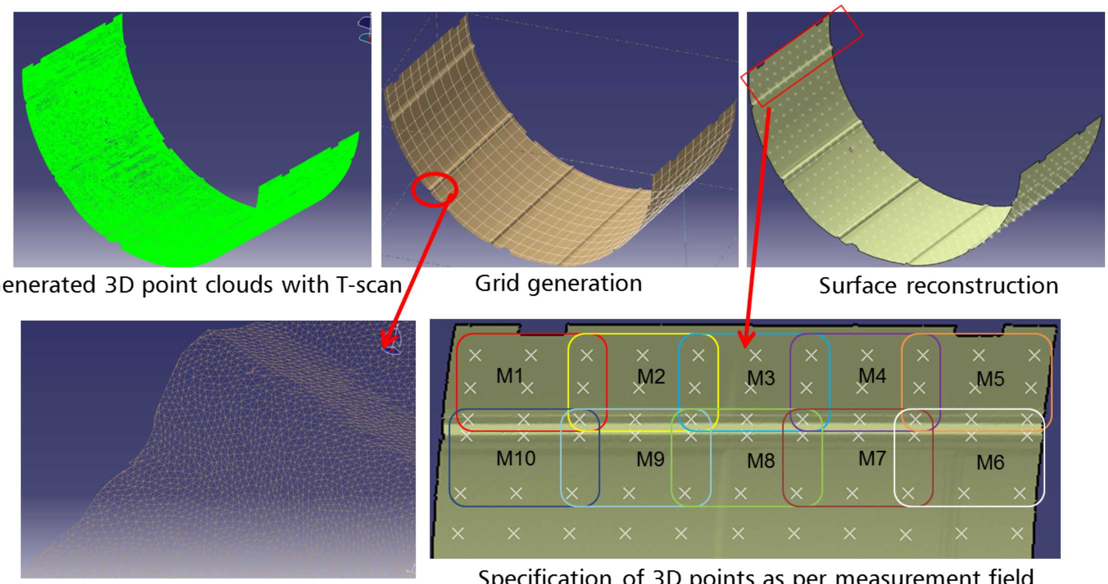

Generated 3D point clouds with T-scan

Grid generation

Surface reconstruction

Enlarged illustration

Specification of 3D points as per measurement field

Figure 3.33: Data preparation for experiment at fuselage

3.5.5 Conclusions

In this test series, an automated thermographic measurement and visualisation of the results in 3D were presented. The results were generated using the DLT method, thus confirming the feasibility of the new concept. This method was successfully applied to both a single-curved and a double-curved component. The individual process steps of automated inline thermography were discussed. Afterwards, a gross system accuracy analysis was carried out and the possible source of error was indicated. An exact overall system analysis and optimisation of the method is carried out in section 3.8. There might be an argument (which needs to be proven) against the method, that the designed points must represent the geometry structure, which can be difficult to implement with complex structures. For the method, this means that more than one projector could be used for complex structures. But this is not an obstacle to the method, because using two projectors instead of one is still more economical and easier than using an external guidance system or another reference system. Also the measurements results of fuselage are good evidence of a successful automated 3D thermography process. Furthermore, alternatives Perspective-n-Point (PnP), LHM, EPnP and PPnP are implemented in the section 3.7. All these methods are then compared and evaluated. In the next section, calculating the projection matrix by using the robot position and the results are discussed.

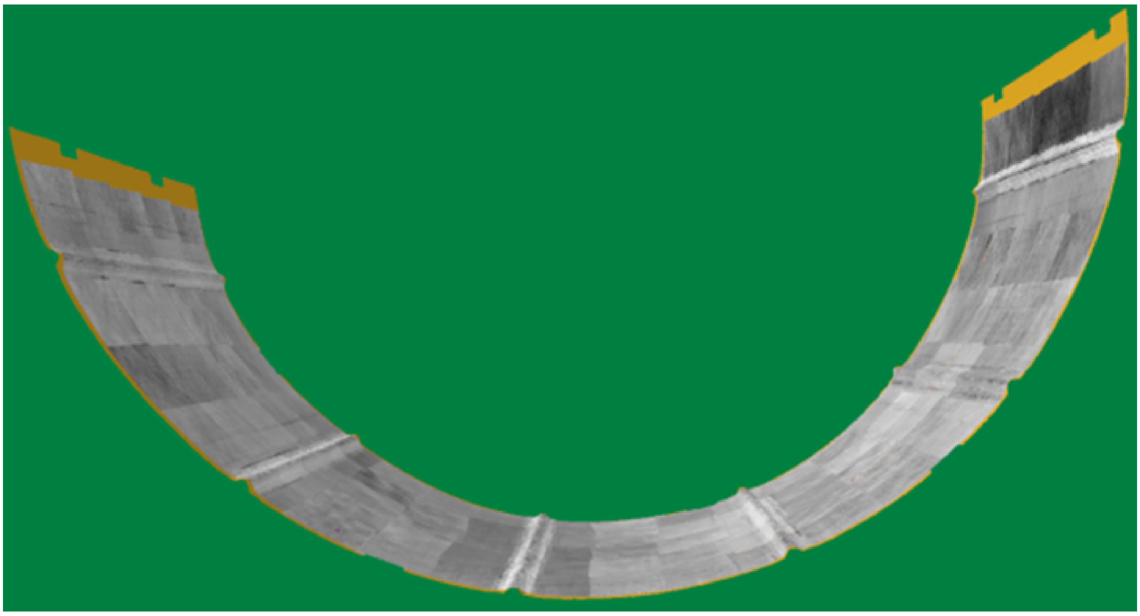

Figure 3.34: 3D visualisation of fuselage

3.6 Implementation of robot-based 3D thermography model

For 3D reconstruction the camera pose has to be calculated in relation to the component from the robot kinematic coordinates relationship. Therefore, the 3x4 projection matrix BT_C, which must be implemented in the already developed toolbox, needs to be calculated according to equation 3.1. As this transformation (see equation 3.35) represents a 4x4 matrix, the last row, which contains 0, will be deleted, in order to multiply with intrinsic parameters and to finally get a 3x4 projection matrix. The relationship between rob-root and flange (RT_F) as well as the transformation between Flange and camera TCP (FT_C) is already known. The BT_R transformations matrix between robot and component needs to be calculated whenever the component's positions change. In general, the world coordinate does not change and the relation between rob-root and world coordinate are calibrated through the KUKA "machine.dat". In general, robot programs can be generated in any coordinates via OLP or directly. The positions of these coordinates are usually object coordinates, rob-root, or world coordinates. Since both absolute and relative accuracy play a role in the robot-based method, the object coordinate was chosen in order to calculate the last component (BT_R) of equation 3.1. Because, according to the authors [77], the further the robot has to be positioned from its measured coordinates, the more the inaccuracy of the robot increases. This also simplifies the calculation of the chain relationship. The author of paper [27] explains that through robot-to-object calibration, the achievable accuracy of the robot can be improved further. For calibration of the object position in relation to the rob-root, the 3-point method given by *KUKA* was applied. The method works as follows: If the measuring tip attached to the robot is moved in four directions in space manually against a constant point in space, the robot controller calculates the position of the measuring tip in relation to the robot flange. The robot controller can take masses attached to the robot into account when moving to desired positions in space and thus tries to compensate for kinematic elasticities. According to the experimental determination in section 3.2, weight plays a role for absolute accuracy. Therefore, the correct data, determined with a load detection function, was entered before the measurement.

3.6.1 Experimental setup

To verify the system, a new experimental setup was prepared (see figure 3.35). The component was approximate 1000 mm long, 500 mm wide and 4 m diameter. 30 measurement fields with a measurement distance of 550 mm were required to cover the complete surface. Further details about the manufacturing process of the component as well as about the thermography measurement results are described in section 4. The component was fixed with clamps on an aluminium profile. 6 target plates were placed on the aluminium profile. The exact positions are depicted in image 3.36. Just as before, the component's real surface and the position of the target plates and reflectors were measured with T-scan. Target plates were actually

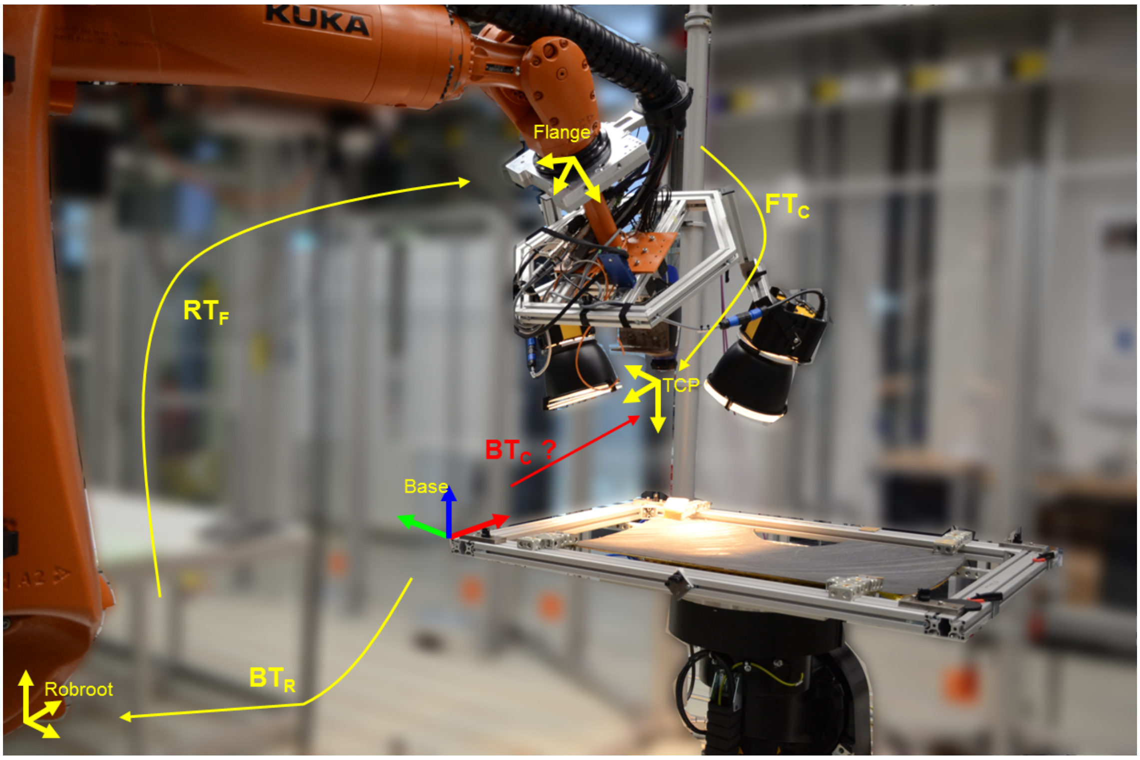

Figure 3.35: Experimental setup thermoplastic component

required for the PnP method (see the results in section 3.7), but can also be used for the robot to measure the base position of the component, as it has sharp edges. 469548 triangulated meshes (STL data) were generated from the point cloud, and the component's base coordinate was set at the corner of target plate 4 (see figures 3.35 and 3.36). Three sides of plate 4 were measured with T-probe to generate the base coordinate. Prior to that, the hand-eye calibration and geometric calibration were performed again. Small changes compared to the last result were identified in hand-eye calibration results, as the camera was disassembled from the end-effector between two experiments.

Thereafter the component's base was measured with the robot by using the 3-point method. The robot controller derives a coordinate system from the 3 points. The first two points define the x- and y-axis and the third point defines the z-axis, which lie normal at plane at the intersection point. It should be noted that although this 3-point method is common in industrial environments, no base coordinate could be measured with the robot from target plate 4 due to the small flat steel edge length. Therefore, for x direction a point on target plate 3, which was mounted opposite to target plate 4, was used for the measurement. As target plate 3 was mounted slightly rotated in relation to target plate 4, a deviation between the calibrated base with the robot and the generated base with T-scan was created. Thus, larger deviations in the result were to be expected. The relative position between target plates 3 and 4 was measured with *Spacial Analyser*. Rotational deviations were in R_x=0.35 °, R_y=0.15 °and R_z=0.25 °. Translational deviations were dx=910.17 mm, dy=4 mm and dz= -0.48 mm. Also, the inaccuracy of manual base measurement will affect the 3D thermography result. If the 0.218 °rotation on the X axis is calculated at a

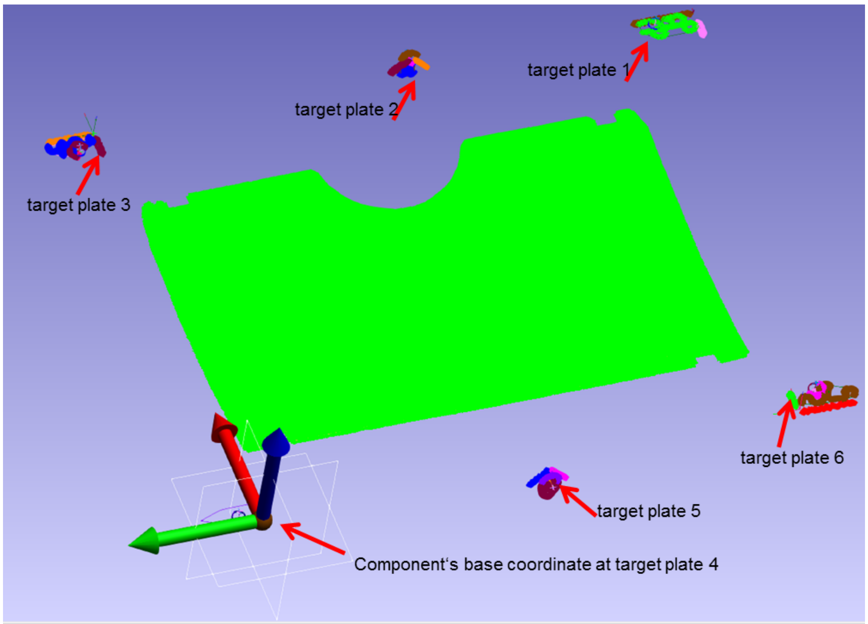

Figure 3.36: Thermoplastic component measurement

distance of 910 mm, an error of approx. 3.5 mm is to be expected. Of course, the deviations on the other axis must be taken into account. However, it is not possible to reconstruct a total error from this because the manual base measurement error, $KUKA$ calculation error and T-scan measurement error must be taken into account too in this calculation.
Thereafter, an offline robot program was generated using measured TCP. A robot program was generated in a base coordinate system. 30 measurement positions were required in order to cover the complete area. After that, the component was measured with the thermography camera by using 0.4 Hz, 0.1 Hz and 0.05 Hz frequencies. The lateral thermal diffusion between two successive measurements was also considered during measuring time. 30 images per frequency, intrinsic parameters, the ".dat" file of the robot program, containing all measured robot positions, and rigid transformation matrices are provided to the software to calculate the projection matrix. By selecting the ".dat" file, the software searches for the correct parameters, which in this case start in line 5 (see in figure 3.37). The translations in the x, y and z axis direction are represented by the values to X, Y, Z, and the rotations α, β, γ are represented by A, B, C. This completely describes the position of the camera coordinate system in relation to the object coordinate system at the time of acquisition. It was specified that the first specified position in the text document corresponds to the first thermography. The programming tasks were implemented as part of the master's thesis [78].

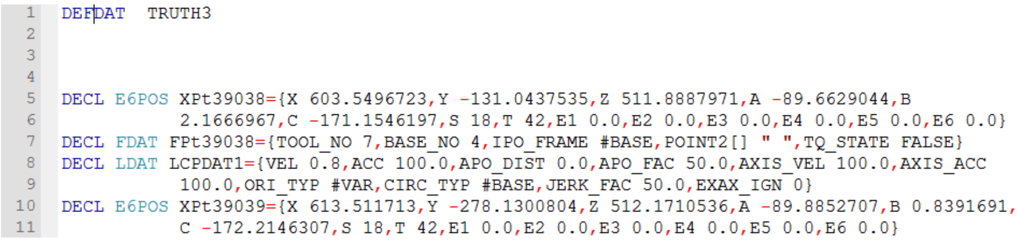

```
 1  DEFDAT  TRUTH3
 2
 3
 4
 5  DECL E6POS XPt39038={X 603.5496723,Y -131.0437535,Z 511.8887971,A -89.6629044,B
 6             2.1666967,C -171.1546197,S 18,T 42,E1 0.0,E2 0.0,E3 0.0,E4 0.0,E5 0.0,E6 0.0}
 7  DECL FDAT FPt39038={TOOL_NO 7,BASE_NO 4,IPO_FRAME #BASE,POINT2[] " ",TQ_STATE FALSE}
 8  DECL LDAT LCPDAT1={VEL 0.8,ACC 100.0,APO_DIST 0.0,APO_FAC 50.0,AXIS_VEL 100.0,AXIS_ACC
 9             100.0,ORI_TYP #VAR,CIRC_TYP #BASE,JERK_FAC 50.0,EXAX_IGN 0}
10  DECL E6POS XPt39039={X 613.511713,Y -278.1300804,Z 512.1710536,A -89.8852707,B 0.8391691,
11             C -172.2146307,S 18,T 42,E1 0.0,E2 0.0,E3 0.0,E4 0.0,E5 0.0,E6 0.0}
```

Figure 3.37: First two positions of robot program

3.6.2 Results and conclusions

For the purpose of visualisation, a 3D thermography model with one frequency (0.4 Hz) is illustrated in figure 3.38. The reconstruction results of all frequencies were exactly the same. If one considers the 3D model in figure 3.38, it creates a good impression at first glance. The dark grey areas as rectangles and circles are built-in flaws. This is described in detail in chapter 4. The exemplary continuous fibre orientation (yellow rectangle) over the whole component shows a high relative accuracy between the images. In case of enlarging, e.g., in the area of the red rectangles (see Figure 3.39), a very high relative accuracy of the method can also be seen. At the merged edges of two images a continuous wrinkling can be observed, showing that the robot controller is able to determine the relative change of the robot axis with sufficiently high accuracy. Otherwise, discontinuities in the progression of the visible structures would occur at the image boundaries.

If one continues to review the image in figure 3.38 at the left edge and at the top right edge (marked with yellow), a dark area can be seen. The thermoplastic component was fixed to the aluminium frame (see figure 3.35) only with four clamps. These clamps areas were cut out of the point cloud during mesh generation. These four areas are clearly visible in the figures 3.38 and 3.36. The remaining outer edges were unobstructed. Since the outer area along all edges was also in the field of view of the camera, the absence of the material caused a different phase shift in the outer area than in the area of the component. For a better understanding, the original 5 pictures are shown in figure 3.40. On the left upper edge as well as on other edges this phenomenon is not present. The reconstruction seems to be rotated and shifted. The direction is marked with a white arrow. After measuring the area on the left edge, a displacement of approx. 5 mm was determined. A major part of these errors was due to incorrect base measurement (see last section 3.6.1). Of course, the error chain is very large, and it is difficult to identify and separate individual error sources.The system will be examined again in more detail in section 3.8 and some error values were identified for that particular experiment. Furthermore, in the red-marked circle (see figure 3.39) two white spots can be observed. This was part of a clamp. Nevertheless, the method was implemented successfully, and the reason for a major cause of avoidable errors could be identified. One may have observed in figure 3.40 a slight phase angle difference between these 5 images. Although the measurement was carried out with offset between individual measurement fields in order to avoid lateral heat flows, it was not possible to avoid this 100 % due to the small component. Furthermore, the ply design and thickness of the component over the surface is different, so that the component does not have the same thermal conductivity everywhere.

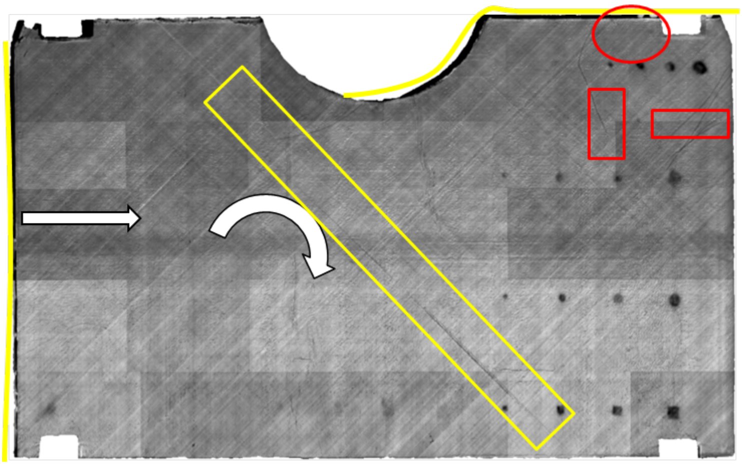

Figure 3.38: 3D thermography results based on kinematic chain relationship

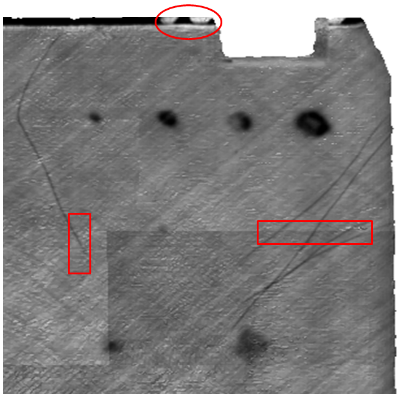

Figure 3.39: Enlarged image of kinematic chain based 3D thermography results

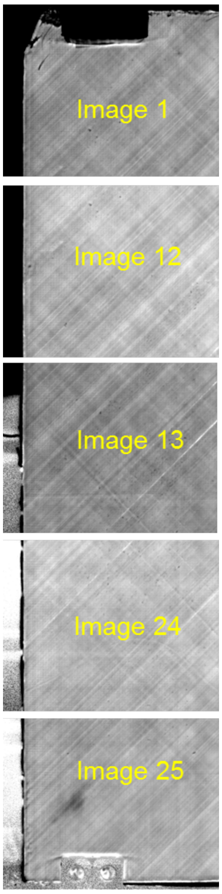

Figure 3.40: Images at left edge of thermoplastic component

3.7 Optimisation of Point to Point (PnP) based 3D thermography model

To compare the previous result (robot-based 3D thermography) with the PnP method, the already-implemented DLT method was applied. Therefore the same setup was used and the 3D points were captured with the camera after laser projector calibration. The robot program remained unchanged. That means that the camera position and orientation are the same for both methods. The result of the DLT method is shown in the figure 3.41. The dark area at the left and right upper edge is not visible here compared to robot-based method. A thin dark line can be seen in the red-marked circular section, which represents the actual fringed edges of the component. Through the detailed analysis in the red-marked circular area (see figure 3.42), fringed fibre at some places along the edge could be observed, which caused a inhomogeneous (dark and light grey) phase shift. Despite the good reconstruction, in the above described areas, major errors can be seen in the measurement fields 15, 17 and 25 (see figure 3.41). The numbers in white represent the measurement field position and the numbers in yellow represent the minimum orthogonal distance regression to plane (see more in section 3.3). By comparing the yellow numbers throughout the measurement fields, it can be noticed, that the numbers in the middle row (red marked) are very small, explained by the quasi-coplanarity data set. At the beginning of this experiment, the measurement fields 13, 14, 16 and 18 could not be reconstructed. Later, the points for the measurement fields 13, 14, 15 and 16 were projected slightly apart to avoid coplanarity and could be reconstructed with much effort. Despite this, the fibre flow between the two images was not good enough.

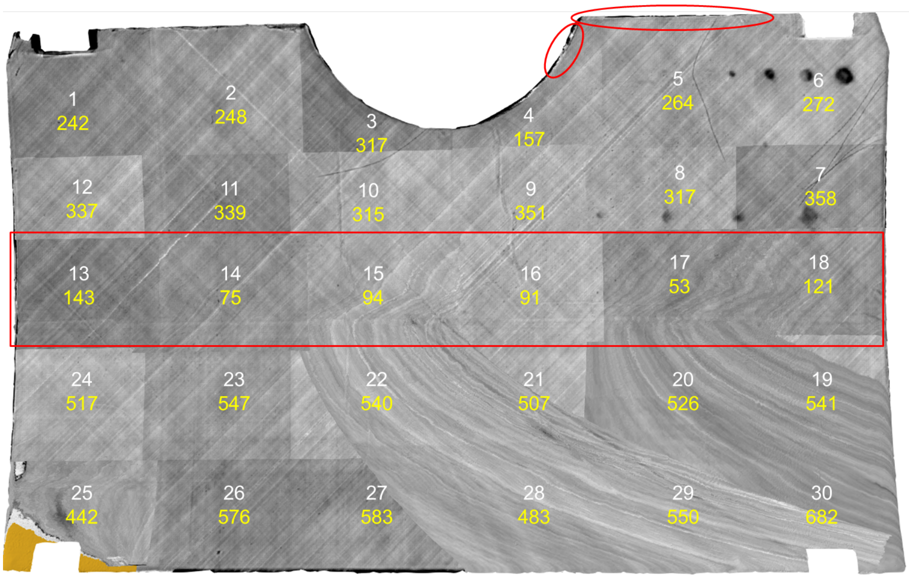

Figure 3.41: 3D thermography model of thermoplastic component with DLT

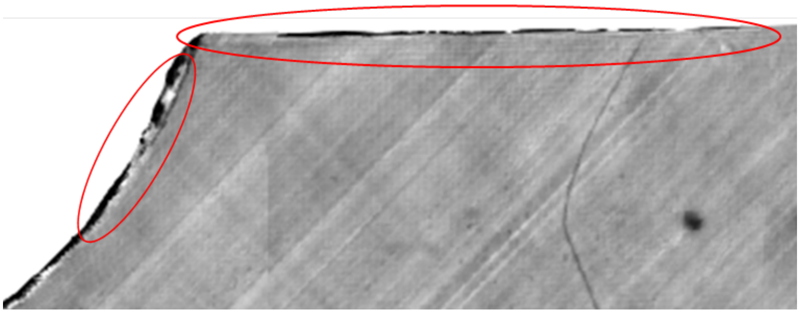

Figure 3.42: Enlarged image of DLT based 3D thermography results

This type of error can be explained as follows:

- If all object points lie on one plane, no solution with the DLT can be obtained, because then the rank (A) sinks or becomes unstable, as the eigenvalues are small. Figures 3.43 (a) and (c) represent the eigenvalues of the projection matrix respectively for image 17 and 1. Thus it becomes apparent that the eigenvectors of the projection matrix of image 17 are very small and therefore the projection matrix has became unstable without finding a unique solution.
- Other factors that could have played a role are:
  - an unknown scaling factor for all points (depth information is lost).
  - DLT is a projective reconstruction and not euclidean or orthographic reconstruction (line parallelism and angle are maintained). Therefore orthonormality will be relaxed for a rotation matrix.

In spite of the relatively long distance to coplanarity, data set 25 is also solved badly. In this data set, there are only 8 instead of 9 different points because points 8 and 9 are on the same position following an error during generation. Furthermore, the camera has prevented the projection of two of nine points. Therefore these two points were projected close to each other. However, it could not be clarified whether this is the reason for the error.

A way to avoid this kind of effect would be increasing the measuring distance. But this can't be a global solution for industrialisation. Therefore other PnP methods need to be integrated, when weakness of the DLT method are addressed. These are primarily depth estimation and the orthonormality of the rotation matrix. A lot of mathematical approaches and algorithms exist based on known intrinsic parameters, so that only extrinsic parameters are to be calculated by maintaining the orthonormality of the rotation matrix. This can be achieved by calculating the correspondence between object points and image points in 3D euclidean objects and camera coordinate respectively. When the intrinsic matrix K (5 degrees of freedom) is known through geometric camera calibration, only the extrinsic calibration parameters rotation and translation have to be determined. The rotation has three degrees of freedom (for example as Euler angle), as well as the translation. Due to the reduction of the degrees of freedom, a smaller number of known points is sufficient for a unique solution. Furthermore these existing algorithms can be distinguished between direct or iterative solutions with linear or non-linear approaches and the number of least-required correspondences. It can be assumed that, due to different approaches or simplifications, certain algorithms are suitable for certain experimental configurations in order to solve the extrinsic parameters. As this makes it difficult to make the right choice, the three most cited algorithms were chosen for implementation. These are: one very famous non-iterative (equivalent to DLT) solution (EPnP) and two widely used iterative solutions (LHM and PPnP). In order to verify the decision, a preliminary study was performed in the master's thesis [78] with a part of the already generated data set (minimum effort[1]) and with the help of a *Matlab* program [79], where all these methods were implemented. According to rotational and translational pose estimation error from *Matlab*, LHM and PPnP methods were better than the not-implemented AsPnP [80], DLS [81] and RPnP [82]) algorithms.

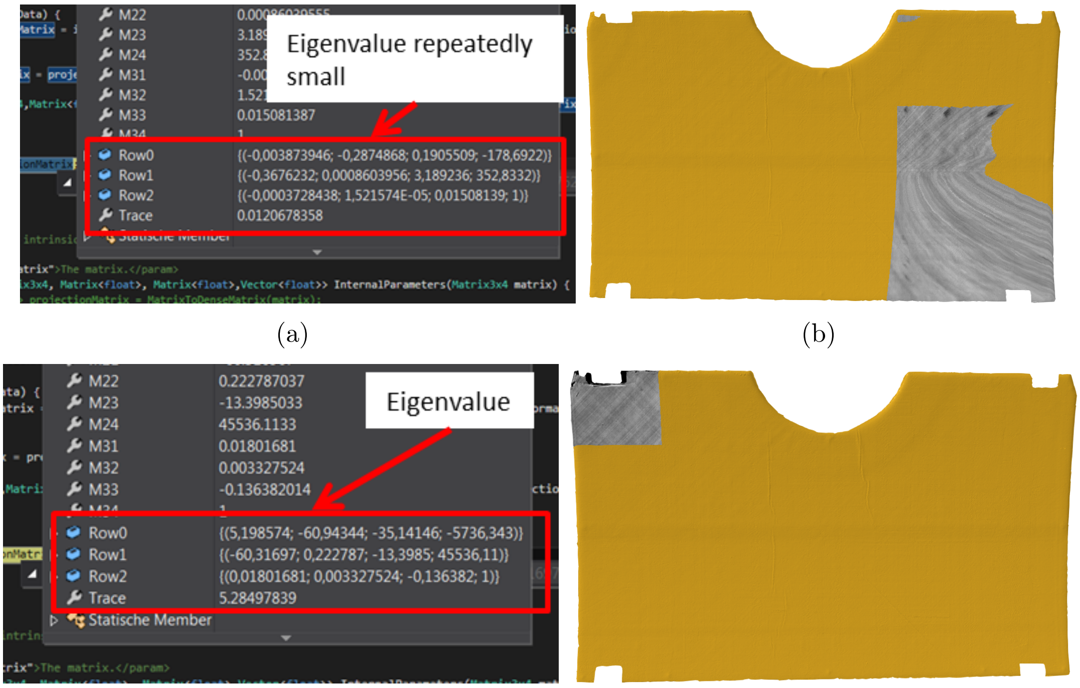

```
M22     0.00086029555
M23     3.189
M24     352.8
M31     -0.00
M32     1.521
M33     0.015081387
M34     1
Row0    {(-0,003873946; -0,2874868; 0,1905509; -178,6922)}
Row1    {(-0,3676232; 0,0008603956; 3,189236; 352,8332)}
Row2    {(-0,0003728438; 1,521574E-05; 0,01508139; 1)}
Trace   0.0120678358
```

(a)

(b)

```
M22     0.222787037
M23     -13.3985033
M24     45536.1133
M31     0.01801681
M32     0.003327524
M33     -0.136382014
M34     1
Row0    {(5,198574; -60,94344; -35,14146; -5736,343)}
Row1    {(-60,31697; 0,222787; -13,3985; 45536,11)}
Row2    {(0,01801681; 0,003327524; -0,136382; 1)}
Trace   5.28497839
Statische Member
```

(c)

(d)

Figure 3.43: (a)Projection matrix for position 17 with DLT; (b)3D reconstruction for position 17 with DLT; (c)Projection matrix for position 1 with DLT; (d)3D reconstruction for position 1 with DLT

In the next sections, the basics of the methods are briefly explained. Then the

---

[1] In general more data set and different experimental setup is required for detail analysis

results of these methods are analysed. Here not only the mathematical approaches are explained but also the fundamental differences of the three selected approaches are highlighted.

3.7.1 Efficient Point to Point (EPnp)

The non-iterative (efficient PnP) EPnP [45] method was developed by *Lepetit*, *Moreno-Noguer* and *Fua* and offers an alternative to DLT. The author claims that this method works faster without requiring an initial guess and as accurate as the iterative method of Lu [1]. Furthermore, this method differs from most of the non-iterative approaches by generating a weighted sum of four virtual points instead of estimating the depth of 3D points in a camera-coordinate system. If object points are defined in euclidean object coordinates by $P_i = 1, ...n$, then the four virtual points $c_j,\ j = 1, ..., 4$ can build an euclidean coordinate system of unit vectors along with the object point coordinate system. This means that four out of 9 3D points will build the coordinate system for a virtual point. For stability reasons the origin should be in the geometric centre of gravity of the known object points. This can be expressed:

$$P_i^w = \sum_{j=1}^{4} \alpha_{ij} c_j^w \quad \text{with} \quad \sum_{j=1}^{4} \alpha_{ij} = 1 \tag{3.68}$$

Whereby α_{ij} are homogenous barycentric coordinate and c_j^w are object coordinate for control/virtual points. One may have noticed that the equation is similar to equation 3.65, where data sets are normalised for DLT. Thereafter these control points will be projected into a camera coordinate system by using a uniquely-defined α_{ij} barycentric coordinate.

$$P_i^c = \sum_{j=1}^{4} \alpha_{ij} c_j^c \quad \text{;where } P_i^c \text{ represents camera coordinate system of virtual point} \tag{3.69}$$

Now to solve the linear equation $Am = 0$, which contains the 12 unknown parameters of four control points $(x_j^c, y_j^c, z_j^c)_{j=1,...,4}$, the equation 3.69 will be multiplied with intrinsic parameters K and can be written:

$$\begin{pmatrix} u_i w_i \\ v_i w_i \\ w_i \end{pmatrix} = K \sum_{j=1}^{4} \alpha_{ij} \begin{pmatrix} x_j \\ y_j \\ z_j \end{pmatrix} \tag{3.70}$$

After substituting the last row of equation 3.70, two linear equations for each control point can be expressed:

$$\sum_{j=1}^{4} \alpha_{ij} f_x x_j + \alpha_{ij}(\sigma_x - u_i) z_j = 0 \tag{3.71}$$

$$\sum_{j=1}^{4} \alpha_{ij} f_y y_j + \alpha_{ij}(\sigma_y - v_i) z_j = 0 \tag{3.72}$$

Where f_x and f_y are focal lengths and σ_x and σ_y are the principal points of intrinsic parameters. One may notice that the projective parameter w_i is eliminated, so that unlike DLT, the normalisation of 2D projection is not required. The solution lies in the kernel of A and needs to be solved by:

$$m = \sum_{i=1}^{N} \beta_i \mathbf{v}_i \tag{3.73}$$

Where **v** represents the columns of the right-singular vector of A and can be solved by calculating the matrix $A^T A$. To solve the appropriate scaling factor β for each point, the author has proposed four mathematical approaches or cases ($\beta_i =_{i=1,\dots,N}$), which depends on the relation between focal length and distance. The detailed information about these four cases is also described in the paper [45]. After calculating the scaling factor, the coefficients of the control points are known in the camera coordinate system.
Thereafter the extrinsic parameters can be calculated by applying the rigid body transformation approach (see section 3.3), as both sets of the control points are in the orthogonal coordinate system. Therefore, the geometrical centroid of the control points c_j^w in the object coordinate and c_j^c in the camera coordinate have to be calculated according to equations 3.37 and 3.38. In order to isolate the translation vector and to only calculate the 3x3 rotational matrix, the centroid of these calculated coordinates has to be substituted from the respective coordinate system by:

$$H = (c^c - \frac{1}{4}\sum_{j=1}^{4} c_j^c)(c^w - \frac{1}{4}\sum_{j=1}^{4} c_j^w)^T \tag{3.74}$$

The rotation matrix can be solved by singular value decomposition. Thereafter, t the translation vector is calculated by:

$$t = \frac{1}{4}\sum_{j=1}^{4} c^c - R(\frac{1}{4}\sum_{j=1}^{4} c^w)^T \tag{3.75}$$

Finally, the 3x3 rotation matrix and 1x3 translation vectors can be put together to build the 3x4 projection matrix, which contains the camera pose to the object.

3.7.2 Procrustes Point to Point (PPnP)

In general, the iterative methods are used to determine the scaling factor that describes the depth estimation of the 3D object points. Hereby a distinction is made between isotropic depth estimation (one factor for all points in object coordinate) and anisotropic depth estimation (individual factor for individual object points). *Garro*, *Crosilla* and *Fusiello* have published their solving method for PnP with "Anisotropic Orthogonal Procrustes Analysis" in *IEEE* 2012 [46]. They have derived a general solution for the anisotropic scaling factor which minimises the length of Δs for all individual points in a least-square sense. Δ represents the perpendicular distance between the joining point of an extended optical ray from a 2D image into a 3D object coordinate (as 3D point) and its corresponding reference 3D point. In order to calculate the projection matrix with the scaling factor, depth coefficients can be added to the general equation in the homogenous coordinate 3.13 by:

$$\zeta_i \tilde{m}_i = K(R|t)\tilde{M}_i \tag{3.76}$$

Where ζ_i represents the depth coefficient of $\tilde{M}_i$, which is the distance between the focal plane and point position. In order to transfer the object point into the camera coordinate, the intrinsic parameter K^{-1} is multiplied by both sides of the equation 3.76 and after some rewriting it becomes:

$$\underbrace{\begin{bmatrix}\zeta_i & 0 & \cdots & 0\\ \vdots & \vdots & \ddots & \vdots \\ 0 & 0 & \cdots & \zeta_n\end{bmatrix}}_{\mathrm{Z}} \underbrace{\begin{bmatrix}\tilde{P}_i^T\\ \vdots\\ \tilde{P}_n^T\end{bmatrix}}_{\mathrm{P}} R + \underbrace{\begin{bmatrix}c^T\\ \vdots \\ c^T\end{bmatrix}}_{\mathrm{1c^T}} = \underbrace{\begin{bmatrix}M_1^T\\ \vdots\\ M_n^T\end{bmatrix}}_{\mathrm{S}} \tag{3.77}$$

where

$c = -R^T t$ = coordinate vector of projection centre
R = orthogonal rotational matrix
P = represents matrix by rows of image coordinate defined in camera coordinate
S = rows of 3D points defined in object coordinate
Z = diagonal matrix with depth information

To calculate the orthogonal procrustes error by means of the least-square solution, Δ is added to the equation 3.77, which can be written in short form as:

$$S = ZPR + e_1 c^T + \Delta \tag{3.78}$$

The least-square solution is solved according to the *Schönemann* equation [83]

$$\min ||\Delta||_F^2 \tag{3.79}$$

by considering $R^T R = I$. Similarly to the EPnP method the rotational matrix, isotropic scale and translational vector will be calculated in this order separately by using the rigid body transformation approach, so that the effect of an unknown parameter can be avoided. F represents the Lagrangian function

$$F = tr(\Delta^T \Delta) + tr(L(R^T R - I)) \tag{3.80}$$

whose derivation is described in detail in paper [46]. The whole algorithm can be summarised in 5 steps. For the initial assumption, the algorithm starts with $Z = 0$ and estimates R with

$$R = U\mathrm{diag}(1, 1, \det(UV^T))V^T \tag{3.81}$$

Then the first projection centre c will be estimated by:

$$c = (S - ZPR)^T 1/n \qquad \text{n} = \text{number of points} \tag{3.82}$$

Thereafter depth information is calculated with

$$Z = \mathrm{diag}(PR(S^T - c_1^T))\mathrm{diag}(PP^T)^{-1} \tag{3.83}$$

These 5 steps have to be repeated until convergence is achieved. This PPnP method is quite similar to the POSIT method [84].

3.7.3 Lu Hager Method (LHM)

The fundamental difference between the iterative LHM and the PPnP methods lies in the calculation of the rotation matrix. With LHM the rotation matrix is calculated in 3D object coordinate instead of in 3D camera coordinate. The developed method (LHM) [1] by *Chien-Ping LU*, *Gregory D. Hager*† and *Eric Mjolsness*‡§ minimises geometric error, based on collinearity in 3D object space, by solving iteratively the rotation matrix in closed-form as non-linear cost function. This converges stably to the global optimum. Then the translation vector will be computed by considering the orthogonal rotation matrix. A good initial pose estimation is important. Otherwise the algorithm might become unstable.

Based on rigid body transformation equation 3.36, for a given 3D point $p_\mathrm{i} = (p_1, p_2, ...p_\mathrm{n}), i = 1, ..., n; n \geq 3$ the corresponding 2D point $q_\mathrm{i} = (q_1, q_2, ...q_\mathrm{n})$ can be formulated by:

$$p_\mathrm{i} = Rq_\mathrm{i} + t \tag{3.84}$$

where R and t represent the 3x3 orthogonal rotation matrix and 3D translational vector. For an ideal case the image point $\boldsymbol{v}_i = (u_i, v_i 1)^t$ will be collinear with q_i. Due to manufacturing tolerances and lens distortions the orthogonal image projection error of q_i on $\boldsymbol{v}_i$ (see figure 3.44) can be considered in the previous equation by:

$$RP_i + t = p_i = F_i p_i \tag{3.85}$$

so that the object-space collinearity error e_i is defined for one point by:

$$e_i = (I - F_i)(Rp_i + t) \tag{3.86}$$

where F_i is the projection operator, and it is defined by:

$$F_i = \frac{\boldsymbol{v}_i \boldsymbol{v}_i^t}{\boldsymbol{v}_i^t \boldsymbol{v}_i} \tag{3.87}$$

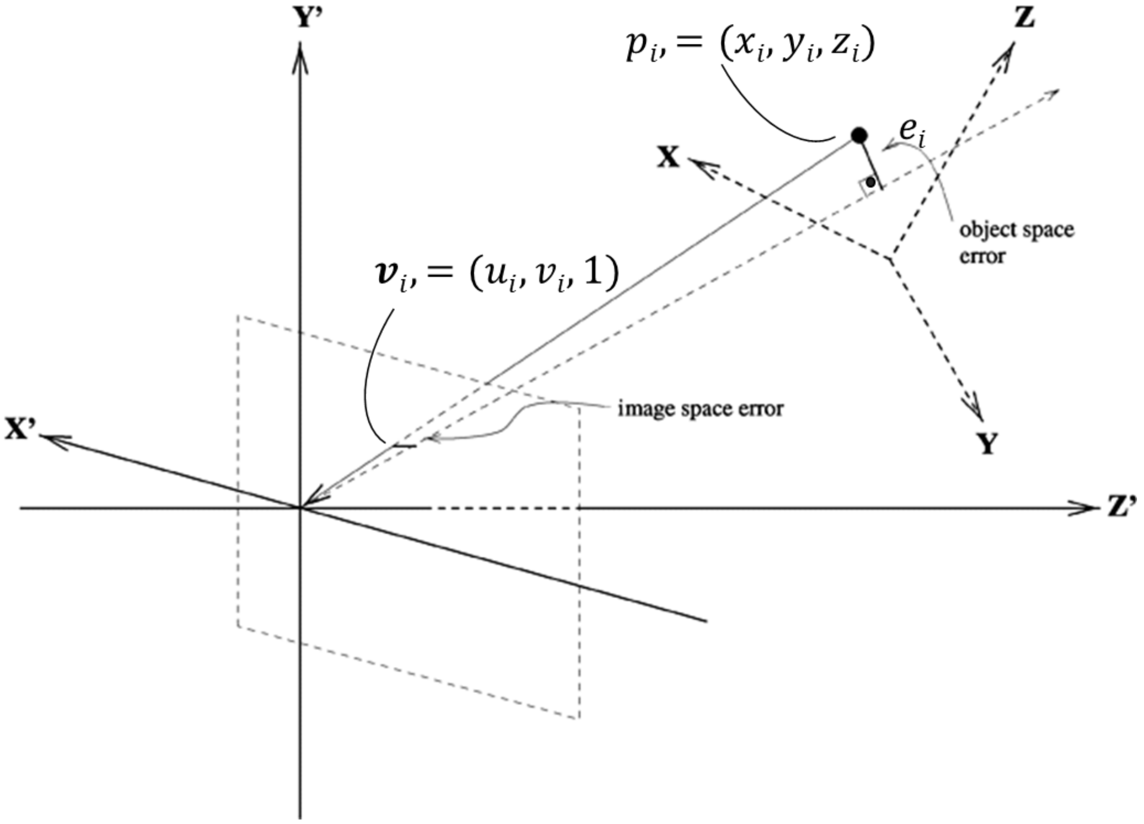

Figure 3.44: LHM image space and object space collinearity error; Source (modified): LHM paper [1]

To minimise the object-space collinearity error e_i, the sum of the smallest error squares of all correspondences, which is defined by:

$$E(R,t) = \sum_{i=1}^{n} ||e_i||^2 = \sum_{i=1}^{n} ||(I - F_i)(Rp_i + t)||^2 \tag{3.88}$$

needs to be performed over R and t. Such an equation can be solved with singular value decomposition (SVD). Therefore, prior to this centroid of both point sets, p_i and q_i need to be calculated by using the equations 3.37 and 3.38. Thus the first initial rotational matrix can be estimated by:

$$M(R) = \sum_{i=1}^{n} q'_i(R) {q'}_i^t \tag{3.89}$$

This is then solved by SVD. After estimating the initial R, the initial t, a function of R, is calculated by:

$$t(R) = \frac{1}{n}(I - \frac{1}{n}\sum_j F_j)^{-1} \sum_j (F_j - I)Rp_j \tag{3.90}$$

Thus the initial R and t are determined. Thereafter the object point p_i needs to be transformed into a camera coordinate by:

$$q_i(R) = F_i(Rp_i + t(R)) \tag{3.91}$$

in order to control/check error value with the equation 3.88. The complete procedure is performed until the error value converges with the given condition and deliver the camera pose or projection matrix.

3.7.4 Results and conclusions

With the same data set, which was used for DLT and robot-based methods, 3D thermography models were created and compared by applying three new PnP methods. Although for the thermography examination each measuring field was measured with several frequencies (see more in section 4), for the accuracy examination only models with 0.4 Hz images were used, because the decisive correspondence data set for the calculation of the projection matrix was the same. In figure 3.45 all three models are illustrated. At a first glance, no noticeable differences between the two iterative (PPnP and LHM) and the non-iterative (EPnP) methods could be recognised. All three methods seem to have achieved a perfect reconstruction. Those wrongly reconstructed dark grey edges (see robot-based method in section 3.6) are also not visible.

Due to the fringed edges an absolute accuracy could not be analysed. Therefore, based on five particularly prominent positions (see figure 3.46), relative accuracy analysis was performed with the models and they were compared to each other. A measuring ruler with 0.5 mm accuracy (for the real component) and CAD function for the 3D thermography model was used to verify the components actual width, which were measured at two prominent positions (see figure 3.46). $\pm 1mm$ deviations could be observed, which should be considered carefully. Furthermore, in all models (see figure 3.45) at the lower edge a tiny dark grey line can be noticed. In order to verify the accuracy, two positions (red-marked circles at positions 1 and 2) along the line were analysed in detail based on surface features which are also visible in the thermal camera. The enlarged 3D thermography model at these positions is illustrated with real images in figure 3.47. Taking into account the tolerable acquisition angle of the real image and the clicked position in CAD, a deviation of <0.5 mm could be determined. The results of this investigation showed no difference among the models and prove reconstruction accuracy within the desired tolerable range of <1 mm.

Three other prominent areas (see the positions 3, 4 and 5 in figure 3.46) were selected for further investigation of the relative transitions accuracy between the image edges. The enlarged images at these positions are illustrated in figure 3.47 and compared with the PnP models as well as with the robot-based method. All models except the EPnP-generated models show no offset to the transition at position 3.

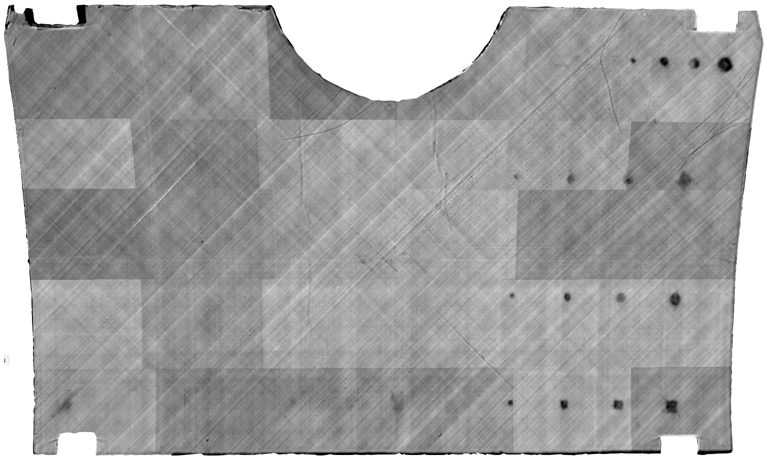

(a)

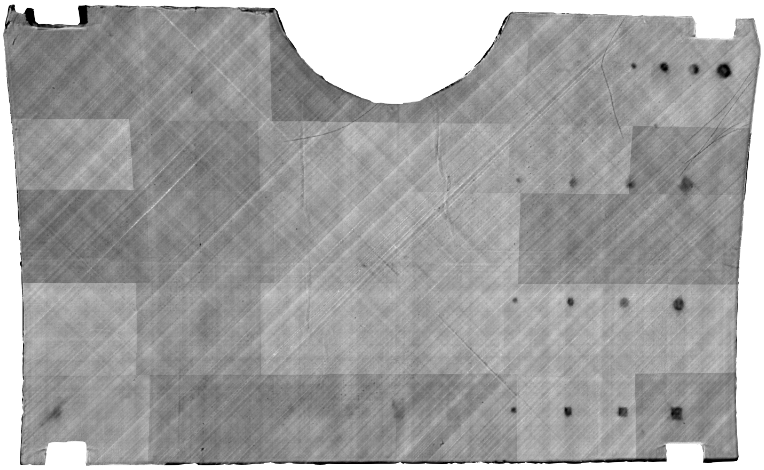

(b)

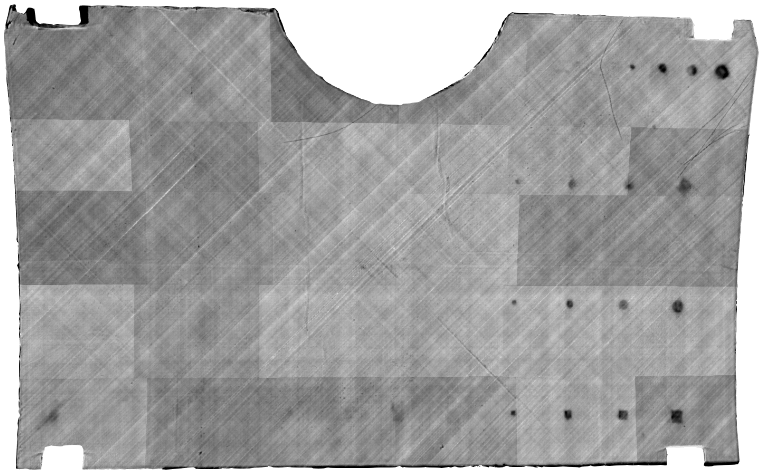

(c)

Figure 3.45: (a)LHM; (b)PPnP; (c)EPnP

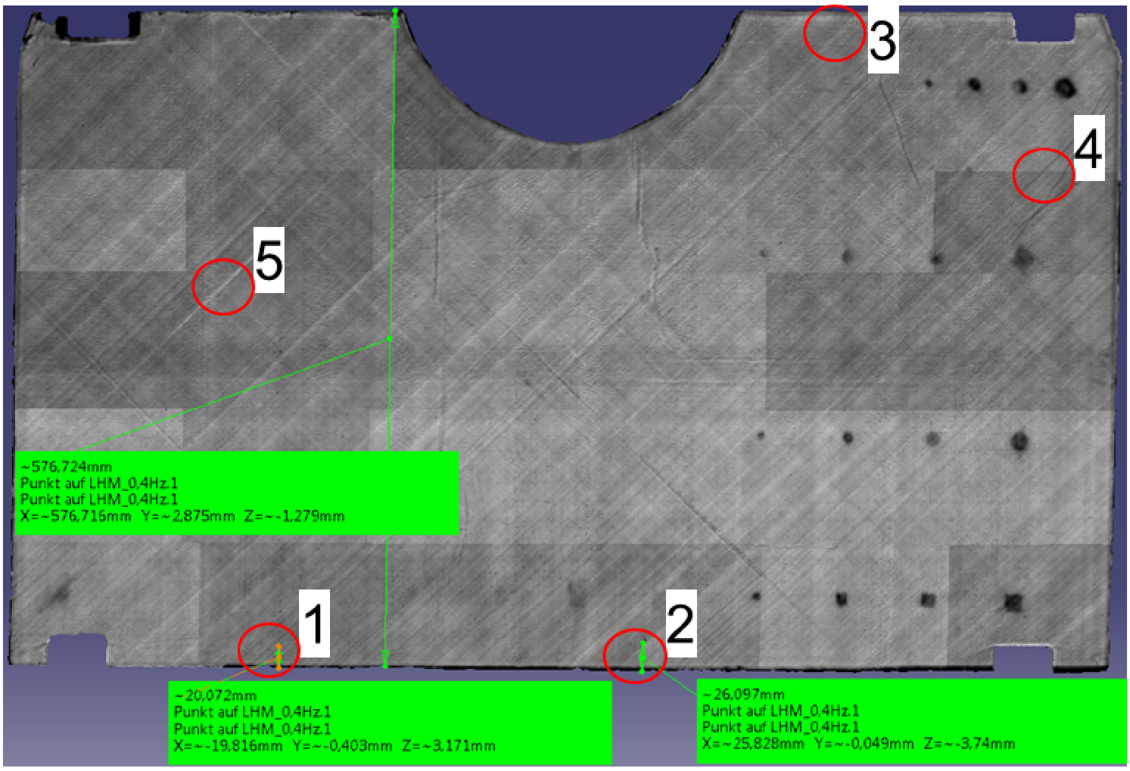

Figure 3.46: Accuracy analysis with LHM model

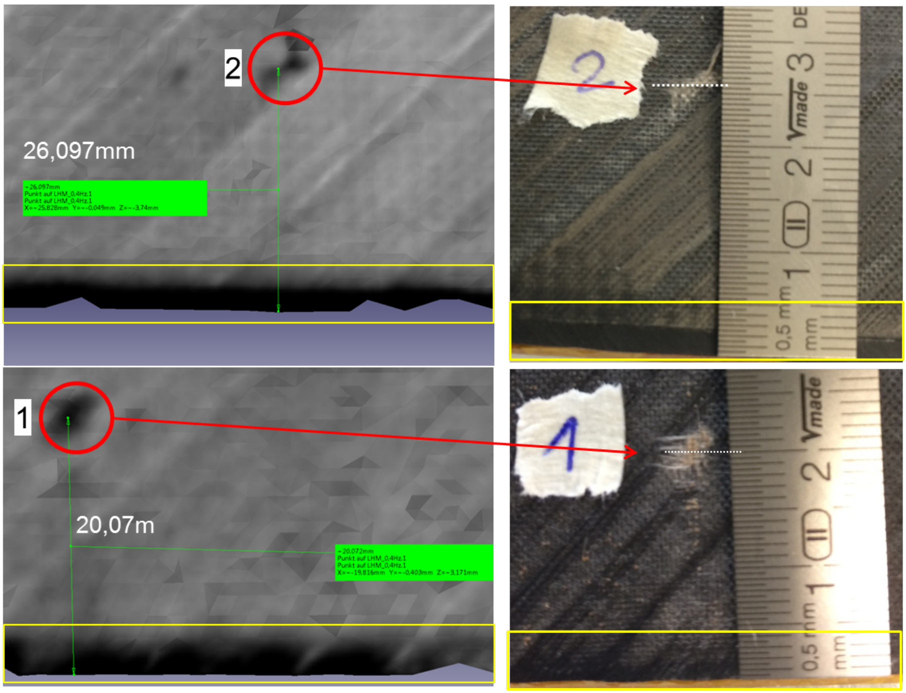

Figure 3.47: Enlarged image: Accuracy analysis with LHM model at positions 1 and 2

In addition the black border in this area looks wider with the EPnP method than with other PnP methods. Of course, in the robot-based variant the edge is even wider than EPnP because of the different base coordinates (see section 3.6). If one compares the structure progression at positions 4 and 5 for all models, a clear difference between the PnP method and the robot-based method can be seen. Namely, the relative accuracy of the robot-based method is much better. Taking into account the inaccurate clicked position in CAD the following deviations (see table 3.4) could be measured. This difference between the robot and PnP method is probably due to the fact that the robot was only moved translatory for all positions with constant orientation to the component. In contrast, with the PnP method, the 3D points were distributed differently for each measurement field. Thus the correspondence data set is different for each measurement field. This leads to slightly different stability of the projection matrix. Thus the relative accuracy of the robot variant is better.

Table 3.4: Relative transitions accuracy of all methods at positions 4 and 5

Methods	Position 4		Position 5	
EPnP	0.5	mm	0.84	mm
LHM	0.65	mm	0.9	mm
PPnP	0.6	mm	0.9	mm
Robot	0.1	mm	0.1	mm

The top views show that the LHM and PPnP solutions are more irregular than the robot solution, but both have yielded identical solutions. The reason for the nearly identical solutions by LHM and PPnP can be explained by a closer examination of the algorithms. It becomes obvious that if the different notations are disregarded, the same relationships are used to determine rotation and translation. With LHM the iterative estimation of the new reference point coordinates in the camera coordinate system is the projection of the previous estimation of the direction vector of the corresponding pixel vectors. PPnP estimates new depths of the pixels. The error to be minimised for both is the distance between the given 3D points in the object coordinate system and the transformed pixels. It was observed, however, that LHM minimises this error about twice as fast as PPnP. In summary, it can be said that the reconstruction quality of both iterative PnP methods is superior to the DLT and EPnP non-iterative methods. Only the relative reconstruction quality generated with robot reference systems is of higher quality. The pose estimates make a regular impression according to the reconstruction quality, whereby the relative accuracy of the PnP method is within the desired tolerance range, namely <1 mm. Since not only the relative but also the absolute accuracy play a decisive role, the absolute accuracy was determined on the basis of a further test series, which is described in section 3.8.

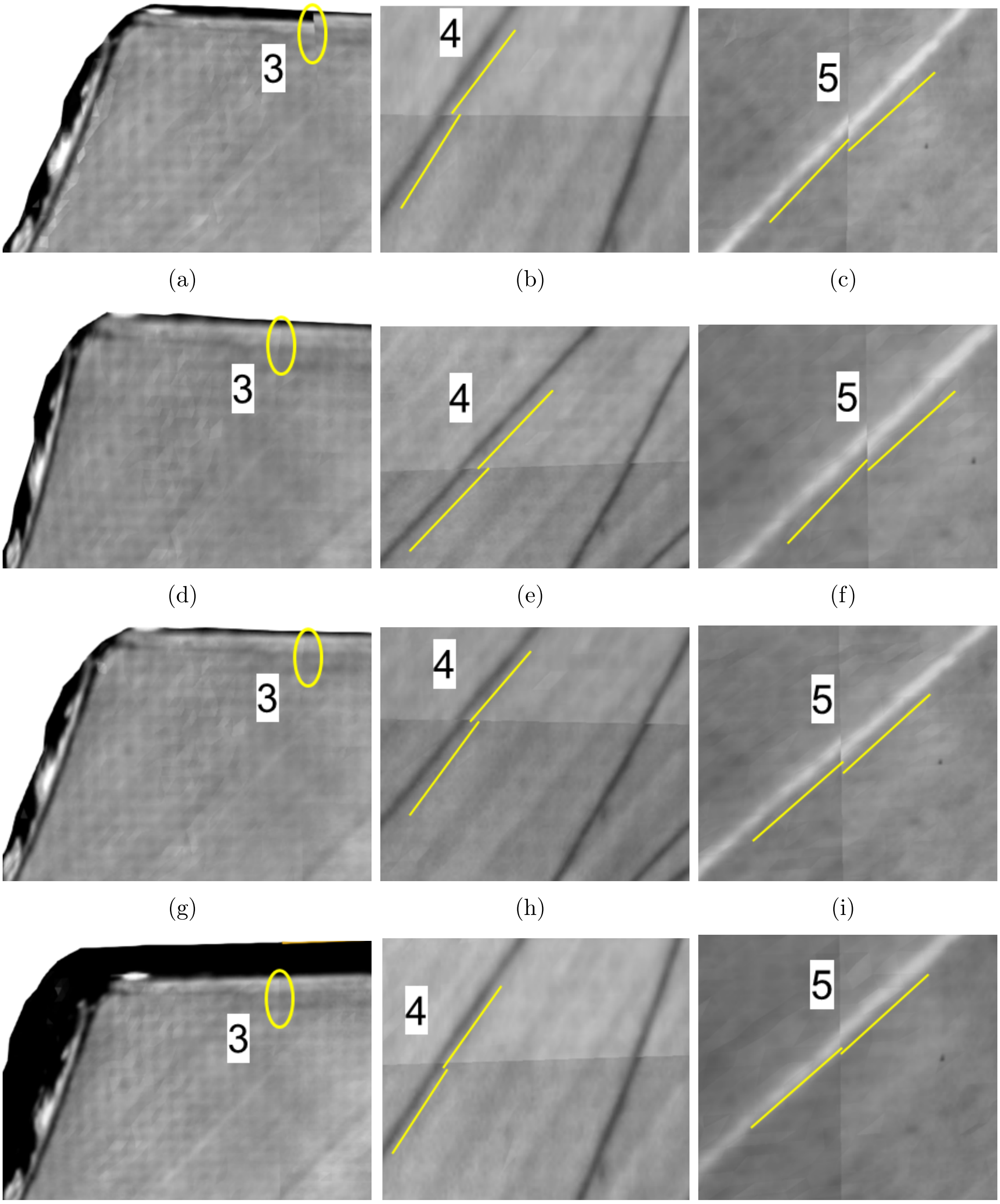

(a) (b) (c)

(d) (e) (f)

(g) (h) (i)

(j) (k) (l)

Figure 3.48: Accuracy analysis enlarged image: (a) EPnP position 3; (b) EPnP position 4; (c) EPnP position 5; (d) LHM position 3; (e) LHM position 4; (f) LHM position 5; (g) PPnP position 3; (h) PPnP position 4; (i) PPnP position 5; (j) Robot position 3; (k) Robot position 4; (l) Robot position 5

3.8 System accuracy evaluation

Finally, both 3D-thermography methods and associated system components need to be evaluated in order to determine the absolute and also relative system accuracy between the two methods. Along with their development phase, in previous chapters 3.5, 3.6 and 3.7, both methods were evaluated individually within the scope of those respective test series. The carbon fibre components, which were used until now for 3D-thermography experiments, had no distinct reference points for an absolute accuracy check and had fringed edges, so that relative accuracy of 3D results were evaluated with only the help of natural surface anomalies. Furthermore, in chapter 2, absolute robot accuracy, and in chapter 3.2, accuracies of laser projection and point detection were discussed. Experiments were conducted in chapter 3.3 for geometric and hand-eye calibration but no evaluation was performed. The robot's absolute accuracy, geometric and hand-eye calibration results are major influencing factors for the noticeably lower accuracy of the robot-based 3D model generation method. Preliminary investigations and system validation in [85] showed that the robot's PTP and LIN movement with override, accurate end-effector load data and the robot's motor temperate increment due to its continuous movement are key parameters for system stability. Therefore, for the complete evaluation of systems, robot movements were generated such a way that the robot itself does not cause any additional errors. Since better results were achieved so far with the point-based 3D method, this evaluation experiment focuses on the robot-based 3D thermography method.

3.8.1 Absolute robot accuracy

To determine absolute robot accuracy without a mounted end-effector at flange, numerous experiments were conducted. Experiment results in [86] have shown that the absolute accuracy decreases with increasing distance from the measured base coordinate. The author of [87] compared the automated TCP measurement process of an end-effector with the manual TCP measurement process. All the experiments were repeated several times, and the results showed that manually determined TCP error value varied between 0.2 and 0.8 due to human influence. Analysing absolute robot accuracy with the mounted thermography end-effector is more complex than without it. Figure 3.49 represents the concept for absolute robot accuracy evaluation as well as for hand-eye calibration. The essential element for this experiment is multi-sided-probe (MSP)[2], which tracks with a Leica laser tracker and delivers 6D absolute position information instead of the 3D information with T-probe. MSP offer the advantage that the robot position can be measured more easily and precisely than with the T-probe measurement. Figure 3.51 shows the mounted MSP with the thermography end-effector at the flange. By measuring the reflector position with

---

[2] MSP is a construction for Leica T-mac and two additional faces for 6D measurement

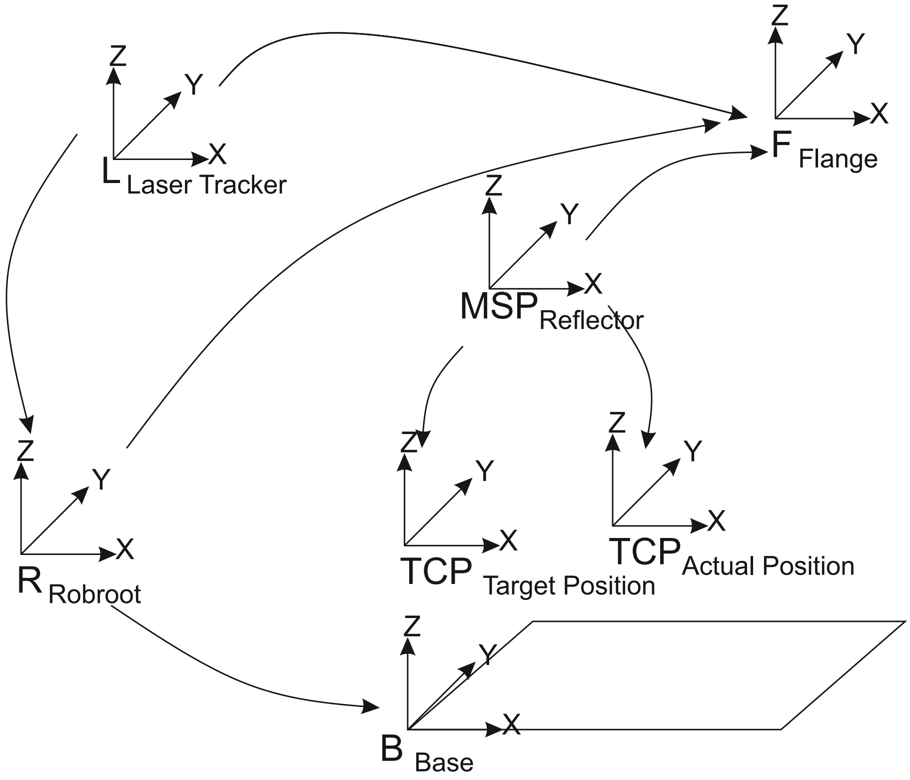

Figure 3.49: Evaluation concept for hand-eye calibration and absolute robot accuracy

the laser tracker, the difference between the robot's target and its actual position can be determined. Therefore, a coordinate relationship between the MSP and the laser tracker was created by best-fit transformation, which was performed by using the Robcal program with randomly-chosen 12 taught robot positions and measured MSP (see Figure 3.50) reflector positions. Robcal delivers 6D coordinate transformation data first between $\mathrm{MSP}_{\mathrm{reflector}}$ and $\mathrm{F}_{\mathrm{flange}}$ (Table 3.5) and secondly between $\mathrm{R}_{\mathrm{rob\text{-}root}}$ and $\mathrm{L}_{\mathrm{laser\ tracker}}$(Table 3.6). Through repeated experimentation with the actual end-effector's load data a 0.24 best-fit transformation error was ascertained compare to 0.42 without it. The actual load data (see Table 3.7), which is essential for better absolute accuracy, was determined with the load detection function provided by KUKA. The smaller error indicate better absolute position accuracy between calculated software data (target position) and actual position data (where the robot is). All this calculated coordinate transformation data was entered in *Spatial Analyser* for further data acquisition and analysis. Furthermore Virtual Tip, as a measuring instrument, was configured with Leica Tracker Pilot software. Virtual Tip, which is determined for now in CAD, contains static coordinate transformation data between $\mathrm{MSP}_{\mathrm{reflector}}$ and $\mathrm{TCP}_{\mathrm{camera}}$. This is necessary for determining hand-eye calibration accuracy. The static coordination transformation data may vary with experimental results in section 3.8.2 and will be updated in that case. After the

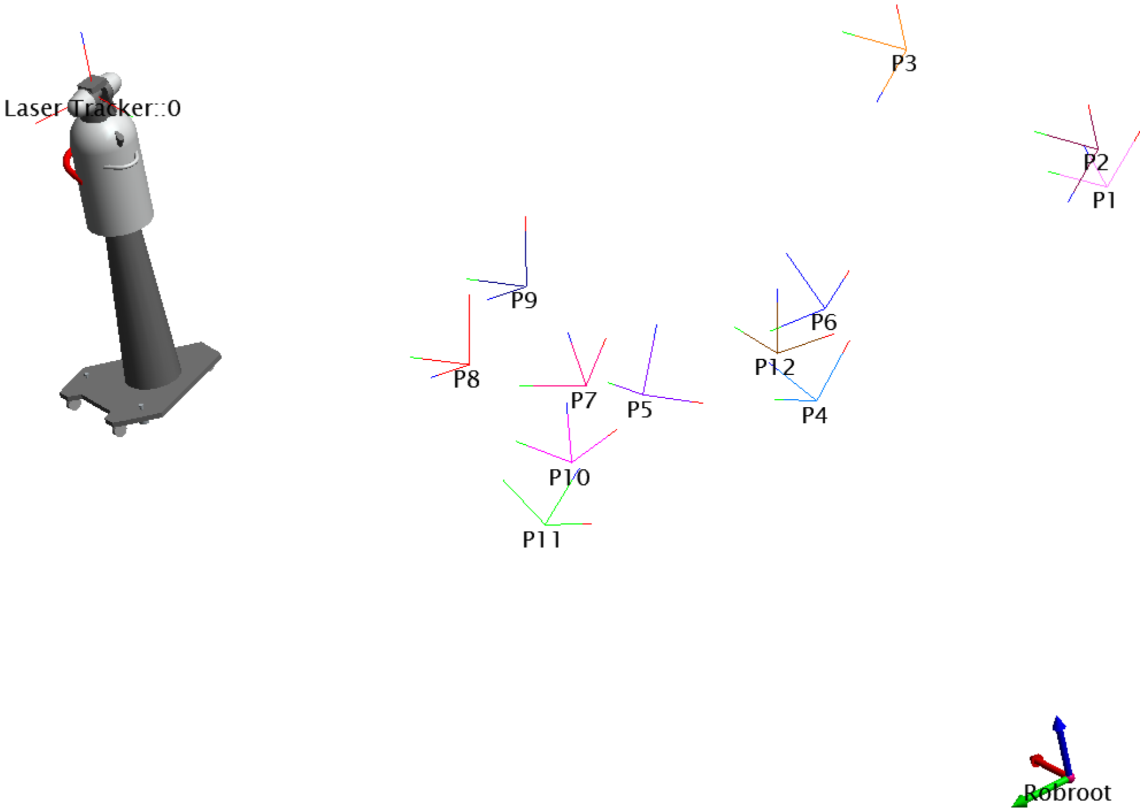

Figure 3.50: Measured MSP reflector Positions for best-fit transformation

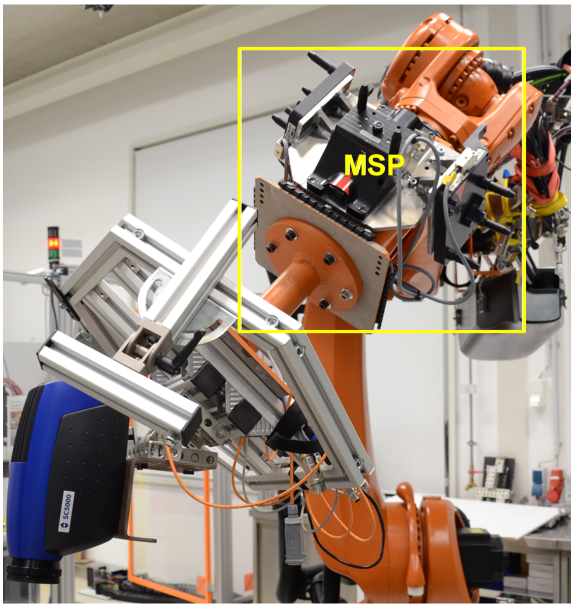

Figure 3.51: MSP with thermography end-effector

Table 3.5: Coordinate Transformation between $\mathrm{MSP}_{\mathrm{reflector}}$ and $\mathrm{F}_{\mathrm{flange}}$

Translation			Orientation	
X	210.122	mm	A	-89.990 °
Y	0.231	mm	B	0.141 °
Z	164.188	mm	C	-89.929 °

Table 3.6: Coordinate Transformation between $\mathrm{R}_{\mathrm{rob\text{-}root}}$ and $\mathrm{F}_{\mathrm{laser\ tracker}}$

Translation			Orientation	
X	5409.473	mm	A	-0.5448 °
Y	239.9946	mm	B	0.045 °
Z	1063.8829	mm	C	88.3478 °

Table 3.7: Load data of thermography end-effector

Mass	M	74.317	kg
Centre of mass			
	X	0.282	mm
	Y	0.152	mm
	Z	271.489	mm
Orientation of mass			
	A	24.578 °	
	B	89.996 °	
	C	114.578 °	
Moment of Inertia			
	J_X	3.0	$\mathrm{kg.m^2}$
	J_Y	6.943,0	$\mathrm{kg.m^2}$
	J_Z	8.181	$\mathrm{kg.m^2}$

experimental setup was ready, a small carbon fibre plate was placed in two different positions (see Figure 3.52 and see corresponding data set in Table 3.8) to determine the robot's absolute accuracy. Base position 2 was selected in ISO-CUBE range to achieve better accuracy and base position 1 was selected outside of ISO-CUBE range, where the plate was moved on the X axis much more than the two other axes with slightly orientation changes. It shall be examined how the robot behaves inside and outside of ISO-CUBE range. The base positions were entered in *Fastsurf* to generate an offline robot program. The [85] thesis had extensively investigated the influence of override function on accuracy with a combination of PTP and LIN movement at 2 m/s velocity in automatic mode. For that autonomous application, 30% override with 2 m/s velocity is recommended. Furthermore, the author suggests more detailed analysis with a 100% override function and indicates other results for different applications. The author has also observed better absolute accuracy with

100% override and 0.6 m/s travelling speed. Therefore the offline robot program was generated with 0.8 m/s velocity and 100% override, to avoid override influence. With an LIN movement in T1[3] mode, the robot was positioned above 550 mm in Z direction to respective base position. Thereafter, the actual $\text{MSP}_{\text{reflector}}$ position was measured with a laser tracker and compared with the target position, or rather with offline program data. Transformations deviation in both positions are presented in (Table 3.9). Base position 1, which is outside of ISO-CUBE range, shows, especially in Z axis, a maximum of 1.597 mm deviation compared to -0.543 mm in base position 2. Also, the values 0.569 mm in X and 0.15 mm in Y direction of base position 2 shows that absolute accuracy decreases outside of ISO-CUBE range, or rather with the increasing distance from $\text{R}_{\text{rob-root}}$. Both absolute and relative deviation in orientation is comparatively smaller than position deviation. But due to the working distance of camera TCP (in this case 550 mm), there is considerable optical leverage, which causes 0.547 mm position deviation for the maximum angle deviation of 0.057°(base 1 angle C). The following applies:

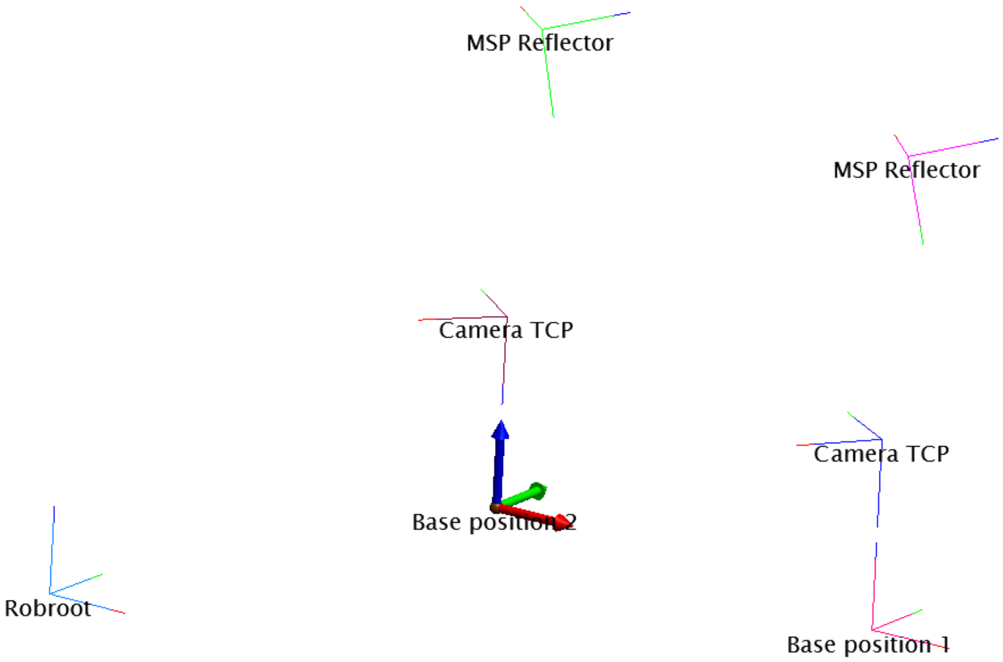

Figure 3.52: Absolute position accuracy check in two different positions

$$\Delta r = tan \Delta\phi \, h \tag{3.92}$$

$$\Delta\phi = 0.057°, h = 550 \, mm \Rightarrow \Delta r \approx 0.547 \, mm \tag{3.93}$$

---

[3] T1 Test mode, Manual Reduced Velocity ($\leqslant$ 250 mm/s)

Table 3.8: Measured two base positions for absolute robot accuracy check

Base position1					Base position2				
X	2771.192	mm	A	1.749 °	X	1371.	mm	A	1.593 °
Y	-74.451	mm	B	-0.191 °	Y	129.957	mm	B	0.075 °
Z	520.756	mm	C	0.05 °	Z	520.486	mm	C	0.006 °

Table 3.9: Absolute position deviation measured with $\mathrm{MSP}_{\mathrm{reflector}}$

Base position1					Base position2				
X	0.5699	mm	A	0.032 °	X	0.1777	mm	A	-0.036 °
Y	0.158	mm	B	-0.04 °	Y	-0.063	mm	B	-0.047 °
Z	1.597	mm	C	-0.057 °	Z	-0.543	mm	C	0.017 °

It must be noted that the deviation was measured in *Spatial Analyser*, where a best-fit transformation error for the creation of a common coordinate was 0.24. Furthermore, the deviation values will change with a different robot or additional external axes, as mentioned in the previous chapter. It is to be expected, that the deviation value will get worse, as the robot used for this experiment was a high-precision robot without any external axis. Neither any other investigation nor any further improvement measures were carried out, as similar results were also achieved in the preliminary investigation in chapter 2. Therefore further experiments were continued with geometric and hand-eye calibration.

3.8.2 Geometric and hand-eye calibration accuracy

Geometric calibration analysis

Geometric and hand-eye calibration method and procedure were already described in Chapter 3.4 as well as in [62] and [56]. Especially the accuracy of geometric calibration was examined in [56] and shows ±0.25 pixel re-projection error. A detailed analysis of geometric thermography camera calibration for both lenses (wide-angle lens with 12 mm focal length and normal lens with 27 mm focal length) was presented and discussed. The hand-eye calibration accuracy was investigated in [61]. The experiment in paper [61] was performed with only a wide-angle lens and was analysed to see weather there is any influence of the robot pose while talking pictures with the robot. The robot's actual position (provided by KUKA software), which may have differed from the target position was taken to calculate HEC. Paper [61] has claimed a max. 0.22 mm translational and 0.03° rotational standard deviation of repeatability accuracy. However, a maximum magnitude pointing error was 1.052°, which was caused by the cable carrier. This pointing error had considerable influence in X and Y directions. Furthermore, the author has mentioned the possible influence of robot velocity. The achieved hand-eye accuracy for a 400 mm working distance was 10.31 mm and 2.87 mm. The author has emphasized poor absolute accuracy caused by the cable carrier as the main reason for such error. In paper [23] the hand-eye calibration results with a normal lens are presented. But no accuracy analysis was performed, as the experiment was focused on the development of robot-based 3D thermography. A ±0.15 pixel re-projection error from geometric calibration was achieved. Therefore, a further experiment was conducted. The aim of the experiment was to find out whether there is any influence from the cable carrier at all and how much this affects absolute accuracy at the measuring position. During the experiment, the cable carrier was disassembled from axis 6 and wrapped around axis 3 in the hope of achieving a better result than before. As a consequence, the cable-carrier effect could be avoided. The experimental setup with MSP (see in section 3.8.1) was applied to determine the accuracy of both calibrations. In general, intrinsic camera parameters were independent of the position and orientation of the camera. The *Matlab* camera calibration toolbox, mostly based on Zhang's model, calculated the intrinsic parameter by using a pinhole camera model. Since the principal point was directly connected to the projection centre (for the pinhole model), the exterior and interior orientations are highly correlated. This means that the extrinsic camera parameters are independent of the intrinsic parameters [88]. The authors of conference paper [89] and Lai [90] devoted experiments to finding linear dependency between extrinsic and intrinsic parameters. Although a paper [61] claims a shifted camera TCP due to robot inaccuracy, there is now a strong assumption that this shifted camera TCP is the calculated principal point. The presented intrinsic camera matrix in equation 3.55 represents a very general optical model, which for the modern camera is often not necessary or recommended, as lenses are manufactured and assembled with less imperfection in centring.

The experiment in this work was started with a geometric calibration with a normal lens (27 mm focal length) for 550 mm working distance. To test this assumption two geometric camera calibrations with the *Matlab* toolbox were performed with two different sets of 10 thermography amplitude images. Images were taken from the same positions. In general, there are three different kinds of distortions, radial distortion, dicentric distortion and thin prism distortion. Both dicentric and prism distortions contain radial and tangential distortion coefficients [91].

As the first two radial coefficients in figure 3.53 are predominant, the default values in the *Matlab* calibration toolbox were changed for skew (i.e. $\text{alpha}_c\!=\!0$), and, the last three radial tangential coefficients ($kc(3)=0$, $kc(4)=0$ and $kc(5)=0$) for the first geometric calibration experiment. This model is also used by Zhang [55]. It is assumed that pixels are rectangular in a 27 mm lens, which has no 4th-order radial and tangential distortions. The results, once with assumed-distortion coefficients with the default setting and once without it, are shown in Tables 3.10 and 3.11 respectively. Comparing both tables, one can see that both tangential and skew coefficients are also almost zero with the default setting (without changing distortions coefficient). This means that the assumptions were correct. The differences between the calibration parameter achieved in chapter 3.4 and the parameter here are extraordi-

Table 3.10: Intrinsic camera matrix with changed distortion coefficients

Focal Length (f_c):	[1962.02836 1962.02836] ± [17.34006 17.34006]
Principal point (cc):	[315.60483 222.51200] ± [5.69753 4.96031]
Skew (α_c):	[0.00000] ± [0.00000]
	angle of pixel axis = 90.00 ± 0.00 degrees
Distortion (K_c):	[-0.19156 -3.89772 0.000 0.000 0.000] ±
	[0.03736 1.16882 0.000 0.000 0.000]
Pixel error(err):	[0.12853 0.11233]

Table 3.11: Intrinsic camera matrix without changing distortion coefficients

Focal Length (f_c):	[1981.79812 1979.75644] ± [16.86725 16.78202]
Principal point (cc):	[316.25993 225.41139] ± [5.34492 4.60791]
Skew (α_c):	[-0.00020] ± [0.00016]
	angle of pixel axis = 90.011 ± 0.009 degrees
Distortion (K_c):	[-0.20327 -4.20002 0.00092 0.00009 0.00000] ±
	[0.03558 1.15174 0.00051 0.00044 0.00000]
Pixel error(err):	[0.11801 0.10161]

Table 3.12: Hand-eye calibration results without changed distortions coefficients

X	17.430544	mm	A	150.535057 °
Y	33.045886	mm	B	0.015125 °
Z	956.868366	mm	C	-35.726906 °

narily small. These little variations of intrinsic parameters are influenced on the one hand by using a different calibration pattern size and on the other by a motorised lens, which is the part of a thermography camera that to adjusts image sharpness according to working distance. Since skew coefficient zero was set, the aspect ratio $f_c(1)/f_c(2)$ has become 1. This means that the focal length in X and Y directions are same in table 3.10. It should be noted that the radial distortions coefficient is highly correlated with focal length, as radial distortion is a function of focal length. Therefore different focal length values can be observed between these two tables. The re-projection error with changed distortions coefficients is 0.01 pixel worse than without it. The result is in tolerance range and leads to an unmeasurable small influence in 3D thermography, and therefore can be ignored. The reference point or coordinate origin is the principal point of the camera model, ideally exactly at the beam centre. But both calibration results show a shifted principal point from the beam centre, which is examined more closely in the hand-eye calibration analysis. Furthermore, 0.6559 and 2.899 pixel differences can be observed in Tables 3.10 and 3.11 at principal point cc(1) and cc(2) respectively. Depending on the orientation of the epipolar lines, the calibration matrix may shift the images in horizontal and vertical directions [92]. Furthermore, J. Tardif and P. Sturm [93] have published a paper about the influence of singular and non-singular distortion centres, which are highly correlated with the optical centre. It could be verified that the geometric calibration is satisfactory with a 0.1 pixel error (see tables 3.10 and 3.11).

Hand-eye calibration analysis

Hand-eye calibration was continued with geometric calibration parameters, which were generated with default values (with the 2nd order of radial and tangential coefficient). Although the radial component of lens distortion is predominant, it is coupled with the tangential one. Therefore measuring image distortion with radial distortion without considering the tangential part is not enough and requires a new calibration. In addition to that, tangential coefficients are almost zero (in our experiment). Hence a further experiment was conducted with both distortions coefficient to generate 3D thermography results, which was also the case for previous 3D thermography results. The experiment was to analyse why TCP is shifted from the beam centre, as claimed in paper [61]. Therefore the same pattern, experimental and camera setup were used, as with geometric calibration. Procedures were already explained in chapter 3.4.2. Results are presented in table 3.12. According to the pinhole camera model for the ideal case, the 3D position of a spot on the plane is derived via the principal of intersection of a line and a plane in 3D space. Derived from Zhang's camera model, it can be assumed that the calculated camera TCP lies on the principal point. Therefore the calculated hand-eye calibration result (new TCP) was entered in the KUKA software and parallelly an offline robot program was generated with it. With this program, the robot was moved such a way that the TCP was perpendicular to the calibration pattern base centre at a distance of 550 mm in z direction. At this position one live image was saved to analyse the image centre relative to the TCP position and a second amplitude image was taken to analyse weather the TCP position was tilted towards the pattern base. According to detector size, the image has 640 x 512 pixels, so that the image centre is at 340 x 256 pixels, beginning from the upper left of the image. In an ideal experimental result, the image centre and pattern base position will be congruent. By analysing figure 3.53 (a) one can observe that the image centre is shifted from the pattern base position. But the principal point is close to the pattern base position. By enlarging the image and comparing it with the principal point in table 3.11 is easily recognisable in 3.53(b) that the calculated TCP is at the principal point, which is close to the pattern base. It should be note that the line was drawn on the live image manually and the pattern base was also measured with the robot manually. In addition to that, the robot's actual position differs from the target position. These are the main reasons why the principal point is not exact at the pattern base position. This proved that the calculated TCP is not randomly offset from the centre of the image, but always at the principal point. The Amplitude image was analysed with the toolbox implemented in *Matlab* tool box by C. Frommel.

This toolbox calculates the amplitude image of all centres of black circles, and fits

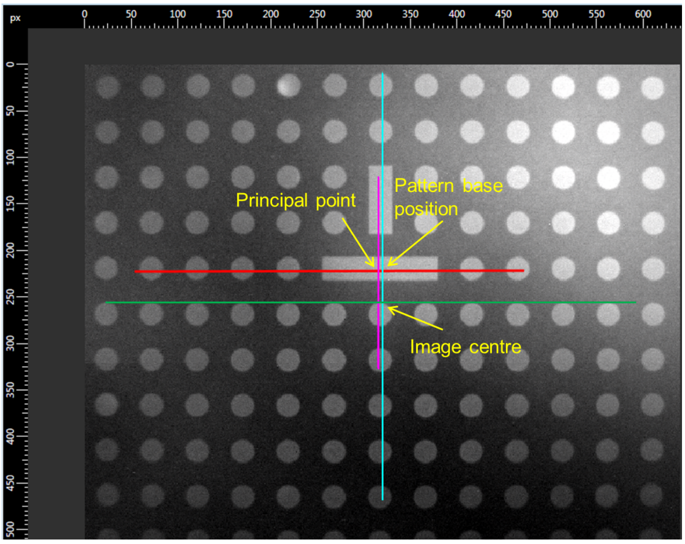

(a) Live thermography image of pattern

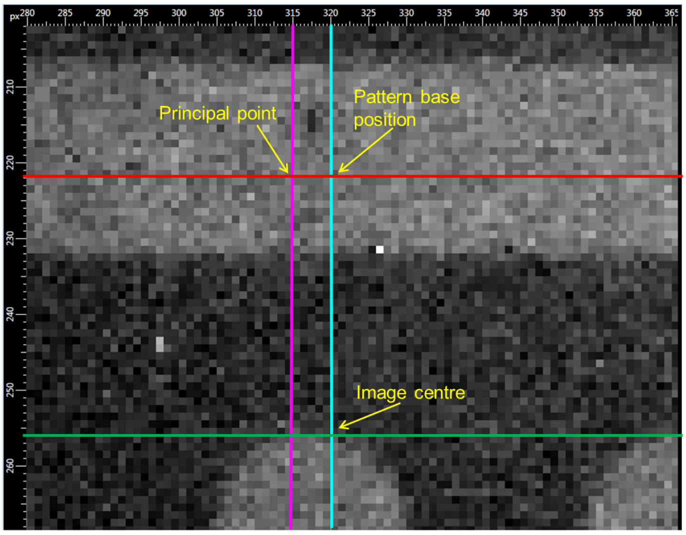

(b) Elargement of left image

Figure 3.53: TCP accuracy analysis related to Principal point

rectangular lines through the circle centre and connects them to each other. In an ideal case, the angle between two connected lines will be 90 °. The presented figure 3.54 shows small deviations in all four angles. The experiment was repeated by means of capturing the amplitude image with different modulation frequencies and amplitude performance. It could be observed that the diameters of the black circles were changing according to heating processes, which led to deviations in the calculated angles. In table 3.13 angle deviations are presented. The average angle deviation is -0.034 ° in upper left, -0.11 ° in upper right, -0.12 ° in lower left, -

0.13 ° in lower right. But according to equation 3.92 the pointing error for a 550 mm working distance and a 0.13 °average TCP tilt angle, will be 1.24 mm. As these deviations are extraordinary small and within the measurement equipment tolerance range, it is difficult to identify the absolute tilt angle of TCP. Therefore 3D thermography accuracy analysis was continued with these calculated geometric and hand-eye calibration data.

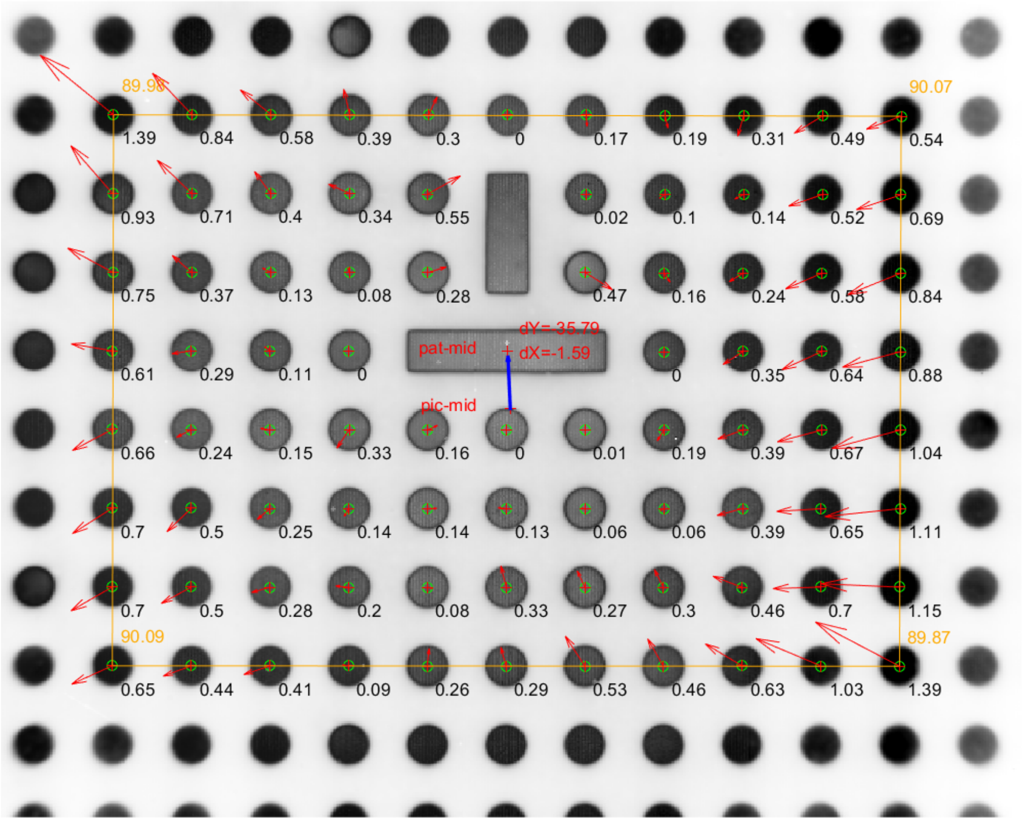

Figure 3.54: Validation of hand-eye Calibration

Table 3.13: Validation of hand-eye Calibration

Upper left	Upper right	Lower left	Lower right
-0.02 °	+0.07 °	+0.09 °	-0.13 °
-0.15 °	+0.28 °	+0.09 °	-0.12 °
-0.14 °	+0.14 °	+0.13 °	-0.15 °
+0.13 °	+0.13 °	+0.14 °	-0.16 °
+0.01 °	-0.05 °	+0.16 °	-0.11 °

3.8.3 3D thermography accuracy

In this subsection, 3D thermography accuracy will be analysed with both developed methods. Although relative comparisons of these to methods were carried out in sections 3.6 and 3.7, the new experiment was conducted for absolute comparison on the one hand and for better relative comparison on the other. Due to the lack of reference points and frayed component edges, it was difficult to make a comparison in sections 3.6 and 3.7. For this reason, a component with sharp edges was selected for the new test and three reference points were chipped with a peening tool. For relative accuracy analysis between two 3D thermography methods, lines were drawn on the component's surface, which had a different thermal contrast than the component itself (see figure 3.56 (c)). In an ideal case, after image stitching, any offset should occur between two connected lines. Moreover, due to the small size of the component, the component should be placed somewhere within the robotic cell in order to investigate the influence of the specific reach of the robot. Thus the component was fixed on an additional plate with six target plates (see figure 3.56 (c)), so that only base measurement is necessary for a new robot position. Normally a single base is measured for a component, no matter how large the component. Robot inaccuracy increases with the distance from the base. Since the component for this experiment was very small, and 3 new base positions were measured after the component was moved, the robot's absolute inaccuracy should be lower. After assembling the component, the positions of all six reflectors on target plates and three reference points (see figure 3.56 (b)) were measured with T-scan, and, the

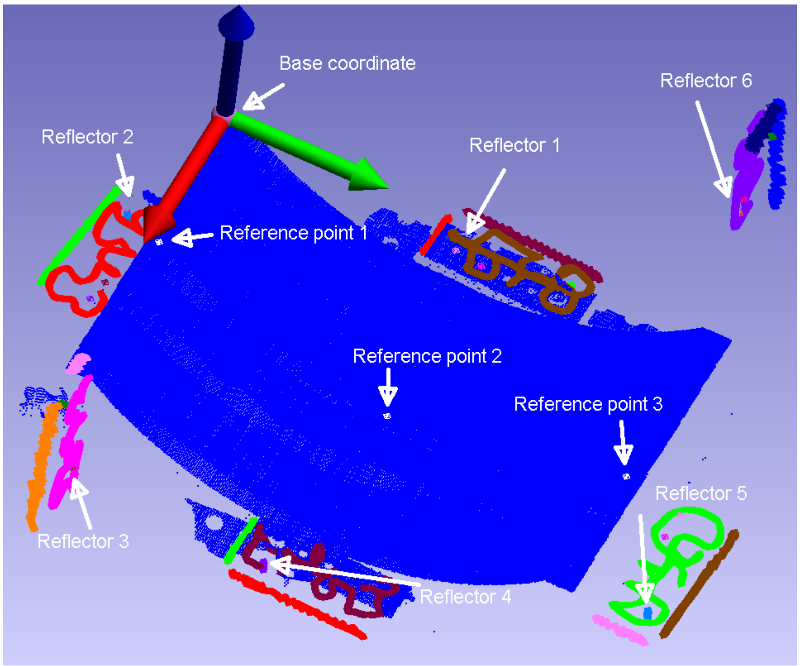

Figure 3.55: Measured point clouds with T-SCAN

point cloud was generated with 0.1 mm point distance (see figure 3.55). From this point cloud a 3D Mesh with 0.5 mm vertex size, calibration data for laser projector and 3D corresponding points for 3D thermography were generated in *Catia*. Afterwards the component was placed in three different positions (see figure 3.57) in the robotic cell. All bases were measured by the robot and a robot program was created with OLP for each base. Individual base measurement errors were for base one 0.25, base two 0.42 and for base three 0.35. The calibration error of the laser projector for this experiment was 0.12. The projecting distance was approx. 3.2 m. Base positions two and three were chosen such a way that the robot had to stretch to its maximum and the laser projector had to project by using its maximum opening angle. Base position one was in ISO-CUBE range. It was expected that the projecting error in the 3D model would be small in base one. In total 6 images were captured for each base position to measure the full component. All developed PnP methods and robot-based methods were applied to generate the 3D thermography model. 3D models which were generated only with the PPnP and robot-based methods are illustrated in figure 3.58. Due to the higher component's curvature, any measurable deviation between the non-linear PnP and linear PnP method could be determined, as it was the case for almost planar surface in chapter 3.7. On the other hand, a clear difference could be ascertained between the robot-based method and the PnP method. In this chapter, for example the PPnP-based 3D model was analysed with the robot-based 3D model. While observing the robot-based model in figure 3.59(a), a non-collinear line between image positions 1 and 6 stands out. The lines are 1.56 mm apart at this position. On closer inspection in figure 3.59(b), a white border with a black spot becomes visible. Since the component structure does not change at this point, the thermal property should not change either. By comparison with the original image it becomes obvious that the white border and black spot do not belong to the component. The 3D model error at this edge lies between 1.21 mm and 1.54 mm. The same analysis with the PPnP model (see figure 3.60) shows no white border at this edge. The connected drawn lines at the stitching position between images shows 0.12 mm average error for PPnP method. In contrast the robot-based model is slightly better except for one position.

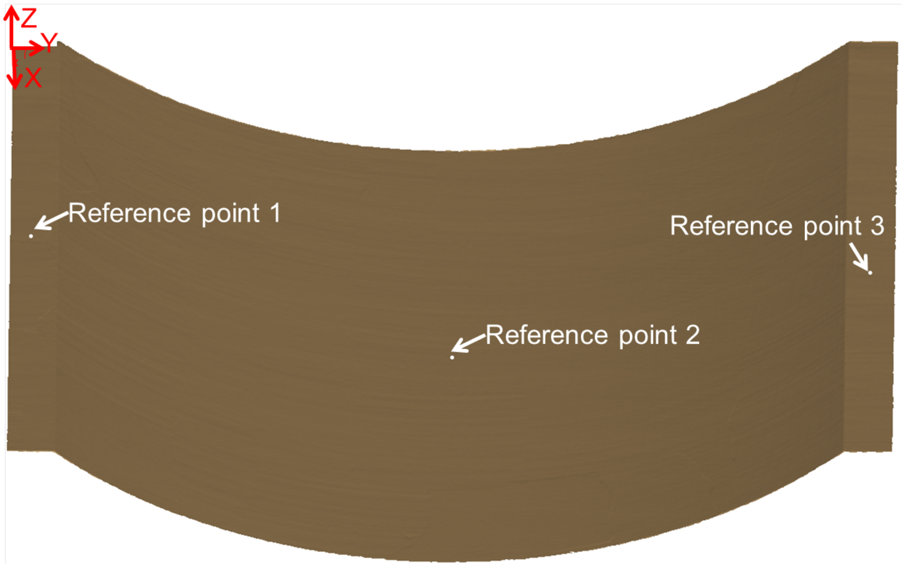

(a)

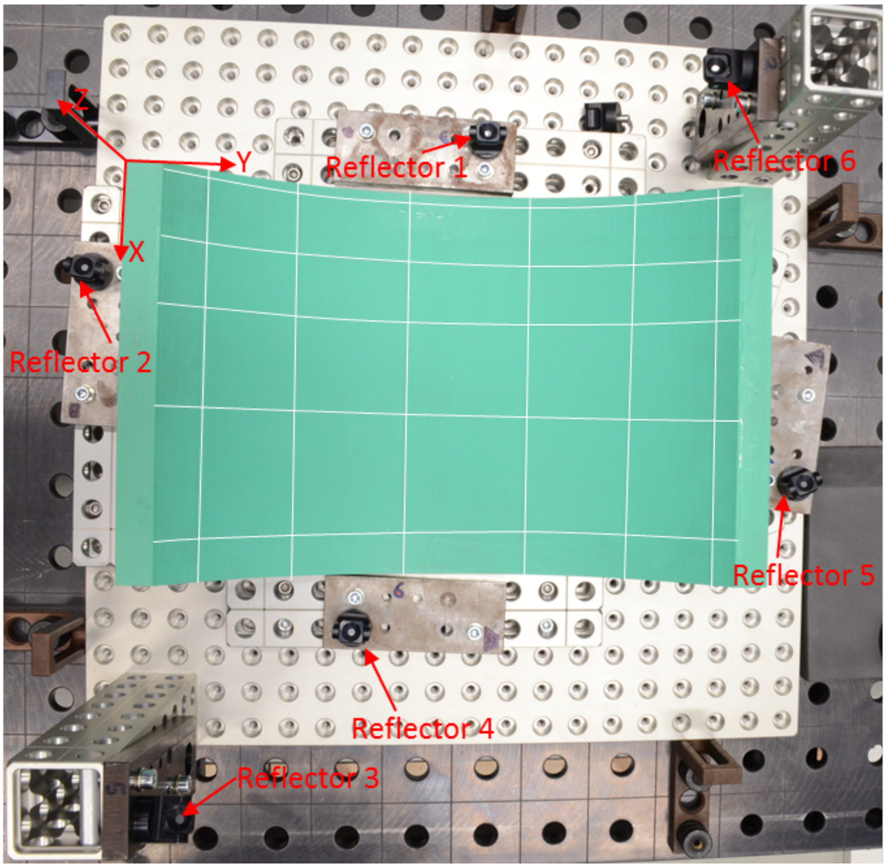

(b)

Figure 3.56: (a) Reference points and 3D Mesh generated from point clouds; (b) Drawn control lines on assembled component for relative accuracy analysis

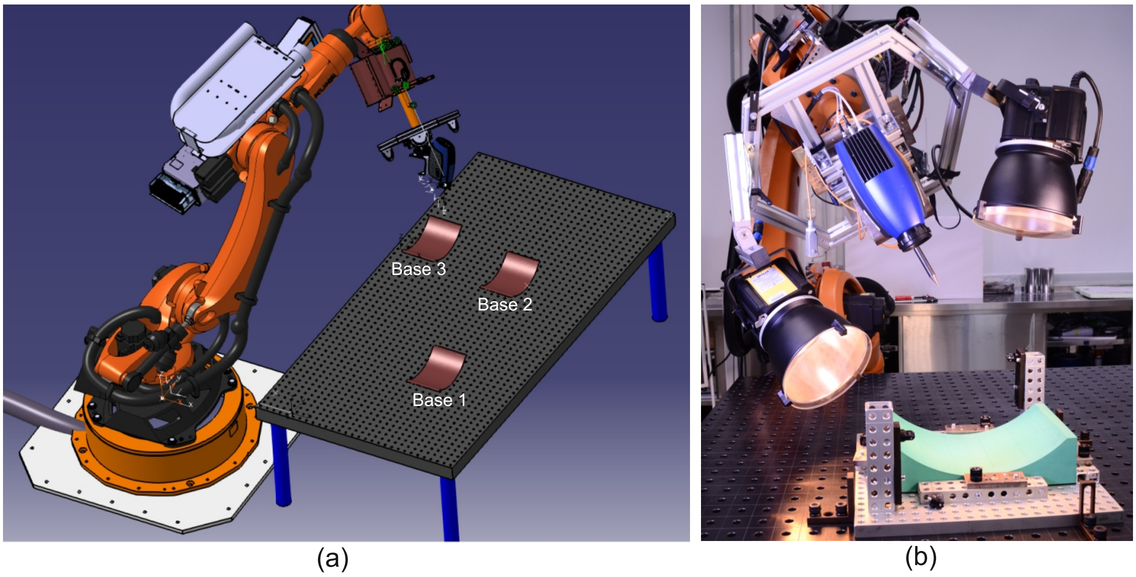

Figure 3.57: (a)Three different base positions; (b) Experimental setup at base position one

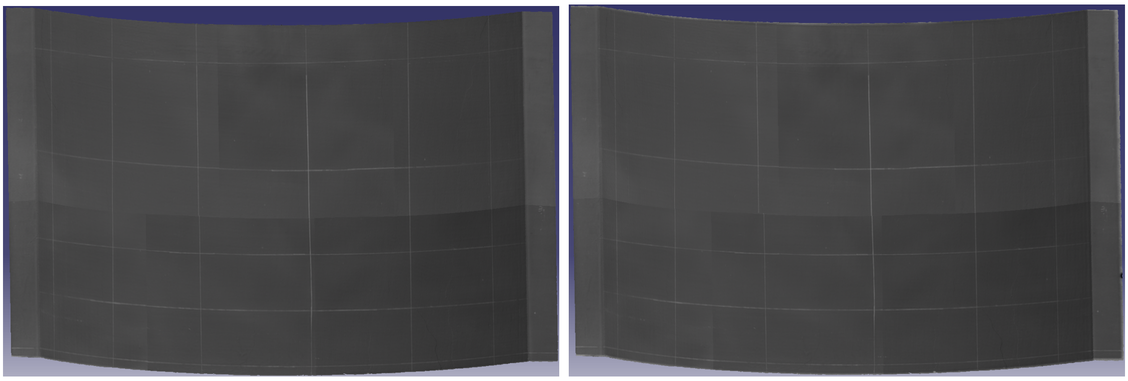

(a)

(b)

Figure 3.58: At base position 3:(a) 3D thermography model generated with PPnP method; (b) 3D thermography model generated with robot-based method

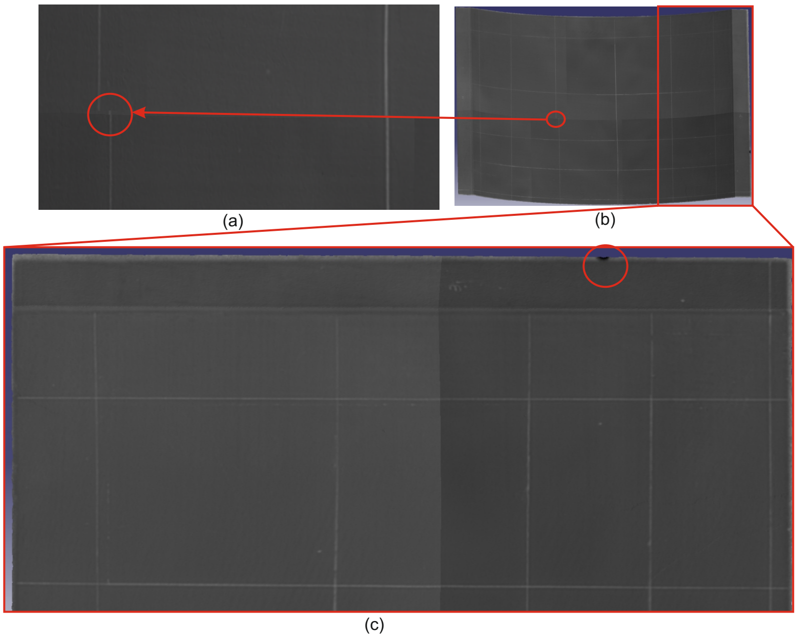

Figure 3.59: Enlarged robot-based 3D model

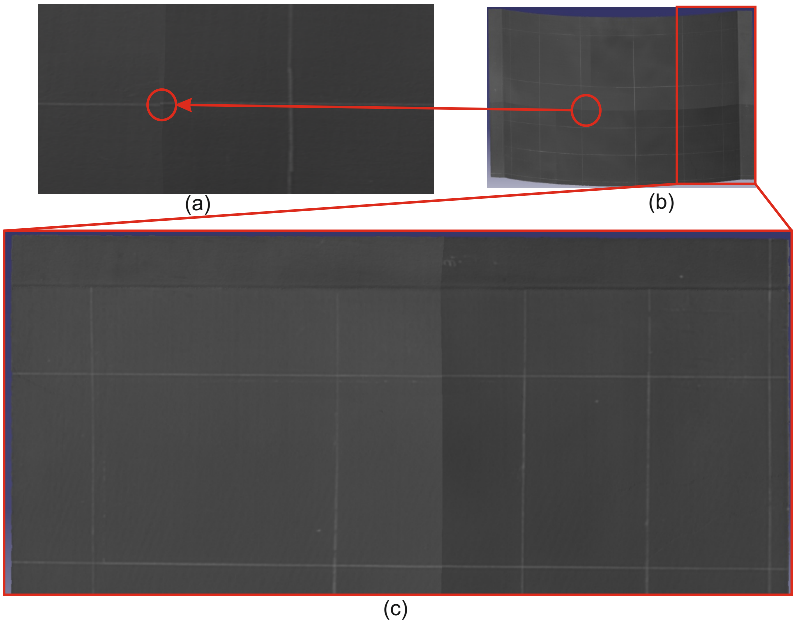

Figure 3.60: Enlarged PPnP based 3D model

A further absolute accuracy analysis was continued with reference points. Therefore both 3D models were superimposed with the reference points onto the *Catia* model. Here also a significant accuracy difference between the two methods could be recognised. Depending on the base position and reference point, a minimum of 0.36 mm and maximum of 0.805 mm positioning error was recognised for the PPnP method. The error for the robot-based method was much higher. The minimum and maximum error were 1.307 mm and 2.067 mm respectively. In figures 3.61, 3.62 the results are illustrated. The selected white points in these figures are constructed reference points and the centre of bright spots (marked as white circle) thermal image represents the same reference points. Due to chipping at these reference points the thermal property is different from the neighbouring surface area. It should be noted that the selection of the middle point of this bright spot was manual. This may lead

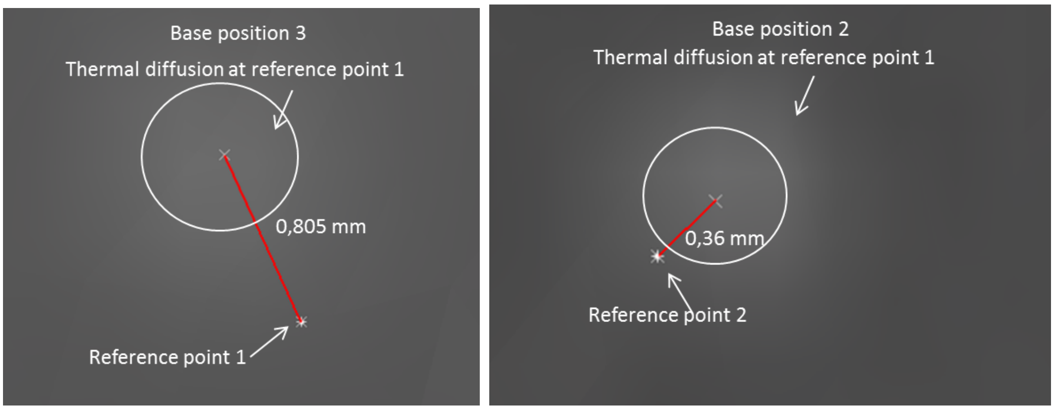

(a) At reference point 1 and base position 3 (b) At reference point 2 and base position 2

Figure 3.61: Min. and Max. error with PPnP method

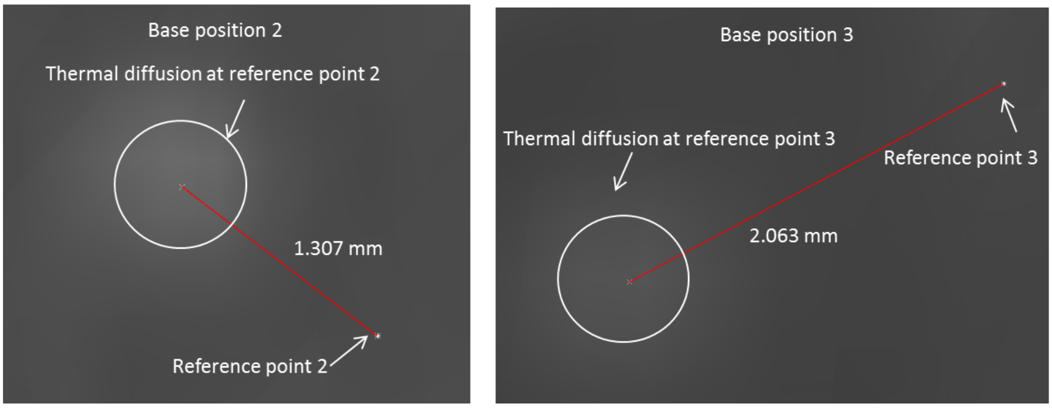

(a) At reference point 2 and base position 2 (b) At reference point 3 and base position 3

Figure 3.62: Min. and Max. error with robot-based method

to varying of the error number a little. Despite of these measurement limitations, it could be shown that the PnP-based method achieved better accuracy. Due to the extraordinarily small 3D mapping error, it is difficult to distinguish the chain of error, as in the previous chapter where an average 0.13 ° TCP tilt angle error was registered along with the robot's absolute inaccuracy.

3.8.4 Conclusions

In this series of tests, the most important elements of the error chain were analysed, especially for the robot-based method. In addition to the absolute robot accuracy investigation in 6D, the influences of geometric and hand-eye calibration could be determined. Since both the absolute robot accuracy and TCP inaccuracy in all three directions and orientations affect the total error of 1.3 mm for the robot-based method, it was difficult to separate the absolute error contribution for each influence. Especially when it comes to TCP determination, it can be said that a better approach or measuring equipment is needed to determine the minor difference, which is in less than one mm range. Although the robot-based method in this test series had achieved the minimum accuracy of 1.307 mm, it can be improved by already recognisable optimisation potentials such as using a laser-tracker-based absolute robot position while determining the TCP. Thus a doubling of the accuracy is conceivable. This kind of external-sensor-based TCP determination needs to be done only once and does not affect robot-based thermography measurement. The PnP-based method has achieved 0.3 mm minimum accuracy and can be used without hesitation for automated processes.

Chapter 4

3D thermography evaluation and defect localisation

The 2D evaluation method is still considered the only way for industrial application. Although 2D thermal imaging is able to quantify the defects in a component, much of the related information in the overall context is not taken into account. This is due to the following drawbacks of 2D evaluation: defect sizes and positions are not accurate for the measured 3D component because of distortions caused by transforming 3D world to 2D representation [94], and thermogram depends on the view of the camera. For a large number of thermal images, which is in general the case for a large component, 2D evaluation of every single image is time-consuming and error-prone, and critical clues can be overlooked. The 3D therography model described in the last chapter may deliver the solution for these drawbacks. Therefore, in this section the evaluation of a component by means of a 3D thermography model will be demonstrated and the Possibilities for improvement will be identified. The same small demopanel (see section 3.7) was used for the evaluation. The model was generated with the developed LHM method. The aim of the investigations presented is to evaluate the internal laminate quality by means of automated thermography test methods. The knowledge of the type and distribution of anomalies enables qualitative and quantitative statements about the component quality.

4.1 Thermography measurement of component

Characteristics of demopanel

As part of a series of tests, the component was manufactured automatically from thermoplastic prepregs material. According to CPD designs, all thermoplastic unidirectional prepregs layers were automatically detected with a camera-based method and placed on the mould at the defined position. The first and all other layers were fixed to each other for the preform process using an ultrasonic spot-welding method. The welding spots were automatically calculated according to the layer geometry.

This has resulted in a cluster of welding spots in some places. Figure 4.1(a) represents the automated manufactured preformed layup. In the yellow-marked circles, layers were fixed with the ultrasonic welding method. The placed artificial flaws in this layup can also be observed in this figure. For the thermography investigation and traceability of the defect detection depth, artificial defect anomalies were placed in positions and in the pre-defined depth between layers. Therefore, prior to this, a defect plan was drawn up for the insertion of the artificial defects with polypropylene film and aluminium foil. Figure 4.2 represents the plan for artificial defects according to position in sub-figure (a) and their depth in sub-figure (b). Accordingly, polypropylene films and aluminium foils were placed at the intended locations prior to consolidation. The numbers in figure 4.2(a) represent the size and position of the flaws, while the depth positions are illustrated as small black lines in figure 4.2(b). Figure 4.1(c) represents the theoretical composition of the artificial flaws and CFRP layers. To produce the artificial defects or flaws, polypropylene films and aluminium foils were cut at the edges as circle and square form in the sizes 6 mm, 9 mm, 12 mm and 15 mm. These flaws were intended to represent artificial delamination. The component was then consolidated in the oven under vacuum.

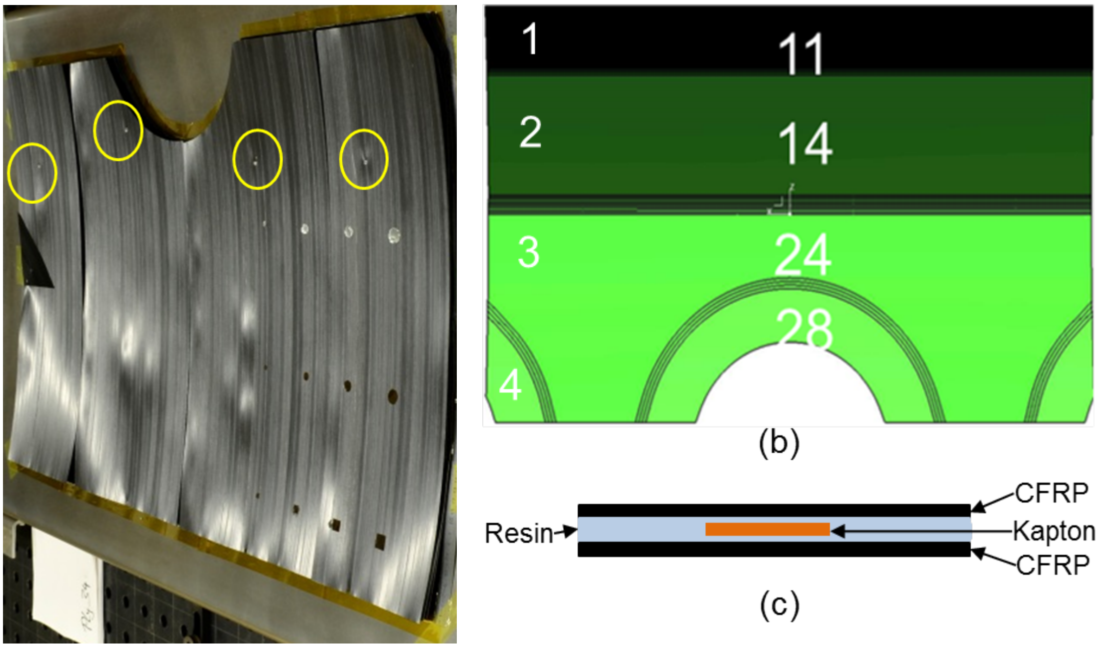

Figure 4.1: (a)Preforming of thermoplastic layup by ultrasonic welding process; (b) Ply-sequences; (c) Theoretical composition of the artificial flaws and CFRP layers

This type of delamination is mostly used for the evaluation of acoustic processes. However, due to the manufacturing process, there were deviations in the sizes. It is therefore to be expected that small flaws will hardly be detected at greater depth. In the new layer structure there are a total of four steps (see Figure 4.1(b)) with an overlap area. The individual layers are approx. 0.2 mm thick. This results in a

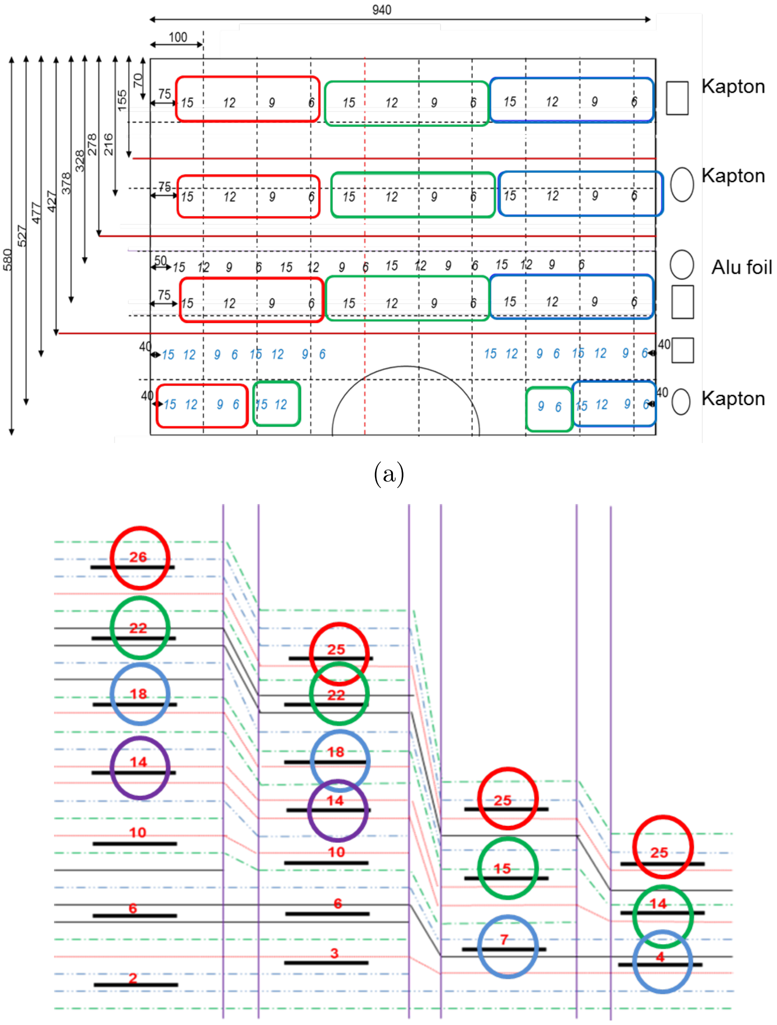

(a)

(b)

Figure 4.2: Plan for artificial defects: (a) Positions and sizes; (b) Artificial defects between different layers

thickness of 2.2 mm in area 1 with 11 layers, 2.8 mm in area 2 with 14 layers, 4.8 mm in area 3 with 24 layers and 5.6 mm in area 4 with 28 layers. Between area 2 and 3 there is a certain overlap area, which represents a contentious step-less transitional zone. The thickness of the component was measured randomly after curing. For example, the component is more than 6 mm thick in area 4 instead of 5.6 mm. This indicates poor consolidation. The first flaw step is at approx. 0,36 mm deep. The aim of this investigation is to detect both artificial defects as well as natural defects such as porosity, delamination or influences of ultrasonic welding.

Measurement

To carry out the measurements, the parameters must first be set. Basically, there is no difference between the measurements in the transmission and reflection arrangements, since 3.9the mathematical approach and the solution are the same. Since the thermal penetration depth depends on the frequency, the depth information is obtained in the reflection arrangement. This means stepwise information depending on the frequency selection. However, since the thermal wave propagates in all directions, and faster in the fibre direction than perpendicular to the fibre, the heat flows faster laterally than perpendicularly. This reduces the depth contrast or phase difference. In a transmission arrangement, the heat is conducted from the rear wall to the front wall. The thermographic camera captures all the heat emitted from the front wall. Since the thermal wave interferes several times more between the interfaces in the transmission arrangement than in the reflection arrangement, the phase images appear very noisy in transmission. In order to get a good excitation signal, several preliminary experiments were performed with the camera settings, excitation powers and measurement parameters in the reflection arrangement, as the component was accessible from one side. The aim was to obtain measuring parameters by a homogeneous illumination and an even temperature over the measuring surface. Table 4.1 shows the optimal measurement parameters with the excitation frequency, the transient period and the measurement period listed.

Table 4.1: Measurement parameters

	Measurement parameters		
Measuring frequency f in Hz	0,4	0,1	0,05
Transient period	4	3	1
Measurement period	5	3	3
Transient time in s	10	30	20
Measurement time in s	12,5	30	60
Total measurement in s	22,5	60	80
Thermal depth μ in mm	0,56	1,12	1,59

In order to detect the defects in different depths, the following measuring frequencies were used: 0.4 Hz; 0.1 Hz; 0.05 Hz. Theoretically, the lower the frequency of the thermal waves are, the longer the measurement time and the deeper its penetration into the test specimen. Although the component is even thicker and even lower frequencies are required to examine the deeper layers, no additional knowledge could be obtained in preliminary tests due to the higher porosity content in the entire component. Therefore, the automated measurement was only carried out with these three frequencies. The depth determination by means of thermographic phase images is only possible indirectly. Since the thermal wave is a highly absorbed wave and it fades rapidly, flaws which lie behind a frequency-dependent maximum penetration depth μ are no longer recognisable or are difficult to recognise [95]. Thus for example with an excitation frequency of 0.4 Hertz, the induced manufacturing and artificial defects at a depth of approx. 0.56 mm are detected while excitation frequencies of 0.1 and 0.05 Hertz, respectively, are used to detect error anomalies up to an depth of 1.12 or 1.59 mm. These thermal depths are calculated by using the equation 1.1 (see on page 7). The thermal penetration depth μ is dependent on the thermal diffusivity α (approx. 0.004 cm^2/s for CFRP, perpendicular to the fibre) of the material and the excitation frequency ω. For each applied excitation frequency, the transient period and the measuring period were determined in such a way, that the measurement area was heated homogeneously to avoid noise effects. If the transient period is too long, the component is warm and noise increases during a short measurement period. The total measurement time can be calculated from the sum of the transient time and measurement time. As described in the previous chapter, 30 measurement fields were required for a 550 mm measuring distance to cover the complete area. For each measurement field, 3 phase images were generated according to measuring frequency. In total, 90 phase images needed to be evaluated. Amplitude was kept constant. Furthermore, the lateral heat flow mentioned above prevented continuous measurement. In order to avoid this influence, the measuring positions were shifted. Thus on the one hand, the measurement time remained the same, and on the other hand, measurement was ensured at all measurement positions. All three 3D thermography models according to thermal depth are evaluated in next section. The 3D thermography models according to their depth were generated with a developed system, especially here with the LHM approach. All three thermography models are illustrated in figures 4.3, 4.4 and 4.5. Thermography measurement results are analysed and validated with CT measurements results in section 4.2.

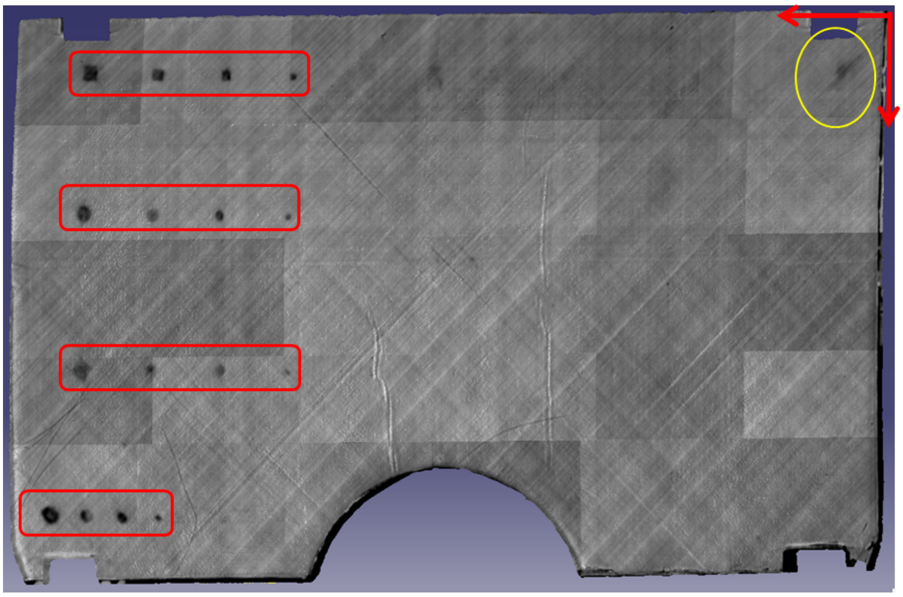

Figure 4.3: Measuring frequency 0.4 Hz and 0.56 mm thermal depth

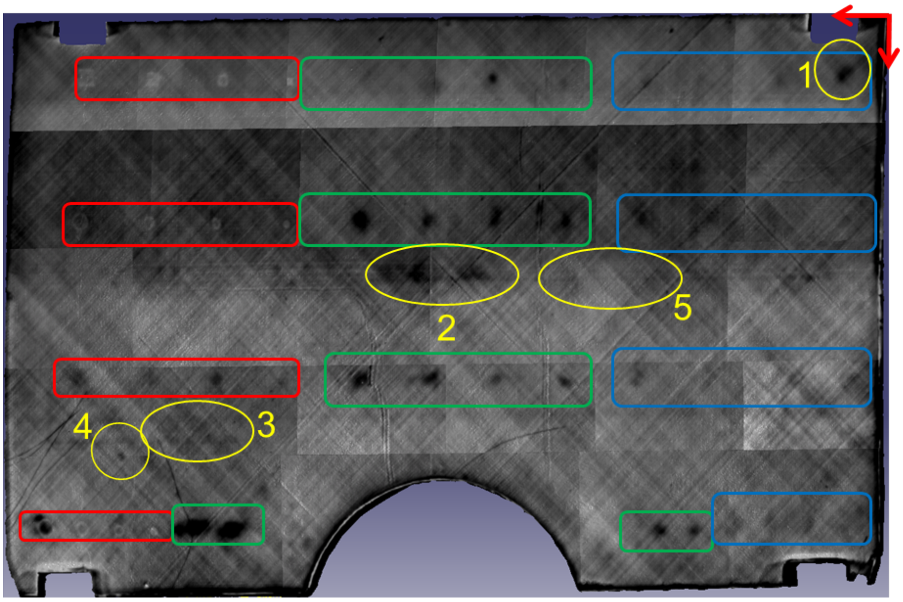

Figure 4.4: Measuring frequency 0.1 Hz and 1.13 mm thermal depth

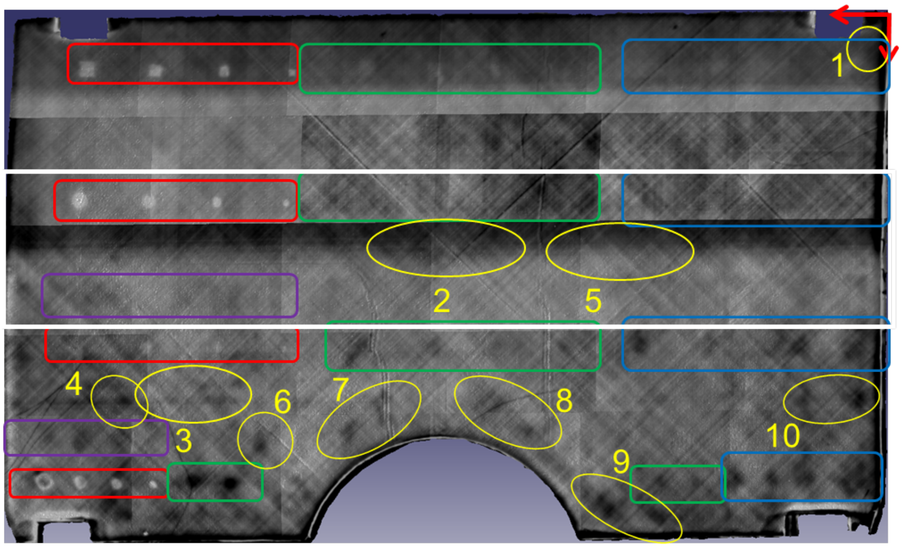

Figure 4.5: Measuring frequency 0.05 Hz and 1.59 mm thermal depth

4.2 Measurement analysis on basis of 3D thermotomography model

Regarding to the evaluation process, an improvement was achieved through a 3D visualisation of all 2D images for each depth. It would be convenient if all this depth information could be visualised layer-wise (e.g. like computer tomography) as an assembly, so that defect depths are resolved and documented in a way that the

NDT specialist will get better knowledge about defect propagation in depth. For such a representation this software would become more complicated, because some functions like buffer needs to be implemented for it to work. Additional measurement toolboxes are required to measure defect sizes and the defect positions in relations to each other. An export possibility of textured 3D measurement models in a format that can be opened by most 3D applications is desirable. For 3D visualisation, the real surface was measured with T-scan and a surface with vertices was generated in *Catia* (see section 3 for more details). Furthermore, for the three thermal depths three offset surfaces (0.56 mm, 1.2 mm and 1.6 mm) with appropriate parameters were generated using *Catia* and exported as *stl* file. Hence it is easier to import these three 3D models again into *Catia*, as all these required functions are basic tools of *Catia*. There are many possibilities (e.g., as IGES file, collada format or VRML format) for importing these 3D thermography models into *Catia*. The Virtual Reality Modelling Language (VRML) [96] ISO 14772-1:1997 is the 3D format supported by most 3D viewers and tools [97]. With VRML, both static and dynamic scenes can be represented. Unlike many other non-commercial 3D formats, the 3D geometries can be linked to external media such as images, other 3D models or even films. As part of the master thesis [78], an export function was implemented. The Unicode plain text-based VRML data contains only the position data of the vertices (three vector indices) with the respective colour values related to part coordinates. Images are then mapped with their corresponding offset surfaces in the software and exported as VRML file format. This file contains all the information about image colours associated with 3D vertices along with their corresponding orientation and positions. The 3D thermo-tomography model is illustrated in figure 4.6.

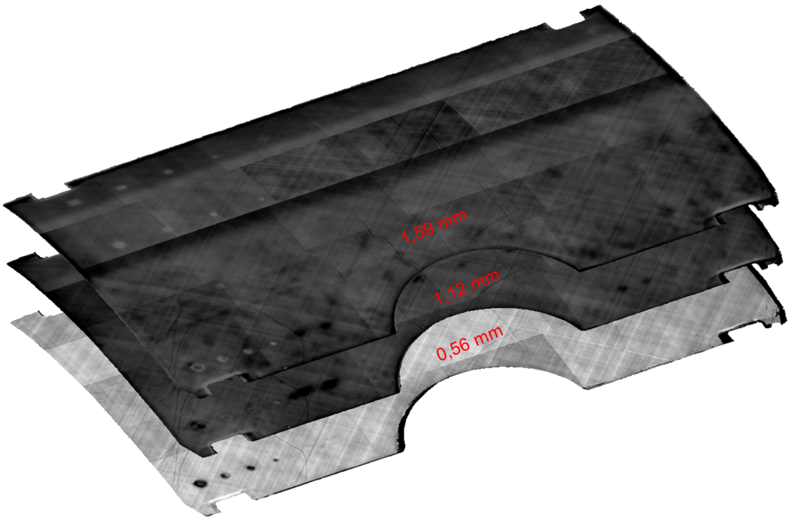

Figure 4.6: 3D thermo-tomography model

This 3D thermo-tomography model represents measurement results according to the desired thermal depth and can also be analysed, e.g., by measuring defect size and position in 3D, using the *Catia's* measurement functions. This thermo-tomography model represents a simplified version of a real computer tomography model. Evaluation of 3D damage propagation is now easier. The implanted kapton foil in different depths was detected with the chosen measuring frequency. To validate the evaluation results, a colleague in Stuttgart also conducted an examination using computer tomography and the water-coupled ultrasonic (WCUS) method. WCUS results were evaluated according to various absorption criteria (thick and thin areas) (see figure 4.7(b)). The component was tested with WCUS from both the tool side and from the Peel-Ply side due to the poor back-wall echo. Figure 4.7(b) shows that the component is very porous in areas 3 and 4 (blue areas). Areas 1 and 2, on the other hand, look better consolidated. Neither artificial defects nor signs of cluster weld spots are visible. In CT measurement, the entire X-ray beam penetrates the object to be measured and strikes the surface detector. During the measurement, the object is placed in the X-ray cone and rotated 360 °. Meanwhile, two dimensional projections are recorded. With the help of mathematical calculation algorithms, these two-dimensional images are reconstructed in 3D. However, one has to make sure that the sample does not collide with the detector and X-ray tube. The spatial resolution or detail detectability (voxel size) depends on the width of the test object and the selected distance between detector and X-ray tube. The smaller the sample is, the greater the spatial resolution. Further details about the CT system can be found here [98]. Since the component was large, the whole component could be measured in 5 runs, and later everything was assembled by hand. The assembled result is illustrated in figure 4.7(a). S1 to S5 represent these 5 runs.

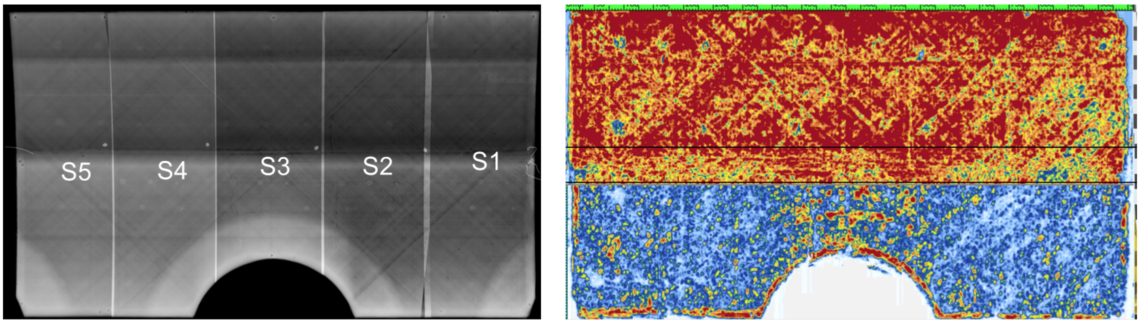

(a) (b)

Figure 4.7: (a) Computer tomography and (b) water-coupled ultrasonic measurement

Evaluation

For the evaluation of the thermographic images, the artificial and manufacturing-induced defect areas were marked with red, green, blue and yellow colours on the models. The red, green and blue markings represent the same markings of the defect plan. Figure 4.3 shows up to 0.56 mm depth over the entire surface a homogeneous structure. This also means that consolidation is good to this depth. A comparison with CT images showed good correlation. Also the artificial defects, which lie at approx. 0.4 mm depth (see red circles in figure 4.2(b)), are all detected. The contours of the defects are clearly visible due to lower lateral thermal flow in fibre direction. Furthermore, a natural anomaly is visible in the upper right corner (yellow marked). The shift in phase angle in the yellow-marked area is due to delamination, which could be confirmed by CT measurement. The direction of the individually placed unidirectional layers to this depth is clearly visible. In addition, these fibre directions appear with a slight phase angle shift (light and dark). The small phase difference in all phase images is most probably due to the manufacturing tolerance of the raw material. In the UD material, the fibre matrix volume content varies across the surface. This typical internal variation of the material can cause a slight phase angle shift.

If one evaluates the 3D model with 0.1 Hz measurement in the green marked areas (see figure 4.4), the next deepest defects are recognisable. Although the artificial defects in the area marked in blue are outside of the thermal penetration depth, there are slight signs of some defects. If the measurement is compared with the previous measurement in figure 4.3, an inhomogeneous structure can be seen over the entire surface. It can be assumed that the upper layers from the Peel-Ply side are better consolidated than in the lower areas. The defect coutures are also not easily recognisable due to the high porosity content. The defects appear much larger, especially in the area marked in green on the bottom left in figure 4.4. If one compares this area with the CT result in figure 4.9 image S4I8, the porosity over the artificial defects is recognisable. A frequency of 0.4 Hz does not conduct the thermal wave to the rear wall. But at lower frequency an indication (through bright and dark areas) of the difference in thickness within the measuring area is recognisable in figures 4.4 and 4.5. This is due to a higher phase shift in the thicker area than in the thinner area. Dr. Spiessberger [95] proved this effect through experiment in his Ph.D thesis. At this contact position (air/component), the thermal wave can hardly be transmitted because of the air. This results in a high phase shift at thin points in the lower frequency range. By measuring with the lower frequency, e.g. 0.1 Hz, the thermal wave is conducted to the back wall in the thin area. In addition, in a few areas the phase angle shift is as high as the artificial defects, which are yellow-marked and labelled with numbers in figures 4.4 and 4.4. These yellow marker defects can be found with the same identification in the CT results (see figures in 4.8 and 4.9). Because of the presence of thickness difference, a continuous step-less transitional zone and two different types of defects (aluminium and Kapton), the white marked area (see in figure 4.5) was by far the most complex area for thermography measurement.

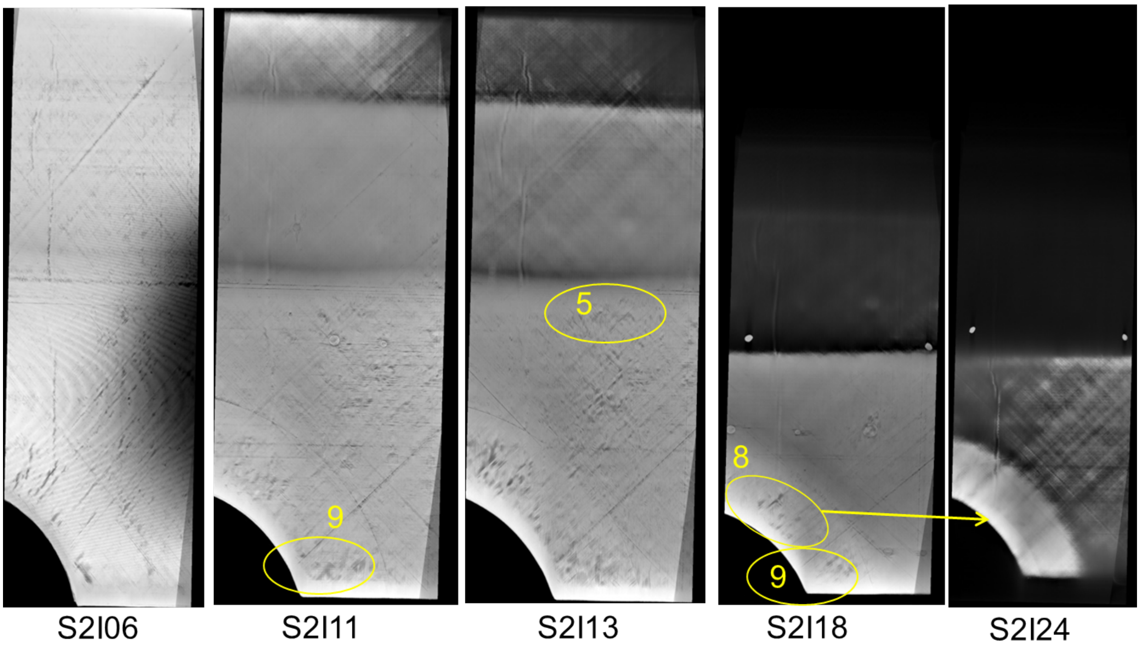

Figure 4.8: CT Measurement results in sections S2 according to their image depth

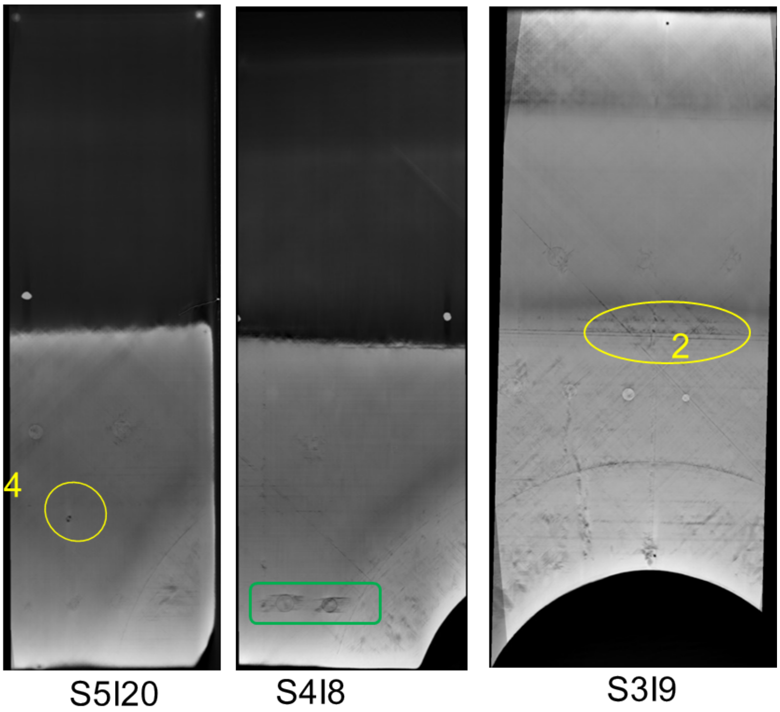

Figure 4.9: CT Measurement results in sections S5, S4 and S3 according to their image depth

Both artificial defects (aluminium foil and kapton foil) indicate a similar phase shift. At least in this noisy phase image, the slight thermal contrast difference between aluminium and kapton is difficult to distinguish. If the frequency is reduced, the best thermal contrasts can only be set in one range because of the thickness differences. If one compares this transitory area, especially in the yellow-marked areas 2 and 5, with the CT results in figure 4.8 (S1B9) and figure 4.9 (S2I8), a high porosity is recognisable. Also, the manufacturing-induced defects in yellow-marked area 4 (see figure 4.3) can also be seen in figure 4.9 on image S5I20. Further examination of figure 4.5 now shows the defects in the blue-marked area more clearly. At the same time, more inhomogeneous areas, which are marked as yellow, enhance their appearance. Further defects could be detected by reducing the frequency. But previous experiment showed negative results, as the component contains high porosity at this depth. The contours of all the artificial defects are poorly recognisable, as a deformation of the defect geometry clearly occurs, especially at lower frequencies. Higher thermal conductivity of the material parallel to the fibre direction leads to a faster heat diffusion in said direction and thus to a spread of the defect contrast.

Conclusions

The inserted defects and also manufacturing-induced defects could be detected. It is known that the detection probability in lock-in thermography is different for different materials and different defect types. Although the thermal difference between CFRP and polypropylene is less than in air, all defects could be identified in a reflection arrangement up to 1.6 mm depth. Normally, this type of flaw is used to qualify the acoustic procedure. The author of [99] had investigated the behaviour of thermal waves in homogeneous layered plates with inserted teflon foils under convective conditions. The selection of this type of flaw is a very conservative approach for the characterisation of a delamination. In order to characterise the anomalies, further investigations must be carried out. In general, with non-destructive testing methods, it is difficult to characterise manufacturing-induced defects without prior knowledge of the component. Despite the difficulties, thermography was able to make better or more precise statements about the defect pattern than the WCUS method. Thermography results had a good match with computer tomography results. It showed that CT has the highest defect contrasts and high resolutions in the representation of inhomogeneity and air inclusions, but lock-in thermography was also able to visualise or detect almost all hidden structural properties. Considering that lock-in thermography can also be used on every component on site and has a high potential for automation, it can be highly recommended as a method for quality assurance during and after the production of CFRP components. However, CT measurements to verify the thermographic results in the initial phase of component qualification play a very important role.

4.3 Superimposed 3D thermo-tomography model

A generally applicable method to enhance 3D thermo-tomography model data carrying depth-related information is presented; in this context, all equations and approaches required for other data fusions are derived. Both the PnP and the robot-based methods can be utilised for laboratory circumstances or for industrial applications at high resolution, but are conveniently usable for large components. Using a 3D model and thermal image data fusion allows the quantification of manufacturing uncertainly, facilitating more precise evaluation and the localisation of defects. Moreover, these models can be superimposed on all other design information, for example, on construction and simulation data. Manufacturing information depending on process step as well as concession information can also be superimposed on a 3D thermo-tomography model. To make a prediction about the service life of a component, the component must be examined and documented over its entire life cycle. Some of these types of documents are still on paper and are prone to errors. Furthermore, the investigations are carried out in different locations. The digital documentation presented here offers the possibility of directly comparing examination results with other data by superimposing this 3D thermo-tomography model on all other data.

Taking the knowledge that derives from detailed documentation allows improvement of the manufacturing process know-how. This should lead to a closed manufacturing loop and therefore a continuous improvement. Consequently an improved rework rate is the outcome. All items mentioned above will put pressure on the development of future NDT to achieve the desired cost efficiency [100].

Within the framework of this test series, the above-mentioned further evaluation possibilities for industrial application were exemplarily demonstrated. The component was designed and manufactured with a manufacturing and engineering edge. After thermography measurement, the component was trimmed along the engineering edge with a water jet system. Ultrasonic weld spots were also automatically generated in *Catia* for preform production. All this information was superimposed on *Catia* and illustrated in figure 4.10. The red and green lines represent the engineering and manufacturing edges accordingly. White spots as single points and clusters are welding positions. By superimposing the two data sets, any influences from the welding points could be determined. The white cross spots in figure 4.11 show the TCP positions of robot movements for the thermography measurements. These points were taken to generate an offline robot program. The circles and squares in different sizes and positions illustrate the plan of inserted artificial defects. One could imagine here that the natural defects that occur during production can also be marked in the same way. In this experiment, the contours and positions of the artificial flaws were manually constructed. In the future, a software program will be able to do this by automatically identifying defects and highlighting critical defects. In this way it is also possible for a preform process to compare the fibre angles of the individual layers and between the layers with the simulation model. In

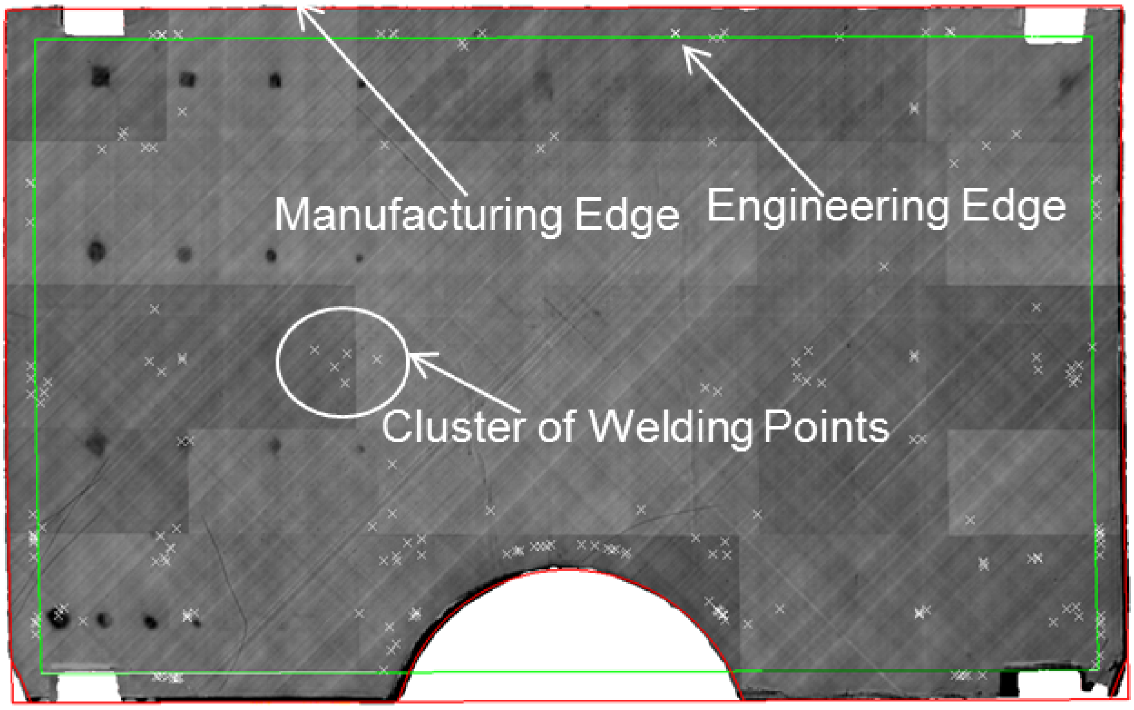

Figure 4.10: Superimposed 3D thermography model with predefined welding positions

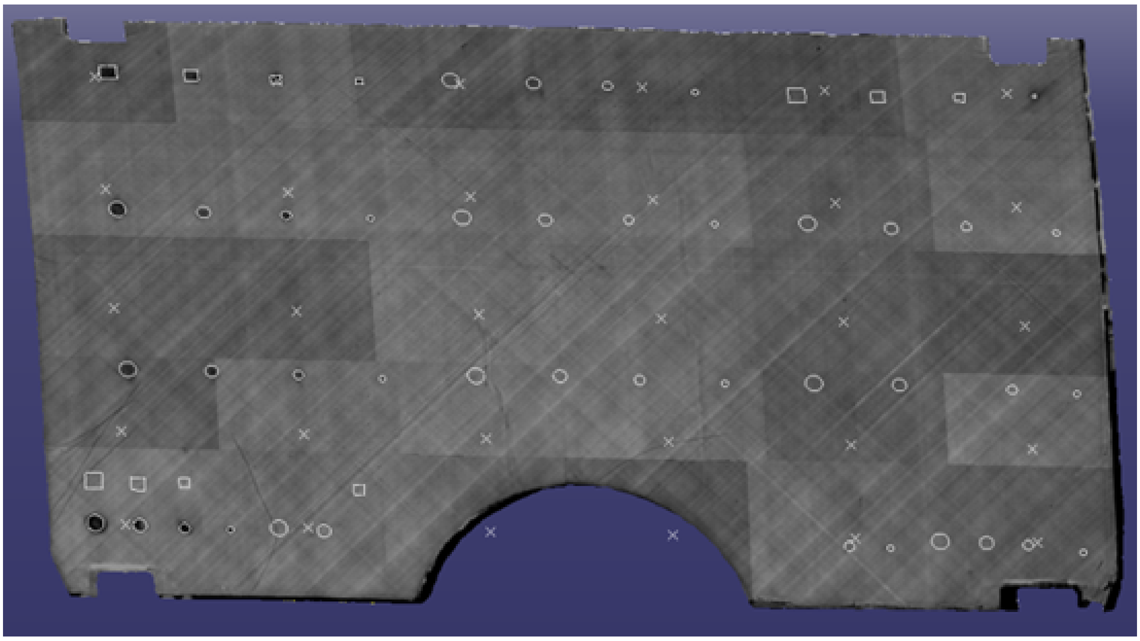

Figure 4.11: Superimposed 3D thermography model with defect size and positions

addition to superimposing all data, the defect positions and sizes can be projected onto the component using the laser projector. This increases accuracy and saves enormous time for a worker who roughly marks the positions on a large component for further processing. For demonstration purposes, for example a few contours of those defects were projected onto the component at the correct position (see in the figure 4.12).

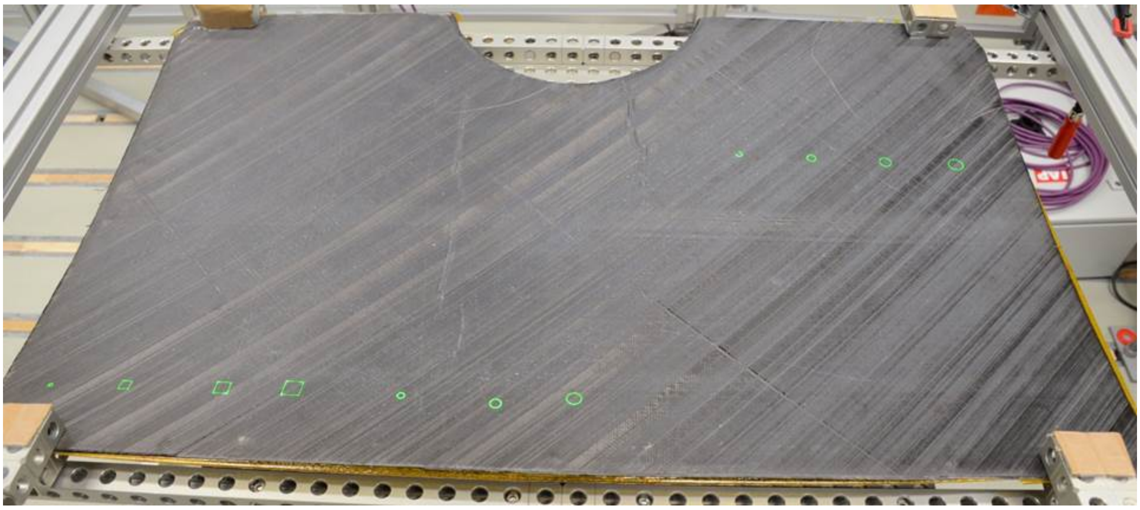

Figure 4.12: Contactless 3D defect size and position localisation

Chapter 5

Conclusions and Outlook

With the increasing demand for fibre composite materials, the 3D-thermo-tomography method has made a significant contribution to the automated use of non-destructive thermography testing. Thus large and complex aeronautical structures can be examined cost-effectively, more quicker (large measuring area at once) and results are reproducible. The robot-based automated inspection method and 3D-visualisation of all results fulfil important industrial requirements, such as a high inspection speed and simple handling and reliability, with the resulting evaluation in 3D with highest conformity. It is therefore competitive to and offers a clear advantage over established NDT methods such as the water coupled ultrasonic method, as shown in a direct comparison in chapter 4.

For this purpose, a customised thermography end-effector was developed, and, it demonstrated the feasibility of automated lock-in thermography in the context of manufacturing process chain observation, especially at different process steps, e.g., at the preform stage as well as cured parts. For automated testing, a prototypical digital workflow was designed and a minimalist process control implemented to select measurement parameters via robot guidance. The individual process steps of automated inline thermography were described. A detailed system accuracy analysis was then carried out and the possible source of error identified. Especially in the case of robot-based 3D thermography, the absolute accuracy of the robot could be determined. Among the influencing factors, which were examined individually in chapter 2, were positional deviations due to the changed mass and centre of gravity. By the exact determination of the load data, 1 mm to 3 mm positional deviations can be minimised to a negligible amount. However, for technical reasons it is not possible to completely avoid the influence of temperature (1.25 mm absolute inaccuracy was determined through the experiment in section 2.4.2), since articulated gear groups of the kinematic chain generate heat under load and lead to time dependent changes with angles. It was observed [85] that the motor temperature of the robot only becomes stable after 1 to 2 hours at a certain constant load. This would limit the flexibility of a process if the thermal drift is not addressed. Besides the system accuracy of automated thermography, deficiencies in evaluation and in

the visualisation method towards automation were identified.
In order to overcome these limitations the automated process was then extended and two improvement concepts to retrieve a 3D thermography reconstruction were presented, investigated and evaluated. Method one projects predefined 3D points per measuring field by using a laser projector and applies a 2D-3D point correspondence algorithm. The second method uses the robot pose, and a kinematic-coordinate relationships algorithm is applied to the images. For both methods, single thermal images were captured by using a thermography camera, which is also used for NDT. The first method is suitable for research and development as well as for production inspection with or without using a robot for camera positioning, while the second method requires a robot and is thus suited only for fully-automated inspection lines. The first method also enables contactless localisation of detected defects.
It was shown that the used laser projector does not have sufficient power to heat several points simultaneously for detection with the thermography camera. Therefore, individual points were projected. This deficit can be overcome by program structure, by high laser power, by using several laser projectors at the same time or by an even more sensitive thermography camera. In this work, it could be shown that the projected contour size and the camera distance (up to 250 mm) to the component are dependent on each other when detecting the laser point. For a reliable laser-point detection, smaller circles with 0.1 mm diameter and the largest possible camera distance is recommended. The correlation value in this test series was between 70% and 80%. According to test results (see chapter 3.2), the deviation at a camera distance of approx. 500 mm is one pixel. According to equation 3.2, maximum 1 pixel deviation in one direction represents approx. 0,27 mm. With a sub-pixel detection accuracy, this error can be reduced further.
Geometric and hand-eye calibration proved to be an important building block for the 3D reconstruction of all thermographic images. The *matlab Calibration Toolbox* was used to perform the geometric calibration (intrinsic parameters) and the necessary process steps were developed from it. This toolbox was extended to execute hand-eye calibration (extrinsic parameters). The influencing parameters of the method for the achieved ±0.07 pixel error were analysed in section 3.4. Both methods were adopted for 3D reconstruction. Later in section 3.8, the accuracy of both methods was again examined in the context of 3D reconstruction. Here a ±0.12 pixel error from geometric calibration was achieved. No measurable positioning errors could be determined from hand-eye calibration, but 0.13 °orientation inaccuracy was obtained for 550 mm working distance, which led to a pointing error of 1.24 mm. As the angular deviations are extraordinary small and within the measurement equipment tolerance range, it was difficult to identify the absolute tilt angle of the TCP. These influences are the scope of further investigations, since a more precise determination of the TCP has a significant influence on robot-based 3D reconstruction. It could be shown that the determined TCP from the camera calibration lies at the principal point.
Afterwards, the DLT method was applied to calculate the projection matrix (the

location and the orientation of the object with reference to the camera) out of the 2D-3D corresponding data set. Using three experimental setups, the first one on a single-curved component, the second on a double-curved component and the third on a large single-curved component (fuselage), the laser-point-based method was validated. One laser projector was used for the first two components and two projectors were used for the fuselage. The results confirm the feasibility of the new concept. The 3D points were not coplanar due to the double curvature of the pressure bulkhead and the selection of a large measuring distance for the fuselage. The issue was investigated on a thermoplastic fuselage skin with increasing laminate thickness together with the robot-based method.

For the implementation of the robot-based 3D reconstruction method, the relatively flat thermoplastic fuselage skin was tested automatically. For the 3D evaluation, artificial flaws were inserted into the component. The previously implemented DLT method brought errors by generating the 3D model from measurement results, because the projected corresponding 3D points were coplanar. Therefore in the next experiment alternative, PnP methods like LHM, EPnP and PPnP were implemented, which considered orthography and a scaling factor. All these methods were then compared and evaluated. A preliminary analysis showed better accuracy for the PnP method. It should be noted, that the measured base position was not accurate, which had a direct influence on the robot-based method. Therefore a further investigation was performed with a Ureol component which had no fringed edges. The experiment was repeated at three positions and both methods were applied. 0.36 mm minimum absolute accuracy was achieved with the PnP method, whereby the minimum error for robot-based method was 1.307 mm. At the same time the robot-based method had better relative accuracy between two images.

After implementation of both 3D reconstruction methods, the thermoplastic component with artificial flaws was thermographically examined with three different measuring frequencies. For every measuring frequency a 3D modelwas generated according to its thermal depth. Afterwards all this information was imported in *Catia* and a 3D-thermo-tomography model was generated. Furthermore, other manufacturing and engineering information was superimposed on this model. The component was then evaluated with the superimposed model, and, the 3D position of the detected defects was determined and projected with the laser projector on the component. With the superimposed model it was possible to analyse the manufacturing influences from the preform process on consolidation. Thus closed-loop manufacturing could be successfully demonstrated by QA. All defects up to 3 mm depth could be detected. Further deeper defects could not be detected due to the high porosity content. At the test part, comparing the thermography measurement results with CT and US measurement, the advantages of the automated 3D-thermo-tomography model could be emphasised. Above all, the measurement time for the thermography measurement is significantly shorter than for the other two methods. In addition, the method is very easy to use for both highly curved components and large simple components. Thus an important process step for the automation of robot-based 3D thermography measurement and evaluation for variable products could be established.

If one considers the diagram 1.4 for closed-loop manufacturing through QA in the section 1 "Scope of the work", one may notice that all of the building blocks in this diagram were dealt with in this work. Of course, some topics were researched in depth and some topics were only superficially investigated. Special topics such as real surface reconstruction from point clouds, data preparation for the 3D reconstruction of measurement data, the automatic data analysis method, and the merging of all types of data were only discussed briefly. The more accurate the mesh generation of the real surface is, the more accurate the 3D reconstruction of the measurement results will be. In this work, the accuracy of both methods was cross validated in one use case.

The 3D-thermo-tomography method used in this thesis was carefully considered and parts of the results published. Nevertheless, detailed improvements are still possible in the methods and further questions arise on the basis of this work:

- It was observed that the laser projector used here does not have sufficient power to detect several points simultaneously with the thermography camera. Therefore, individual points were projected. Effect of a high laser power or by simultaneous application of several laser projectors, or by an even more sensitive thermography camera needs to be analysed, in order to optimise the performance of PnP method.
- Until now, 3D points were defined manually in CAD. This step should be improved by mathematical approaches in the future.
- In this work, the goal was to detect the laser point with a template matching algorithm. Basically, that algorithm searches for the laser spot in a black and white picture by comparing it with an ideal laser spot template. The main outputs of the algorithm are the center (x- and y-component) of the detected laser spot and the percentage of how good the ideal template fits the real image of the spot. This percentage match is assumed to be the most important indicator of how precise the center of the laser spot could have been determined. As a first attempt, a 32 x 32 template image had been created by hand. Thereby it could had been reached percentages of round about 72.6% in average. So in future the percentage match could be increased by using a new template, which is generated according to a Gaussian distribution function or Empirical template, or by additionally processing the original images with several filters like Median blurring, Gaussian blurring or 2D Convolution beforehand.
- In the future, the developed technologies need to be analysed in further use cases, in order to ultimately standardise the technology. This could ensure sustainable product quality and manufacturing costs.

Bibliography

[1] C.-P. LU, G. D. Hager†, and E. Mjolsness‡§, “Fast and Globally Convergent Pose Estimation from Video Images,” *IEEE Transactions on Pattern Analysis and Machine Intelligence*, vol. 22, no. 6, 2000.

[2] S. R. N., S. T.G.A., R. K.P., and R. G.V.V., “Carbon Composites are becoming competitive and cost effective,” tech. rep., External Document copyright(C) 2018 Infosys Limited, Sept 2014.

[3] M. L. Jay, “Rise of the robots,” 5th Sept 2017. `http://compositesmanufacturingmagazine.com/2017/09/composites-industry-will-benefit-from-robotics-and-automation`.

[4] W. A. K. Deutsch, M. Stahlber, R. Kattwinkel, M. Joswig, and M. Rödding, “Ultraschall-Tauchtankprüfung von Stangen für Luftfahrt-Anwendungen,” in *DGZfP-Jahrestagung 2014 – Poster 24*, 2014.

[5] G. Sakas, L.-A. Schreyer, and M. Grimm, “Preprocessing and volume rendering of 3D ultrasonic data,” *IEEE Computer Graphics and Applications*, vol. 15, pp. 47–54, Jul 1995.

[6] S. I. Nikolov, J. P. G. Gonzaléz, and J. A. Jensen, “Real time 3D visualization of ultrasonic data using a standard PC,” *ELSEVIER, Ultrasonics*, vol. 41, no. 6, pp. 421–426, 2003.

[7] CompositeWorld, “Facc receives boeing qualification for active thermography,” 21th Aug 2017. `https://compositesworld.com/news/facc-receives-boeing-qualification-for-active-thermography`.

[8] U. Siemer, *Einsatz der Thermografie als zerstörungsfreies Prüfverfahren in der Automobilindustrie.* PhD thesis, Naturwissenschaftlich-Technischen Fakultät III, Chemie, Pharmazie und Werkstoffwissenschaften der Universität des Saarlandes, Saarbrücken, 2010.

[9] G. Mahler and C. Eitzinger, “Konzeption und Aufbau einer robotergestützten Plattform für optisch angeregte Wärmefluss-Thermografie,” in *DGZFP, Thermografie-Kolloquium 2013, Vortrag 14*, 2013.

[10] E. Wiedemann, T. Scholz, R. Schott, J. TIsch, and A. Wolf, "First Utilization of Energy Transfer in Structured Light Projection - Infrared 3D Scanner," in *Key Engineering Materials, Volume 613*, May 2014.

[11] F. Jonietz, R. Krankenhagen, M. Noack, K. Geschenke, and E. Wiedemann, "3D-Formbestimmung mit integrierter thermografischer Qualitätsprüfung," in *DGZFP, Thermografie-Kolloquium*, 2017.

[12] V. Carl and K. Eisler, "3D-Formerfassung im Infraroten und Sichtbaren sowie Techniken zum Visualisieren," in *DGZFP, Thermografie-Kolloquium 2011, Vortrag 18*, 2011.

[13] G. Cardone, A. IaniroGe, nnaro dello Ioio, and A. Passaro, "Temperature maps measurements on 3D surfaces with infrared thermography," *Experimental in Fluids*, vol. 52, pp. 375–385, Feb 2012.

[14] J. Schlichting, *Integrale Verfahren der aktiven Infrarotthermografie.* PhD thesis, Verkehrs- und Maschinensysteme der Technischen Universität Berlin, 2012.

[15] M. Rahamer, *Nachweis von Impact-Schäden in Faserkunststoffverbunden mittels Resonanter Frequenzsweep Thermografie.* PhD thesis, Verkehrs- und Biotechnik der Universität Stuttgart, 14.03.2018.

[16] G. Riegert, *Induktions-Lockin-Thermografie - ein neues Verfahren zur zerstörungsfreien Prufung.* PhD thesis, Luft- und Raumfahrttechnik und Geodäsie der Universität Stuttgart, 29.03.2007.

[17] F. Ciampa, P. Mahmoodi, F. Pinto, and M. Meo, "Recent Advances in Active Infrared Thermography for Non-Destructive Testing of Aerospace Components," in *SENSORS, MDPI*, 16 Feb. 2018.

[18] Infretec, "The high-end infrared camera imageir® 9300." `https://www.infratec.eu/thermography/infrared-camera/imageir-9300/`.

[19] T. Schmidt and S. Dutta, "CFRP manufacturing process chain observation by means of automated thermography," in *5th International Symposium on NDT in Aerospace*, 13-15th November 2013, Singapore.

[20] L. Beyer, *Genauigkeitssteigerung von Industrierobotern.* PhD thesis, Von Fachbereich Maschienenbau, Universität der Busdenwehr Hamburg, 29.10.2004.

[21] T. Bongardt, *Methode zur Kompensation betriebsabhängiger Einflüsse auf die Absolutgenauigkeit von Industrierobotern.* PhD thesis, Lehrstuhl für Werkzeugmaschinen der Technischen Universität München, 02.09.2003.

[22] O. Gossel, *Steigerung der Genauigkeit von Industrierobotern basierend auf einer durchgängigen Genauigkeitsanalyse.* PhD thesis, Technische Universität Hamburg-Harburg Arbeitsbereich Werkzeugmaschinen und Automatisierungstechnik, 1996.

[23] S. Dutta, Prof. Dr.-Ing. K. Drechsler, Prof. Dr.-Ing. M. Kupke, Dr. A. Schuster, and J.-P. Tuppatsch, "Automated single view 3D Texture Mapping and Defect Localisation of Thermography Measurements on large Components utilising an industrial robot and a laser system," in *14th Quantitative InfraRed Thermography Conference*, 2018.

[24] S. Dutta and T. Schmidt, "New concept for higher Robot position accuracy during thermography measurement to be implemented with the existing prototype automated thermography end-effector utilising an industrial robot and laser system," in *12th Quantitative InfraRed Thermography Conference*, 07-12th July 2014, University of Bordeaux.

[25] V. Stephen and M. Peyman, "A handheld 3D thermography system for energy auditing," *Energy and Buildings, Science Direct, Elesvier*, pp. 445–460, Feb 2014.

[26] A. S. Jordt, "Selbstkalibrierung eines Kamerarobotersystems," Master's thesis, Christian-Albrechts-Universität zu Kiel, Germany, 2008.

[27] M. Drust, *Entwicklung eines Sensorsystems und eines Verfahrens zur Berechnung der Roboterpose auf Basis von projizierten Strukturen.* PhD thesis, Von der Fakultät Konstruktions-, Produktions- und Fahrzeugtechnik der Universität Stuttgart, 27.07.2016.

[28] M. Ulrich, A. Forstner, and G. Reinhart, "High-accuracy 3D image stitching for robot-based inspection systems," *2015 IEEE International Conference on Image Processing (ICIP)*, December 2015.

[29] R. A. Boby and S. K. Saha, "Single Image based Camera Calibration and Pose Estimation of the End-effector of a Robot," *IEEE International Conference on Robotics and Automation (ICRA)*, June 2016.

[30] L. Pèrez, Ínigo Rodríguez†, N. Rodríguez†, R. Usamentiaga, and D. F. García, "Robot Guidance Using Machine Vision Techniques in Industrial Environments: A Comparative Review," in *Sensots*, 05th March 2016.

[31] L. Laser, "Cad-pro - the laser template projector for industry and small businesses." `https://www.lap-laser.com/general-industries/projection/laser-projectors/cad-pro`.

[32] Y. H. †and K. ichi Anjyo †Kiyoshi Arai, "Tour into the picture: using a spidery mesh interface to make animation from a single image," in *SIGGRAPH Proceedings of the 24th annual conference on Computer graphics and interactive techniques*, 1997.

[33] A. Criminisi, I. Reid, and A. Zisserman, "Single View Metrology," in *Department of Engineering Science, University of Oxford Oxford, UK, OX1 3PJ.*

[34] P. F. Sturm and S. J. Maybank, "A Method for Interactive 3D Reconstruction of Piecewise PlanarObjects from Single Images," in *British Machine Vision Conference 1999*, 1999.

[35] P. E. Debevec, C. J. Taylor, and J. Malik, "Modeling and Rendering Architecture from Photographs: A hybrid geometry- and image-based approach," tech. rep., Computer Science Division, University of California at Berkeley, Jan 1996.

[36] J. A. M. Flores, "Basic Geometric Transformations in 2D and 3D," A Tutorial, published 2012.

[37] J. Corso, "Geometric Camera Calibration," EECS 598-08 Fall 2014, Foundations of computer vision.

[38] C. Stachniss, "A short Introduction to Homogenous Coordinates, Robot Mapping." Universität Freiburg, Autonomus Intellegent Systems, Lecture notes.

[39] H. Schwarz and M. Pilop, "Mathematische Grundlagen, Räume, Koordinatensysteme, Projektionen." Humboldt Universität Berlin, Institur für Informatik, Lecture notes, WS 2002/2003.

[40] S. Jokel, "3-dimensionale Rekonstruktion einer Tischszene aus monokularen Handkamera-Bildsequenzen im Kontext autonomer Serviceroboter," Master's thesis, Universität Hamburg, Germany, 2006.

[41] V. Larsson, "Computational Methods for Computer Vision." LUND University, Autonomus Intellegent Systems, Lecture notes, published 2018-01-01.

[42] G. Wang and J. Wu, *Guide to three Dimensional Structure and motion Factorization.* Springer-Verlag, London Limited, 2011.

[43] J. Beyerer, L. F. Puente, and C. Frese, *Automated Visual Inspection: Theory, Practice and Applications.* Springer-Verlag, Machine Vision, 2016.

[44] D. Kostić, "Introduction Robotics," WTB Dynamics and Control, September - Oktober 2009.

[45] V. Lepetit, F. Moreno-Noguer, and P. Fua, "EPnP: An Accurate O(n) Solution to the PnP Problem," *International Journal of Computer Vision*, vol. 81, 2009.

[46] V. Garro, F. Crosilla, and A. Fusiello, "Solving the PnP Problem with Anisotropic Orthogonal Procrustes Analysis," *IEEE: Second Joint 3DIM/3DPVT Conference: 3D Imaging, Modelling, Processing, Visualization and Transmission*, 2012.

[47] J. H. Challis, "A Procedure for Determining Rigid Body Transformation Parameters," *J.Biomechanic, Elsevier Sceince Ltd.*, vol. 28, no. 6, 1995.

[48] K. S. Arun, T. S. Huang, and S. D. Blostein, "Least-Squares Fitting of two 3-D Point Sets," *IEEE Transactions on Pattern Analysis and Machine Intelligence*, vol. PAMI-9, no. 5, 1987.

[49] D. W. Eggert, A. Lorusso, and R. B. Fisher, "Estimating 3-D rigid body transformations: a comparison of four major algorithms," *Machine Vision and Applications, Springer Verlag*, vol. 9, 1997.

[50] C. Olsson, "Lecture 3: Camera Calibration, DLT, SVD," 2013.

[51] N. Ho, "Finding optimal rotation and translation between corresponding 3d points," Last visited: 02.04.2019. `http://nghiaho.com/?page_id=671`.

[52] R. Y. Tsai, "A Versatile Camera Calibration Techniaue for High-Accuracy 3D Machine Vision Metrology Using Off-the-shelf TV Cameras and Lenses," *IEEE Journal of Robotics and Automation*, vol. RA-3, August 1987.

[53] H. Malm and A. Heyden, "Simplified Intrinsic Camera Calibration and Hand-Eye Calibration for Robot Vision," *Proceedings of the 2003 IEEE/RSJ Intl. Conference on Intelligent Robots and Systems*, August 2003.

[54] O. D. Faugeras, *Three-Dimensional Computer Vision: A Geometric Viewpoint.* The MIT Press, 1993.

[55] Z. Zhang, "Flexible camera calibration by viewing a plane from unknown orientations ," *Seventh IEEE International Conference on Computer Vision*, 20-27 Sept. 1999.

[56] T. Schmidt, "Hand-eye-calibration of a robotized thermography end-effector," in *6th International Symposium on NDT in Aerospace*, 2014.

[57] Jean-Yves.bouguet, "Camera calibration toolbox for matlab," Last visited: 11.11.2018. `http://robots.stanford.edu/cs223b04/JeanYvesCalib/index.html#parameters`.

[58] C. Wengert, "Hand-eye calibration addon for the matlab camera calibration toolbox," Last visited: 11.11.2018. `https://github.com/christianwengert/calib_toolbox_addon`.

[59] J. Heikkilä and O. Silvén, “A Four-step Camera Calibration Procedure with Implicit Image Correction ,” *Proceedings of IEEE Computer Society Conference on Computer Vision and Pattern Recognition*, June 1997.

[60] R. Y. Tsai and R. K. Lenz, “A new technique for fully autonomous and efficient 3D robotics hand/eye calibration ,” *IEEE Transactions on Robotics and Automation*, vol. 5, June 1989.

[61] T. Schmidt and C. Frommel, “Geometric calibration in active thermography applications,” in *19th World Conference on Non-Destructive Testing*, 2016.

[62] T. Schmidt and C. Frommel, “Geometric calibration for thermography cameras,” in *7th International Symposium on NDT in Aerospace*, 2015.

[63] D. C. Brown, “Decentering Distortion of Lenses,” *Photometric Engineering*, vol. 32, no. 3, pp. 444–462, 1966.

[64] H. González, S. L. Jorge, J. Armesto, and P. Arias, “Calibration and verification of thermographic cameras for geometric measurements,” *Elsevier, Infrared Physics and Technology*, pp. 92–99, January 2011.

[65] T. Luhmann, J. Ohm, J. Piechel, and T. Roelfs, “Geometric Calibration of Thermographic Cameras,” *International Archives of Photogrammetry, Remote Sensing and Spatial Information Sciences*, vol. XXXVIII, no. 5, 2010.

[66] R. Yang, W. Yang, Y. Chen, and X. Wu, “Geometric Calibration of IR Camera Using Trinocular Vision,” *IEEE, Journal of Lightwave Technology*, vol. 29, pp. 92–99, December 2011.

[67] A. Ellmauthaler, E. A. B. da Silva, C. L. Pagliari, and J. N. Gois, “A Novel Iterative Calibration Approach for Thermal Infrared Camera,” *IEEE International Conference on Image Processing*, 15-18 September 2013.

[68] S. Prakash, P. Y. Lee, T. Caelli, and T. Raupach, “Robust Thermal Camera Calibration and 3D Mapping of Object Surface Temperatures,” *Proceedings of SPIE - The International Society for Optical Engineering*, 8th April 2006.

[69] S. Y. Cheng, S. Park, and M. M. Trivedi, “Multiperspective Thermal IR and Video Arrays for 3D Body Tracking and Driver Activity Analysis,” *IEEE Computer Society Conference on Computer Vision and Pattern Recognition (CVPR’05) - Workshops*, 21-23 September 2005.

[70] S. Vidas, R. Lakemond, S. Denman, C. Fookes, S. Sridharan, and T. Wark, “A Mask-based Approach for the Geometric Calibration of Thermal-Infrared Cameras,” *IEEE Transactions on Instrumentation and Measurement*, vol. 61, June 2012.

[71] P. Bagavac, "LOCK-IN THERMOGRAPHY IMAGE PROCESING," 2016.

[72] Y. C. Shiu and S. Ahmed, "A Mask-based Approach for the Geometric Calibration of Thermal-Infrared Cameras," *IEEE Transactions on Robotics and Automation*, vol. 5, pp. 16–29, February 1989.

[73] R. Horaud, B. Conio, O. Leboulleux, and B. Lacolle, "An analytic solution for the perspective 4-point problem," *Proceedings CVPR '89: IEEE Computer Society Conference on Computer Vision and Pattern Recognition*, June 1989.

[74] B. S. Manjunath, "Homework 3: Computation of the Camera 1 Matrix Solution," Lecture notes, published 2004.

[75] R. Hartley and A. Zisserman, *Multiple View Geometry in computer vision*, ch. 4.1 The Direct Linear Transformation (DLT) algorithmy, pp. 88–93. Cambridge University Press, New York, 2000.

[76] P. Keller and S. Dutta, "A new application for texture mapping using 2D-3D correspondences," Master's thesis, Julius-Maximilians-Universität Würzburg Institut für Informatik, Germany, 2016.

[77] S. Dutta, "Robotergenauigkeit Verwendung verschiedener Koordinatensysteme und deren Auswirkung," tech. rep., Institut für Bauweisen und Strukturtechnologie, Zentrum für Leichbau und Produktionstechnologie, Juni 2015.

[78] J.-P. Tuppatsch and S. Dutta, "Implementierung von Roboter-Bezugssystemen in eine Software zur 3D-Visualisierung von Lock-in-Thermografien," Master's thesis, Technology Arts and Sciences TH Köln, Germany, 2018.

[79] S. Urban, J. Leitloff, and S. Hinz, "PnP - A Real-Time Maximum Likelihood Solution to the Perspective-n-Point Problem," *ISPRS Annals of Photogrammetry, Remote Sensing and Spatial Information Sciences*, vol. 3, pp. 131–138, 2016.

[80] Z. Yinqiang, S. Shigeki, and O. Masatoshi, "ASPnP: An Accurate and Scalable Solution to the Perspective-n-Point Problem," *IEICE Transactions on Information and Systems*, vol. 96, pp. 1525–1535, July 2013.

[81] J. A. Hesch and S. I. Roumeliotis, "A Direct Least-Squares (DLS) Method for P*n*P," *International Conference on Computer Vision*, Nov 2012.

[82] S. Li, C. Xu, and M. Xie, "A Robust *O(n)* Solution to the Perspective-*n*-Point Problem," *IEEE TRANSACTIONS ON PATTERN ANALYSIS AND MACHINE INTELLIGENCE*, vol. 34, July 2012.

[83] P. H. Schönemann, *A generalized solution of the orthogonal procrustes problem.* Psychometrika, Sprinhger Link, 1966.

[84] G. Schweighofer and A. Pinz, "Roboust Post Estimation from a Planar Target," *IEEE TRANSACTIONS ON PATTERN ANALYSIS AND MACHINE INTELLIGENCE*, vol. 28, December 2006.

[85] A. Schuster, *Autonomes System zur Herstellung von Organoblechen und Preforms*. PhD thesis, Mathematisch-Naturwissenschaftlich-Technischen Fakultät der Universität Augsburg, 2015.

[86] S. Dutta, "Absolute Genauigkeit bei der Basevermessung," tech. rep., DLR ELIB, Sept 2014.

[87] F. Krebs, "Automatische Werkzeug Vermessung," tech. rep.

[88] S.-W. Shih, Y.-P. Hung, and W.-S. Lin, "Accuracy analysis on the estimation of camera parameters for active vision systems," *IEEE Computer Graphics and Applications*, August, 1996.

[89] R. Kumar and A. H. Hanson, "Sensitivity of the Pose Refinement Problem to Accurate Estimation of Camera Parameters," in *Proceedings the Third International Conference Computer Vision*, 1990.

[90] J. ZC and Lai, "On the sensitivity of camera calibration," *ELSEVIER, Image and Vision Computing*, vol. Volume 11, no. Issue 10, December 1993.

[91] Duane.C.Brown, "Close-range camera calibration ," *Photogrametric engineering*, vol. 37, no. 8, 1971.

[92] OpenCV and D. team, "Camera calibration and 3d reconstruction," 10th Nov 2014. `https://docs.opencv.org/3.0-beta/modules/calib3d/doc/camera_calibration_and_3d_reconstruction.html`.

[93] J.-P. Tardif, P. Sturm, M. Trudeau, and S. Roy, "Calibration of Cameras with Radially Symmetric Distortion," *IEEE Transactions on Pattern Analysis and Machine Intelligence*, vol. 31, 2009.

[94] S. Ekanayake, C. Isenberg, and R. H. Schmitt, "Method for quantitative 3D evaluation of defects in CFRP using active lock-in thermography," *2017 ElSEVIER 1st Cirp Conference on Composite Materials Parts Manufacturing, cirp-ccmpm2017*, vol. 66 (2017), p. 254 – 258, 2017.

[95] C. Spißberger, *Merkmalsanalyse mit thermischen Wellen in der zerstörungsfreien Werkstoff und Bauteilprüfung*. PhD thesis, Von der Fakultät Luft- und Raumfahrttechnik und Geodäsie der Universität Stuttgart, 05.09.2012.

[96] VRML, "The virtual reality modeling language," 24.04.2018. `https://www.web3d.org/x3d/specifications/vrml/ISO-IEC-14772-VRML97`.

[97] X3D and VRML, “The most widely used 3d formats,” 24.04.2018. `http://www.web3d.org/x3d-vrml-most-widely-used-3d-formats`.

[98] R. Jemmali, “Computertomographie (ct),” DLR/Stuttgart. `https://www.dlr.de/bt/desktopdefault.aspx/tabid-2488/3746_read-10098/`.

[99] W. Bai and B. S. Wong, “Evaluation of defects in composite plates under convective environments using lock-in thermography,” *Measurement Science and Technology*, vol. 12, no. 2, 2001.

[100] J. Sloan, “Carbon fiber emphasizes automation in composites manufacturing,” 11th June 2017. `https://www.compositesworld.com/news/carbon-fiber-emphasizes-automation-in-composites-manufacturing`.